

16. Validation of multiphase flow models

Engineering science is associated with solving the right equations with known accuracy. But how to judge whether the equations are right and how to estimate the accuracy of the solution?

16.1 Introduction

Creating computer codes for numerical integration of systems of partial differential equations governing multiphase multicomponent flows is an important part of scientific activities in the last 30 years. Whatever the result of such activity is, it has to be validated for a class of practical applications. The validation is a complex process consisting of many elements. The first question asked in this case is: is the adequate equation set solved properly? To answer the question several iteration steps are necessary. The formal check whether the numerical algorithm provides the expected results is usually performed on simplified mathematical benchmarks that possess analytical solutions. Order-of-magnitude estimates and global balances that have to be fulfilled are very important in more complex cases. The verification of computer codes for more complex processes is mainly associated with an experimental data base on two different levels. The closure correlations are usually based on separate effect experiments. The system behavior in which a variety of the elements of the computer code are interacting is checked on system experiments.

There is no absolute proof for the validity of a computer code solving complex problems in the multiphase dynamics. There is only increasing trust in the results obtained by an increasing number of successful predicted experiments.

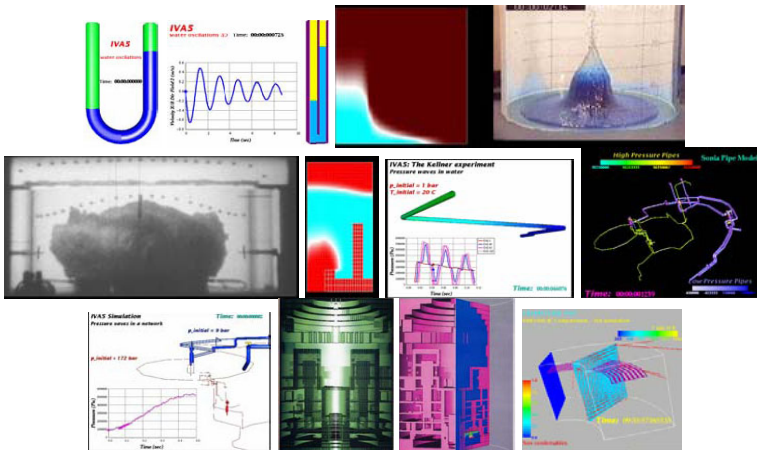
Note that the falsification for a given class of problems is much easier than the verification. That is why this critical step has to be taken first. Then verification in general is not possible because of the variety of complex combinations between processes. The so-called fitness for purpose strategy is the common one used in science and technology. This strategy is usually performed after the basic formal tests and the separate effect tests are completed. It contains selection of experimental data for the class of problems of interest and comparisons of the code predictions with them. In the case of success, or after removing misconceptions and errors and then reaching successful prediction, the code is considered to be verified for this particular class of applications. There is an enormous amount of experimental activity worldwide for collecting experimental data for different applications. The review of this process is beyond of the scope of this chapter. This chapter provides a small number of selected analytical benchmarks and experimental tests and gives an example of how predictions of the computer code IVA compare with these data. The code is based on the methods described in the five volumes of this monograph.

16.2 Quick look at IVA computer code

Transient 3D-multiphase flows consisting of many chemical constituents in nature and technology (Figs. 16.2.1 and 16.2.2) are the common case of flows. In many technical applications we have to deal with particular realization of the multiphase flows like steady-state flows, or single-component flows or single-phase flows, etc.



Fig. 16.2.1 The fascinating picture of the discovery start, the peace of the universe, the tornado, the volcano, the flows in the human heart or even the “pure” water or the sky in the picture of Van Gogh are in fact different forms of multiphase flows



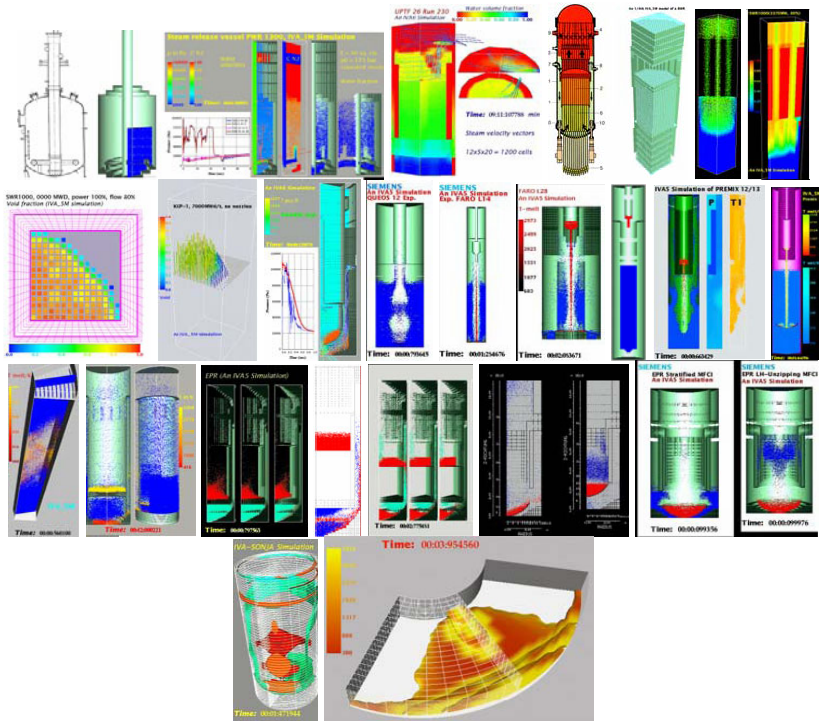


Fig. 16.2.2 Examples of multiphase flows in the nuclear technology, see <http://www.herzovision.de/kolev-nikolay/>

IVA is a computer code for computational simulation of transient multiphase flows based on three multicomponent velocity fields in porous structure that may change its geometry in time. The foundations of the computer code IVA allows applications for mathematical simulation of variety of processes. From two-phase gas-plasma multicomponent hydrogen detonation in a pipe network with dissociation of the gases, Fig. 16.2.3, through condensation water–steam shock waves in complex pipe networks, Fig. 16.2.4, gas solution and dissolution in liquids, dissolved gas release from water in pipe network and gas-slug formation and transport, Fig. 16.2.5, diesel injection problems, Fig. 16.2.6, particles sedimentation in water, Fig. 16.2.7, turbulent mixing and transport in a NPP sump, Fig. 16.2.8, thermite injection by high-pressure steam–hydrogen mixture into air environment, melt–water interaction in postulated SWR 1000 severe accidents, alumina melt jet dropped into a subcooled water, urania melt jet dropped in water, Fig. 16.2.9, void formation in existing-, Fig. 16.2.10, or future boiling water reactors, Fig. 16.2.11, all this demonstrates the capability of a single model architecture to handle different material systems, different intensities of interactions, and a large variety of the spatial and temporal scales of the simulated processes.

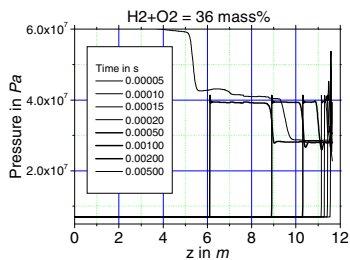


Fig. 16.2.3 Pressure as a function of the distance for different times after the ignition [1.11] p. 432

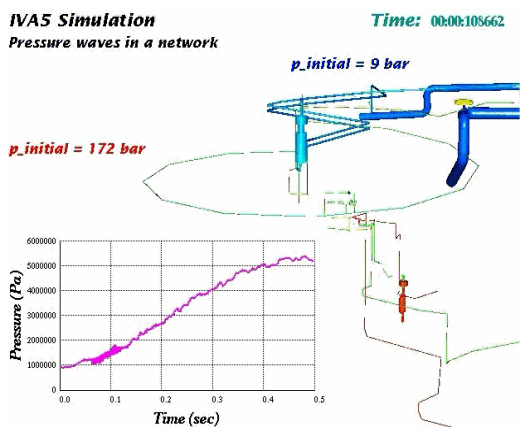
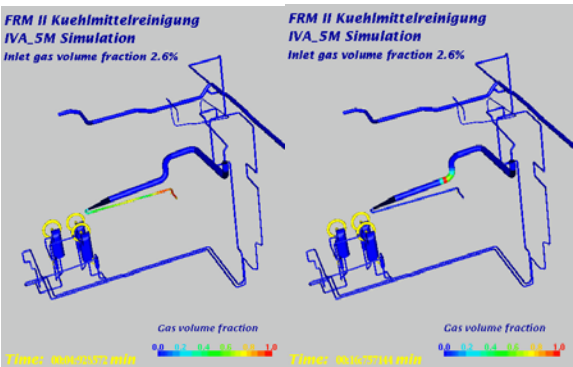


Fig. 16.2.4 Tube ruptures into a main recirculation pump seal water heat exchanger



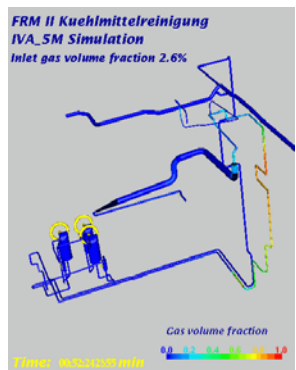


Fig. 16.2.5 Gas release from water in pipe network – gas-slug formation and transport

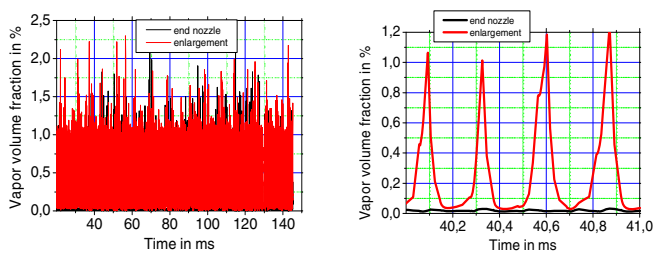


Fig. 16.2.6 Diesel vapor volume fraction at the end of a 300-μm diesel injection nozzle and at the enlargement immediately after the nozzle. The collapses damage the surface

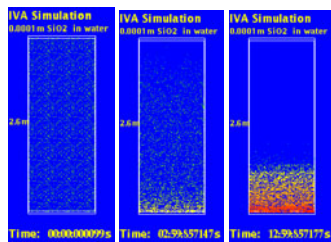


Fig. 16.2.7 Sedimentation of 100-μm sand particles (SiO₂). a) Initial state of 10% volume fraction of initially homogeneously distributed in a 2.6-m deep water pool; b) after 3 min; c) 13 min

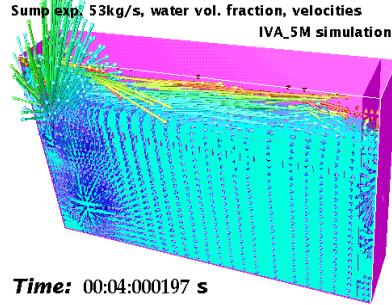


Fig. 16.2.8 Free fall of two phase jet into the left end of a water reservoir causing sloshing and mixing. Vortex burst and reflection at the wall

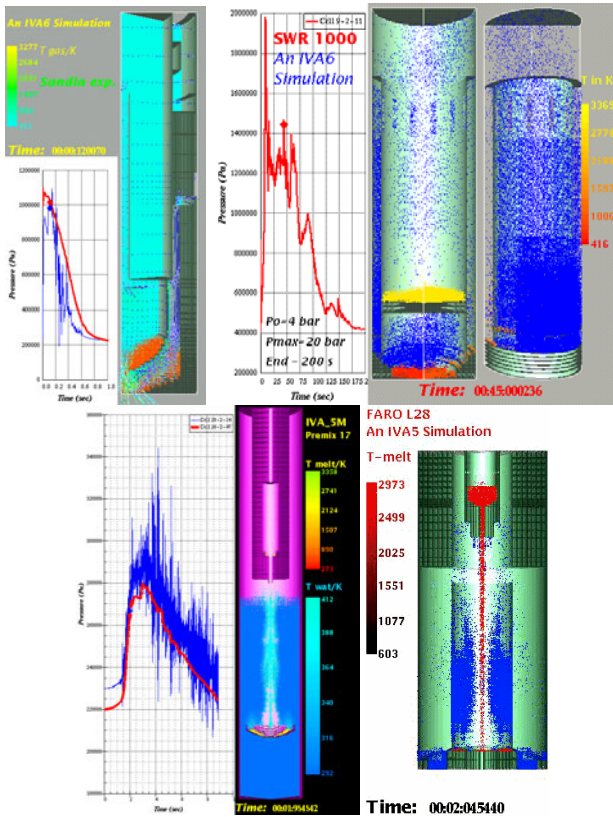


Fig. 16.2.9 a) Thermite injection by high-pressure steam–hydrogen mixture into air environment; b) Melt–water interaction in postulated SWR 1000 severe accidents; c) Alumina melt jet dropped into a subcooled water; d) Urania melt jet dropped in water

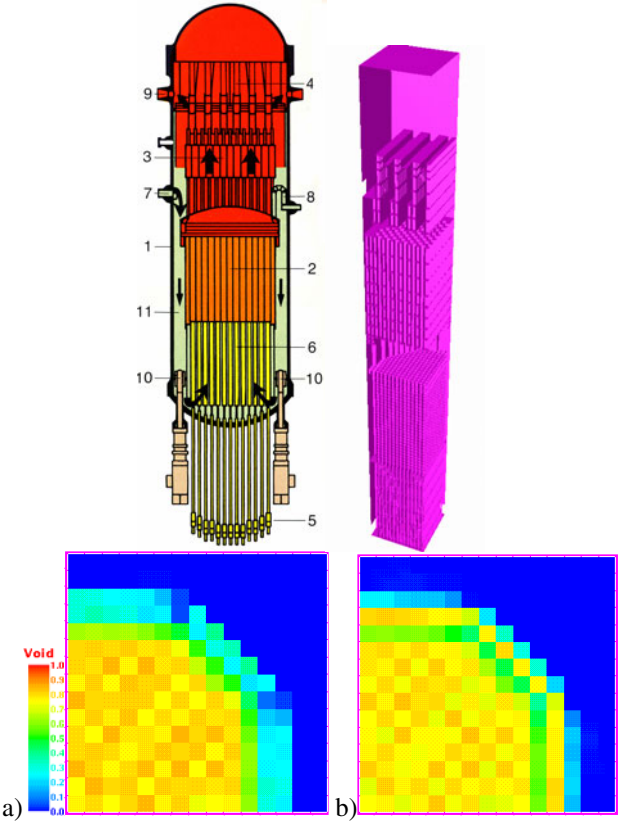
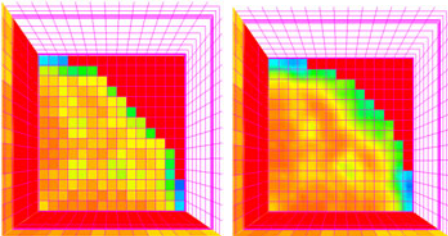


Fig. 16.2.10 Void at the exit of a core of BWR for the case (a) without additional nozzles and (b) with nozzles



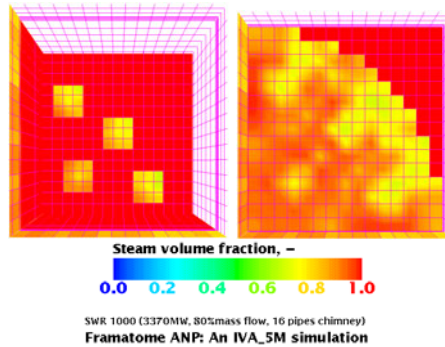


Fig. 16.2.11 Void fraction at different elevation inside a SWR 1000, case studies for different geometry

As already mentioned the flow in IVA model is described by means of three velocity fields. Each of the fields consists of several chemical components.

The first field presents gas mixtures of up to 13 real gases in addition to water vapor. The water-vapor properties are valid up to 2000 bar pressure and 6000 K temperature. The thermal dissociation of the vapor is taken into account. The gases may be air, nitrogen, helium, oxygen, carbon dioxide, methane, carbon oxide, hydrogen, ethane, propane, n-butane, sulfur dioxide and argon, in arbitrary combination. The number and the kind of the appearing components have to be specified as a part of the input. The components are allowed to move by turbulent or molecular diffusion inside the gas field in addition to the macro-scale movement in the space of the gas field. Hydrogen combustion single-step kinetics is available.

The gas components O_2 , N_2 , H_2 are allowed to be solved or dissolved by the liquid water component in the fields 2 and 3.

The second and the third velocity fields consist of liquid water and inert components of different species. In the limiting case of absence of water in one of these fields or in both of them the inert components are allowed to be a material either in a molten state, or in a solid–liquid equilibrium state, or in liquid state. One of the following inert materials may be chosen: uranium dioxide, nuclear reactor corium (mixture consisting of 76% UO_2 , 24% ZrO_2), zirconium, zirconium dioxide, stainless steel, aluminum dioxide, silicon dioxide, iron oxide, molybdenum, aluminum and boron oxide. If water is present in the fields 2 or 3 the inert component inside this field is solid, being in thermal equilibrium with the water (having the temperature of the water) and is allowed to move by turbulent or molecular diffusion inside the corresponding fields in addition to the macro-scale movement in the space. An example of such situation is boron oxide and water mixture used frequently in the nuclear reactor technology.

Each of the three velocity field possesses its own velocity and temperature. Thus, the flow is in a complete thermodynamical and mechanical nonequilibrium with all consequences for interfacial heat, mass and momentum transfer.

The fields are allowed to be continuous or disperse. The transition of the fields between continuum and dispersion as well as the local size of the dispersions are modeled by means of dynamic fragmentation and coalescence techniques.

$k-\varepsilon$ models for each field are available for modeling of multiphase flow turbulence. For the time being they are used for the continuous field with two-ways coupling to the dispersed phase.

Some special capabilities like computing of critical heat flux for bundles using a simplified method and successive initialization of the 3D model for refining the analysis is available. Another special feature is the modeling of cells as a cyclone and labyrinth-type separators with predefined characteristics.

The geometry of the space within which the flow is simulated is described either in Cartesian or cylindrical coordinates in a single block.

Another capability of the code is the description of multiphase flows in multiple interconnected blocks with boundary-fitted orthogonal grids.

In addition, pipe networks are simulated consisting of an arbitrary number of pipes and components like, pumps, valves, etc. The pipe network is connected with the three-dimensional space.

Local surface permeabilities in the three main directions and local volumetric porosities are defined as a function of time as for the 3D space. The same is valid also for the pipe network.

Inside the blocks different kinds of structure types can be simulated like heat-conducting 3D structures and/or heat transmitting 1D structures. The heat conducting 3D structures may have internal heat sources prescribed by the user. The structures are connected to the 3D flow in the 3D space, or to the pipe flow by complete heat-transfer mechanism including all known heat-transfer regimes to single-, two- and multiphase flows. Special kinds of structure like a nuclear reactor core can also be defined and simulated.

The numerical method used for integration of the system of the governing partial differential equations is: first-order donor-cell discretization for the convective terms, second-order central differencing for the diffusion terms, first-order time discretization, implicit. The method is characterized by a strong coupling between the velocity fields obtained by analytical reduction of the algebraic problem to a pressure equation and successive substitutions.

The code possesses powerful visualization systems, SONJA, for input processing, post-processing, on-line visualization and movie production.

IVA is written in FORTRAN 95 language and can run on all modern computers and platforms having this compiler. SONJA is written in C and works on platforms having this compiler and OpenGL. These may be either UNIX workstations or PCs under LINUX.

References documenting the IVA computer code development are given below.

16.3 References documenting the IVA-code development

- 1.1. Kolev NI (May 17–19 1984) Model of transient equilibrium three phase three component flow, 6-th National Conf. “Heat and Nuclear Energy Problems of People's Republic of Bulgaria” held in Varna, Bulgaria, p 37–42, in Bulgarian
- 1.2. Kolev NI (June 23–27, 1985) Transient three-phase three-component non equilibrium non homogeneous flow described by 1D-three-velocity fields slip model, Proc. Specialists Meeting on Small Break LOCA Analysis in LWRs, Pisa, vol 3, p 363–378
- 1.3. Kolev NI (1985), Transient one-dimensional equilibrium three-phase, three-component flow, Atomkernenergie/Kerntechnik, vol 47 no 3, p 198–203
- 1.4. Kolev NI (1986) Transient three phase three component non equilibrium non homogeneous flow, Nucl. Eng. Des., vol 91 p 373–390
- 1.5. Kolev NI (1986) Transient three-dimensional three-phase three-component nonequilibrium flow in porous bodies described by three-velocity fields, Kernenergie, vol 29 no 10, p 383–392. Also in (March 1985) Transiente Dreiphasen Dreikomponenten Stroemung”, Teil 1: Formulierung des Differentialgleichungssystems, KfK 3910, in German
- 1.6. Kolev NI (1987) Transient three-phase three-component non equilibrium non homogeneous flow described by 1D-three-velocity fields slip model, Atomkernenergie/Kerntechnik, vol 49 no 4, p 217–221. Also in (August 1985) Transiente Dreiphasen Dreikomponenten Stroemung”, Teil 2: Eindimensionales Schlupfmodell Vergleich Theorie-Experiment, KfK 3926, in German
- 1.7. Kolev NI (August 1987) A three field-diffusion model of three-phase, three-component flow for the transient 3D-computer code IVA2/01, Nuclear Technology, vol 78, p 95–131. Also in (1986) Transiente Dreiphasen Dreikomponenten Stroemung, Teil 3: 3D-Dreifluid-Diffusionsmodell, KfK 4080, in German, Also in (April 27–30, 1987) Proc. of the Int. Top. Meeting on “Advances In Reactor Physics, Mathematics And Computation”, Paris, France, vol 3, p 1899–1911
- 1.8. Kolev NI (1987) IVA-2 A computer code for modeling of three dimensional, three-phase, three-component flow by means of three velocity fields in cylindrical geometry with arbitrary internal structure including nuclear reactor core, Atom Energy, vol 63, pp 381–386. Also in (October 1986) Proc. of the int. seminar “Thermal physics 86” held in Rostock, German Democratic Republic, in Russian. Also in (September 26–30, 1988) Proc. of the Int. Seminar “Thermal Physics 88” held in Warsaw, Poland, in Russian. Also in (1986) KfK 4088, in German
- 1.9. Kolev NI (October 1988) IVA2 Verification: High pressure gas injection in a liquid pool, Nuclear Technology, vol 83 no 1 p 65–80. Also in (4–9 September 1988), Proc. of the First World Conf. Experimental Heat Transfer, Fluid Mechanics And Thermodynamics, Dubrovnik, Yugoslavia. Shah RK, Ganic EN, Yang KT eds, p 827–881. Also in (1987) KfK 4310, September in German

- 1.10. Kolev NI (March 23–24, 1989) IVA2 Application: Three dimensional effects during APWR LOCA, 7th Eurotherm Seminar, Thermal Non-Equilibrium in Two-Phase Flow, Rome, p 235–252. Also in (September 18–21, 1989) Multiphase Flow and Heat Transfer, Second International Symposium, Sian, China. Xue-Jun Chen, Veziroglu ZN, Tien CL eds., vol 2 p 949–958. Also in (September 1987) KfK 3419
- 1.11. Kolev NI (1989) A practical description of three-phase multi-component nonequilibrium flow by means of one dimensional multi-velocity field slip model, Kerntechnik, vol 54 no 3 p 186–190
- 1.12. Kolev NI (1990) Derivatives for the state equations of multi-component mixtures for universal multi-component flow models, Nucl. Sci. Eng., vol 108 p 74–87
- 1.13. Kolev NI (Sept. 1991) A three-field model of transient 3D multi-phase, three-component flow for the computer code IVA3, Part 1: Theoretical Basics: Conservation and state equations, numerics, KfK 4948, Kernforschungszentrum Karlsruhe
- 1.14. Kolev NI (Sept. 1991) A three-field model of transient 3D multi-phase, three-component flow for the computer code IVA3, Part 2: Models for the interfacial transport phenomena, code validation, KfK 4949, Kernforschungszentrum Karlsruhe
- 1.15. Kolev NI (Sept. 1991) IVA3: Computer code for modeling of three dimensional three phase flow in complicated geometry, Program Documentation: Input Description, KfK 4950, Kernforschungszentrum Karlsruhe
- 1.16. Kolev NI, Tomiyama A, Sakaguchi T (1991) Modeling of the mechanical interaction between the velocity fields in three phase flow, Exp. Thermal Fluid Sci., vol 4 no 5 p 525–545
- 1.17. Kolev NI (June 23–28, 1991) IVA3 Verification: Drag forces for three phase flow - comparison with experimental data, Proc. of the First World Conf. On Experimental Heat Transfer, Fluid Mechanics and Thermodynamics, Dubrovnik, Yugoslavia
- 1.18. Kolev NI (July 21–25, 1991) IVA3, A transient 3D three-phase, three-component flow analyzer, Proc. of the Int. Top. Meeting on Safety of Thermal Reactors, Portland, Oregon, p. 171–180. The same presented at (August 27 to 29, 1991) 7th Meeting of the IAHR Working Group on Advanced Nuclear Reactor Thermal-Hydraulics, Kernforschungszentrum Karlsruhe
- 1.19. Kolev NI (August 27 to 29, 1991) IVA3 Modeling of corium water interaction in deep pool, Presented at 7th Meeting of the IAHR Working Group on Advanced Nuclear Reactor Thermal-Hydraulics, Kernforschungszentrum Karlsruhe
- 1.20. Kolev NI (1993) Fragmentation and coalescence dynamics in multi-phase flows, Exp. Thermal Fluid Sci., vol 6 p 211–251
- 1.21. Kolev NI (1993), The code IVA3 for modelling of transient three-phase flows in complicated 3D geometry, Kerntechnik, vol 58 no. 3 p 147–156, Also in (October 5–8, 1993) Proc. of the Sixth Int. Top. Meeting on Nuclear Reactor Thermal Hydraulics, Grenoble, France
- 1.22. Kolev NI (1994) The influence of the mutual bubble interaction on the bubble departure diameter, Exp. Thermal Fluid Sci., vol 8 p 167–174
- 1.23. Kolev NI (1994) The code IVA5: Modeling of mass conservation in multi-phase multi component flows in heterogeneous porous media, Kerntechnik, vol 59 no 4–5 p 226–237
- 1.24. Kolev NI (1994) The code IVA5: Modeling of momentum conservation in multi phase flows in heterogeneous porous media, Kerntechnik, vol 59 no 6 p 249–258
- 1.25. Kolev NI (1995) The code IVA5: Second law of thermodynamics for multi-phase multi-component flows in heterogeneous media, Kerntechnik, vol 60 no 1 p 28–39

- 1.26. Kolev NI (1995) The code IVA5: Nucleation and flashing model, *Kerntechnik*, vol 60 no 2 p 157–164. Also in (April 3–7, 1995) Proc. Second Int. Conf. On Multiphase Flow, Kyoto; (August 13–18, 1995) ASME & JSME Fluid Engineering Conference International Symposium on Validation of System Transient Analysis Codes, Hilton Head (SC) USA; (October 9–11, 1995) Int. Symposium on Two-Phase Flow Modeling and Experimentation, ERGIFE Place Hotel, Rome, Italy
- 1.27. Kolev NI (1995) How accurately can we predict nucleate boiling, *Exp. Thermal Fluid Sci.*, vol 10 p 370–378
- 1.28. Kolev NI (April 3–7 1995) IVA5 Computer code: The model for film boiling on a sphere in subcooled, saturated and superheated water, Proc. of Second Int. Conference On Multiphase Flow, Kyoto, Japan. Also presented in (November 14–15, 1994) Workshop zur Kühlmittel/Schmelze - Wechselwirkung, Cologne, Germany
- 1.29. Kolev NI (April 23–27, 1995) IVA5 computer code: Dynamic fragmentation model for liquid and its application to melt–water interaction, Proc. ICON3-3, The Third International Conf. on Nucl. Engineering, “Nuclear Power and Energy Future”, Kyoto, Japan. Also presented in (November 14–15, 1994) Workshop zur Kühlmittel/Schmelze - Wechselwirkung, Cologne, Germany
- 1.30. Stewart HB (November 2, 1994) Assessment of the IVA3 code for multifield flow simulation, Brookhaven Nation Laboratory, Report BNL 52473 FZ Karlsruhe Report FZKA 5591 (July 1995)
- 1.31. Vaeth L (March 1995) Radiative heat transfer for transient three-phase, three-component flow model IVA-KA, Forschungszentrum Karlsruhe, Internal Report 32.21.02/10A
- 1.32. Jacobs H (January 9–13 1993) Analysis of large-scale melt-water mixing events, Proc. CSNI Specialists Meeting of Fuel-Coolant Interactions, Santa Barbara, CA. U.S. Nuclear Regulatory Commission Report NUREG/CP-0127, NEA/CSNI/R(93) (March 1994), p 14–26
- 1.33. Jacobs H, Lummer M, Meyer L, Stehle B, Thurnay K, Vöth L (March 9–13, 1995) Multifield simulations of premixing experiments, NSFJSPS Seminar, Santa Barbara
- 1.34. Meyer L, Schumacher G, QUEOS, a simulation experiment of the premixing phase of steam explosion with hot spheres in water base case experiments, Forschungszentrum Karlsruhe, FZKA 5612
- 1.35. Kolev NI (1995) IVA5 computer code: Modeling of melt-water droplet interaction for very high melt temperatures, unpublished. Later some of this material is used in volume two of this monograph
- 1.36. Kolev NI and E Hofer (August 1996) Uncertainty and sensitivity analysis of post experimental IVA5 simulations of melt water interaction, *Exp. Thermal Fluid Sci.*, vol 13 p 98–116
- 1.37. Kolev NI (October 15–16, 1996) Three fluid modeling with dynamic fragmentation and coalescence - fiction or daily practice? 7th FARO Experts Group Meeting Ispra; (5th–8th November 1996) Proceedings of OECD/CSNI Workshop on Transient thermal-hydraulic and neutronic codes requirements, Annapolis, Md, U.S.A.; (June 2–6, 1997) 4th World Conference on Experimental Heat Transfer, Fluid Mechanics and Thermodynamics, ExHFT 4, Brussels; (June 22–26, 1997) ASME Fluids Engineering Conference & Exhibition, The Hyatt Regency Vancouver, Vancouver, British Columbia, CANADA Invited Paper; (May 22–24, 1997) Proc. of the International Seminar on Vapor Explosions and Explosive Eruptions (AMIGO-IMI), Aoba Kinen Kaikan of Tohoku University, Sendai-City, Japan

- 1.38. Kolev NI (19th–21st May 1997) Verification of the IVA4 film boiling model with the data base of Liu and Theofanous, Proceedings of OECD/CSNI Specialists Meeting on Fuel-Coolant Interactions (FCI), JAERI-Tokai Research Establishment, Japan
- 1.39. Kolev NI (Japan 19th–21st May 1997) Numerical modeling of in-vessel melt water interaction in large scale PWRs, Proceedings of OECD/CSNI Specialists Meeting on Fuel-Coolant Interactions (FCI), JAERI-Tokai Research Establishment
- 1.40. Kolev NI (May 22–24, 1997) IVA4 Analysis of the FARO L14 Experiment (ISP 39), Proceedings of the International Seminar on Vapor Explosions and Explosive Eruptions (AMIGO-IMI), Aoba Kinen Kaikan of Tohoku University, Sendai-City, Japan
- 1.41. Kolev NI (May 26–30, 1997) Is large melt water mixing possible under low pressure, Proceedings of ICON 5: 5th International Conference on Nuclear Engineering, Nice, France
- 1.42. Kolev NI (June 2–6, 1997) Film boiling: vertical plates, Proceedings of 4th World Conference on Experimental Heat Transfer, Fluid Mechanics and Thermodynamics EXHFT 4, Brussels, Belgium
- 1.43. Kolev NI (1997) Comments on the entropy concept, *Kerntechnik*, vol 62 no 1 pp 67–70
- 1.44. Kolev NI (1998) On the variety of notation of the energy conservation principle for single phase flow, *Kerntechnik*, vol 63 no 3 pp 145–156
- 1.45. Kolev NI (1998) Film boiling on vertical plates and spheres, *Exp. Thermal Fluid Sci.*, vol 18 pp 97–115
- 1.46. Kolev NI (August 1999) In-vessel melt–water interaction caused by core support plate failure under molten pool, Part1: Choice of the solution method. *Kerntechnik* vol 64 no 4 pp 209–215
- 1.47. Kolev NI (1999) In-vessel melt–water interaction caused by core support plate failure under molten pool, Part 2: Analysis, *Kerntechnik* vol 64 no 5 pp 278–283
- 1.48. Kolev NI (2000) Detonation waves in melt-coolant interaction, Part.1: Theory, *Kerntechnik* vol 65 no 5–6 pp 254–260. Also in EU Nr. INV-MFCI(99)-D038
- 1.49. Kolev NI and Hulin H (2001) Detonation waves in melt-coolant interaction, Part. 2: Applied analysis, *Kerntechnik* vol 66 no 1–2 pp 21–25. Also in MFCI Project, 6th progress meeting, CEA, Grenoble, 23–24 June 1999, EU Nr. INV-MFCI(99)-D038
- 1.50. Kolev NI, Chen T, Kollmann T, Schlicht G (June 8–12, 1998) Visual multi-phase flow analysis, Third International Conference On Multiphase Flow, Lyon, France
- 1.51. Kolev NI (17 December 1998) Verification of IVA5 computer code for melt–water interaction analysis, 5th MFCI Project Meeting, Forschungszentrum Karlsruhe, Germany 1998
- 1.52. Magallon D, Berthoud G, Schuetz W, Alemberti A, Seghal R, Buerger M, Colombo G, Turland B, Zero S (Nov. 1997) Characterization of processes which govern quenching of molten corium in water including steam explosions, Proc. FISA-EU research on severe accidents, Luxemburg, EUR 18258 EN (1998)
- 1.53. Kolev NI (April 19–23, 1999) Verification of IVA5 computer code for melt–water interaction analysis, Part 1: Single-, two-, and three-phase flows without melt fragmentation, Proc. of the 7th International Conference on Nuclear Engineering, Tokyo, Japan, ICONE-7359
- 1.54. Kolev NI (April 19–23, 1999) Verification of IVA5 computer code for melt–water interaction analysis, Part 2: Three-phase flows with melt fragmentation, Proc. of the 7th International Conference on Nuclear Engineering, Tokyo, Japan, ICONE-7507

- 1.55. Kolev NI (April 19–23, 1999) In-vessel melt–water interaction caused by core support plate failure under molten pool, Proc. of the 7th International Conference on Nuclear Engineering, Tokyo, Japan, ICONE-7360
- 1.56. Kolev NI (17 December 1998) Ex-vessel melt–water interaction caused by symmetric lower head unzipping within the reactor pit, 5th MFCI Project Meeting, Forschungszentrum Karlsruhe, Germany. Slightly modified in (April 19–23, 1999) Proc. of the 7th International Conference on Nuclear Engineering, Tokyo, Japan, ICONE-7361. Extended version in (October 3–8,1999) Proc. of the Ninth International Topical Meeting on Nuclear Reactor Thermal Hydraulics (NURETH-9), San Francisco, California, Log. Nr. 317
- 1.57. Kolev NI (August 15–17, 1999) Verification of IVA5 computer code for melt–water interaction analysis: Part 1 and 2, Experimental Study of Multiphase Flow, Proc. of the 33rd National Heat Transfer Conference, Albuquerque, New Mexico
- 1.58. Kolev NI (October 3–8,1999) Verification of IVA5 computer code for melt–water interaction analysis, Part 1: Single phase flow, Proc of the Ninth International Topical Meeting on Nuclear Reactor Thermal Hydraulics (NURETH-9), San Francisco, California, Log. Nr. 315_1
- 1.59. Kolev NI (October 3–8,1999) Verification of IVA5 computer code for melt–water interaction analysis, Part 2: Two-phase flow, three-phase flow with cold and hot solid spheres, Proc. of the Ninth International Topical Meeting on Nuclear Reactor Thermal Hydraulics (NURETH-9), San Francisco, California, Log. Nr. 315_2
- 1.60. Kolev NI (October 3–8,1999) Verification of IVA5 computer code for melt–water interaction analysis, Part 3: Three-phase flow with dynamic fragmentation and coalescence, Proc. of the Ninth International Topical Meeting on Nuclear Reactor Thermal Hydraulics (NURETH-9), San Francisco, California, Log. Nr. 315_3
- 1.61. Kolev NI (October 3–8,1999) Verification of IVA5 computer code for melt–water interaction analysis, Part 4: Three-phase flow with dynamic fragmentation and coalescence – alumina experiments, Proc. of the Ninth International Topical Meeting on Nuclear Reactor Thermal Hydraulics (NURETH-9), San Francisco, California, Log. Nr. 315_4
- 1.62. Kolev NI (1988) In-vessel melt–water interaction caused by core support plate failure under molten pool, Part 1: Choice of the solution method, 5th MFCI Project Meeting, 17 December 1998, Forschungszentrum Karlsruhe, Germany. Also in (October 3–8, 1999) Proc. of the Ninth International Topical Meeting on Nuclear Reactor Thermal Hydraulics (NURETH-9), San Francisco, California, Log. Nr. 316_1. Also in (August 1999) Kerntechnik vol 64 no 4 pp 209–215
- 1.63. Kolev NI (1998) In-vessel melt–water interaction caused by core support plate failure under molten pool, Part 2: Analysis, 5th MFCI Project Meeting, 17 December 1998, Forschungszentrum Karlsruhe, Germany. Also in (October 3–8,1999) Proc. of the Ninth International Topical Meeting on Nuclear Reactor Thermal Hydraulics (NURETH-9), San Francisco, California, Log. Nr. 316_2. Also in (1999) Kerntechnik vol 64 no 5 pp 278–283
- 1.64. Kolev NI (5–10 September, 1999) Applied multi-phase flow analysis and its relation to constitutive physics, 8th International Symposium on Computational Fluid Dynamics, ISCFD '99 Bremen, Germany. Also in (April 2000) Journal for Computational Fluid Dynamics, vol 9 no 1 pp 549–561, Invited Lecture
- 1.65. Magalon D, Huhtiniemi H, Dietrich D, Bertoud G, Valette M, Schuetz W, Jacobs H, Kolev N, Graziosi G, Sehgal R, Buerger M, Buch M, Colombo G, Turland B, Dobson G, Monhardt D (29 Nov.–1 Dec. 1999) Molten fuel coolant interaction (MFCI), FISA-99 Symposium, EC, Jean Monnet Building, Luxemburg

- 1.66. Kolev NI and Roloff-Bock I (1998) IVA5 Computer code: Relief and back pressing valve models, KWU NA-T/1998/E000, Project R&D
- 1.67. Kolev NI (1998) Can melt–water interaction jeopardize the containment integrity of the EPR? Part 3: Fragmentation and coalescence dynamics in multi-phase flows, KWU NA-T/1998/E083a, Project EPR
- 1.68. Lanzenberger K (1996) Comments to the entropy equation and its discretisation in the numerical code IVA4, KWU-NA-M/96/E046b
- 1.69. Lanzenberger K (1996) IVA4 Computer Code: Material properties of 13 pure gases and their mixtures, KWU-NA-M/96/E017
- 1.70. Lanzenberger K (1996) IVA4 Computer Code: Mixture properties of core melt, KWU-NA-M/96/E045
- 1.71. Lanzenberger K (1997) Gas propagation in a reactor containment computed with the system code IVA4, Jahrestagung Kerntechnik '97 in Aachen, Analyse und Beherrschung schwerer Störfälle
- 1.72. Dombrovsky L (1997) Radiation heat transfer between nuclear fuel rods and in dispersed corium, KWU NA-T/1997/E047
- 1.73. Lanzenberger K (1998) Thermal radiation in multiphase flow, KWU NA-T/98/E011. Karl Wirtz Prize für Junge Wissenschaftler – 1997: Lanzenberger K, Thermal radiation in multiphase flow - Application to the severe accident scenario of molten fuel coolant interaction (MFCI), Siemens AG, Power Generation (KWU)
- 1.74. Fjodorow A (1998) Entwicklung eines verbrennungsmodells für den computercode IVA-5, KWU NA-T/1998/101
- 1.75. Wittmaack R (10.12.1997) SURTRAC, a subprogram to determine surfaces of discontinuity inside of control volumes. KWU NA-T/1997/E062, Erlangen
- 1.76. Roloff-Bock I (1998) IVA5: Interface description for graphical analysis, KWU NA-T/1998/E093r
- 1.77. Roloff-Bock I (1998) IVA5 Computer Code: Pipe network input generation, KWU NA-T/1998/E017
- 1.78. Kolev NI and Roloff-Bock I (1998) IVA5 Computer Code: Relief and back pressing valve model, KWU NA-T/1998/E058
- 1.79. Roloff-Bock I (1998) IVA4-NW: Interface description for graphical analysis, KWU NA-T/1998/E059
- 1.80. Roloff-Bock I (1999) IVA5 related programs, KWU NA-T/1999/E040.
- 1.81. Kollmann T (1999) MovieView – Short Description, Siemens AG, Erlangen
- 1.82. Kollmann T (1999) MovieTrans – Short Description, Siemens AG, Erlangen
- 1.83. Kollmann T (1999) DataGraph – Short Description, Siemens AG, Erlangen
- 1.84. Kolev NI (April 2–6, 2000) Computational analysis of transient 3D-melt–water interactions, Proc. of the 8th International Conference on Nuclear Engineering, Baltimore, Maryland USA, ICONE-8809. Also in (May 22–25, 2000) CFD 2000 in Trondheim Norway. Also in abbreviated form in (November 5–11, 2000) Symposium on “Dispersed Flows in Combustion, Incineration and Propulsion Systems”, ASME International Mechanical Engineering Congress & Exposition, Orlando, FL
- 1.85. Kolev NI (June 11–15, 2000) Needs of industrial fluid dynamics applications, Invited lecture, 2000 ASME Fluids Engineering Division Summer Meeting (FEDSM), Industry Exchange Program, Sheraton Boston Hotel, Boston, Massachusetts,

- 1.86. Kolev NI, Seitz H and Roloff I (May 27–June 1, 2001) Hot Leg Injection: IVA 3D Versus 1D Three Velocity Fields Modeling and Comparison with UPTF 26 Run 230 Experiment, ICMF-2001, CD-Proceedings of the 4th International Conference on Multiphase Flow, New Orleans, Louisiana, U.S.A. Also in (September 24–28, 2001) Proc. ExHFT-5, 5th World Conference on Experimental Heat Transfer, Fluid Mechanics and Thermodynamics, Thessaloniki, Greece
- 1.87. Kolev NI (May 29–June 1, 2001) Conservation equations for multi-phase multi-component multi-velocity fields in general curvilinear coordinate systems, 2001 ASME Fluids Engineering Division Summer Meeting (FEDSM), Keynote Lecture, New Orleans, Louisiana
- 1.88. Kolev NI (April 2–12, 2001) SWR 1000 Severe accident control through in-vessel melt retention by external RPV cooling, 9th International Conference on Nuclear Engineering, Nice, France
- 1.89. Kolev NI (May 29–June 1, 2001) International cooperation to develop computational fluid dynamic technology: opportunities and obstacles, 2001 ASME Fluids Engineering Division Summer Meeting (FEDSM), New Orleans, Louisiana, Invited Lecture
- 1.90. Kolev NI (5–10 September 1999) Applied multi-phase flow analysis and its relation to constitutive physics, 8th International Symposium on Computational Fluid Dynamics, ISCFD '99, Bremen, Germany. Also (April 2000) Japan Journal for Computational Fluid Dynamics, vol 9 no 1 pp 549–561, Invited Lecture
- 1.91. Kolev NI (June 10–13, 2002) IVA_5M numerical method for analysis of three-fluid multi-component flows in boundary-fitted multi-blocks, The 40th European Two-Phase Flow Group Meeting, Stockholm, Sweden
- 1.92. Kolev NI (April 14–18, 2002) Simple analytical U-tube benchmarks appropriate for testing of pipe-network computer codes, Proceedings of ICONE10: Tenth International Conference on Nuclear Engineering - Arlington, Virginia (Washington, D.C.), USA ICONE10-22711
- 1.93. Kolev NI (2002, 2004) Multiphase Flow Dynamics, Vol. 1 Fundamentals, 2nd ed., with 114 Figures and CD-ROM Springer, Berlin, New York, Tokyo, ISBN 3-540-2206-0, see the content in <http://www.springeronline.com/east/3-540-22106-9>
- 1.94. Kolev NI (2002, 2004) Multiphase Flow Dynamics, Vol. 2 Thermal and mechanical interactions, 2nd ed. with 81 Figures, Springer, Berlin, New York, Tokyo, ISBN 3-540-22107-7, see the content in <http://www.springeronline.com/east/3-540-22107-7>
- 1.95. Kolev NI (April 20–23, 2003) Controlling the moisture content in the steam by using nozzles in BWR'S, Eleventh International Conference on Nuclear Engineering, ICONE 11, Keio Plaza Inter-Continental, Shinjuku, Tokyo, Japan, ICONE11-36306; ETPFG, European Two-Phase Flow Group Meeting 2003 Norway; The 10th International Topical Meeting on Nuclear Reactor Thermal Hydraulics (NURETH-10) Seoul, Korea, October 5–9, 2003.
- 1.96. Kolev NI (27–29 November 2002) 3D-Multiphase-Fluid-Dynamik: Reduzierung der Dampffuchte am RDB-Austritt der Siedewasserreaktoren, Betriebsleitertagung, Geneve; in English: Controlling the moisture content in the steam by using nozzles in BWRs, Eleventh International Conference on Nuclear Engineering, ICONE 11, Keio Plaza Inter-Continental, Shinjuku, Tokyo, Japan, April 20–23, 2003, ICONE11-36306, The 10th International Topical Meeting on Nuclear Reactor Thermal Hydraulics, Seoul, Korea, October 5–9, 2003, E00301
- 1.97. Kolev NI (17–20 June 2003) IVA_5M numerical method for analysis of three-fluid multi-component flows in boundary-fitted multi-blocks, Second M.I.T. Conference on Computational Fluid and Solid Mechanics, Boston

- 1.98. Kolev NI (5–9 October 2003) Analysis of the PREMIX 17 and 18 experiments with IVA_5M computer code, The 10th International Topical Meeting on Nuclear Reactor Thermal Hydraulics, Seoul, Korea, E00106
- 1.99. Kolev NI (June 13–17, 2004) External cooling - the SWR 1000 severe accident management strategy, Proceedings of ICONE-12 '04 Arlington VA, USA, April 25–29, 2004, Paper ICONE12-49055, Presented first as SWR 1000 In-Vessel Melt Retention, STUK Meeting held at 13.8.2003 in Helsinki, Finland; (Nov.17–18, 2005) European BWR Forum, 11th Seminar on SWR1000 Design Features, Framatome ANP, Offenbach, Germany
- 1.100. Kolev NI (April 25–29, 2004) 25-Years three-fluid modeling-experience: successes and limits, Proceedings of ICONE-12 '04 Arlington VA, USA, Paper ICONE12-49054. Also in 4th ECCOMAS (European Congress on Computational Methods in Applied Sciences and Engineering, Finland July 24–28, 2004. Also in 6th WCCM (World Congress of Computational Mechanics) Beijing Sept. 5–10 2004. In extended form in 6th International Topical Meeting on Nuclear Reactor Thermal Hydraulics, Operations and Safety, October 4–8, 2004, Nara-Ken New Public Hall, Nara, Japan, NUTHOS6-N6P380
- 1.101. Kolev NI (October 4–8, 2004) External cooling - the SWR 1000 severe accident management strategy, Part 2: Analysis: vessel-, penetrations-, and containment integrity during the external cooling, 6th International Topical Meeting on Nuclear Reactor Thermal Hydraulics, Operations and Safety, Nara-Ken New Public Hall, Nara, Japan, NUTHOS6-N6P382
- 1.102. Kolev NI (October 4–8, 2004) External cooling - the SWR 1000 severe accident management strategy Part 1: Motivation, strategy, analysis: melt phase, vessel integrity during melt–water interaction, Proceedings of 6th International Topical Meeting on Nuclear Reactor Thermal Hydraulics, Operations and Safety, Nara-Ken New Public Hall, Nara, Japan, NUTHOS6-N6P381
- 1.103. Kolev NI (April 17–21, 2005) Common features of heterogeneous nucleate boiling & flashing for water, 6th World Conference on Experimental Heat Transfer, Fluid Mechanics, and Thermodynamics Matsushima, Miyagi, Japan
- 1.104. Kolev NI (May 15–19, 2005) Uniqueness of the elementary physics driving heterogeneous nucleate boiling and flashing, Proceedings of ICAPP '05, Seoul, KOREA, Paper 5678. In abbreviated form ICCHMT' 05 Fourth International Conference on Computational Heat and Mass Transfer, Paris (France) 17 to 20 May 2005, Paper reference No: ICCHMT'05 – 491
- 1.105. Kolev NI (30 May – 3rd June 2005) Is it possible to design universal multi-phase flow analyzer? 6th World Congress on Structural and Multidisciplinary Optimization WCSMO6 Rio de Janeiro; International Conference “Nuclear Energy for New Europe 2005”, September 5–8, 2005, Bled (Slovenia)
- 1.106. Kolev NI, Roloff-Bock I and Schlicht G (June 14–17, 2005) Gas release driven dynamics in research reactors piping, Third M.I.T Conference on Computational Fluid and Solid Mechanics, Cambridge, Massachusetts. ICAPP '06 Reno, NV USA, June 4–8, 2006, ICAPP06 Paper 6053, submitted for publication
- 1.107. Kolev NI (October 2–6, 2005) Flow boiling in bundles: Comparison of IVA predictions for 153 experiments for variety of bundles, flow regimes including DO, steady state and transients, The 11th International Topical Meeting on Nuclear Reactor Thermal-Hydraulics (NURETH-11) Log Number: 547, Popes Palace Conference Center, Avignon, France

-
- 1.108 Kolev NI (October 2–6, 2005) Strictly conservative limiter for fourth order CIP methods for multi-fluid analyses, The 11th International Topical Meeting on Nuclear Reactor Thermal-Hydraulics (NURETH-11) Log Number: 006, Popes Palace Conference Center, Avignon, France
 - 1.109 Kolev NI (September 12–15, 2005) Do we have appropriate constitutive sets for sub-channel and fine-resolution 3D-analyses of two-phase flows in rod bundles? Mathematics and Computation, Supercomputing, Reactor Physics and Nuclear and Biological Applications Palais des Papes, Avignon, France, on CD-ROM, American Nuclear Society, LaGrange Park, IL (2005)
 - 1.110 Kolev NI (27–29 June 2005) IVA Simulations of exercises 1 of phase 1 and 2 of the OECD/NRC benchmark based on NUPEC BWR full-size fine-mesh bundle tests (preliminary), Second Workshop on OECD/NRC Benchmark based on NUPEC BWR Full-size Fine-mesh Bundle Tests (BFBT), State College, PA, USA
 - 1.111 Kolev NI (2006) Uniqueness of the elementary physics driving heterogeneous nucleate boiling and flashing, Nuclear Engineering and Technology, vol 38 no 1, pp 33–42, Seoul, Korea
 - 1.112 Kolev NI (2003, 2005) IVA_5M numerical method for analysis of three-fluid multi-component flows in boundary-fitted multi-blocks, Computers & Structures, vol 83 (2005) pp 499–523, USA. Presented in Second M.I.T. Conference on Computational Fluid and Solid Mechanics, (17–20 June 2003) Boston
 - 1.113 Kolev NI (July 17–20, 2006) Verification of IVA computer code for flow boiling stability analysis, Proceedings of ICONE-14 '06, Miami, Florida, USA, Paper ICONE14-89034, submitted for publication
 - 1.114 Kolev NI (2006) Check of the 2005 look-up table for prediction of CHF in bundles, Nucl. Eng. Des., doi:10.1016/j.nucengdes.2006.10.021
 - 1.115 Kolev NI (2009) To the nucleate boiling theory, Nucl. Eng. Des., vol 239 pp 187–192
 - 1.116 Kolev NI (May 16–19, 2011) Analysis of boiling, Proceedings of ICONE19, 19th International Conference on Nuclear Engineering, Chiba, Japan, ICONE19-43770
 - 1.117 Kolev NI (May 16–19, 2011) Bubble dynamics in single component fluid, Proceedings of ICONE19, 19th International Conference on Nuclear Engineering, Chiba, Japan, ICONE19-43771

16.4 IVA-validation database

Example of the strategy of the validation. Consider that a given computer code has to be applied for the analysis of melt–water interaction. Some important elements of the models of melt–water interaction can be illustrated by a simple example. Let us start with the simple example of a closed volume filled with water and gas in which melt initially separated from the water is dropped into the water. The overall pressure increase is governed by the simplified form of the volume-conservation equation $dp/d\tau \approx \rho a^2 \mu_1 / \rho_1$ derived in Chapter 5, see also Ref. [2.43], p. 37, Eq. (103). Here, μ_1 is the evaporating mass per unit time and unit volume, ρ_1 is the density of the steam, ρ is the mixture density and a is the velocity of sound for the mixture. For gas volume fractions α_1 of 10% or more we can write as a very good approximation

$$dp/d\tau \approx a_1^2 \mu_1 / \alpha_1. \quad (16.4.1)$$

This simple equation is remarkable. Bearing in mind that during the short time in which melt–water interaction takes place, e.g., 0.001 to 3 s, the volume of steam in the closed system and the steam temperature do not change very much, we see that 1) the pressure change is directly proportional to the evaporation rate and 2) the smaller the void fraction the stronger this dependence.

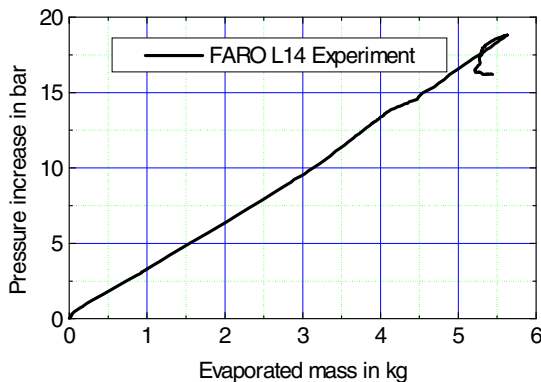


Fig. 16.4.1 Validity of Eq. (16.4.1) for the FARO L14 experiment - IVA simulation

Figure 16.4.1 shows the pressure increase versus the evaporated mass for the FARO L14 experiment simulated with the IVA computer code. The linear dependence as prescribed by Eq. (16.4.1) is reflected surprisingly well even after solving 21 complicated partial differential equations in time and space.

The evaporation rate caused by the energy transfer from the melt into the water is $\mu_1 \approx (F_3^{2\sigma} / \text{Vol}) \chi_3^{2\sigma} (T_3 - T_2) / \Delta h_{12}$. Here, $(F_3^{2\sigma} / \text{Vol})$ is the surface of the melt that is surrounded by water divided by the system volume. For dispersed melt we have $F_3^{2\sigma} / \text{Vol} = f_{\text{wet}} 6\alpha_3 / D_3$. Here, f_{wet} is the portion of the melt able to produce steam, which means the portion of the melt not surrounded by gas but by water. $\chi_3^{2\sigma}$ is some averaged heat-transfer coefficient, $T_3 - T_2$ is the driving temperature difference and Δh_{12} is the latent heat of evaporation. With this, the expression for the pressure generation is

$$\frac{dp}{d\tau} \approx f_{\text{wet}} \frac{\alpha_3}{\alpha_1} \frac{6a_1^2}{D_3} \chi_3^{2\sigma} \frac{T_3 - T_2}{\Delta h_{12}} \approx f_{\text{wet}} \frac{\alpha_3}{\alpha_1} \frac{6}{D_3} \chi_3^{2\sigma} (\kappa_1 - 1) c_{p1} T_1 \frac{T_3 - T_2}{\Delta h_{12}}. \quad (16.4.2)$$

We learn from this simple expression that 1) the geometrical pattern of the material distribution in the space during the interaction reflected by $f_{\text{wet}} \frac{\alpha_3}{\alpha_1}$ called material relocation is very important, 2) the melt particle size D_3 is very important, 3) the local heat-transfer conditions reflected by $\chi_3^{2\sigma}$ are very important, and 4) the history of the phase temperatures

$$a_1^2 (T_3 - T_2) \approx (\kappa_1 - 1) c_{p1} T_1 (T_3 - T_2), \quad (16.4.3)$$

is very important. Here κ_1 and c_{p1} are the vapor isentropic exponent and the specific vapor heat capacity at constant pressure, respectively.

We readily accept that mathematical models created to reflect the melt–water interactions have to be validated on experimental information for each of those particular groups of physical phenomena.

Another important point is the multidimensional nature of the interaction. The material relocation and the local flow conditions are obviously strong functions of time and space. Thus, the lumped-parameter approach, as introduced here for the sake of simplicity, holds true only after averaging over the total volume.

In particular, the phenomena identified to be important for the melt–water interaction scenarios are summarized in Tables 16.4.1 to 16.4.11. Many phenomena for the so-called classical applications of the multiphase flow analysis are subdomains of the melt–water interaction. Therefore, codes undergoing this very challenging verification program are of course applicable in the subdomains, e.g., of missing melt, or missing components, or missing dimensions, etc.

Table 16.4.1 IVA: Tested physical phenomena against experimental data and analytical benchmarks: **Gravitational material relocation**

No	Phenomena successfully reproduced by IVA computer code	Experiment (e) or analytical benchmark (a)
1	2D waves	(e) <i>Maschek</i> [2.72]
26	Single-phase natural convection in uniformly heated vertical part of a U-tube	(a) <i>Kolev</i> [2.67, 1.93, 1.94]
27	Single-phase natural convection in uniformly heated inclined part of a U-tube	(a) <i>Kolev</i> [2.67, 1.93, 1.94]
28	Single-phase natural convection in U-tube with inclined part heated by steam condensation	(a) <i>Kolev</i> [2.67, 1.93, 1.94]
45	Critical gas flow in nozzles and pipe	(e) <i>Frössel</i> [2.113]
46	Discharge from gas vessel through pipe	(a) <i>Kolev</i> , vol. 1

Table 16.4.2 IVA: Tested physical phenomena against experimental data and analytical benchmarks: **Single-phase flow**

No	Phenomena successfully reproduced by IVA	Experiment (e) or analytical benchmark (a)
20	Steady-state single-phase nozzle flow	(e) <i>BNL</i> [2.1]
	1D pressure waves	
2	In gas	(a) <i>Oertel</i> [2.85]
3	In water	(a) <i>Kellner et al.</i> [2.26]
4	2D pressure waves in gas	(e) <i>SGI</i> [2.73, 2.92]

Table 16.4.3 IVA: Tested physical phenomena against experimental data and analytical benchmarks: **Adiabatic two phase flow**

No	Phenomena successfully reproduced by IVA	Experiment (e) or analytical benchmark (a)
4	2D pressure waves	(e) <i>SGI</i> [2.73, 2.92]
	1D pressure waves in a single pipe	
5	- without intensive mass exchange	(e) <i>Kellner et al.</i> [2.26]
6	- with intensive evaporation – flashing	(e) <i>Edwards et al.</i> [2.17]
25	Pressure waves in complex networks	(a) <i>Kolev</i> [1.93, 1.94]
33	Droplet fragmentation for Weber numbers of 1 to 1000	(e) see in <i>Kolev</i> [1.94]
24	Heterogeneous nucleation, bubble generation frequency	(e) see in <i>Kolev</i> [1.94]
21	Film entrainment in pipe flow	(e) <i>UPTF</i> [2.65]
23	Water flashing in nozzle flow	(e) <i>BNL</i> [2.1]
29	3D small break loss of coolant	(e) <i>Kevchishvili et al.</i> [2.27]
30	3D hot leg emergency water injection against steam flow	(e) <i>UPTF</i> [2.65]

Table 16.4.4 IVA: Tested physical phenomena against experimental data and analytical benchmarks: **Diabatic two-phase flow**

No	Phenomena successfully reproduced by IVA	Experiment (e) or analytical benchmark (a)
31	Bubble departure diameter, nucleation frequency, bubble generation frequency, nucleate boiling	(e) see in <i>Kolev</i> [1.94]
22	Boiling in pipes	(e) <i>Sabotinov</i> [2.88], <i>Pierre</i> [2.87], <i>Egen et al.</i> [2.18], <i>Bartolomei et al.</i> (1980) [2.112]
22	Boiling in rod bundles	(e) <i>Nylund</i> [2.84],
7	Film boiling in pipes	(e) <i>Bennet</i> [2.12]
7	Film boiling at plates	(e) <i>Okkonen et al.</i> [2.86]
7	Film boiling at spheres	(e) <i>Liu et al.</i> [2.70]

Table 16.4.5 IVA: Tested physical phenomena against experimental data and analytical benchmarks: **Three-phase solid sphere flow**

No	Phenomena successfully reproduced by IVA	Experiment (e) or analytical benchmark (a)
32	Drag forces in solid-spheres–water–air bubble flows	(e) <i>Sakaguchi</i> [2.32]
8	2D dropping cold spheres into water	(e) <i>Kolev et al.</i> [2.32], <i>QUEOS</i> [2.75–79]
9,10	2D dropping extremely hot spheres into water	(e) <i>QUEOS</i> [2.75–79]

Table 16.4.6 IVA: Tested physical phenomena against experimental data and analytical benchmarks: **3D-effects in single-phase flow**

No	Phenomena successfully reproduced by IVA	Experiment (e) or analytical benchmark (a)
17	Rigid-body steady-rotation problem	(a) <i>Harison et al.</i> [2.21]
18	Pure radial symmetric flow	(a) <i>Harison et al.</i> [2.21]
19	Radial-azimuthal symmetric flow	(a) <i>Harison et al.</i> [2.21]

Table 16.4.7 IVA: Tested physical phenomena against experimental data and analytical benchmarks: **Melt–water interaction with dynamic fragmentation and coalescence**

No	Phenomena successfully reproduced by IVA	Experiment (e) or analytical benchmark (a)
11,1 2,13	Fragmentation of interpenetrating water, melt and vapor using corium as melt	(e) FARO L14, L20, L24 [2.71, 2.13, 2.22, 2.2, 2.3, 2.4]
14	Uncertainty in the prediction of nonexplosive melt–water interactions	(a, e) FARO L14 and [2.48]

15	Effect of the geometry	(e) FARO L28, L31 [2.91, 2.90]
16	Fragmentation of interpenetrating saturated water, melt and vapor using alumina as melt	(e) PREMIX 13, 15, [2.24, 2.25]
34	Fragmentation of interpenetrating subcooled water, melt and vapor using alumina as melt	(e) PREMIX 17, 18 [2.94, 2.95, 2.96, 2.97]

Table 16.4.8 IVA: Tested physical phenomena against experimental data and analytical benchmarks: **Flow boiling instability in natural circulation loop containing rod bundle**

No	Phenomena successfully reproduced by IVA	Experiment (e) or analytical benchmark (a)
35	Mass flow rate as a function of power, frequencies, decay factors	(e) <i>Schäfer</i> and <i>Beisiegel</i> [2.94]

Table 16.4.9 IVA: Tested physical phenomena against experimental data and analytical benchmarks: **3D steady-state flow boiling in rod bundle**

No	Phenomena successfully reproduced by IVA	Experiment (e) or analytical benchmark (a)
36	8×8 BWR rods, void fractions, NUPEC experiments	<i>Morooka</i> et al. [2.95], <i>Yagi</i> et al. [2.96], <i>Inoue</i> et al. [2.97–99]
37	8×8 BWR rods, void fractions, 15 NUPEC experiments in a framework of an ECD/USNRC, different power profiles	<i>Kolev</i> [2.100]
38	36 rods, void fractions, FRIGG experiments, different power profiles	<i>Nylund</i> et al. [2.101, 2.102]
39	8×8 PWR rods, void profiles, dry out position	<i>Anklama</i> and <i>Miller</i> [2.103]
41	Regional void fraction in ATRIUM 10XP at various peaking patterns	<i>Spierling</i> [2.105]

Table 16.4.10 IVA: Tested physical phenomena against experimental data and analytical benchmarks: **3D transient flow boiling in rod bundle subchannel**

No	Phenomena successfully reproduced by IVA	Experiment (e) or analytical benchmark (a)
43	Void for mass flow or pressure or inlet temperature variations	(e) <i>Hori</i> et al. [2.106–109]
44	5–5 PWR bundle, void for power or mass flow variations	(e) <i>Hori</i> et al. [2.106, 109], <i>Akiyama</i> et al. [2.110, 2.111]

Table 16.4.11 IVA: *Tested physical phenomena against experimental data and analytical benchmarks: 3D dry out in rod bundle*

No	Phenomena successfully reproduced by IVA	Experiment (e) or analytical benchmark (a)
40	4×4 BWR rods	(e) <i>Lucchini and Marinelli</i> [2.104]
42	ATRIUM 10-9Q 10×10 bundle	(e) AREVA proprietary

IVA was extensively used during the licensing process of the research reactor FRM II in Munich for melt–water-interaction analysis. The German state authority accepted the analysis as appropriate and correct.

The code was used during the melt–water interaction study for the EPR design.

The code was used for design of the concept for handling severe accidents in the BWR1000 design. The Finish authority STUK judged positive this concept.

The code is being used for solving daily problems in engineering practice at Siemens.

The references used during the verification procedure and the documents containing the results of the verification are summarized in the list given below.

16.5 References of data sources and references documenting the validation of IVA

- 2.1 Abuaf N, Wu BJC, Zimmer GA, and Saha P (June 1981) A study of non equilibrium flashing of water in a converging diverging nozzle, vol 1 Experimental, vol 2 Modeling, NUREG/CR-1864, BNL-NUREG-51317
- 2.2 Annunziato A, Addabbo C, Leva G (1996) OECD-CSNI International standard problem 39 on FARO test L-14, Reference specification, JRC Technical Note I.96.xx, Draft
- 2.3 Annunziato A, Addabbo C, Magallon D (Oct. 1996) FARO test L-20 quick look report, Technical Note No. I.96.163, JRC Ispra, Italy
- 2.4 Annunziato A, Addabbo C, Magallon D, FARO Test L-24 Quick Look Report, Technical Note No. I.97.185, JRC Ispra, Italy
- 2.5 Batchelor GK (ed) (1958) Collected works of G. I. Taylor, Cambridge University Press, Cambridge, MA
- 2.6 Basu S, Ginsberg T (Aug. 1996) A reassessment of the potential for an alpha-mode containment failure and a review of the current understanding of broader fuel-coolant interaction issues, NUREG-1524
- 2.7 Bracco FV (Feb. 25–March 1, 1985) Modeling of engine sprays, Proc. International Congress & Exposition Detroit, Michigan, pp 113–136
- 2.8 Bürger M, Buck M, Saied-Ahmad A, Schatz A (December 1996) Experimental and theoretical investigation on the fragmentation of melt drops in relative flow, Report INV-MFC (98)-D016, Institut für Kernenergetik und Energiesysteme, Universität Stuttgart, IKE 2-135
- 2.9 Bürger M (July 1998) Comparison and theoretical interpretation of the experiments on hydrodynamic drop fragmentation, Report INV-MFC (98)-D014, Institut für Kernenergetik und Energiesysteme, Universität Stuttgart, IKE 2-FB-16
- 2.10 Bürger M, Cho SH, von Berg E, A Schatz (Nov. 1998) Modeling of drop fragmentation in thermal detonation waves and experimental verification, Report INV-MFC (98)-D016, Institut für Kernenergetik und Energiesysteme, Universität Stuttgart, IKE 2-FB-15
- 2.11 Coste P, Valette M and Berthoud G (23–24 June, 1999) Pb-Bi droplets fragmentation in liquid water (Li et al. experiment, ICMF 98): comparison of the existing code correlations and calculations with MC3D, 6th MFCI Project Meeting, CEA Grenoble, France
- 2.12 Bennett AW et al. (1967) Heat transfer to steam-water mixtures flowing in uniformly heated tubes in which the critical heat flux has been exceeded, AERE-R5373
- 2.13 Benuzzi A, Magalon D (December 1994) FARO-LWR programme L-14 test quick look report, JRC Technical Note I.94.171
- 2.14 Chen JC (1963) A correlation for film boiling heat transfer to saturated fluids in convective flow, ASME Publication-63-HT-34, p 2–6

- 2.15 Corradini ML, Rohsenow WM and Todreas NE (1980) The effect of sodium entrainment and heat transfer with two-phase UO₂ during a hypothetical core disruptive accident, NSE, vol 73 pp 242–258
- 2.16 Crowe CT, Sharma MP, and Stock DE, (June 1977) The particle-in-cell (PSI-Cell) model for gas droplet flows, ASME, Transactions, Series I – J. Fluids Eng., vol 99 pp 325–332
- 2.17 Edwards AR and O'Brien TP (1970) Studies of phenomena connected with the depressurization of water reactors, J. Brit. Nucl. Energy Soc., vol 9 nos 1–4 pp 125–135
- 2.18 Egen RA, Dingee DA and Chastain JW (1957) Vapor formation and behavior in boiling heat transfer, AEC Report BMI – 1167
- 2.19 Groeneveld DC et al. (1996) The 1995 look-up table for critical heat flux in tubes, Nucl. Eng. Des., vol 163 pp 1–23
- 2.20 Haraldsson HO, Li HX, Dinh TN, Green JA and BR Sehgal (July 6, 1999) Effect of solidification and coolant voiding on breakup of molten metal jet in water, Royal Institut of Technology (KTH), NPS, EU report INV-MFCI(00)-D048, Report EU-KTH/NPS/MFCI1-9907-SE, Stockholm
- 2.21 Harison RG and Johnson EC (eds) (July 1992) Developmental assessment of the multidimensional component in RELAP5 for Savannah River Site thermal hydraulic analysis, EGG-EAST-9803, DE93 001942, EG&G Idaho, Inc., Idaho Falls, Idaho 83415
- 2.22 Hohmann H, Magallon D, Huhtiniemi I, Annunziato A, Yerkess A (October 24–26, 1994) Advance in the FARO/KROTOS Melt Quenching Test Series, 22nd Water Reactor Safety Meeting, Bethesda (Maryland)
- 2.23 Hughes ED, MP Paulsen and LJ Agee (1981) A drift-flux model of two phase flow for RETRAN, Nuclear Technology, vol 54 p 410
- 2.24 Kaiser A, Schütz W, Will H (1998) PREMIX experiment, EC 4th Framework Program on Reactor Safety Shared Cost Actions, Contract no FI4s-CT96-0037, MFCI PROJECT, Yearly Progress Report no 1
- 2.25 Kaiser A, Schütz W, Will H (17 December 1998) PREMIX: Investigation of premixing behavior of a hot melt being poured into water, Test PM15, 16.9.1998, 5th MFCI Project Meeting, Forschungszentrum Karlsruhe, Germany
- 2.26 Kellner A and Gissler D (7.2.1984) Programsystem SAPHYR: Anwendungsbeispiel II, Notiz Nr.70.02748.4, Interatom GmbH
- 2.27 Kevchishvili NA and Dementev BS (1985) Investigation of the influence of the decay heat on the blow down characteristics of steam-water mixtures, Teploenergetika, vol 7 p 67
- 2.28 Kolev NI (1986) Transiente Zweiphasenströmung (Transient Two-Phase Flow), Springer Verlag
- 2.29 Kolev NI (1986) Transiente Dreiphasen Dreikomponenten Strömung, Teil 3: 3D-Dreifluid-Diffusionsmodell, KfK 4080
- 2.30 Kolev NI (1986) Ein Computerprogramm zur Modellierung transienter 3D - Dreiphasen Dreikomponenten Strömungen mittels drei Geschwindigkeitsfeldern in zylindrischer Geometrie mit beliebigen Einbauten einschließlich der Spaltzone eines PWR/BWR. KfK 4088
- 2.31 Kolev NI (September 1987) IVA2 verification expansion phase experiment in SNR geometry, KfK 4310
- 2.32 Kolev NI, Tomiyama A, Sakaguchi T (Sept. 1991) Modeling of the mechanical interaction between the velocity fields in three phase flow, Exp. Thermal Fluid Sci., vol 4 no 5 pp 525–545

-
- 2.33 Kolev NI (Sept. 1991) A three-field model of transient 3D multi-phase, three-component flow for the computer code IVA3, Part 1: Theoretical basics: Conservation and state equations, numerics. KfK 4948, Kernforschungszentrum Karlsruhe
- 2.34 Kolev NI (Sept. 1991) A three-field model of transient 3D multi-phase, three-component flow for the computer code IVA3, Part 2: Models for the interfacial transport phenomena. Code validation. KfK 4949, Kernforschungszentrum Karlsruhe
- 2.35 Kolev NI (1993) Fragmentation and coalescence dynamics in multi-phase flows, *Exp. Thermal Fluid Sci.*, vol 6 pp 211 – 251
- 2.36 Kolev NI (1993) The code IVA3 for modeling of transient three-phase flows in complicated 3D geometry, *Kerntechnik*, vol 58 no 3 pp 147–156
- 2.37 Kolev NI (1994) The code IVA4: Modeling of mass conservation in multi-phase multi component flows in heterogeneous porous media, *Kerntechnik*, vol 59 no 4–5 pp 226–237
- 2.38 Kolev NI (1994) The code IVA4: Modeling of momentum conservation in multi-phase multi component flows in heterogeneous porous media, *Kerntechnik*, vol 59 no 6, pp 249–258
- 2.39 Kolev NI (1994) The influence of the mutual bubble interaction on the bubble departure diameter, *Exp. Thermal Fluid Sci.*, vol 8 pp 167–174
- 2.40 Kolev NI (14–15 Nov. 1994) IVA4 computer code: Dynamic fragmentation model for liquid and its application to melt water interaction, Presented at the Workshop zur Kühlmittel/Schmelze - Wechselwirkung, Köln, Germany. (Apr. 23–27, 1995) *Proc. ICONE-3, The Third International Conf. on Nucl. Engineering, “Nuclear Power and Energy Future”*, Kyoto, Japan
- 2.41 Kolev NI (27–29 September 1995) IVA4 computer code: An universal flow analyzer for multiphase flows and its applicability to melt water interaction, Technical Committee Meeting on Advances in and Experience with Accident Consequences Analysis IAEA Headquarters, Vienna, Austria
- 2.42 Kolev NI (1995) The code IVA4: Nucleation and flashing model, *Kerntechnik*, vol 60 no 6 pp 157–164. Also in: (Apr. 3–7, 1995) *Proc. Second Int. Conf. On Multiphase Flow*, Kyoto; (Aug. 13–18, 1995) *ASME & JSME Fluid Engineering Conference International Symposium on Validation of System Transient Analysis Codes - Hilton Head (SC) USA*; (October 9–11, 1995) *Int. Symposium on Two-Phase Flow Modeling and Experimentation*, ERGIFE Place Hotel, Rome, Italy
- 2.43 Kolev NI (1995) The code IVA4: Second law of thermodynamics for multi phase flows in heterogeneous porous media, *Kerntechnik*, vol 60 no 1 pp 1–39
- 2.44 Kolev NI (1995) The code IVA4: Nucleation and flashing model, *Kerntechnik* vol 60 no 6 pp 157–164. Also in: (Apr. 3–7, 1995) *Proc. Second Int. Conf. On Multiphase Flow*, Kyoto; (Aug. 13–18, 1995) *ASME & JSME Fluid Engineering Conference International Symposium on Validation of System Transient Analysis Codes - Hilton Head (SC) USA*; (October 9–11, 1995) *Int. Symposium on Two-Phase Flow Modeling and Experimentation*, ERGIFE Place Hotel, Rome, Italy
- 2.45 Kolev NI (1995) How accurate can we predict nucleate boiling, *Exp. Thermal Fluid Sci.*, *Exp. Thermal Fluid Sci.*, vol 10 pp 370–378
- 2.46 Kolev NI (Apr. 3–7, 1995) IVA4 computer code: The model for film boiling on a sphere in subcooled, saturated and superheated water, *Proc. Second Int. Conference On Multiphase Flow*, Kyoto, Japan. Presented also in (Nov. 14–15, 1994) “Workshop zur Kühlmittel/Schmelze - Wechselwirkung”, Köln, Germany

-
- 2.47 Kolev NI (1995) IVA4 Computer code: Dynamic fragmentation model for liquid and its application to melt water interaction, Proc. ICONE-3, The Third International Conf. on Nucl. Engineering, "Nuclear Power and Energy Future", Apr.23–27 1995, Kyoto, Japan. Presented at the "Workshop zur Kühlmittel/ Schmelze - Wechselwirkung", 14–15 Nov. 1994, Köln, Germany
- 2.48 Kolev NI and Hofer E (1996) Uncertainty and sensitivity analysis of post experimental IVA4 simulations of melt Water Interaction, Exp. Thermal Fluid Sci., vol 13 pp 98–116
- 2.49 Kolev NI (October 15–16, 1996) Three fluid modeling with dynamic fragmentation and coalescence, fiction or daily practice? 7th FARO Experts Group Meeting Ispra; (5th–8th November 1996) Proceedings of OECD/CSNI Workshop on Transient thermal-hydraulic and neutronic codes requirements, Annapolis, MD, USA; (June 2–6, 1997) 4th World Conference on Experimental Heat Transfer, Fluid Mechanics and Thermodynamics, ExHFT 4, Brussels; (June 22–26, 1997) ASME Fluids Engineering Conference & Exhibition, The Hyatt Regency Vancouver, Vancouver, British Columbia, CANADA Invited Paper; (May 22–24, 1997) Proceedings of 1997 International Seminar on Vapor Explosions and Explosive Eruptions (AMIGO-IMI), Aoba Kinen Kaikan of Tohoku University, Sendai-City, Japan
- 2.50 Kolev NI (May 19–21, 1997) Numerical modeling of in-vessel melt water interaction in large scale PWR's, Proceedings of OECD/CSNI Specialists Meeting on Fuel-Coolant Interactions (FCI), JAERI-Tokai Research Establishment, Japan
- 2.51 Kolev NI (May 26–30, 1997) Is large melt water mixing possible under low pressure, Proceedings of ICON 5: 5th International Conference on Nuclear Engineering, Nice, France
- 2.52 Kolev NI (1997) Comments on the entropy concept, Kerntechnik, vol 62 no 1 pp 67–70
- 2.53 Kolev NI (19th–21st May 1997) Verification of the IVA4 film boiling model with the data base of Liu and Theofanous, Proceedings of OECD/CSNI Specialists Meeting on Fuel-Coolant Interactions (FCI), JAERI-Tokai Research Establishment, Japan
- 2.54 Kolev NI (May 22–24, 1997) IVA4 analysis of the FARO L14 experiment (ISP 39), International Seminar on Vapor Explosions and Explosive Eruptions (AMIGO-IMI), Aoba Kinen Kaikan of Tohoku University, Sendai-City, Japan
- 2.55 Kolev NI (June 2–6, 1997) Film boiling: vertical plates, Proceedings of 4th World Conference on Experimental Heat Transfer, Fluid Mechanics and Thermodynamics EXHFT 4, Brussels, Belgium
- 2.56 Kolev NI (1998) Film boiling on vertical plates and spheres, Exp. Thermal Fluid Sci., vol 18 pp 97–115
- 2.57 Kolev NI (1998) On the variety of notation of the energy conservation principle for single phase flow, Kerntechnik, vol 63 no3 pp 145–156
- 2.58 Kolev NI (17 December 1998) In-vessel melt–water interaction caused by core support plate failure under molten pool, Part 1: Choice of the solution method, 5th MFCI Project Meeting, Forschungszentrum Karlsruhe, Germany. (October 3–8, 1999) Proc. of the Ninth International Topical Meeting on Nuclear Reactor Thermal Hydraulics (NURETH-9), San Francisco, California. (August 1999) Kerntechnik, vol 64 no 4
- 2.59 Kolev NI (17 December 1998) In-vessel melt–water interaction caused by core support plate failure under molten pool, Part 2: Analysis, 5th MFCI Project Meeting, Forschungszentrum Karlsruhe, Germany. (October 3–8, 1999) Proc. of the Ninth International Topical Meeting on Nuclear Reactor Thermal Hydraulics (NURETH-9), San Francisco, California. (1999) Kerntechnik, vol 64 no 5

- 2.60 Kolev NI and Hulin H (23–24 June 1999) Detonation waves in melt-coolant interaction, Part 2: Applied analysis, MFCI Project, 6th progress meeting, CEA, Grenoble. EU Nr. INV-MFCI(99)-D038. (2001) *Kerntechnik*, vol 66 no 1–2 pp 21–25
- 2.61 Kolev NI (1999) The IVA5 dynamic droplet fragmentation and coalescence models and their verification data base: Part 1 (INV-MFCI(99)-D027) and Part 2 (INV-MFCI(99)-D028)
- 2.62 Kolev NI (5–10, September 1999) Applied multi-phase flow analysis and its relation to constitutive physics, 8th International Symposium on Computational Fluid Dynamics, ISCFD '99 Bremen, Germany. (April 2000) *Jpn. J. Comput. Fluid Dyn.*, vol 9 no 1
- 2.63 Kolev NI (October 3–8, 1999) Verification of IVA5 computer code for melt–water interaction analysis, Part 1: Single phase flow, Part 2: Two-phase flow, three-phase flow with cold and hot solid spheres, Part 3: Three-phase flow with dynamic fragmentation and coalescence, Part 4: Three-phase flow with dynamic fragmentation and coalescence – alumina experiments, Proc of the Ninth International Topical Meeting on Nuclear Reactor Thermal Hydraulics (NURETH-9), San Francisco, California
- 2.64 Kolev NI (2000) Detonation waves in melt-coolant interaction, Part 1: Kernenergie, vol 65 pp 254–260
- 2.65 Kolev NI, Seitz H and Roloff-Bock I (2000) Hot-leg injection: 3D versus 1D three velocity fields modeling and comparison with UPTF experiment, Siemens report KWU NA-T/00/E027, R&D Project 903060, Verification IVA6
- 2.66 Kolev NI (April 2–6, 2000) Computational analysis of transient 3D-melt–water interactions, 8th International Conference on Nuclear Engineering, Baltimore, Maryland, USA, ICONE-8809. See also (November 5–11, 2000) ASME International Mechanical Engineering Congress & Exposition Dispersed Flow in Combustion, Incineration and Propulsion Systems
- 2.67 Kolev NI (April 14–18, 2002) Simple analytical U-tube benchmarks appropriate for testing of pipe-network computer codes, Proceedings of ICONE10: Tenth International Conference on Nuclear Engineering, Arlington, Virginia (Washington, D.C.), USA ICONE10-22711
- 2.68 Lanzenberger K (1998) Thermal radiation in multiphase flow, KWU NA-T/98/E011. 1998 Karl Wirtz Award for Young Scientists: K. Lanzenberger, Thermal radiation in multiphase flow - Application to the severe accident scenario of molten fuel coolant interaction (MFCI), Siemens AG, Power Generation (KWU)
- 2.69 Levy S (1967) *Int. J. Heat Transfer*, vol 10 pp 351–365
- 2.70 Liu C and Theofanous TG (August 1995) Film boiling on spheres in single- and two-phase flows part 1: Experimental studies ANS Proceedings, Part 2: A Theoretical Study, National Heat Transfer Conference, Portland
- 2.71 Magallon D, Leva G (February 1996) FARO LWR programme test L-14 data report, JRC Technical Note I.96.25
- 2.72 Maschek W, Roth A, Kirstahler M, Meyer L (Dec. 1992) Simulation experiments for centralized liquid sloshing motions, Kernforschungszentrum Karlsruhe, KfK 5090
- 2.73 Meyer L, Kirstahler M (September 4–9, 1988) Experimental investigation of the fluid dynamic of gas jet expansion in a liquid pool, Proc. 1st World Conf. Experimental Heat Transfer, Fluid Mechanics, and Thermodynamics, Dubrovnik, Yugoslavia. (1988) Shah K, Ganic EN, Yang KT (eds), Elsevier, New York, Amsterdam, London
- 2.74 Meyer L and Wilhelm D (March 1994) Investigation of the fluid dynamics of gas jet expansion in a liquid pool, Kernforschungszentrum Karlsruhe, KfK 5307

- 2.75 Meyer L and Schumacher G (April 1996) QUEOS a simulation-experiment of the premixing phase of steam explosion with hot spheres in water base case experiments, Wissenschaftliche Berichte FZKA 5612, Forschungszentrum Karlsruhe Technik und Umwelt, Karlsruhe
- 2.76 Meyer L (Aug.3–6, 1996) The interaction of falling mass of hot spheres with water, ANS Proceedings 1996 National Heat Transfer Conference, Houston, Tx., vol 9, pp 105–114, American Nuclear Society, La Grange Park, Illinois
- 2.77 Meyer L (July 1997) QUEOS a simulation-experiment of the premixing phase of steam explosion with hot spheres in water, Results of the Second Test Series, Internal Report 32.21.02/INR1962/PSF3267, Forschungszentrum Karlsruhe Technik und Umwelt, Karlsruhe
- 2.78 Meyer L (1998) QUEOS, an experimental investigation of premixing phase with hot spheres, Nucl. Eng. Des., vol 18
- 2.79 Meyer L and Kuhn D (May 23–25, 1999) The interaction of very hot particles falling into water, 2nd Int. Symp. on Two-Phase Flow Modeling and Experimentation Pisa, Italy
- 2.80 Miropolskij ZL (1963) Heat transfer in film boiling of steam-water mixture in steam generating tubes. Teploenergetika, vol 10 no 5 pp 49–53
- 2.81 Mitchel et al. DE (1981) Intermediate scales steam explosion phenomena: Experimental analysis SAND8-0124
- 2.82 Nelson LS and Duda PM (September 1981) Steam explosion experiments with single droplet of CO₂ laser melted with iron oxide. Report NUREG/CR-2295 (SAND 81-1346)
- 2.83 Nelson LS and Duda PM (September 1985) Steam explosion experiments with single droplet of CO₂ laser melted with iron oxide. Part 2. Parametric Studies. Report NUREG/CR-2718 (SAND 81-1105)
- 2.84 Nylund D et al. (1968) Hydrodynamic and heat transfer measurements on a full-scale simulated 36-rod Marviken fuel element with uniform heat flux distribution, FRIG-2, Danish Atomic Energy Commission
- 2.85 Oertel H (1966) Stossrohre, Springer Verlag, Wien-New York
- 2.86 Okkonen T, et al. (August 3–6, 1996) Film boiling on a long vertical surface under high heat flux and water subcooling conditions, Proc. of the 31st Nat. Heat Transfer Conference, Houston, Texas
- 2.87 Pierre CCS (1965) ANL-7041
- 2.88 Sabotinov LS (1974) Experimental investigation of void fraction in subcooled boiling for different power distribution laws along the channel. Moskva PhD Thesis in Russian
- 2.89 Saha P and Zuber N (1974) Proc. Int. Heat Transfer Conference Tokyo Paper B4.7
- 2.90 Silverii R, Magallon D (June 1999) FARO LWR Programme Test L-31 Data Report, Technical Note No. I.99.100, INV-MFCI(99)-D035, JRC, ISIS, Ispra (VA), Italy
- 2.91 Silverii R and Annunziato A, FARO LWR program, Test L-28 data report, Technical Note No.I.99.76, INV-MFCI(99)-D033, JRC Ispra, Italy
- 2.92 Wilchelm D, Kirstahler M (1987) Versuchsanlage zur schnellen Gasinjektion in einen wassergefüllten Behälter, KfK-4321, Kernforschungszentrum Karlsruhe
- 2.93 Yamano N, Sugimoto J, Moryama Y and Soda K (1992) Studies of fuel coolant interactions during core melt accident of nuclear power plants, NURETH-6th Int. Meeting On Thermal-Hydraulics, pp 271–281
- 2.94 Schäfer H and Beisiegel A (17.03.1992) Feasibility of stability tests under natural circulation conditions in the Karlstein test loop, Siemens technical report E32/92/e14a, proprietary

- 2.95 Morooka S, Inoue A, Oishi M, Aoki T, Nagaoka K and Yoshida H (1991) In-bundle void measurement of BWR fuel assembly by X-ray CT Scanner, The 1st JSME/ASME Joint International Conference on Nuclear Engineering, pp 237–243
- 2.96 Yagi M, Mitsutake T, Morooka S and Inoue A (1992) Void fraction distribution in BWR fuel assembly and the evaluation of subchannel code. In: Ninokata H and Aritomi M eds., *Subchannel Analysis in Nuclear Reactors*, pp 141–167, Tokyo, Japan
- 2.97 Inoue A, Futakuchi M, Yagi M, Kurosu T, Mitsutake T and Morooka S (1995) Void fraction distribution in a boiling water reactor fuel assembly and the evaluation of subchannel analysis codes, *Nuclear Technology*, vol 112 no 3 pp 388–400
- 2.98 Inoue A, Kurosu T, Oaki T, Futaguchi M, Yagi M, Morooka S, Hoshida A, Ishizuka T, Yoshimura K, Yoshida H, Mitsutake T, Abe N, Kozima A, Nakajima T, Nakamura S and Sawa T (1995) Void measurement of BWR fuel assembly, *J. At. Energy Soc. Japan*, vol 37 no 8 pp 710–720 (in Japanese)
- 2.99 Inoue A, Kurosu T, Oaki T, Yagi M, Mitsutake T and Morooka S (1995) Void fraction distribution in boiling water reactor fuel assembly and evaluation of subchannel code”, *J. Nucl. Sci. Technol.*, 32 no 7, 629–640
- 2.100 Kolev NI (27–29 June 2005) IVA Simulations of exercises 1 of phase 1 and 2 of the OECD/NRC benchmark based on NUPEC BWR full-size fine-mesh bundle tests (preliminary), Second Workshop on OECD/NRC Benchmark based on NUPEC BWR Full-size Fine-mesh Bundle Tests (BFBT), State College, PA, USA
- 2.101 Nylund O et al. (1968) Hydrodynamic and heat transfer measurements on a full scale simulated 36-rod Marviken fuel element with uniform heat flux distribution, FRIGG-2, AB Atomenergi, Stockholm, Sweden, ASEA, VÄSTERAS, R-4-447/RTL-1007
- 2.102 Nylund O et al. (1970) Hydrodynamic and heat transfer measurements on a full scale simulated 36-rod BHW fuel element with non-uniform axial and radial heat flux distribution, FRIGG-4, AB Atomenergi, Stockholm, Sweden, ASEA, VÄSTERAS, R4-502/RL-1253
- 2.103 Anklama TM and Miller RF (1982) Void fraction under high pressure, low flow conditions in rod bundle geometry, *Nucl. Eng. Des.*, vol 75 pp 99–108
- 2.104 Lucchini F and Marinelli V (1974) Experimental data on burn-out in simulated BWR fuel bundle, *Nucl. Eng. Des.* vol 31 pp 371–378
- 2.105 Spierling H (Sep. 24, 2002) Regional void fraction in ATRIUM 10XP at various peaking patterns, Framatome-ANP report, FGT, A1C-1311669-1, proprietary
- 2.106 Hori K, Miyazaki K, Kurosu T, Sugiyama S, Matsumoto J and Akiyama Y (1993) In bundle void fraction measurement of PWR fuel assembly, *Proceedings of ICONE 2*, vol 1 pp 69–76
- 2.107 Hori K, Akiyama Y, Miyazaki K, Kurosu T and Sugiyama S (1994) Transient void fraction measurement in a single Channel simulating one channel for a PWR Fuel Assembly, 10th Proceedings of Nuclear Thermal-Hydraulics, ANS Winter Meeting, pp 56–68
- 2.108 Hori K, Akiyama Y, Miyazaki K, Kurosu T and Sugiyama S (1995) Void fraction in a single channel simulating one subchannel of a PWR fuel assembly, *Proceedings of the First International Symposium on Two-Phase Flow Modelling and Experimentation*
- 2.109 Hori K, Akiyama Y, Miyazaki K, Nishioka H and Takeda N (1996) Total evaluation of in bundle void fraction measurement test of PWR fuel assembly, *Proceedings of ICONE-4*, vol 1, Part B, pp 801–811
- 2.110 Akiyama Y, Hori K, Miyazaki K, Nishioka H and Sugiyama S (23–27 April 1995) Evaluation of the bundle void fraction measurement data of PWR fuel assembly, The 3rd JSME/ASME Joint International Conference on Nuclear Engineering, Kyoto International Conference Hall, Kyoto, Japan, vol 1, pp 211–216

- 2.111 Akiyama Y, Hori K, Miyazaki K, Nishioka H and Sugiyama S (Dec. 2005) Pressurized water reactor fuel assembly subchannel void measurement, Nucl. Technol., vol 112, pp 412–421
- 2.112 Bartolomei GG, Batashova GN, Brantov VG et al. (1980) Heat and Mass Transfer IV, Izd. ITMO AN BSSR, Minsk, vol 5, p 38, in Russian
- 2.213 Frössel W (1936) Strömung in glatten, geraden Rohren mit Über- und unterschalgeschwindigkeit, Forsch. vol 7 no 2 pp 75–84

16.6 Material relocation: gravitational waves (1D, 2D), density waves in boiling and condensing systems

16.6.1 Flow through straight microchannel with constant cross-section

One of the simplest benchmarks is the computation of the mass flow through a straight channel as a function of the pressure difference. Before starting any thing more complex we consider the following simple task.

Consider *fully developed flow* in rectangular channel ($300\text{ }\mu\text{m} \times 303\text{ }\mu\text{m}$) over a length of 1 mm. Compute the mass flow through this channel as a function of pressure difference for the diesel fuel once analytically,

$$\rho_w F = F \sqrt{2 \rho \Delta p D_h / (\lambda L)},$$

and once using the computer code, and then compare the so-obtained results. The inlet pressure is 100 bar and the fuel temperature is 30°C. The density at these conditions is 829.088 kg/m³ and the cinematic viscosity 4×10^{-6} m²/s. For the analytical computation the properties are taken as constant. The computation with the computer code takes into account the variable properties. The results are given in Table 16.6.1 and presented in Fig. 16.6.1. The friction coefficient $\lambda = \lambda(\rho_w D_h / \eta, k / D_h)$, is a function of the Reynolds number and the relative roughness. The resulting transcendent system of equations in the analytical model is solved by a few iterations. It is computed in both the computer code and the analytical solution. The friction coefficient is computed in accordance with the algorithms presented in *Idelchik* (1993) p.113. The larger the pressure difference, the larger the density change. This is not considered in the analytical solution, but is taken into account in the code. If we “hard wire” the density as being constant in the code the predictions are very close to the analytical computation – see Fig. 16.6.1. This clear demonstrates that a) the code predicts properly mass flows for *developed flow* as function of pressure difference for microchannels with constant cross-section, and that b) the variation of the properties is getting important as the pressure variations become larger than 80–100 bar.

Table 16.6.1 Mass flow as a function of the pressure difference for a straight channel with constant cross-section

Δp bar	Mass flow, kg/s analytic	Mass flow, kg/s IVA_5M	Re, -	Friction coefficient, -
25	0.01282	0.012799	12 867	0.0618
50	0.01844	0.018127	18 515	0.0597
75	0.02259	0.021882	22 676	0.0597
99	0.02595	0.024800	26 053	0.0597

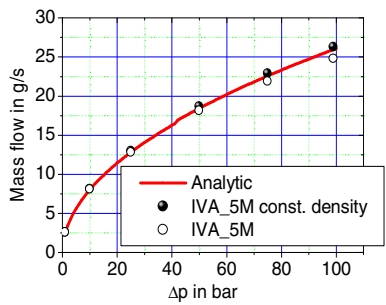


Fig. 16.6.1 Mass flow as function of pressure difference for rectangular channel ($300\text{ }\mu\text{m} \times 303\text{ }\mu\text{m}$) width and 1 mm length

16.6.2 Critical gas flow through nozzles and pipes with constant cross-section

Another classical example is the gas flow through short nozzle and pipes with a given length. Consider air flow through a 2-cm diameter pipe with inlet condition 1 bar and $20\text{ }^{\circ}\text{C}$. Compute the critical mass flow rate for pipes with $L/D_h = 0, 100$ and 350 and compare the results with the measurements reported by *Frössel* (1936).

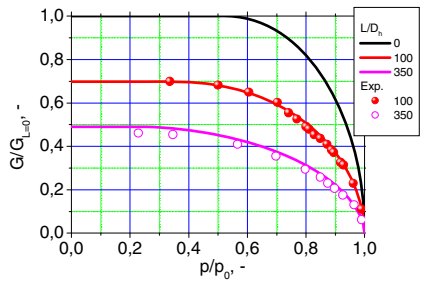


Fig. 16.6.2 Mass flow rate ratio as a function of the inlet outlet pressure ratio. $D_h = 0.02\text{ m}$, $p_0 = 1\text{ bar}$, $T_0 = 20\text{ }^{\circ}\text{C}$, air. Experimental data reported by *Frössel* (1936).

Using the perfect gas theory we perform this computation and present the results in Fig. 16.6.2. We see that the perfect gas theory works well in this particular case.

Now, use the system computer code IVA and perform the same analysis for $L/D_h = 350$. Compare the results with the prediction of the perfect gas theory. The comparison is presented in Fig. 16.6.3. The slight deviations are explained with the use of variable properties in the computer code along the tube.

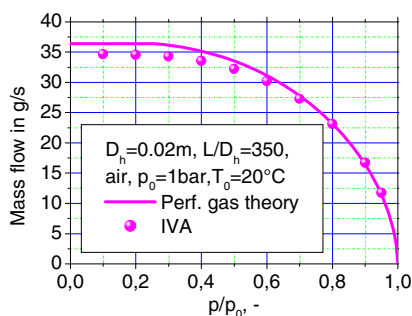


Fig. 16.6.3 Comparison between the prediction of the perfect gas theory and IVA computer code

Now consider a 1-m² vessel filled initially with 10 bar and 100 °C air connected with the environment by a 1-cm diameter pipe with length $L/D_h = 100$ and 350. Compute with the system computer code the discharge process with low spatial resolution, 20 computational cells only, and compare it with the solution resulting from the perfect gas theory. The solution is presented in Fig. 16.6.4. We see that even with very low resolution the computer code prediction is reasonable.

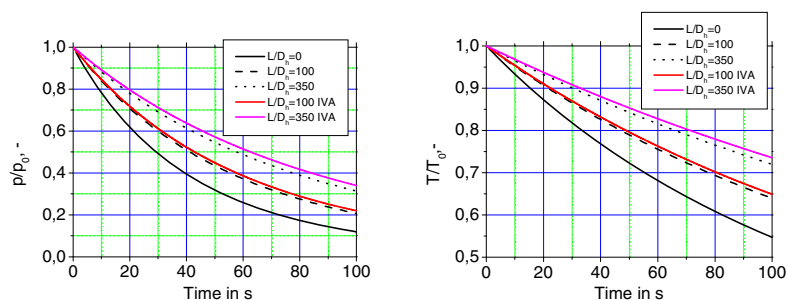


Fig. 16.6.4 Air release from a 1-m³ vessel through 1-cm diameter pipes. Pressure and temperature as functions of time.

16.6.3 U-tube benchmarks

16.6.3.1 Adiabatic oscillations

Consider the U-tube presented in Fig. 16.6.5a filled with water. The initial level deviates from the equilibrium one. The resulting oscillation period can be analytically computed for the frictionless case $\Delta\tau_{analytical} = 2\pi\sqrt{L/(2g)} = 1.608$ s. This makes this benchmark very suitable for verifying the dynamic performance of the code for gravitationally driven flow. The computed velocity is given in Fig. 16.6.5b.

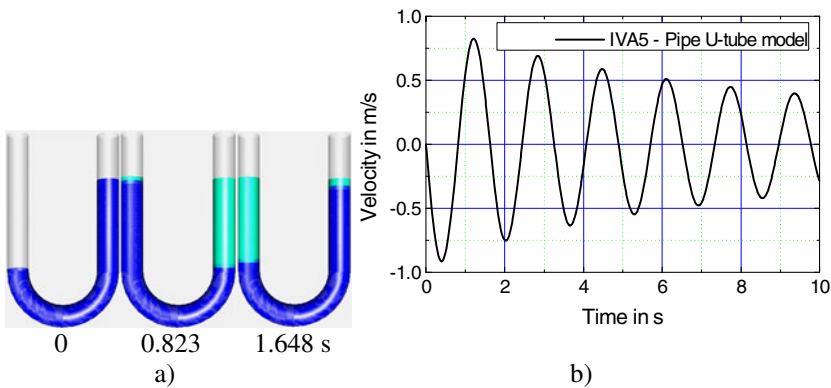


Fig. 16.6.5 IVA5 simulation of the U-tube benchmark. Length of the water axis $L = 1.285$ m. Analytical oscillation period 1.608 s neglecting the friction. Computed oscillation period 1.63 s (with friction + numerical diffusion). a) The first water oscillation. b) Velocity as a function of time. The process visualization was performed with SONJA

A similar case is modeled as a two-dimensional flow having the same cross-section of the vertical channels – see Fig. 16.6.6a. The resulting velocity as a time function is presented in Fig. 16.6.6b. We see that IVA5 predicts pretty well the period for the first case. Note that the period is only slightly influenced by the friction. In the second case the predicted period is 6.5% larger than the theoretical one. In the second case the cross-section normal to the flow velocity is not constant in the lower part. This is one of the reasons for this difference. In general, the damping of the amplitude is a result of the friction and of the numerical diffusion. The numerical diffusion is predominant compared to the friction for both cases.

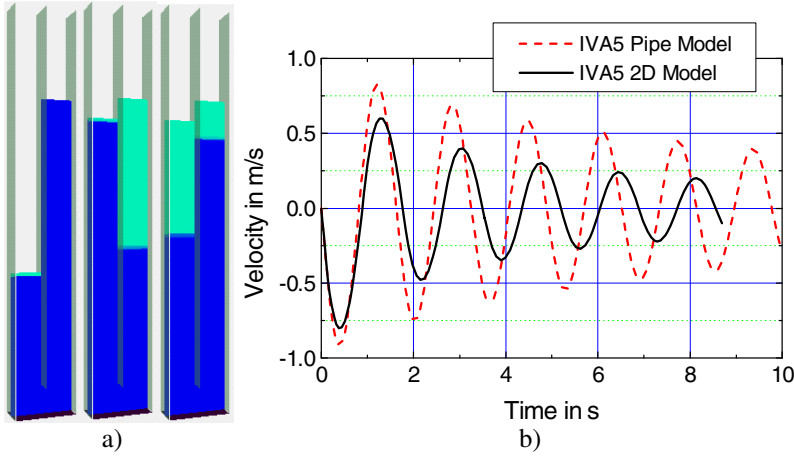


Fig. 16.6.6 IVA5 simulation of the 2D U-tube benchmark. Length of the water axis $L = 1.282$ m. Analytical oscillation period for 1D tube 1.606 s neglecting the friction. Computed averaged oscillation period 1.71 s. a) The first water oscillation. b) Velocity as a function of time. The process visualization was performed with SONJA

16.6.3.2 Single-phase natural convection in uniformly heated vertical part of a U-tube

We consider a U-tube with the following parameters: heated vertical part $\Delta z_{heat} = 1m$, total length $L = 2.1m$, pipe diameter $D_{pipe} = 0.032m$, constant heat flux density $\dot{q}'' = 78946 \text{ W/m}^2$. The fluid is water at atmospheric pressure with thermal properties: density $\rho_{fr} \approx 993 \text{ kg/m}^3$, thermal expansion $d\rho/dT = -0.408 \text{ kg/(m}^3\text{K)}$, specific capacity at constant pressure $c_p = 4169 \text{ J/(kgK)}$. The friction factor is $\lambda_R = 0.0357$ for a turbulent flow with $Re = 6912$. In this case the analytical solution *Kolev* (2002) for the mass flow rate is

$$G = \left(-4\Delta z_{heat}^2 \frac{g\rho_{in}}{\lambda_R L} \frac{d\rho}{dT} \frac{\dot{q}''}{c_p} \right)^{1/3}$$

$$= \left(4 \times 1^2 \frac{9.81 \times 993}{0.0357 \times 2.1} 0.408 \frac{78946}{4169} \right)^{1/3} = 158.95 \text{ kg/(m}^2\text{s)}.$$

With this mass flow rate the *Reynolds* number takes the value already mentioned. The relative density change in this case is

$$B = \frac{1}{\rho_{in}} \frac{d\rho}{dT} \frac{\dot{q}''}{G c_p} \frac{4\Delta z_{heat}}{D_h} = -\frac{0.408 \times 78946 \times 4 \times 1}{993 \times 158.95 \times 4169 \times 0.032} = -6.1625 \times 10^{-2},$$

which makes the influence of the density change on the friction and on the acceleration inertia negligible. We simulate the process with 42 equidistant computational cells. The prediction of IVA6 is

$$G_{IVA6} = 157.82 \text{ kg} / (\text{m}^2 \text{ s}).$$

The relative difference is less than 0.7%. We consider this agreement as excellent.

16.6.3.3 Single-phase natural convection in uniformly heated inclined part of a U-tube

We consider a U-tube consisting of three parts: the first is vertical and starts at $\Delta z_0 = 2.94 \text{ m}$ below a given horizontal plane. It has a length $\Delta z_1 = 2.94 \text{ m}$. The second part of length $\Delta z_{\text{heated}} = 4.2 \text{ m}$ is inclined at an angle 1.47063 rad with respect to the upwards directed vertical. The third part has a length $\Delta z_3 = 5.46 \text{ m}$, is vertical and ends at the above-mentioned horizontal plane. The total length of the pipe is $L = 12.6 \text{ m}$. The pipe has a diameter $D_{\text{pipe}} = 0.032 \text{ m}$. The heated part receives the heat flux density $\dot{q}'' = 78946 \text{ W/m}^2$. The fluid is water with thermal properties $\rho_{\text{in}} = 996.4 \text{ kg/m}^3$, $\frac{d\rho}{dT} = -0.465 \text{ kg/(m}^3 \text{ K)}$, $c_p = 4175 \text{ J/(kg K)}$. The friction factors for the three parts are $\lambda_{R1} = 0.0316$, $\lambda_{R2} = 0.02951$, $\lambda_{R3} = 0.02809$ for a turbulent flow with $\text{Re} = 16396$. The length-weighted averaging of the friction coefficient gives $\bar{\lambda}_R = 0.02938$. In this case the analytical solution *Kolev* (2002) gives

$$\begin{aligned} G &= \left[-g \frac{8}{\bar{\lambda}_R} \rho_{\text{in}} \frac{d\rho}{dT} \frac{\dot{q}''}{c_p} \frac{\Delta z_{\text{heated}}}{L} \left(\Delta z_3 + \Delta z_{\text{heated}} \frac{1}{2} \cos \varphi \right) \right]^{1/3} \\ &= \left(9.81 \frac{8}{0.02938} 996.4 \times 0.465 \frac{78946}{4175} \frac{4.2}{12.6} \left[5.46 + \frac{4.2}{2} \cos(1.47063) \right] \right)^{1/3} \\ &= 353.65 \text{ kg} / (\text{m}^2 \text{ s}). \end{aligned}$$

Neglecting the contribution of the inclined heated part results in $349.23 \text{ kg} / (\text{m}^2 \text{ s})$, which is only 1.25% less, which means that the main contribution comes from the vertical nonheated part filled with hot fluid. With this mass flow rate the *Reynolds* number takes the value already mentioned. The relative density change in this case is

$$B = \frac{1}{\rho_{\text{in}}} \frac{d\rho}{dT} \frac{\dot{q}'' 4 \Delta z_{\text{heated}}}{G c_p D_1} - \frac{0.465 \times 78946 \times 4 \times 4.2}{996 \times 354.65 \times 4175 \times 0.032} = -1.307 \times 10^{-2},$$

which justifies the use of length-weighted averaging of the friction coefficient and the neglect of the inertia effect due to the density change. We simulate the process using IVA6 with 126 equidistant computational cells and obtain

$$G_{IVA6}(126cells) = 336.30 \text{ kg} / (\text{m}^2 \text{ s}),$$

which is 4.9% less than the analytical prediction. We learn from this example that appropriate discretization is crucial especially in the case of a sensible balance between small driving forces, friction and momentum loss due to numerical diffusion.

16.6.3.4 Single-phase natural convection in a U-tube with inclined part heated by steam condensation

As in the previous case we consider a U-tube consisting of three parts: the first is a vertical one and starts at $\Delta z_0 = 2.94 \text{ m}$ below a given horizontal plane. It has a length $\Delta z_1 = 2.94 \text{ m}$. The second part of length $\Delta z_{heated} = 4.2 \text{ m}$ is inclined at an angle 1.47063 rad with respect to the upwards directed vertical. The third part has a length $\Delta z_3 = 5.46 \text{ m}$, is vertical and ends at the above mentioned horizontal plane. The total length of the pipe is $L = 12.6 \text{ m}$. The pipe has a diameter $D_{pipe} = 0.032 \text{ m}$. The thickness of the pipe is 3 mm . The wall heat conduction coefficient used is that for steel, $\lambda_w = 14.93 \text{ W} / (\text{mK})$. The heated part receives the heat flux density $\dot{q}'' = 78946 \text{ W/m}^2$. The fluid is water with thermal properties $\rho_{in} = 995.78 \text{ kg} / \text{m}^3$, $\frac{d\rho}{dT} = -0.465 \text{ kg} / (\text{m}^3 \text{ K})$, $c_p = 4175 \text{ J} / (\text{kgK})$. The friction factors for the three parts are $\lambda_{R1} = 0.0312$, $\lambda_{R2} = 0.0293$, $\lambda_{R3} = 0.0283$, respectively, for a turbulent flow with $\text{Re} = 11886$. The length-weighted averaging of the friction coefficient gives $\bar{\lambda}_R = 0.02926$. For both heat-transfer coefficients we use the values $\alpha_{conv} = 1727 \text{ W} / (\text{m}^2 \text{ K})$ and $\alpha_{cond} = 10396 \text{ W} / (\text{m}^2 \text{ K})$. In this case, the analytical solution Kolev (2002) gives

$$G_1 = \sqrt{-2g\rho_{in} \frac{d\rho}{dT} (T_{cond} - T_{in}) (1 - e^{-a}) \frac{D_1}{\bar{\lambda}_R L} \left[\Delta z_3 + \Delta z_{heated} \left(\frac{1}{1 - e^{-a}} - \frac{1}{a} \right) \cos \varphi \right]},$$

or $G = 296.27 \text{ kg} / (\text{m}^2 \text{ s})$, with

$$\bar{\lambda}_R = \lambda_{R1} \frac{\Delta z_1}{L} + \lambda_{R2} \frac{\Delta z_{heated}}{L} \frac{\ln \left\{ \varepsilon_0 \left[(1/\varepsilon_0 + 1) e^a - 1 \right] \right\}}{a(1 + \varepsilon_0)} + \lambda_{R3} \frac{\Delta z_3}{L} \frac{1}{1 + B}.$$

The thermal power computed for 4 times 120 pipes is $P(4 \times 120 \text{ pipes}) = 13.151 \text{ MW}$. Note that the expression

$$\frac{\ln \left\{ \varepsilon_0 \left[(1/\varepsilon_0 + 1)e^a - 1 \right] \right\}}{a(1 + \varepsilon_0)} = 1.00498,$$

is very close to one. With this mass flow rate the *Reynolds* number takes the value already mentioned. The relative density change in this case is $B = -9.14 \times 10^{-3}$, which justifies the use of length-weighted averaging of the friction coefficient and the neglect of the inertia effect due to the density change. The computed outlet water temperature is 330.68 K. The coefficient “ a ” is about $\frac{1}{2}$, which defines the local distribution of the water temperature.

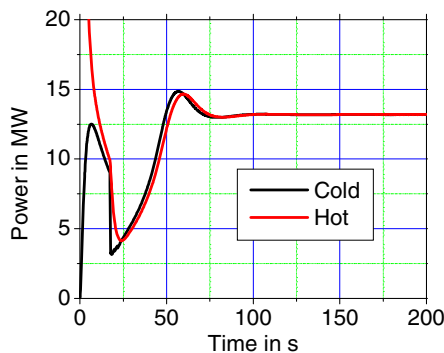


Fig. 16.6.7 Power of a condenser with 4 times 120 pipes as a function of time at the two sides of the heat-conducting pipe

We simulate the process with 126 equidistant computational cells on the primary side. The secondary size is simulated by a large-diameter pipe (0.1 m) which is concentric with the heated part and has a bend at the lower end going downwards. The secondary pipe is then equidistantly discretized with 52 cells. The boundary conditions at the secondary pipe are atmospheric pressure and saturated steam. The transient behavior is given in Fig. 16.6.7. The steady state solution is

$$G_{IVA6}(126 \text{ cells}) = 312.17 \text{ kg / (m}^2 \text{ s)},$$

$$P_{IVA6}(4 \times 120 \text{ pipes}) = 13.1932 \text{ MW},$$

which is in very good agreement with the analytical prediction. The computed outlet water temperature is 329.36 K, which compared to the analytical solution of 330.68 K is also in a very good agreement. Note that to allow for correct comparison with the analytical solution, we took the averaged values of the

friction coefficients, and of the heat-transfer coefficients, as well as the thermal properties as computed by IVA6 and used them in the analytical solution.

16.6.4 Flow boiling stability

Natural circulation loops are known to behave like the already-discussed U-tube manometers. They have their own eigenfrequency of oscillations, depending on the square of the length of the liquid axis. In addition, heat input into the fluid without or with boiling can excite damped or not damped oscillations depending on the input power. In boiling loops density waves interact with their own “U-tube” oscillations. Therefore, each natural circulation loop has its own signature. For many practical reasons it is always of interest for a given geometry and inlet flow properties to find the mass-flow–power relation and the stability region. Analytical benchmarks for loops heated by external condensation and the successful validation of the IVA performance on them are provided in the previous section (see also in *Kolev (2002)*). The specific physics in those cases was that condensation deposits the latent heat into the wall and that the feedback of the power to the mass flow is very sensitive.

Our intention is to verify the computer code IVA for stability analysis of boiling bundles in loops. Thermal hydraulic instabilities in boiling systems are reviewed by *Yadigaroglu (1978, 2005)*, *Nakanishi (1981)* and *Kakac (1985)*. In the last 50 years the stability of boiling systems has usually been analyzed by using simplified linearized models applying perturbation theory. It is outside the scope of this section to review this subject but let us recall some of the representative works:

- 1) Linear stability analysis using homogeneous equilibrium models are reported in *Wallis and Heasley (1961)*, *Stenning and Veziroglu (1965, 1967)*, *Lahey and Yadigaroglu (1973)*, *Yadigaroglu and Lahey (1975)*, *Furutera (1986)*, *Lahey and Moody (1993)*, *Nayak et al. (1998)*, *Delmastro et al. (1991)*, *Lee and Lee (1991)*, *Wang et al. (1994)* among others. *Ambrosini and Ferreri (2006)* demonstrated that numerical accuracy is crucial to obtain consistent results. Bad spatial resolution for instance either degrades or shifts the boundaries in the stability maps.
- 2) Linear stability analysis using slip or drift flux equilibrium models are reported in *Fukuda et al. (1984)*, *Ishii (1971)*, *Saha and Zuber (1978)*, *Park et al. (1986)*, *Rizwan-Uddin and Doming (1986)*, *van Bragt et al. (2000)* among others.
- 3) *Saha (1974)* and *Saha et al. (1976)* extended the earlier work by adding a subcooled boiling model. Using such types of models *Chan (1979)* and *Chan and Yadigaroglu (1981)* analyzed the stability of steam generators, and *Wolf et al. (1982)* analyzed stability of solar-thermal steam generators. Allowing for flushing in such models by enforcing equilibrium outside the subcooled boiling region *Zhou and Yadigaroglu (1988)*, *Inada et al. (2000)* analyzed the stability of small heating reactors with flashing driven by pressure changes. Coupling this type of coolant modeling with nodal neutron kinetics

was done by *Park et al.* (1983a, b, c), *Peng et al.* (1985, 1986), *Taleyarkhan* (1982), *Taleyarkhan et al.* (1985, 1994). Finally, one should mention the recent development of the MATSTAB program *Hänggi* (2001) *Hänggi et al.* (1999) that is a linearized version of the RAMONA computer program – a time-domain code which is often used for BWR stability analysis.

The advantage of this method – its simplicity – is also its drawback. Nonlinearities that come from the complex physics are not taken into account and therefore essential instability modes may not be revealed. The computational power of the recent computers allows applying complete nonlinear models to instability analyses and overcoming these difficulties. Moreover, the instability analysis is also a fundamental tests for thermal-hydraulics computer codes, allowing to judge whether the codes possess the appropriate mathematical correctness to reflect real oscillations of the process parameters.

In this section we select one experimental data set obtained by *Schäfer* and *Beisiegel* in 1992 on the AREVA/FANP KATHY loop and compare the results of the simulation with IVA computer code. Finally, conclusions are drawn.

In the case considered here a test series with no. 11 for ATRIUM-10B fuel bundle, see Fig. 16.6.8, performed on the AREVA/FANP KATHY loop, *Schäfer* and *Beisiegel* (1992), is used. An electrically heated 1:1 simulator for this bundle is used. The schematic loop representation of the geometry is given in Fig. 16.6.9a.



Fig. 16.6.8 71-MWd/kgU burnup ATRIM 10-rod bundle

This geometry was modeled using the network capability of IVA. Some inevitable approximations of the geometry are done here and there. So for instance several irreversible friction contributions before the entrance of the bundle section are lumped in an irreversible friction coefficient 25.62 related to the flow cross-section in the bundle. The inlet temperature was assumed to be 560.89 K although some small variations from experiment to experiment are recorded.

We prescribe for the computation the time evolution of the electrical power of the bundle as shown in Fig. 16.6.9b. After each jump the power remains constant to see the steady-state solution as shown in Fig. 16.6.10. Figure 16.6.10 shows the mass flow as a function of time.

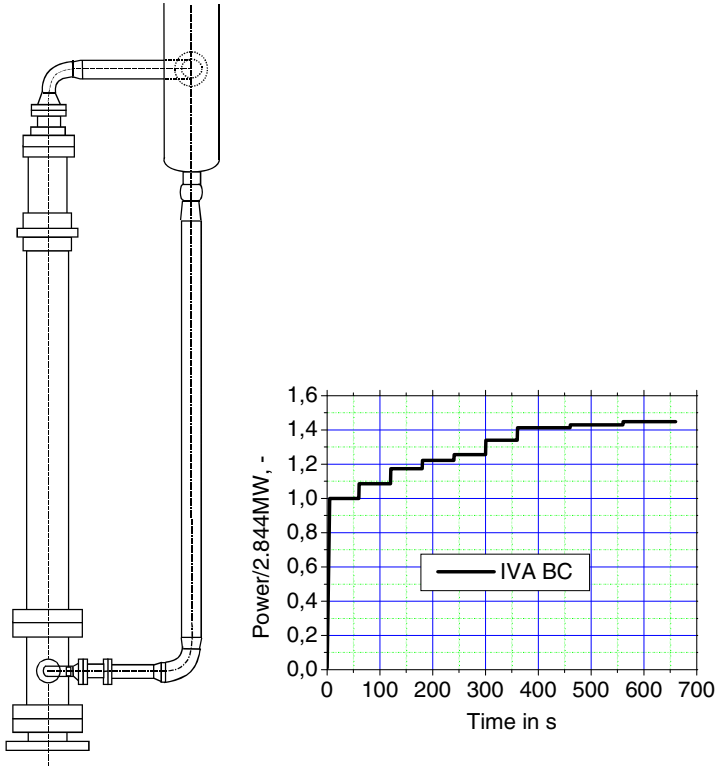


Fig. 16.6.9 a) Geometry of the test section in the AREVA/FANP KATHY loop *Schäfer and Beisiegel* (1992); b) Bundle power as a function of time in the IVA simulations

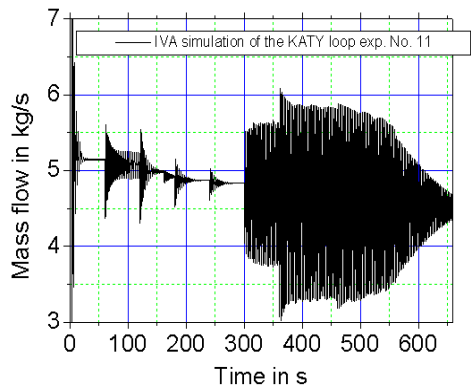


Fig. 16.6.10 Mass flow as a function of time for changing bundle power as given in Fig. 16.6.9b

Analyzing the solution we obtain the results presented in Figs. 16.6.11a and 16.6.12a.

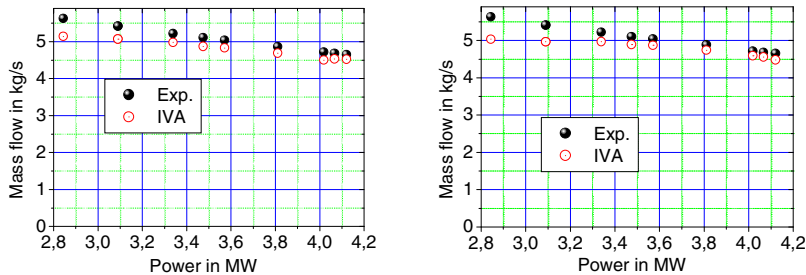


Fig. 16.6.11 Mass flow as a function of the bundle power, *Kolev* (2006): a) Power change as given in Fig. 16.6.9b; b) Power jump from zero.

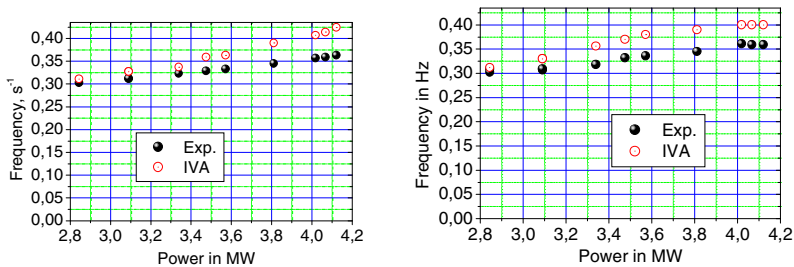


Fig. 16.6.12 Frequency of the oscillation of the total mass flow, *Kolev* (2006): a) Power change as given in Fig. 16.6.9b; b) Power jump from zero.

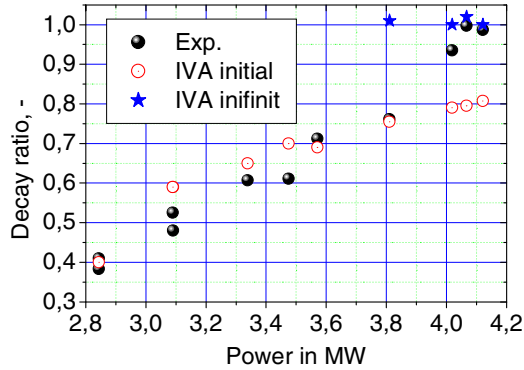


Fig. 16.6.13 Decay ratio of the oscillation as a function of power, *Kolev* (2006)

In order to check whether the obtained solutions are dependent on the way the power disturbance is imposed we repeat the computation with imposing a jump of the power from zero to each measured value.

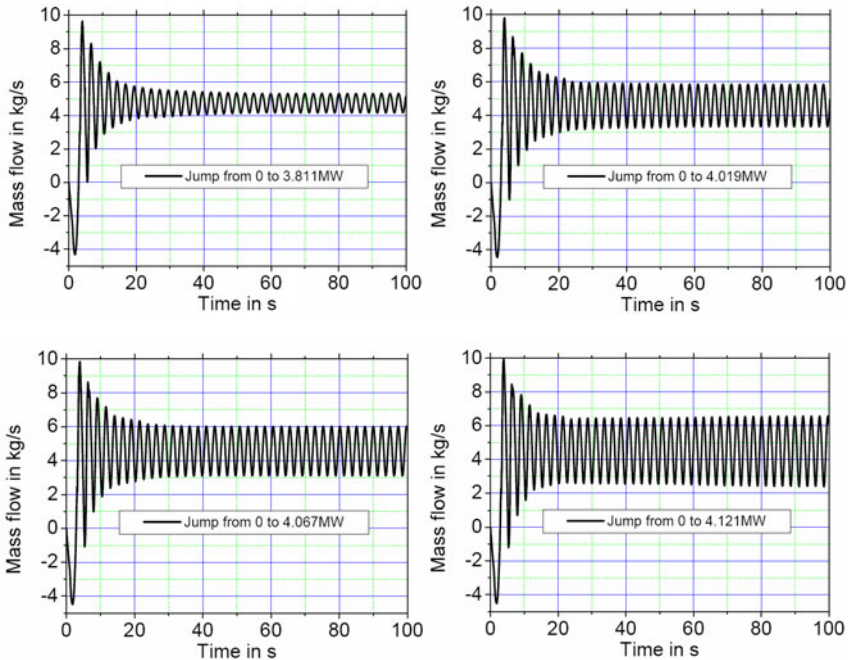


Fig. 16.6.14 Mass flow as a function of time for the cases approaching the stability limit

The results are presented in Figs. 16.6.11b and 16.6.12b. Figure 16.6.11 shows the mass flow as a function of the power. Increasing the power increases the void over the heated section and after it and causes a larger pressure loss that itself reduces the mass flow. The measured trend is properly predicted. The selected irreversible friction coefficient is obviously somewhat larger than the real one. The observed frequencies of the oscillations slightly increase with the power increase, as shown in Fig. 16.6.12. This trend is also properly predicted by IVA. The difference between the computed and observed oscillation frequencies slightly increases with the power. The decay ratio for each case is presented in Fig. 16.6.13. We see that up to 3.6 MW the predicted and the measured decay ratios agree well with the experiment. Up 3.811 MW, as shown in Fig. 16.6.14, the initial perturbation is damped but the final steady state is a harmonic oscillation. Increasing of the power results in exponential increasing of the amplitude as shown in Fig. 16.6.15. The structure of the density waves for the case of 4.121 MW is illustrated on Fig. 16.6.16, where mass flow rates and void fractions at different elevations are presented as a time functions.

$$\text{Mass flow in kg / s} = 0.48556 + 3.70165 \times 10^{-15} \exp\left[(\text{Power in MW})/0.12228\right]$$

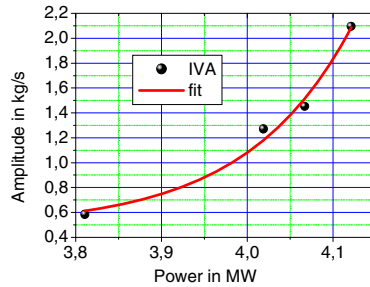


Fig. 16.6.15 Amplitude of the oscillations as a function of the bundle power close to the stability limit.

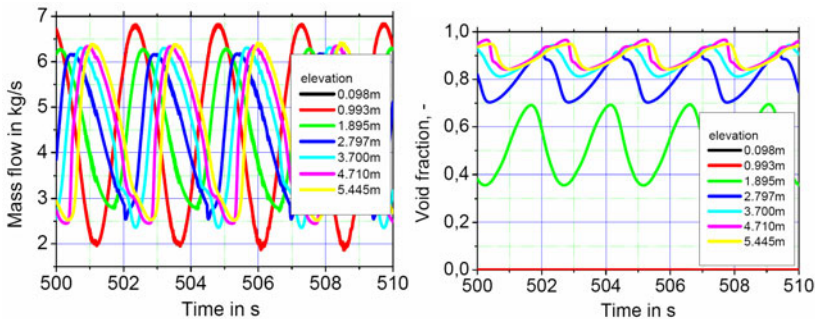


Fig. 16.6.16 Structure of the density waves for the 4.121-MW case: a) Mass flow as a function of time at different elevations; b) Void fractions as a function of time at different elevations.

At powers above 4.15 MW nondamped oscillations are expected. We see a correct prediction of the measured phenomena by IVA computer code.

Conclusions

There are two important conclusions drawn from this analysis: one regarding the mathematical modeling of the complex boiling dynamics in bundles in oscillating systems and the other regarding the practical usefulness of the computer tool for such analyses.

1. The complete simulation of the dumped and not dumped instability observed in the eleven experiments with all complexities of the interactions of different physical mechanisms, mathematical methods, geometry descriptions, etc. is a severe challenge for any computer code simulating flow boiling. The IVA computer code successfully reproduces the complexity of the observed processes.
2. Besides the condensation-induced instability benchmarks reported in the previous section this benchmark demonstrates the capability of IVA to be successfully used for stability analyses in boiling loops and in particular for boiling loops of BWR type.

Acknowledgment: This study was motivated by the fruitful discussion with *Douglas Pruitt* and *Yousef Farawila* from Framatome-ANP in the US. The data processing done by *Eva Ziegerer* from the University of Erlangen is highly appreciated.

16.6.5 Flow condensation stability

Condensation processes are similar to the boiling processes in the sense of occurrence of density-wave oscillations. I will consider here experimentally observed in-pipe condensation and will try to reproduce the experiments performed in the Research Center Jülich by *Schaffrath* (1996) with the IVA computer code. Many interesting features will be discussed in the course of this comparison. 8 condenser steel pipes with averaged length 9.8m, 0.0378 m internal diameter and 0.0029 m thickness as shown in Fig. 16.6.17 are used. The pipes are placed as shown in Fig. 16.6.18 in a 1 bar secondary water reservoir containing saturated water. The condensate pipes are connected with a high-pressure vertical cylinder as shown in Fig. 16.6.19. The nozzle at the entrance reduces the cross-section to 0.462 of the inlet pipe cross-section and at the exit to 0.432. This is taken into account.

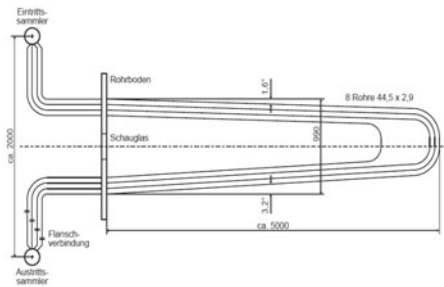


Fig. 16.6.17 Condenser pipes

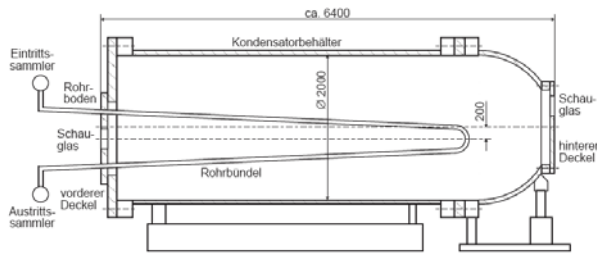


Fig. 16.6.18 Condenser pipes in secondary vessel

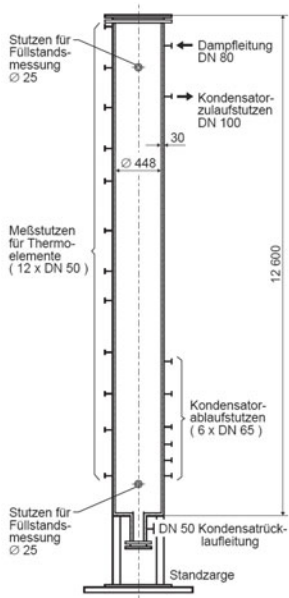
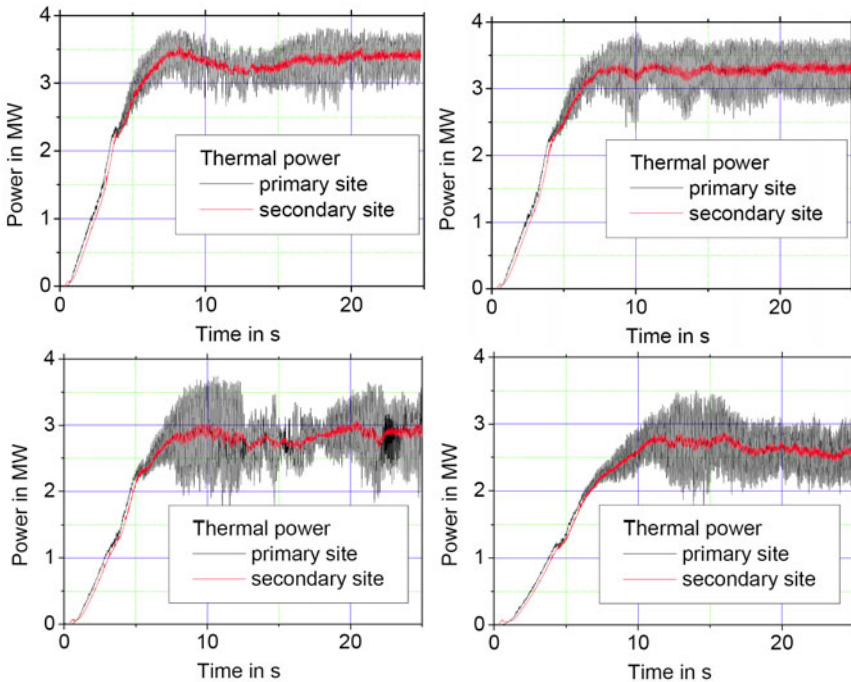


Fig. 16.6.19 Pressure vessel

The experiments designated with A are performed with steam at 70, 50 30, 10 and 3 bar and different levels of water above the condensate outflow nozzle. After adjusting the water level the power was measured in different ways. The secondary temperature was the saturation temperature at 1 bar pressure. Vertical plates are used to direct the secondary flow vertically. The main result of the experiment is the thermal power as a function of the water level above the condensate exit pipe.

The simulation performed with the pipe network features of IVA has a 10-cm spatial resolution. The secondary site is very approximately modeled by enforcing water flow through a countercurrent environment allowing almost constant external wall temperature corresponding to boiling. The initial conditions are: condenser system filled with water. At time zero the condensate exit pressure is set to the pressure corresponding to the water level. Computationally, the simulated emptying process which takes about 10 s initiates the condensation process. Then, a quasisteady state is computationally established and the power reached is recorded. The first observation is that the steady state is a stable oscillatory state. The time-averaged thermal power is used for comparison with the measurements.

Next, I will discuss in some detail the dynamic behavior of such a system based on the A3 experiment series. Figures 16.6.20a–e show the primary and the secondary power as a function of time. The obtained dynamical steady state is clearly visible.



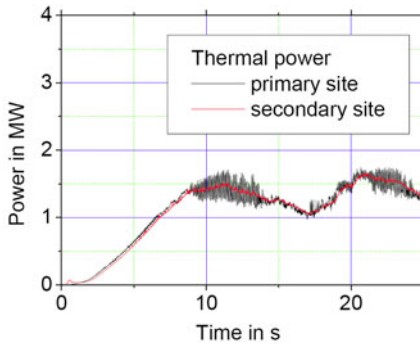


Fig. 16.6.20 Jülich emergency condenser experiment: Thermal power as a function of time. Vessel pressure 70 bar. Water level over the drainage nozzle: a) 0.88 m; b) 1.8 m; c) 3.4 m; d) 4.9 m; e) 6.3 m

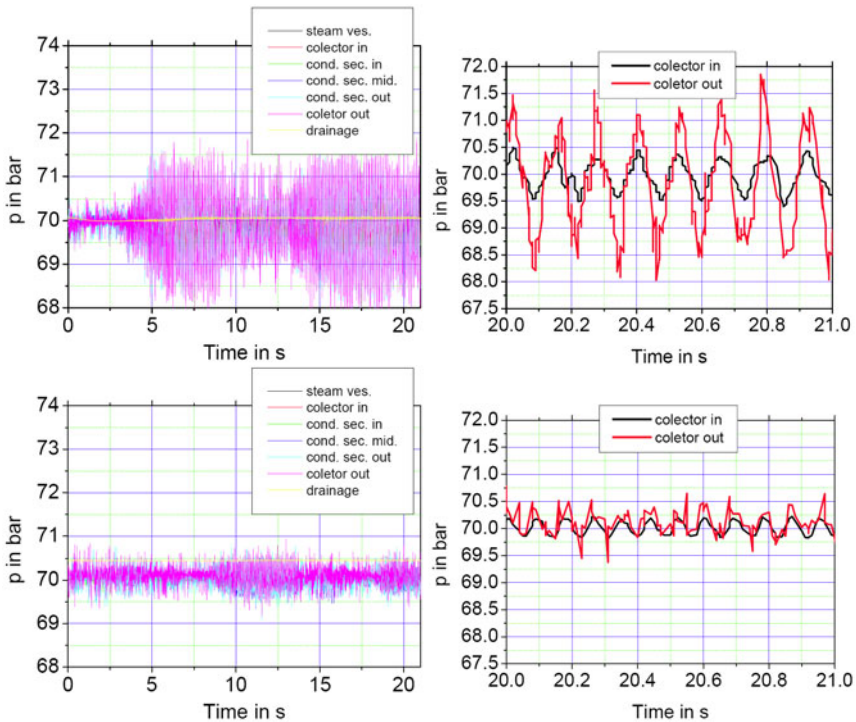
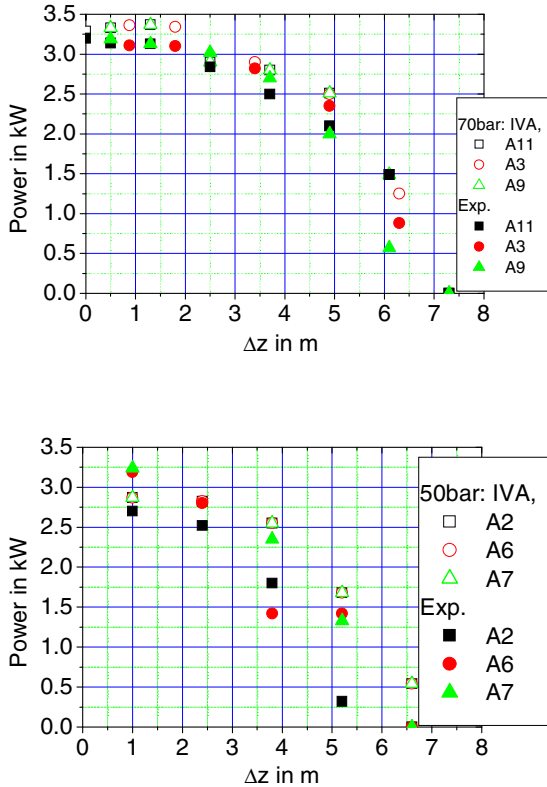


Fig. 16.6.21 Pressures at different places in the primary site as a function of time for 0 m water level above the condensate outlet nozzle: a) 0.88 m; b) 6.3 m

Plotting the pressures in the primary site at different places we realize that the condensation is associated with oscillations. Figure 16.6.21 illustrate this phenomenon. The pressures at different places in the primary site are presented as a function of time for 0.88 m and 6.5m water level above the condensate outlet

nozzle. Oscillations of 0.2–2 bar amplitudes with frequency about 8 Hz are expected. Increasing the level up to 6.3 m increases the frequency up to about 12 Hz by reducing the amplitude.

Figure 16.6.22a shows the computed thermal power as a function of the water level above the exit nozzle. It is as expected, a decreasing function of the submergence of the exit pipe. The experimental data points are also entered in this figure.



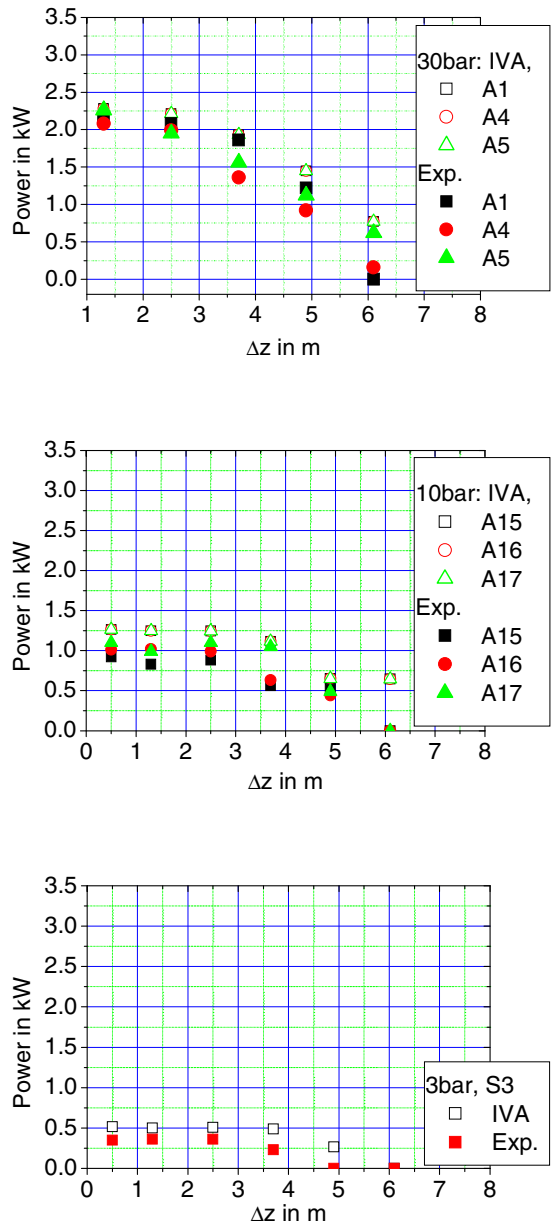


Fig. 16.6.22 Power as a function of the water level above the condensate exit nozzle

I perform similar analysis for all 73 available states for pressures of 70, 50, 30, 10 and 3 bar. The groups of data are plotted on Figs. 16.6.22a–e. Before judging the accuracy of the computation let us see Fig. 16.6.23 that is taken from p. 68 of *Schaffrath's* work. It shows that the error is below 10% for powers larger then 1.5 MW. For smaller power the error exponentially increases.

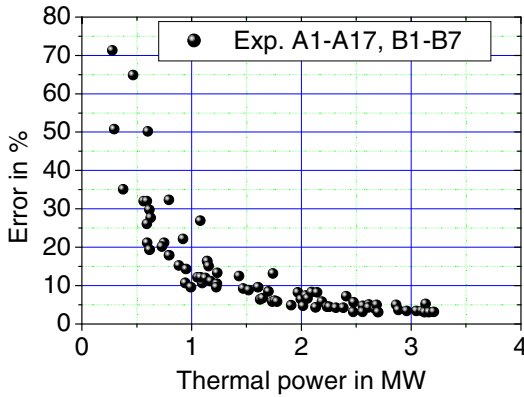


Fig. 16.6.23 *Schaffrath* (1996): Measurement error in % estimated by three different methods

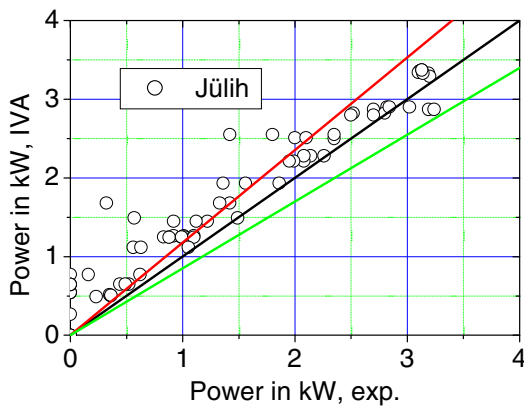


Fig. 16.6.24 Power estimated using IVA computer code compared to the real measured experimental power

Figure 16.6.24 shows the power estimated using IVA computer code compared to the real measured experimental power for all 73 points. The 15% error band is also given.

One source of error of the modeling is the not very accurate simulation of the secondary site. But I believe that this has a minor contribution in this particular case because the secondary heat transfer is nucleate boiling. Due to the very high secondary heat-transfer coefficient the main thermal resistance is on the condensation site.

Comparing Figs. 16.6.23 and 16.6.24 we realize that as long as the measurements are accurate, the agreement with the analysis is very good.

With decreasing thermal power the measurement error increases exponentially making data comparison not informative.

The important output of such analysis is obtaining the oscillating characteristics of the gravitationally removed condensate and the interaction with the condensing steam. At small power, the amplitudes are low but with increasing power the amplitudes increases. Therefore, the structural design of such facilities has to take this into account.

16.6.6 Gravitational 2D waves

An experiment performed by *Maschek* et al. (1992) was used to study the capability of IVA5 to model gravitational relocation of water, the so-called dam-break problem. The predicted water volume fraction as a function of radius and height for different times is presented in Fig. 26.6.25. Good agreement between IVA5 prediction and experiment is obtained from the start of the experiment to the moment when the water reaches the external boundary. The next part of the experiment is associated with growth of the surface instabilities and strong turbulization of the water. Note that in the experimentally observed data circumferential instability occurs, with 16 to 18 eruptions taking place with peaks located approximately equidistantly in one circle. 2D modeling of the three-dimensional process does not predict this 3D effect as expected. Here, the code predicts relatively compact movement of the water with weaker “turbulence” and fragmentation of the surface than that actually observed in the experiment.

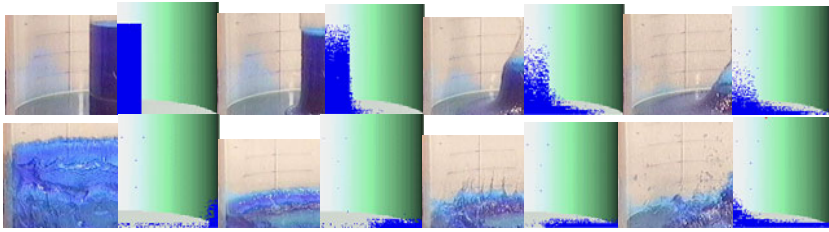


Fig. 16.6.25 Comparison between the IVA5 prediction of the water volume fraction as a function of radius and height and the experimental observation by Maschek et al. with the time used as a parameter: 0, 0.08, 0.16, 0.20, 0.40, 0.56, 0.64, 0.72 s (from left to right)

Note that *Fannelop* and *Waldman* (1972) reported an analytical solution for the position of the triple point at the bottom as a function of time:

$$r(\tau) = 2 \left[\frac{g \text{ Vol } Fr}{\pi(4 - Fr)} \right]^{0.25} \sqrt{\tau}.$$

Here *Vol* is the initial liquid volume of the cylinder and the *Froude* number $Fr = V/\sqrt{ge}$ is defined as a function of the bottom spreading velocity *V* and the thickness of the depth of the fluid at the leading edge *e*.

Conclusion. From this comparison it can be concluded that the hydraulic model of IVA5 works properly for cases in which gravitational acceleration is driving the liquid flow, and that it needs improvement for cases in which strong surface turbulence and surface droplet entrainment occur. Note that turbulence modeling for general multiphase flows is at the very beginning of its development. High-order modeling of the free surface, as already done by some authors, will substantially improve the results.

References

- Ambrosini, W., Ferreri, J.C.: Analysis of basic phenomena in boiling channel instabilities with different flow models and numerical schemes. In: Proc. of ICONE14, Int. Conf. on Nuclear Engineering, Miami, FA, USA, July 17-20 (2006)
- Chan, K.C.: Thermal-hydraulic stability analysis of steam generators. Ph.D. Thesis, Department of Nuclear Engineering, University of California Berkeley (1979)
- Chan, K.C., Yadigaroglu, G.: Two-phase flow stability of steam generators. In: Bergles, A.E., Ishigai, S. (eds.) *Two-Phase Flow Dynamics*, pp. 365–377. Hemisphere Publishing Corp., Washington (1981)
- Delmastro, D.F., Clausse, A., Converti, J.: The influence of gravity on the stability of boiling flows. *Nucl. Eng. Des.* 127, 29–139 (1991)

- Fannelop, T.K., Waldman, G.D.: Dynamics of oil slicks. *AIAA J* 10(4), 506–510 (1972)
- Frössel, W.: Strömung in glatten, geraden Röhren mit Über- und unterschalgeschwindigkeit. *Forsch.* 7(2), 75–84 (1936)
- Fukuda, K., Kato, A., Hasegawa, S.: Two-phase flow instability at low flow rate conditions. *J. Nucl. Sci. Technol.* 21, 491–500 (1984)
- Furutera, M.: Validity of homogeneous flow model for instability analysis. *Nucl. Eng. Des.* 95, 65–77 (1986)
- Hänggi, P., Smed, T., Lansäker, P.: A fast frequency domain based code to predict boiling water reactor stability using detailed three dimensional model. In: *NURETH-9*, San Francisco (1999)
- Hänggi, P.: Investigating BWR stability with a new linear frequency-domain method and detailed 3D neutronics. Doctoral dissertation. Swiss Federal Institute of Technology, Zurich BTHZ (2001)
- Idelchik, I.E.: Handbook of hydraulic resistance, 3rd edn. Begell House, New York (1993)
- Inada, F., Furuya, M., Yusuo, A.: Thermo-hydraulic instability of boiling natural circulation loop induced by flashing (analytical consideration). *Nucl. Eng. Des.*, 187–199 (2000)
- Ishii, M., Zuber, N.: Thermally induced flow instabilities in two-phase mixtures. In: *4th International Heat Transfer Conference*, Paris, vol. 5 (1970)
- Ishii, M.: Thermally induced flow instabilities in two-phase mixtures in thermal equilibrium. PhD Thesis. School of Mechanical Engineering, Georgia Institute of Technology (1971)
- Kakac, S.: Review of two-phase flow instabilities. *Metu. J. Pure and Applied Sciences* 18, 171–252 (1985)
- Kolev, N.I.: Simple analytical U-tube benchmarks appropriate for testing of pipe-network computer codes. In: *Proceedings of ICONE10: Tenth International Conference on Nuclear Engineering*, Arlington, Virginia (Washington, D.C.), USA ICONE10-22711, April 14–18 (2002)
- Kolev, N.I.: Verification of IVA computer code for flow boiling stability analysis. In: *Proceedings of ICONE-14 2006*, Miami, Florida, USA, Paper ICONE14-89034 (July 17–20, 2006)
- Lahey Jr., R.T., Moody, F.J.: The thermal-hydraulics of a boiling water nuclear reactor. *ANS* (1993)
- Lee, S.Y., Lee, D.W.: Linear analysis of flow instabilities in an open two-phase natural circulation loop. *Nucl. Eng. Des.* 128, 317–330 (1991)
- Maschek, W., Roth, A., Kirstahler, M., Meyer, L.: Simulation experiments for centralized liquid sloshing motions, Kernforschungszentrum Karlsruhe, KfK 5090 (December 1992)
- Nakanishi, S.: Recent Japanese research on two-phase flow instabilities. In: *Proceedings of Japan–US Seminar on Two-phase Flow Dynamics*, Hemisphere Publishing Corporation, Washington, D.C (1981)
- Nayak, A.K., Vijayan, P.K., Saha, D., Venkat Raj, V., Aritomi, M.: Linear analysis of thermohydraulic instabilities of the advanced heavy water reactor (AHWR). *J. Nucl. Sci. Technol.* 35, 768–778 (1998)
- Park, G.C., Podowski, M., Becker, M., Lahey Jr., R.T.: The modeling of density-wave oscillations in boiling water nuclear reactors. In: Kakac, S., Ishii, M. (eds.) *Advances in Two-Phase flow and Heat Transfer*. Martinus Nijhoff Publishers, Boston (1983a)
- Park, G.C., Podowski, M., Becker, M., Lahey Jr., R.T.: The development of NUFREQ-N, An analytical model for the stability analysis of nuclear coupled density-wave oscillations in boiling water nuclear reactors. *NLIREC/CR3375* (1983b)

- Park, G.C., Becker, M., Park, G.C.: Nodal analysis for reactor kinetics and stability. NUREG/CR-3377 (1983c)
- Park, G.C., Podowski, M., Becker, M., Lahey, R.T., Peng, S.J.: The development of a closed-form analytical model for the stability analysis of nuclear-coupled density-wave oscillations in Boiling Water Reactors. Nucl. Eng. Des. 92, 253–281 (1986)
- Peng, S.J., Podowski, M., Beker, M., Lahey Jr., R.T.: NUFREQNP computer code for the linear stability analysis of boiling water reactors. NUREG/CR-4116 (1985)
- Peng, S.J., Podowski, M., Lahey Jr., R.T.: BWR linear stability analysis (NUFREQ-NP). Nucl. Eng. Des. 93, 25–37 (1986)
- Taleyarkhan, R.P.: An analysis of density wave oscillations in ventilated boiling channels. PhD Thesis, RPI, Troy, NY (1982)
- Taleyarkhan, R.P., Podowski, M.Z., Lahey Jr, R.T.: Ventilated channel instability analysis. 1. Heat Transfer 107, 175–181 (1985)
- Taleyarkhan, R.P., McFarlane, A.F., Lahey Jr., R.T., Podowski, M.Z.: Benchmarking and qualification of the NUFREQ-NPW code for best-estimate prediction of multi-channel stability margins. Nucl. Eng. Des. 151, 151–171 (1994)
- Rizwan-Uddin, D.J.: Some nonlinear dynamics of a heated channel. Nucl. Eng. Design 93, 1–14 (1986)
- Saha, P.: Thermally induced two-phase flow instabilities, including the effect of thermal non-equilibrium between the phases. Ph.D. Thesis, School of Mechanical Engineering, Georgia Institute of Technology (1974)
- Saha, P., Ishii, M., Zuber, N.: An experimental investigation of the thermally induced flow oscillations in two-phase systems. J. Heat Transfer, Trans. ASME 98, 616–622 (1976)
- Saha, P., Zuber, N.: An analytical study of the thermally induced two-phase flow instabilities including the effects of thermal non-equilibrium. Int. J. Heat Mass Transfer 21, 415–426 (1978)
- Schäfer, H., Beisiegel, A.: Feasibility of stability tests under natural circulation conditions in the Karlstein test loop, Siemens technical report E32/92/e14a, proprietary (March 17, 1992)
- Schaffrath, A.: Experimentelle und analytische Untersuchungen zur Wirksamkeit des Notkondensators des SWR600/1000, Institut für Sicherheitsforschung und Reaktortechnik, Forschungszentrum Jülich GmbH, 3326, D294 (Diss. Universität Bochum 1996) (1996) ISSN 0944-2952
- Stenning, A.H., Veziroglu, T.N.: Flow oscillation modes in forced convection boiling. In: Proceedings of the 1965 Heat Transfer and Fluid Mechanics Institute, pp. 301–316. Stanford University Press, Palo Alto (1965)
- Stenning, A.H., Veziroglu, T.N.: Oscillations in two component two phase flow, vol. 1, NASA CR-72121; Flow oscillations in forced convection boiling, vol. 2, NASA CR72122 (1967)
- van Bragt, D.D.B., Rizwan-Uddin, van der Hagen, T.H.J.J.: Effect of void distribution parameter and axial power profile on boiling water bifurcation characteristics. Nucl. Sci. Eng. 134, 227–235 (2000)
- Wallis, G.B., Heasley, J.H.: Oscillations in two-phase flow systems. J. Heat Transfer, Trans. ASME 83, 363 (1961)
- Wang, F., Hu, L., Chin, P.: Thermal and stability analysis of a two-phase natural circulation loop. Nucl. Sci. Eng. 117, 33–46 (1994)
- Wolf, S., Chan, K.C., Chen, K., Yadigaroglu, G.: Dynamic instabilities in radiation-heated boiler tubes for solar central receivers. ASME Paper 82-WA/HT 8 (1982)

- Yadigaroglu, G.: Two-phase flow instabilities and propagation phenomena, in two-phase flows in nuclear reactors. Von Karman Institute of Fluid Dynamics Lecture Series (1978)
- Yadigaroglu, G., Lahey Jr., R.T.: A Lagrangian analysis of two-phase hydrodynamic and nuclear-coupled density wave oscillations. In: Proceeding of the Fifth International Heat Transfer Conference, Tokyo, September 3-7, vol. 4 (1975)
- Yadigaroglu, G.: Boiling water reactor stability revised: The effect of flashing. Nucl. Eng. Des. 235, 1093–1105 (2005)
- Zhou, Z.W., Yadigaroglu, G.: Stability of natural circulation with gravity-induced flashing. Trans. ANS 57, 379–381 (1988)

16.7 Steady-state single-phase nozzle flow

The prediction of steady-state pressure variation in a nozzle with variable cross-section is used in the test presented in this section. Tables 16.7.1 and 16.7.2 give the geometry, the initial and the boundary conditions for the tests performed in *Abuaf et al. (1981)*. Subcooled water is used in these tests. The parameters for the particular experiment defined in Table 16.7.1 are chosen in order to have no flashing in the nozzle.

Table 16.7.1 Geometry of the test sections

Author	Geometry	Length m	Hydraulic diameter	
			z / m	$D_{hyd,max} / m$
<i>BNL Abuaf</i> et al. (1981)	Circular nozzle	0.6	0	0.051
			0.02	0.051
			0.028	0.02546
			0.58	0.051
			0.6	0.051

Table 16.7.2 Initial conditions

Author	Test Nr.	Pressures	Mass flow rate (comp.)	Temperature
		$p_{in}, p_{out} / bar$	$G / kg / (m^2 s)$	T_{in} / K
<i>BNL Abuaf</i> et al. (1981)	006	682 000 620 000	7010 (6319)	300.85
	008	695 000 661 000	4710 (4362)	300.05
	009	709 000 688 000	3130 (2991)	300.25

Equidistant discretization is used in this case. The computed results are compared in Fig. 16.7.1 with those obtained experimentally. The agreement is good. The mass flow rate as a function of the pressure difference is computed within a 10% error band. For practical analysis we recommend nonequidistant discretization with a finer grid around the throat, as discussed in *Kolev (1986)*. It is also known that for accelerating flows the friction coefficient is larger than the steady-state value, which was not taken into account here.

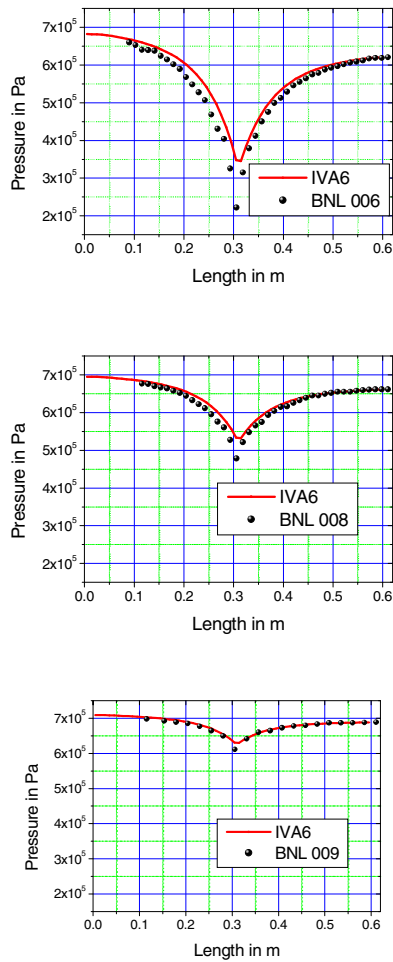


Fig. 16.7.1 Comparison between the IVA5 predictions of the pressure as a function of the axial coordinate with the measured pressure

References

- Abuaf, N., Wu, B.J.C., Zimmer, G.A., Saha, P.: A study of non equilibrium flashing of water in a converging diverging nozzle, vol. 1 Experimental, vol. 2 Modeling, NUREG/CR-1864, BNL-NUREG-51317 (June 1981)
- Kolev, N.I.: Transiente Zweiphasenströmung (Transient Two-Phase Flow). Springer, Heidelberg (1986)

16.8 Pressure waves – single phase

Pressure waves are common in piping systems like those presented in Fig. 16.8.1. In his remarkable work from 1898 *Joukowsky* responded to the need of the St. Petersburg administration to analyze the “strange strokes” in the urban city supply system if somebody close a valve to fast. *Joukowsky* devises an experimental facility and an ingenious method to record the pressure waves and discovered the first solution waves in the pipe networks. Moreover, systematically changing the pipe velocity before closure he found the relation for computing the first peak of the pressure that is used by present engineers. Then, not having a computer, he devised a graphical solution method based on the *Rieman*’s work from 1858–1859 known currently as a method of characteristics. So the pipe-network fluid dynamics was born.

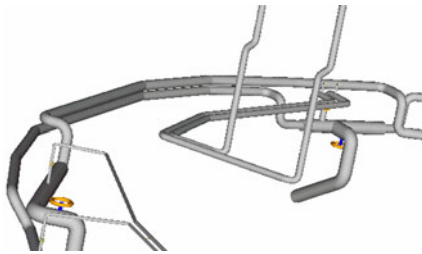


Fig. 16.8.1 Pipe network

In the following 100 years engineers wrote more than 100 single-phase computer codes based on the method of characteristics, performed many experiments in different geometries, and finally understood that there is no pure water in technical systems but water with dissolved gases and impurities that influence the inception of cavitation and many other processes, and that the pressure shocks caused by the collapsing bubbles in water, called water hammer, are much stronger than those in single-phase liquids.

Void in liquids causes nonlinear response to pressure waves depending on the frequency, a fact that is unfortunately used by the military engineers for amplification of the submarine pressure wave impact. Collapsing bubbles create a temperature increase at the center of the bubble up to a sun temperatures opening a new way for nuclear fusion in small laboratory scale *Lahey, et al. (2005), Nigmatulin (2005)*. Another fascinating outcome of the cavitation is the reduction of skin friction on immersed bodies opening a new field for producing high-speed marine vehicles.

The kinetics of the void origination and disappearance can dramatically change the character of the processes. Last but not least, the waves cause movements of the structures as well as elastic or plastic change of the pipe cross-sections. Both phenomena have a feedback to the flow that may be very strong, depending on the pressure/elasticity ratio. As long as the methods do not cause cavitation, a single-phase method coupled with fluid–structure interaction does a good job but this is rather the exception in real systems than the rule. Moreover, the damage caused by water hammer still lead to large losses in industry.

It turned out that there is no single-phase method for an adequate description pressure waves in liquid systems in general.

Therefore, the sophistication of the methods for description of this complex of phenomena leads to the multiphase flow dynamics. Only the methods of multiphase flow dynamics allow detection in the analyses of the conditions for void inception, the kinetics of the void production and disappearance, and therefore provide the appropriate mathematical framework for general pressure-wave analyses in industrial pipe network systems.

The purpose of the present section is to document part of the verification basis for the multiphase computer code IVA for pressure waves in systems initially filled with gas or liquid.

16.8.1 Gas in a shock tube

Consider air in a 1-m pipe with initial conditions of 100 and 50 bar, respectively in the two separate halves, and initial temperature 600 K. The analytical solution to this problem is presented by *Oertel* (1966). We will compare the analytical solution for the problem defined at $\tau = 250\mu\text{s}$ with the numerical solution predicted by IVA5. A detailed discussion to this problem is available in Chapter 4 of Vol. 1 of this monograph or in *Kolev* (1998).

Figure 16.8.2 shows the pressure as a function of time computed with the computer code IVA5 that exploits the first-order donor-cell method, as discussed in Chapter 12 of Volume 1 or in *Kolev* (1996). The code uses equations of state for air as a real gas. Surprisingly, the IVA5 donor cell method is more accurate than the first-order method of characteristics and the method of characteristics using third-order spatial interpolation *Kolev* (1998). The pressure at the two different ends of the pipe as a function of time is presented in Fig. 16.8.3. As discussed in Chapter 4 of Vol. 1 or in *Kolev* (1998), comparing Fig. 16.8.2 with the solutions obtained by using the internal energy form instead of the energy conservation in entropy form we obtained almost indistinguishable solutions. The total mass and energy conservation error is shown in Fig. 16.8.4. Again, we observe from Fig. 16.8.4 that the IVA5 numerical method is better than the first- and third-order method of characteristics.

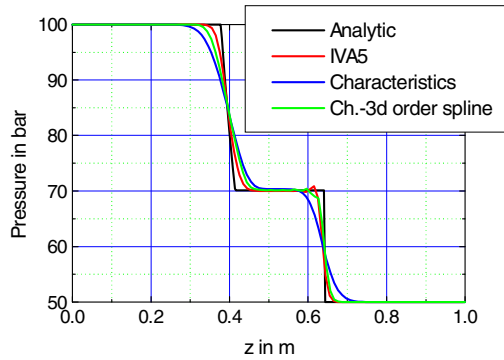


Fig. 16.8.2 Pressure as a function of the distance from the left closed end of the pipe at $\tau = 250\mu s$

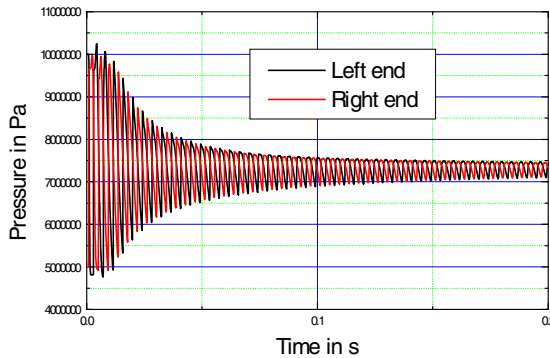


Fig. 16.8.3 Pressure at the two ends of the pipe as a function of time (air). The energy conservation is used in terms of specific entropy in IVA5

Now we perform a similar test with IVA5, replacing the air with a molten oxide mixture called corium at 3300 K initial temperature. The initial pressure distribution is the same as in the previous examples. The velocity of sound of the system is around 1500 m/s. For this test we developed a special set of equations of state and their derivatives, which are strictly consistent with each other following the instructions given in Chapter 3 of Volume 1. The pressure at the two ends as a function of time is shown in Fig. 16.8.5 and the corresponding cumulative relative mass and energy conservation error is given in Fig. 16.8.6. We see that the order of magnitude is 10^{-7} , which is much better than for the case of the strongly compressible gas. The slight difference in steady-state pressures is due to the geodetic pressure difference because the pipe is considered to be vertical and the fluid is very heavy.

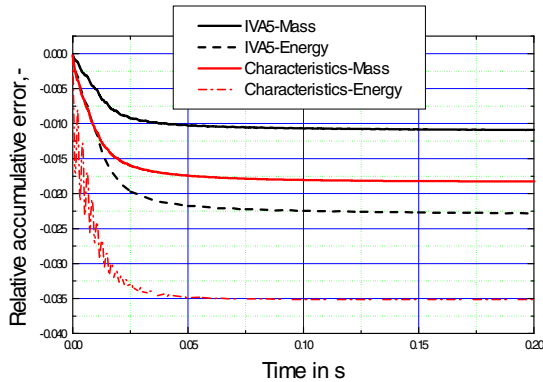


Fig. 16.8.4 Comparison between the overall mass and energy conservation error of the IVA5 numerical method and the first-order method of characteristics

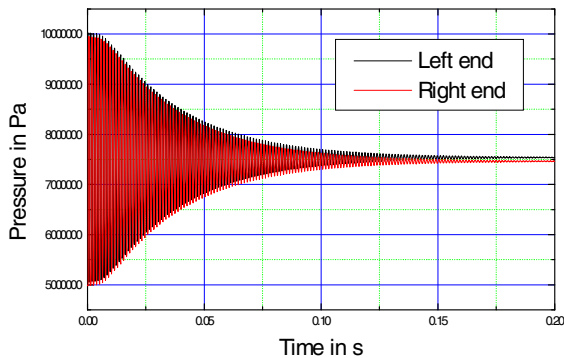


Fig. 16.8.5 Pressure at the two ends of the pipe as a function of time (corium melt 3300 K). The energy conservation is used in terms of specific entropy in IVA5

Conclusions

- IVA5 exhibits the expected behavior for the first-order donor-cell solution method. The accuracy is better than the classical first-order method of characteristics and the method of characteristics using bicubic spatial spline interpolation.
- For practical applications in large-scale facilities a spatial resolution of 1 cm is hardly achievable and therefore the expected errors for single-phase flows will be higher, corresponding to the size of the cells.

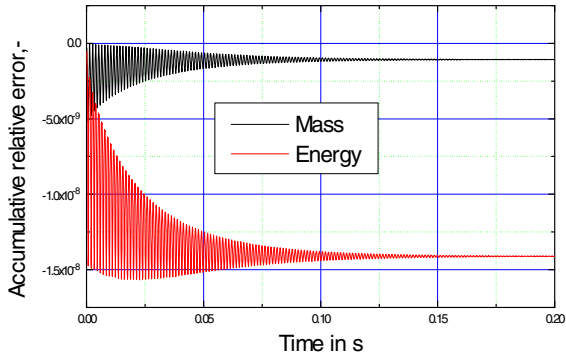
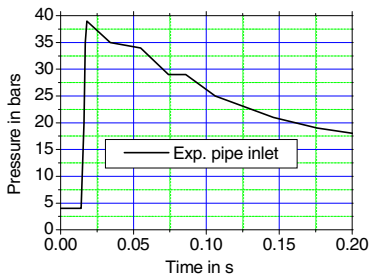


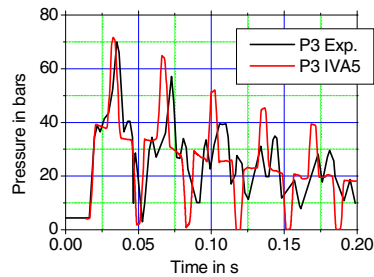
Fig. 16.8.6 Relative overall mass and energy conservation error as a function of time (corium melt 3300 K). The energy conservation is used in terms of specific entropy in IVA5

16.8.2 Water in a shock tube

The *Kellner* and *Gissler* (1984) experiment was used for this comparison. Pressure-wave propagation in a single pipe with five bends and one dead end was simulated by using a 1D representation – Fig. 16.8.8. The experiment was initiated by igniting an oxygen–hydrogen gas mixture. The imposed pressure function at the pipe inlet is shown in Fig. 16.8.7a. A comparison of predicted and measured responses as shown in Figs. 16.8.7b–d shows good agreement.



a)



b)

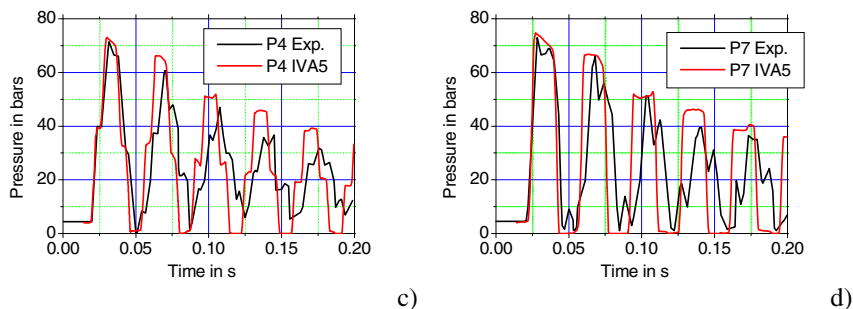


Fig. 16.8.7 a Comparison of IVA5 prediction with the experimental data of *Kellner* and *Gissler* (1984). Pipe length 13.12 m, diameter 0.1 m, 4 bends at 4.8, 10.2, 12.6, 13.64 m from the inlet. Initial conditions: water at atmospheric temperature and pressure. a) Pressure at the pipe inlet as a function of time as measured by *Kellner* and *Gissler* (1984). b) At 4.08 m from the pipe inlet. c) At 8.18 m from the pipe inlet. d) At 12.5 m from the pipe inlet

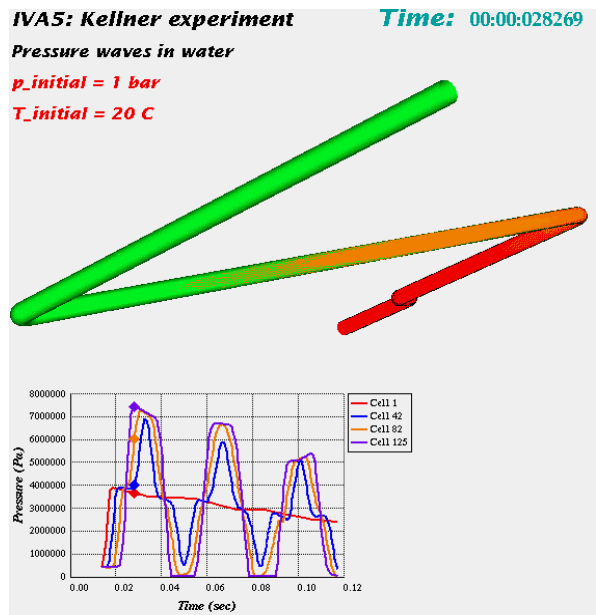


Fig. 16.8.8 A SONJA visualization of the pressure wave. Excitation pressure jump 40 bar results in a maximum of the pressure at the opposite end of about 80 bar

Conclusion. From comparison with experiments that feature pressure wave propagation in pipes initially filled with water, we conclude that the code is able to reproduce wave dynamics in single-phase water flow.

16.8.3 The 1983 Interatome experiments

In the framework of the research activities devoted to the German fast breeder nuclear reactor *Dumm* et al. (1983) performed in 1983 a systemic experimental study of pressure-wave propagation from simple to complicated pipe network systems with variety of modes of fluid–structure interactions: The report is still proprietary, hence I do not disclose here materials, geometrical sizes, fixed points, etc. The water quality was not quantitatively estimated in one group of the experiments. Degassed water is used in some of the experiments. Pressure waves are generated by hydrogen detonation and recorded as boundary conditions for successive code validations. Pressures at different position are measured together, in some experiments, with the characteristics of the structure motion. We confine our attention to those of the experiments that did not manifest plastic deformations and those that did not manifest strong pipe relocations. The reason is that IVA computer code takes into account only the elastic deformation of local volume and its feedback on the flow.

16.8.3.1 Experiment 1.2

Given a pipe with known material, geometry, wall thickness and fixed points as schematically presented in Fig. 16.8.9. The computation with IVA is performed with a spatial resolution of about 10 cm.

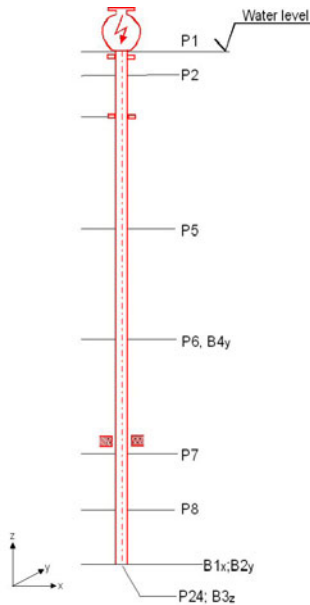


Fig. 16.8.9 Schematic pipe geometry for exp. 1.2 and 1.3

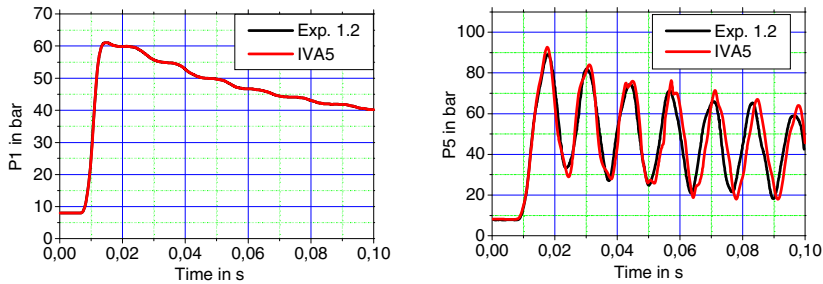


Fig. 16.8.10 Experiment 1.2: Pressure as a function of time. a) P1 pressure - boundary condition; b) Comparison with IVA prediction for P5 pressure.

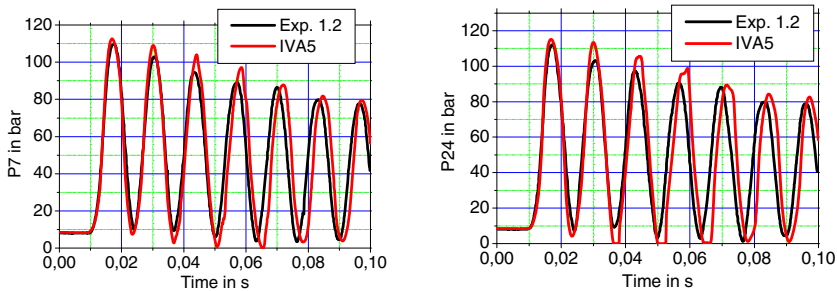


Fig. 16.8.11 Experiment 1.2: Pressure as a function of time. Comparison with IVA predictions for: a) P7; b) P24

The results of the computation are compared with data on Figs. 16.8.10 and 16.8.11. Note that without taking into account the elasticity of the pipe the comparison was poor. Only after taking into account the elastic change of the cross-section due to the variable pressure difference do we arrive at the results given in the figures. We realize that for a first-order donor-cell method with 10 cm spatial step the frequency and the magnitudes are well resolved. This result serves also as a recommendation of how to use the code for such pressure magnitudes/elasticity ratios.

16.8.3.2 Experiment 1.3

Given is the same geometry as in exp. 1.2. The important difference is in the stiffness of the pressure-jump boundary condition as given in Fig. 16.8.12.

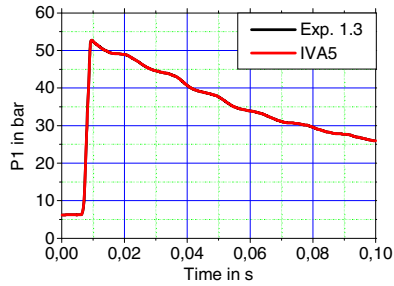


Fig. 16.8.12 Experiment 1.3: Pressure as a function of time. a) P1 pressure – boundary condition;

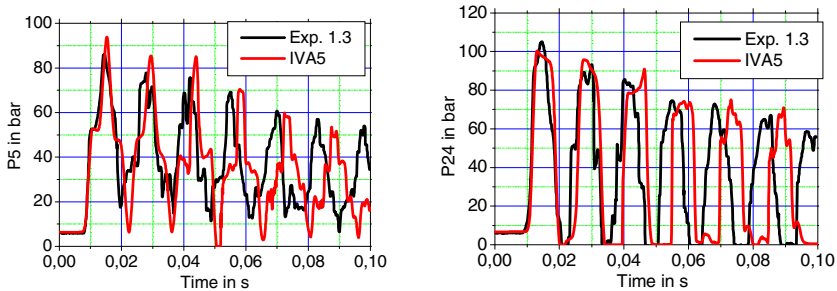


Fig. 16.8.13 Experiment 1.3: Pressure as a function of time. Comparison with IVA predictions for: a) P5; b) P24

The magnitude of the first wave is strongly connected with the stiffness of the pressure ramp. The larger the stiffness, the larger the first magnitude. The reflection of the wave causes a tension state of the liquid and delayed nucleation and vapor generation. So, the smooth wave characteristics from the single-phase case change significantly. The results of the predictions are given in Fig. 16.8.13. The wave signature that depends on the void production is properly predicted. We realize that for increasing time the frequency shifts to a smaller frequency. We will analyze in more detail this phenomenon. First, we allow for the tension state of the water also for pressures less than 650 Pa. The following results are obtained with this option. Figure 16.8.14 presents the results with different bubble growth models. We realize that the differences are not substantial.

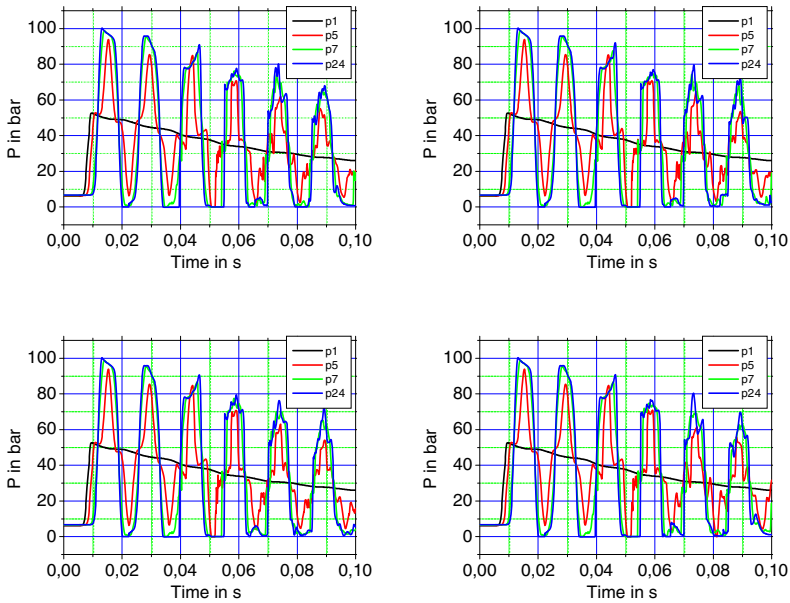
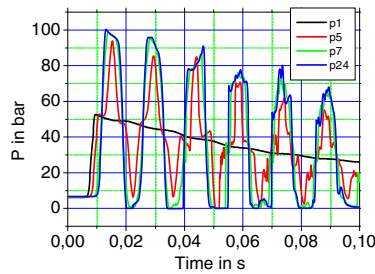


Fig. 16.8.14 Influence of the used flushing models: a) Implicit, internal circulation *Hunt* and *Issenberg*, thermal boundary layer in liquid; b) *Mikic et al.* model 1970 ; c) *Labunzov* – thermal-controlled bubble-growth model 1964; d) *Jones and Zuber*, variable pressure, thermal-controlled bubble-growth model 1978



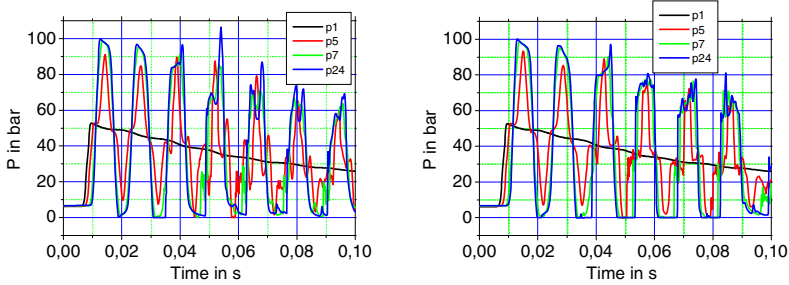


Fig. 16.8.15 Influence of the fluid structure interaction modeling on the frequency: a) Implicit, internal circulation *Hunt* and *Issenberg*, thermal boundary layer in liquid; e) as a) without fluid–structure interaction, elasticity modulus $E = 2.0 \times 10^{11}$ Pa; f) as a) without fluid–structure interaction, elasticity modulus $E = 2.5 \times 10^{11}$ Pa.

Figures 16.8.15a and b show computations with and without fluid–structure interaction. Obviously not taking into account the fluid–structure interactions, results in prediction of frequencies that are larger than the observed. Because our model does not take into account the increased stiffness of the flange and of the dead end we simply increase the elasticity modulus from 2 to 2.5×10^{11} Pa to see the tendency. As expected it increase slightly the frequency as seen in Fig. 16.8.15c compared to 16.8.15a. Therefore, we attribute the slight frequency shift not to flushing modeling but to the fluid–structure interaction modeling. More accurate reproduction of the frequencies requires more accurate structure models than those we use here.

16.8.3.3 Experiment 10.6

Given a pipe with known material, geometry, wall thickness and fixed points as schematically presented in Fig. 16.8.16. The type of the boundary condition is different from the proceeding experiments – Fig. 16.8.17a. The computation with IVA is performed with spatial resolution of about 10 cm.

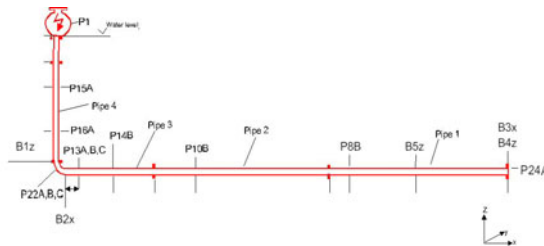


Fig. 16.8.16 Schematic pipe geometry for exp. 10.6

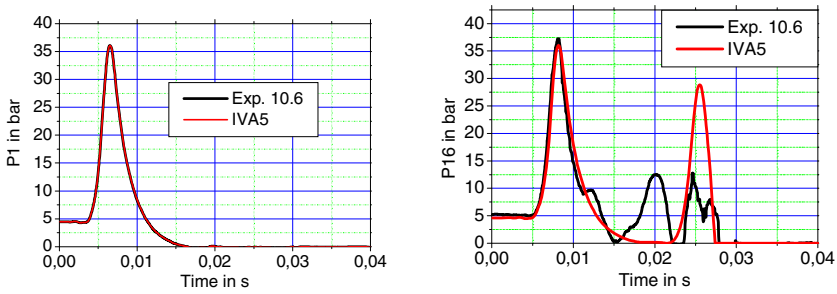


Fig. 16.8.17 Experiment 10.6: a) $P1$ pressure – boundary condition; b) Comparison with IVA prediction for $P16$ pressure.

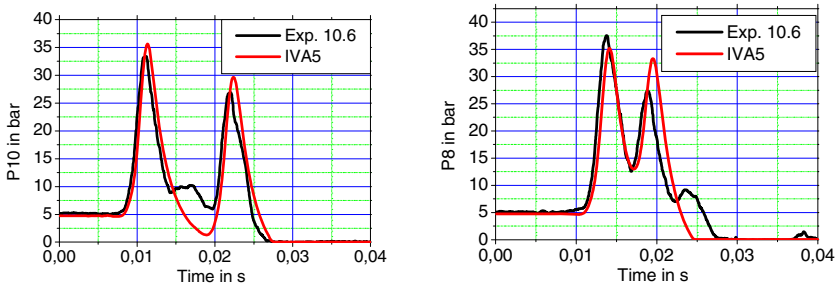


Fig. 16.8.18 Experiment 10.6: Pressure as a function of time. Comparison with IVA predictions for: a) $P10$; b) $P8$

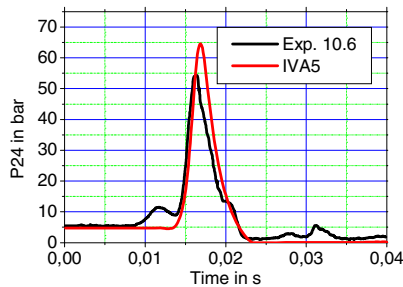


Fig. 16.8.19 Experiment 10.6: Pressure as a function of time. Comparison with IVA predictions for $P24$

The predictions of IVA are presented in Figs. 16.8.17, 16.8.18 and 16.8.19. The arrival of the wave at the end of the test section and its form is properly predicted.

Note that this is not the case if the elastic deformation of the pipe were not taken into account. The timing and the double-peak structure of the wave in the horizontal-pipe segment, see Fig. 16.8.18, is again properly predicted, indicating that the basics physics is reflected by the IVA model. The measurements in Fig. 16.8.17b indicate that there is a kind of earlier reflection either from the bend or from the stiff portion of the pipe. We do not model those places of the pipe that are stiff but consider the entire pipe in this simulation as elastic everywhere. It is obvious that this practice has to be improved in the future.

16.8.3.4 Experiment 11.3

This experiment differs slightly from 10.6 in the replacement of the bend with the T-junction, as given in Fig. 16.8.20.

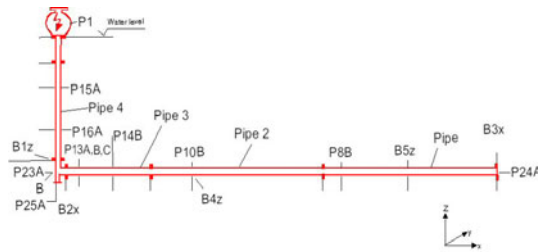


Fig. 16.8.20 Schematic pipe geometry for exp. 11.3

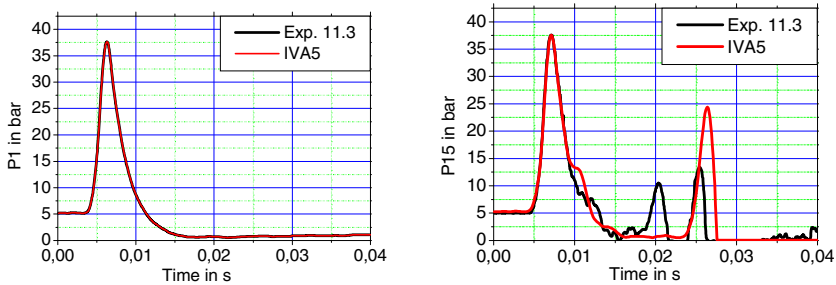


Fig. 16.8.21 Experiment 11.3: a) P1 pressure – boundary condition; b) Comparison with IVA prediction for P15 pressure.

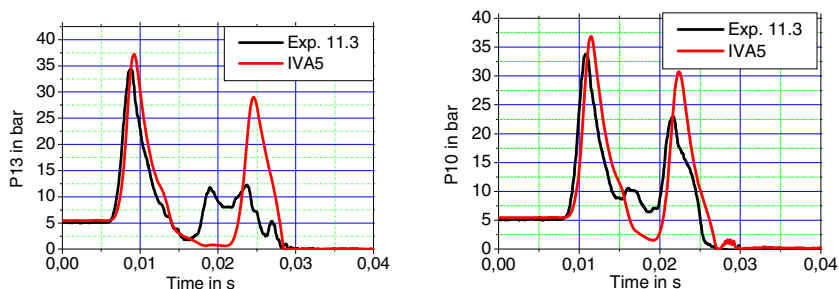


Fig. 16.8.22 Experiment 11.3: Pressure as a function of time. Comparison with IVA predictions for: a) P13; b) P10

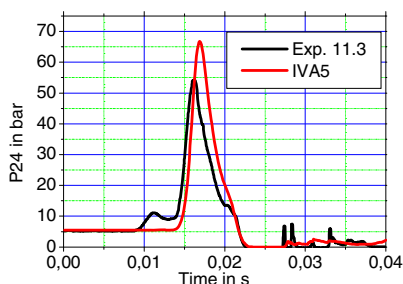


Fig. 16.8.23 Experiment 11.3: Pressure as a function of time. Comparison with IVA predictions for P24

The results are presented in Figs. 16.8.21, 16.8.22 and 16.8.23. The findings are very similar to those already discussed for experiment 10.6.

16.8.3.5 Experiment 21

Given a pipe network with known material, geometry, wall thickness and fixed points as schematically presented in Fig. 16.8.24. The pressure boundary condition is defined by Fig. 16.8.25a. The computation with IVA is performed with a spatial resolution of about 10 cm.

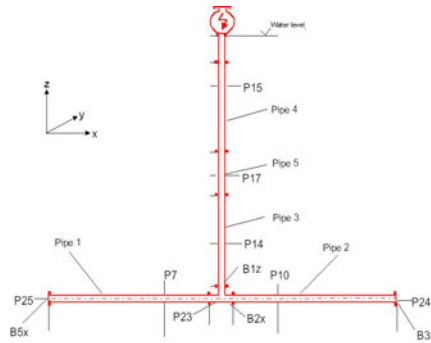


Fig. 16.8.24 Schematic pipe geometry for exp. 21

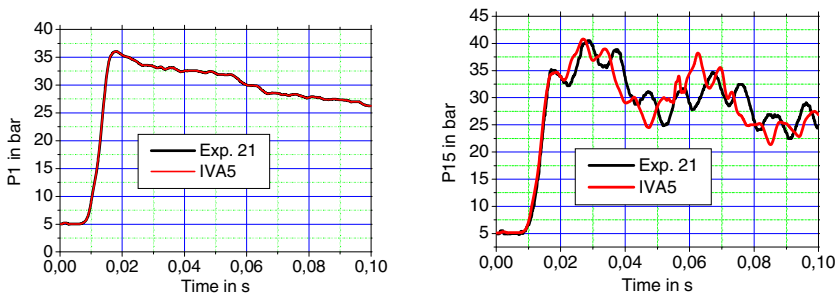


Fig. 16.8.25 Experiment 21: a) P1 pressure – boundary condition; b) Comparison with IVA prediction for P15 pressure.

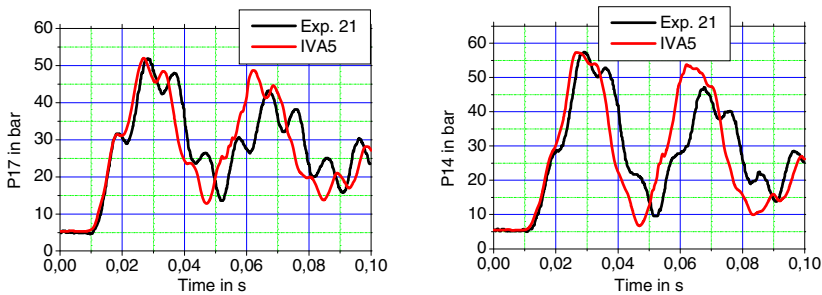


Fig. 16.8.26 Experiment 21: Pressure as a function of time. Comparison with IVA predictions for: a) P17; b) P14

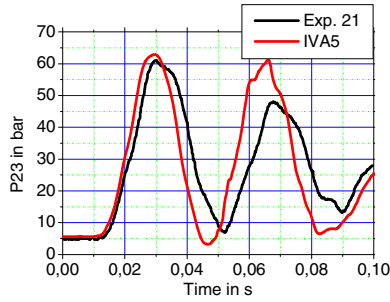


Fig. 16.8.27 Experiment 21: Pressure as a function of time. Comparison with IVA predictions for a) P23

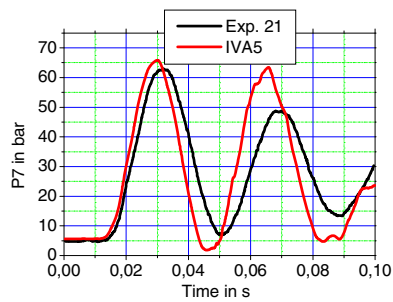
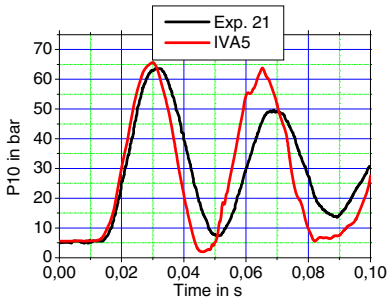


Fig. 16.8.28 Experiment 21: Pressure as a function of time. Comparison with IVA predictions for: a) P10; b) P7

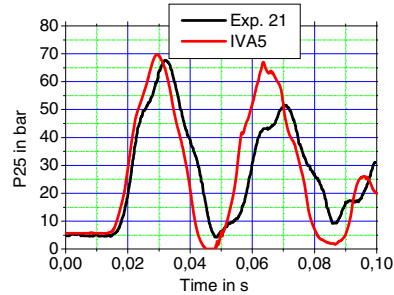
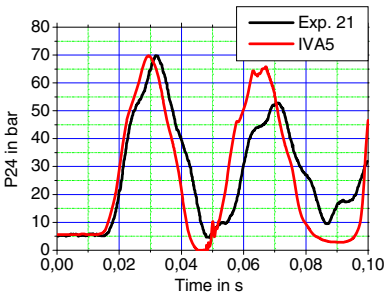


Fig. 16.8.29 Experiment 21: Pressure as a function of time. Comparison with IVA predictions for: a) P24; b) P25

First, we see that the signature of the waves is well reproduced by IVA. The observed symmetry presented in Figs. 16.8.28 and 16.8.29 is satisfactorily reproduced. The second wave magnitudes are more damped in reality than in the

computation. We attribute this to the approximate fluid–structure interaction we use.

16.8.3.6 Experiment 5

Given a pipe network with known material, geometry, wall thickness and fixed points as schematically presented in Fig. 16.8.30.

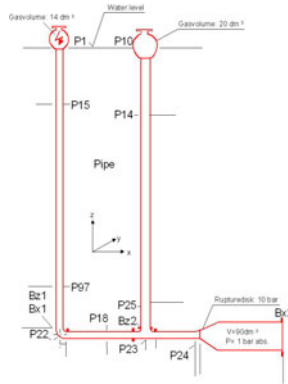
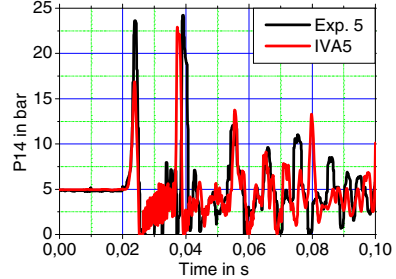
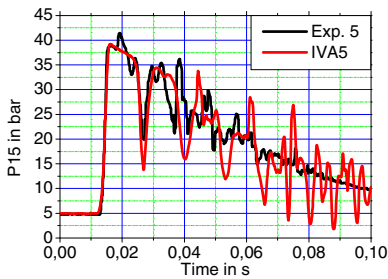
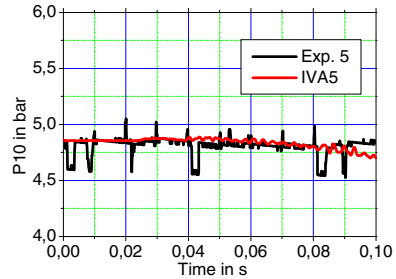
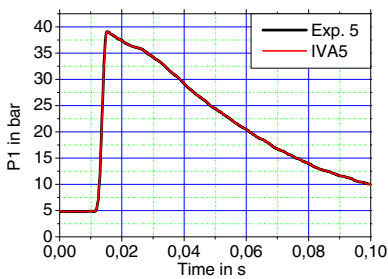


Fig. 16.8.30 Schematic pipe geometry for exp. 21



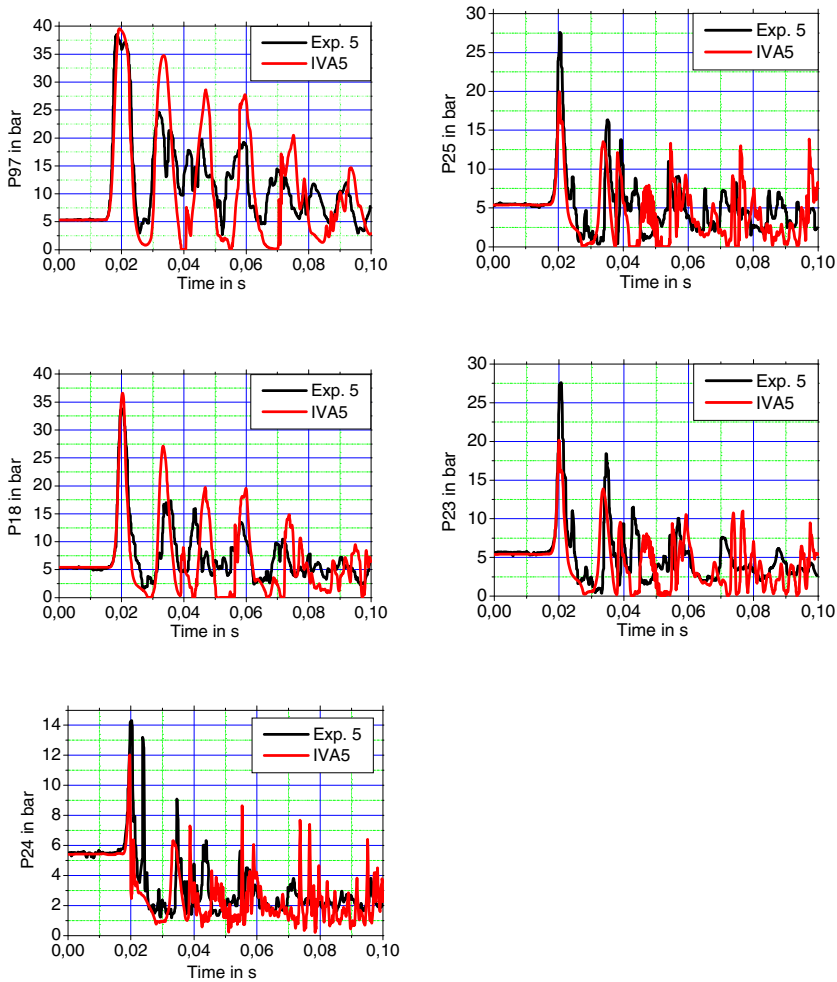


Fig. 16.8.31 Experiment 5: Pressure as a function of time. Comparison with IVA predictions. -1) though -9) from left to right and from top to the bottom.

This is a remarkable experiment having a low-pressure region divided by a rupture disk from the high-pressure region. The rupture disk breaks at a prescribed pressure for a prescribed time. In addition, a gas expansion space is available atop of the right vertical pipe. This is from the very beginning a two-phase two-component flow experiment. The pressure boundary condition is defined by Fig. 16.8.31a. The computation with IVA is performed with spatial resolution of about 10 cm. Figure 16.8.31 presents the comparison. One can not expect a perfect reproduction of complex pressure waves in this system but one realizes how many important features of this complex process are reproduced by IVA.

16.8.3.7 Experiment 15

Given a pipe network with known material, geometry, wall thickness and fixed points as schematically presented in Fig. 16.8.32. This is an experiment similar to 5 but not having a low-pressure region and rupture disk. In addition, a gas expansion space is available atop of the right vertical pipe having again different geometry compared to experiment No. 5. This again is from the very beginning a two-phase two-component flow experiment. The pressure boundary condition is defined by Fig. 16.8.31a. The computation with IVA is performed with a spatial resolution of about 10 cm.

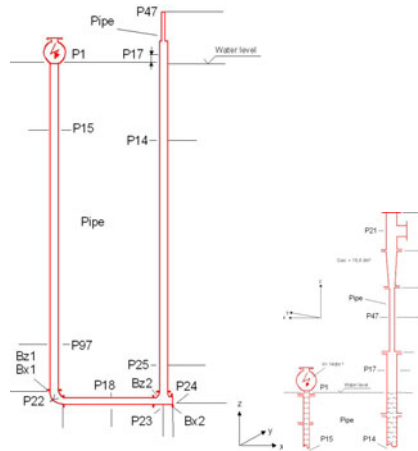
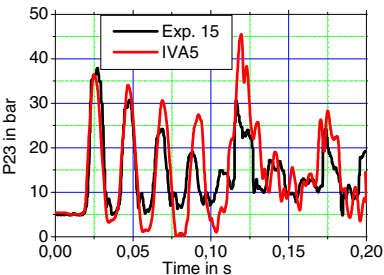
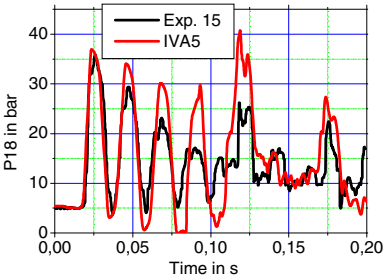
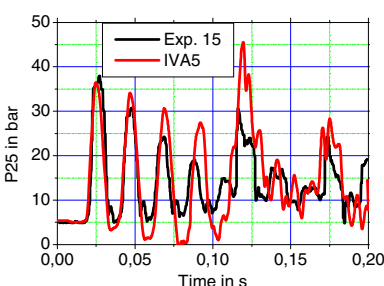
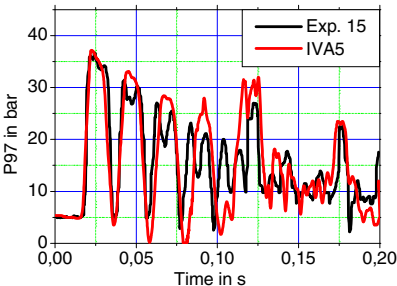
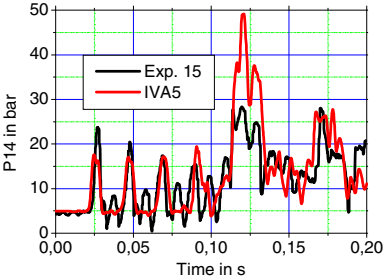
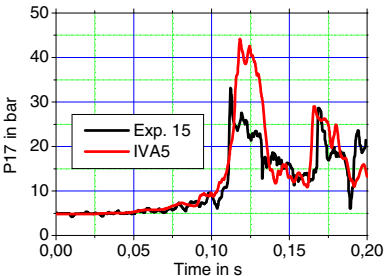
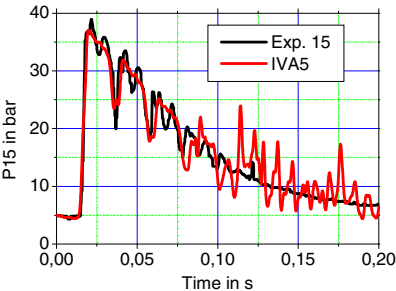
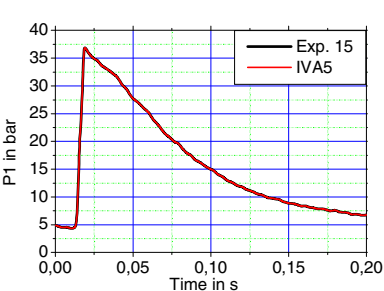


Fig. 16.8.32 Schematic pipe geometry for exp. 15

Figure 16.8.33 presents the comparison. Again, as in experiment 5 one can not expect a perfect reproduction of complex pressure waves in this system but one realize again how many important features of this complex process are reproduced by IVA.

Conclusions: The comparison with the above-discussed experiments demonstrates the capability of the IVA computational model to reproduce the most important characteristics of the process like cavitation due to the reflection of the strong pressure waves, collective bubble collapse leading to strong pressure wave generation, pressure wave propagation in pipe networks with rupture discs etc. Therefore, the use of the code in such fields has to be associated with uncertainties regarding magnitudes and frequencies documented here.

Acknowledgment: The data processing done by Iris Roloff-Bock from Framatome ANP and Eva Ziegerer from the University of Erlangen is highly appreciated.



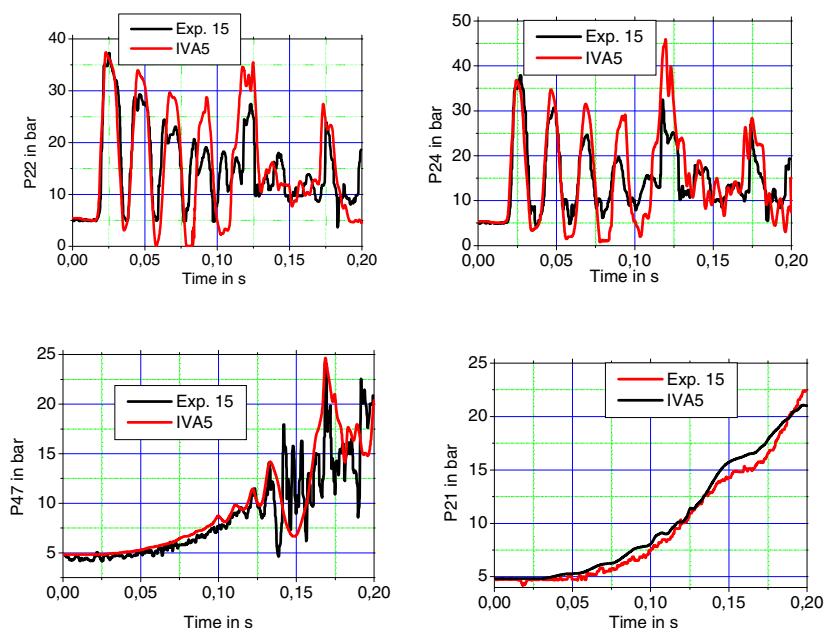


Fig. 16.8.33 Experiment 15: Pressure as a function of time. Comparison with IVA predictions: 1) though -12) from left to right and from top to the bottom.

16.8.4 Pressure-wave propagation in a cylindrical vessel with free surface (2D)

In order to study triggered melt–water interactions high gas pressure sources are usually used as a trigger. In order to model adequately the triggered melt–water interaction the trigger has first to be well defined and appropriately reproduced by the computer code. The experiment considered here was performed by *Huhtiniemi et al.* (1996) in the vessel presented in Fig. 16.8.34. At the bottom of the internal cylinder there is a 15 cm³ gas capsule charged at 138.9 bar. Breaking the membrane releases the pressure wave into the water above. The water has a free surface. The results of the compared computed and measured pressure traces are presented in Figures 16.8.35(1)–(6). We see that the propagation of the first pressure pulse in the two-dimensional space regarding propagation speed, magnitude, and duration is appropriately predicted by the IVA computer code, except for the K5 magnitude, which is predicted to be smaller than the measured value by a factor of two.

Conclusion. Therefore, the method and the resolution used can be applied for trigger simulation in a melt–water interaction analysis.

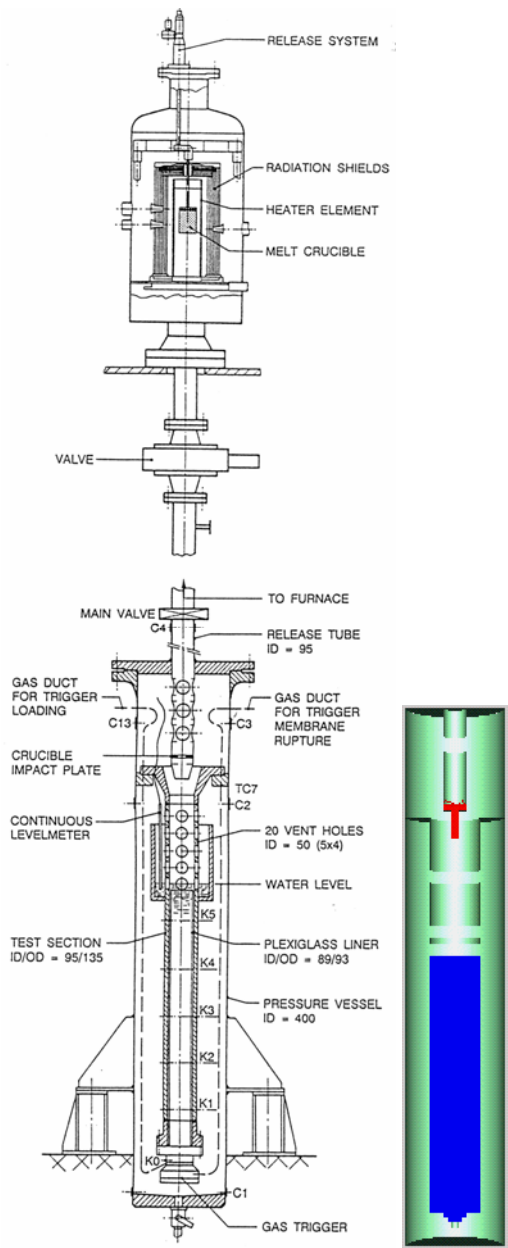
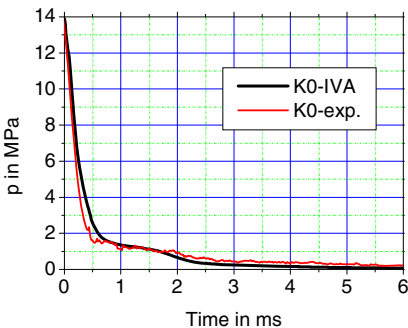
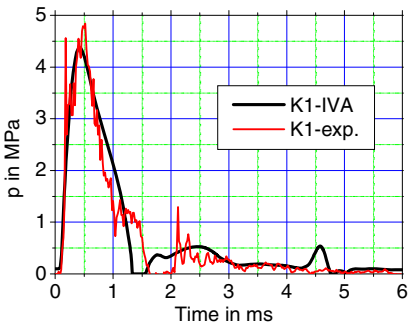


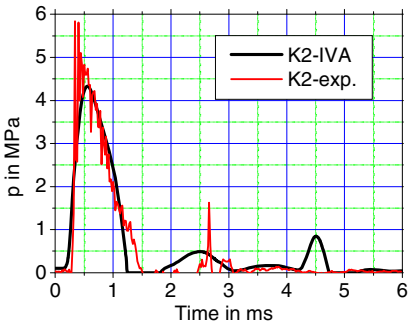
Fig. 16.8.34 KROTOS test facility *Huhtiniemi et al. (1996)* and IVA_5M computer model



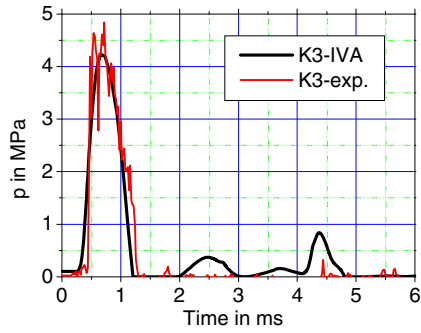
(1)



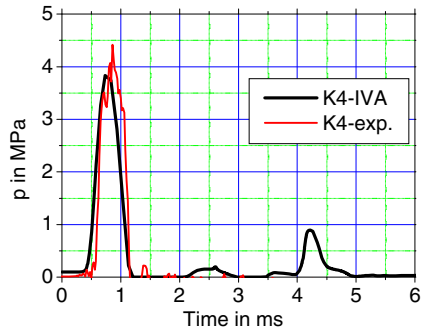
(2)



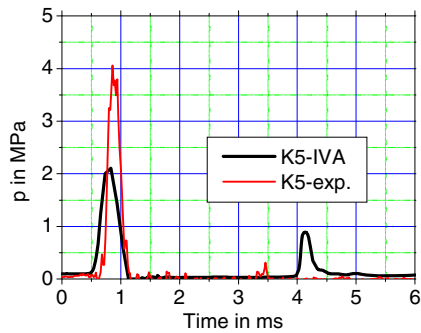
(3)



(4)



(5)



(6)

Fig. 16.8.35 Trigger pulse in pure water. The pulse was produced by a gas capsule charged at 138.9 bar, volume 15 cm³. Pressure at the wall as a function of time. Distance from the bottom plate: (1) 0 m; (2) 0.15 m; (3) 0.35 m; (4) 0.55 m; (5) 0.75 m; (6) 0.95 m.

References

- Dumm, K., Voss, J., Kellner, A., Dörner, G., Lang, H., Joist, G.: Untersuchungen zur Wechselwirkung zwischen Druckwellen und Bauteilen in flüssigkeitsgefüllten Systemen, INTAT 5204706, 62.04706.9, Interatom Internationale Atomreaktorbau GmbH (April 1983)
- Huhtiniemi, I., Hohmann, H., Faraoni, R., Flied, M., Gambaretti, G., Klein, K.: KROTOS 38 to KROTOS 44: Data report, Technical Note No.I.96.37, Institute for Safety Technology, Reactor Safety Program, Joint Research Center, Ispra (March 1996)
- Joukowsky, N.: Ueber den hydraulischen Stoss in Wasserleitungsröhren, Voss, Petersburg und Leipzig, 1990, pp. 1–72 (April 24, 1898)
- Kellner, A., Gissler, D.: Programmsystem SAPHYR: Anwendungsbeispiel II, Notiz Nr.70.02748.4, Interatom GmbH (February 7, 1984)
- Kolev, N.I.: Three fluid modeling with dynamic fragmentation and coalescence fiction or daily practice? 7th FARO Experts Group Meeting Ispra (October 15–16, 1996); Proceedings of OECD/CSNI Workshop on Transient thermal-hydraulic and neutronic codes requirements, Annapolis, MD, USA (November 5–8, 1996); 4th World Conference on Experimental Heat Transfer, Fluid Mechanics and Thermodynamics, ExHFT 4, Brussels (June 2–6, 1997); ASME Fluids Engineering Conference & Exhibition, The Hyatt Regency Vancouver, Vancouver, British Columbia, Canada Invited Paper; Proceedings of 1997 International Seminar on Vapor Explosions and Explosive Eruptions (AMIGO-IMI), Aoba Kinen Kaikan of Tohoku University, Sendai-City, Japan (May 22–24, 1997)
- Kolev, N.I.: On the variety of notation of the energy conservation principle for single phase flow. *Kerntechnik* 63(3), 145–156 (1998)
- Lahey Jr., R.T., Taleyarkhan, R.P., Nigmatulin, R.I.: Sonofusion – fact or fiction? In: The 11th International Topical Meeting on Nuclear Reactor Thermal-Hydraulics (NURETH-11) Paper: 517, Popes' Palace Conference Center, Avignon, France, October 2–6 (2005)
- Nigmatulin, R.: Nano-scale thermonuclear fusion in imploding vapour bubbles in acoustically cavitated deuterated liquid. In: The 11th International Topical Meeting on Nuclear Reactor Thermal-Hydraulics (NURETH-11) Paper: 517, Popes' Palace Conference Center, Avignon, France (October 2–6, 2005)
- Oertel, H.: Stossrohre. Springer, Wien, New York (1966)
- Riemann, B.: Über die Fortpflanzung ebener Luftwellen von endlicher Schwingungsweite, Abhandlungen der Königlichen Gesellschaft der Wissenschaften zu Göttingen. Band 8, S43–S65 (1858–1859)

16.9 2D: N₂ explosion in space filled previously with air

A full description of the experimental facility, instrumentation, and experimental procedure is given in *Wilchelm and Kirstahler (1987)*, *Meyer and Kirstahler (1988)*. An axially symmetric vessel was used – Fig. 16.9.1. The vessel was divided into high- and low-pressure regions by sliding doors. Above the sliding doors an aluminum rupture foil separated the low-pressure region from the rest of the facility. The high-pressure region consisted of a 0.6 MPa nitrogen source. The low-pressure region comprised 0.1 MPa air at room temperature. The experiment was initiated by igniting an oxygen-hydrogen gas mixture in the sliding door driving mechanism. This caused the sliding doors to accelerate, opening the cross-section, starting from the center within 0.4 ms. The pressure was measured at different points.

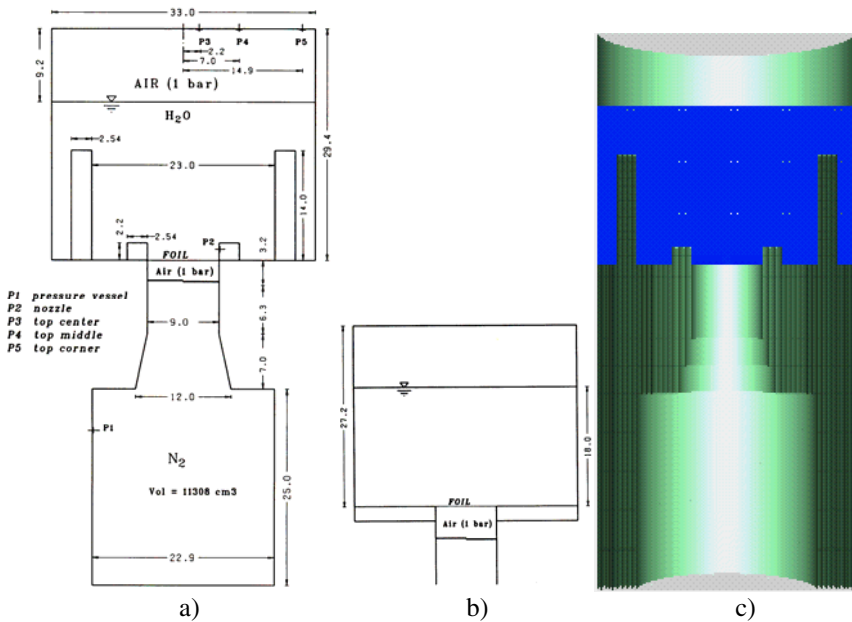
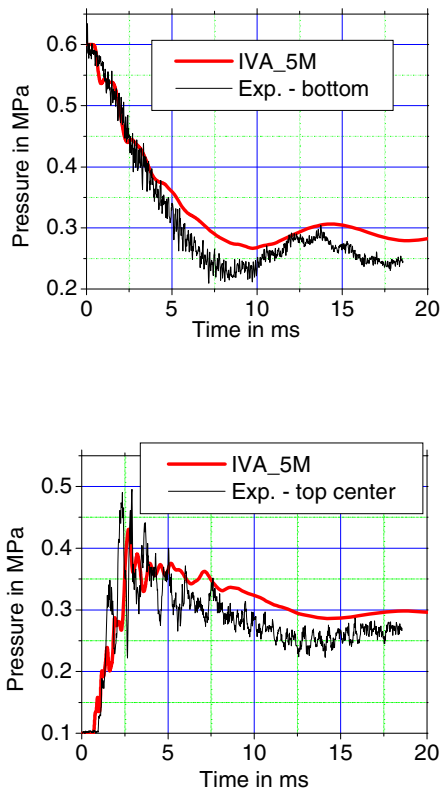


Fig. 16.9.1 a) Geometry of the experimental test section with internals. b) Geometry of the experimental test section without internals. c) IVA_5M finite-volume grid for computational analysis

In the computational simulation a symmetrical process is assumed, neglecting the asymmetries observed in *Meyer* and *Kirstahler* (1988). The geometry was represented by 1144 cells (26×44) in only one angular sector with cylindrical coordinates – see Fig. 16.9.1c. Variable surface permeabilities were used to simulate the opening process for the sliding doors. The *Poisson*-type equation was solved for the whole (r, z) plane directly.



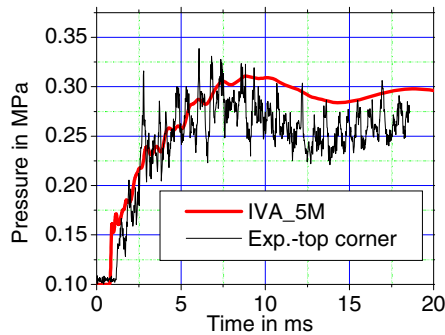


Fig. 16.9.2 Pressure as a function of time at different positions. An IVA_5M prediction for the Meyer and Kirstahler gas-in-gas explosion experiment

In this simulation it is the *multiblock boundary fitted* code architecture and the code integrator that are addressed, without addressing any empirical correlation, except for the gas state and transport properties.

The comparison between the predicted and the measured pressures is shown in Figs. 16.9.2. IVA_5M essentially provides a good prediction of the trends of the pressures at the r - z locations (0.022, 0.693), (0.07, 0.693) and (0.148, 0.693). We learn that especially in regions in which pressure spikes are expected the spatial resolution has to be selected carefully. This was already demonstrated in 1987 in Koley (1987) by using IVA2 to the same test problem.

Conclusion. From comparison with experiments featuring gas explosions in a 2D space filled previously with gas we conclude that the code essentially provides a good prediction of the trends of the pressures. Especially in regions in which pressure spikes are expected the spatial resolution has to be selected carefully.

References

- Koley, N.I.: A three field-diffusion model of three-phase, three-component flow for the transient 3D-computer code IVA2/01. Nucl. Technol. 78, 95–131 (1987)
- Meyer, L., Kirstahler, M.: Experimental investigation of the fluid dynamic of gas jet expansion in a liquid pool. In: Shah, K., Ganic, E.N., Yang, K.T. (eds.) Proc. 1st World Conf. Experimental Heat Transfer, Fluid Mechanics, and Thermodynamics, Dubrovnik, Yugoslavia. Elsevier, Amsterdam (1988)
- Wilhelm, D., Kirstahler, M.: Versuchsanlage zur schnellen Gasinjektion in einen wasser-gefüllten Behälter, KfK-4321, Kernforschungszentrum Karlsruhe (1987)

16.10 2D: N₂ explosion in space with internals filled previously with water

Consider the very practical case of failure of the melt confined by a crust in in-vessel melt–water interaction analysis, see Fig. 16.10.1 Assume that the crust failure is restricted to a limited region. The melt penetrates this region, driven by gravity. Fragmentation and subsequent steam generation create a high-pressure zone. The vapor of this zone removes all the surrounding liquids (water and melt) towards the available venting cross-sections. The steam also penetrates the surrounding liquids by creating *Taylor* instability entrainment at the surface as discussed in *Corradini, et al. (1980)*. Complicated pressure wave dynamics arises in this case.

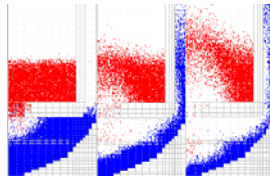


Fig. 16.10.1 Illustration showing steam generation after premixing and its action on the surrounding water and melt for in-vessel melt–water interaction

We analyze the capability of IVA5 to simulate the gas-driven explosions into liquid without strong evaporation, *Kolev (1987)*, by comparing with the experimental data for fast acoustic processes in two-phase mixtures in a complex geometry obtained by *Wilhelm and Kirstahler (1987)*, *Meyer and Kirstahler (1988)*. The calculation is repeated for the same geometry as in the previous section with the same discretization and the same initial and boundary conditions, but with the following changes. The low-pressure region consists here of degassed water with an air volumetric fraction of 0.002 to 0.005 *Meyer and Wilhelm (1994)*, and with air above the water at $p = 0.1$ MPa and room temperature, Fig. 16.10.1c. The walls containing the low-pressure region are transparent. Two high-speed cameras (90° apart, 7 frames/ms) were used to record the “bubble growth” from the region at the nozzle entrance. The photographs show bubble growth, quantitatively measured in *Meyer and Kirstahler (1988)* and entrainment of droplets from the “bubble surface” due to instability.

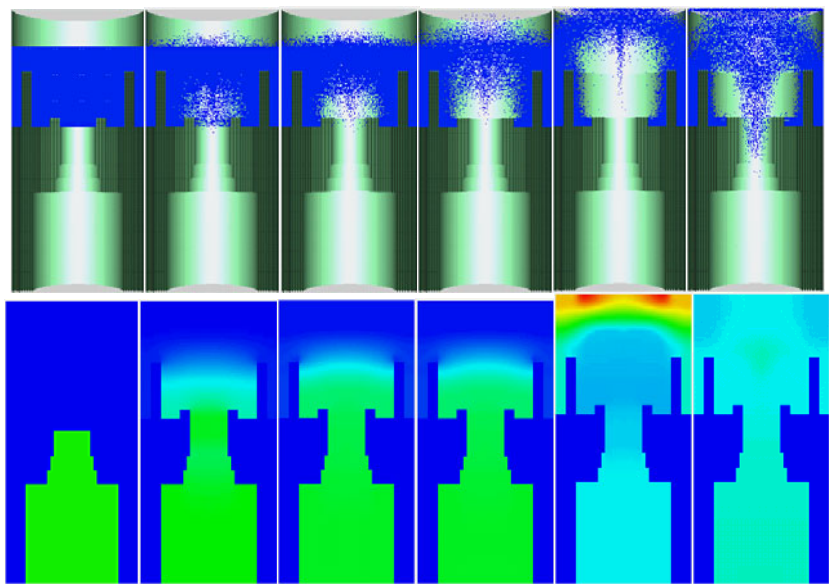


Fig. 16.10.2 An IVA6 prediction of the *Meyer and Kirstahler* gas-in-water explosion experiment. 1st row: water volume fractions as a function of space. 2nd row: pressure as a function of space. Parameter-time: 0, 0.0029, 0.0052, 0.0068, 0.0115, 0.02 s

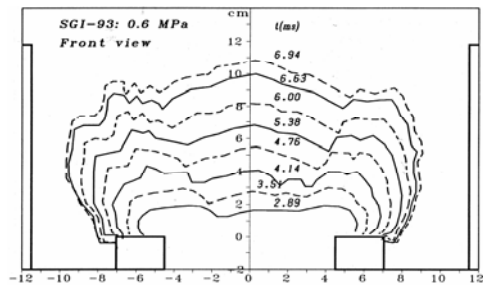
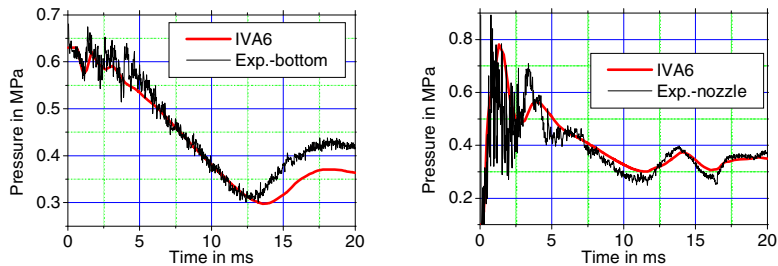


Fig. 16.10.3 Observed (bottom) gas-water “interface” as a function of space. Parameter – time



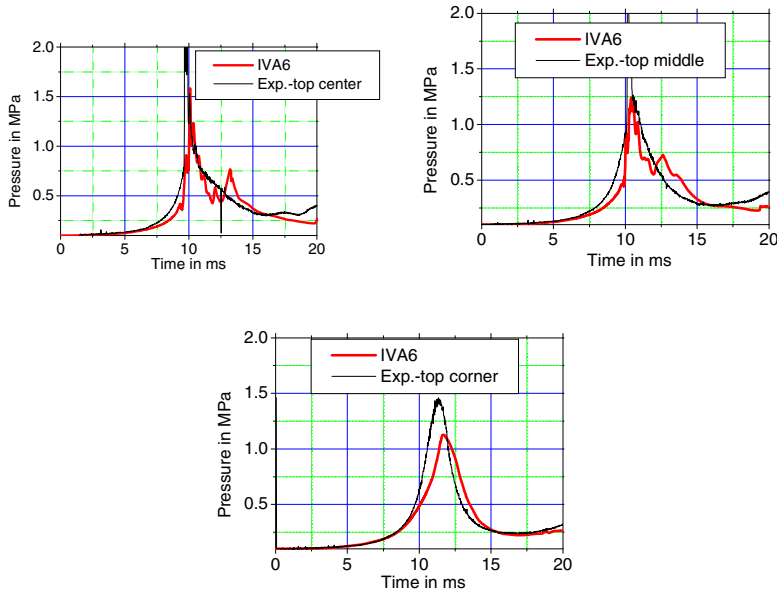


Fig. 16.10.4 An IVA6 prediction of the *Meyer* and *Kirstahler* gas-in-water explosion experiment. Pressure as a function of time at different positions

Figure 16.10.2 shows the predicted water volume fraction as a function of space. The dynamic displacement is evident from the time sequences. A comparison between the predicted and the measured lower gas/water “interface” is possible by comparison of Figs. 16.10.2 and 16.10.3. Figures 16.10.4a–e give a comparison of the computed and measured pressures at the bottom, nozzle, top-center, top-middle and top-corner, respectively. There is reasonable agreement between prediction and experiment.

Conclusion. From comparison with experiments on gas explosions in a 2D space with internals previously filled with liquid we conclude that there is reasonable agreement for fast material relocation. The code essentially provides a good prediction of the pressure impulses, which is essential for fluid structure interaction analysis. Again, just as in the single-phase case, the spatial resolution has to be selected carefully particularly for regions in which pressure spikes are expected.

Now, we simulate the same case with the multiblock boundary fitted computer code IVA_5M, *Kolev* (2004). The results are presented in Fig. 16.10.5.

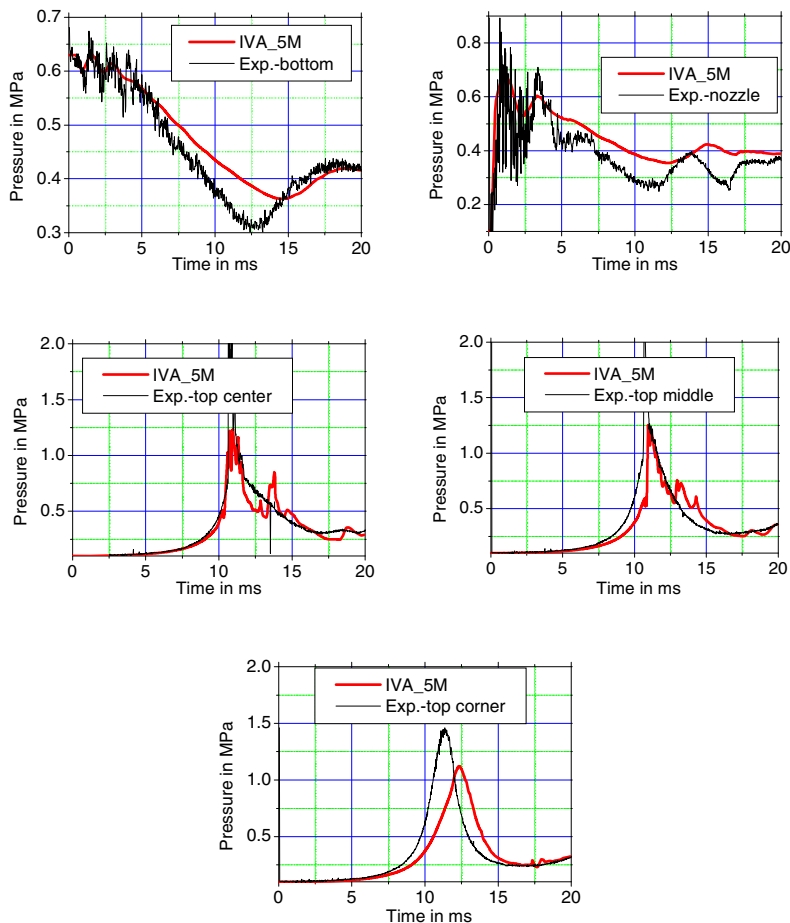


Fig. 16.10.5 An IVA_5M prediction of the *Meyer* and *Kirstahler* gas-in-water explosion experiment. Pressure as function of time at different positions

Conclusion. From comparison with experiments on gas explosions in a 2D space with internals previously filled with liquid we conclude that there is reasonable agreement for fast material relocation IVA_5M essentially provides a good prediction of the pressure impulses, which is essential for fluid structure interaction analysis. We see the expected adequate performance of the IVA_5M method under the new programming architecture and data management compared with the old architecture of single block in IVA6.

References

- Corradini, M.L., Rohsenow, W.M., Todreas, N.E.: The effect of sodium entrainment and heat transfer with two-phase UO₂ during a hypothetical core disruptive accident. NSE 73, 242–258 (1980)
- Kolev, N.I.: IVA2 verification expansion phase experiment in SNR geometry, KfK 4310 (September 1987)
- Kolev, N.I.: IVA_5M numerical method for analysis of three-fluid multi-component flows in boundary-fitted multi-blocks. Presented in Second M.I.T. Conference on Computational Fluid and Solid Mechanics, Boston, June 17–20. Computers & Structures, vol. 83, pp. 499–523 (2004)
- Meyer, L., Kirstahler, M.: Experimental investigation of the fluid dynamic of gas jet expansion in a liquid pool. In: Shah, K., Ganic, E.N., Yang, K.T. (eds.) Proc. 1st World Conf. Experimental Heat Transfer, Fluid Mechanics, and Thermodynamics, Dubrovnic, Yugoslavia, September 4–9, Elsevier, New York (1988)
- Meyer, L., Wilhelm, D.: Investigation of the fluid dynamics of gas jet expansion in a liquid pool, Kernforschungszentrum Karlsruhe, KfK 5307 (March 1994)
- Wilhelm, D., Kirstahler, M.: Versuchsanlage zur schnellen Gasinjektion in einen wasser-gefüllten Behälter, KfK-4321, Kernforschungszentrum Karlsruhe (1987)

16.11 Film entrainment in pipe flow

Entrainment of continuous liquid is an important fragmentation mechanism. The UPTF test Nr.26, *Kolev*, et al. (2000) is appropriate to test the physical modeling in this field. Details of this study are provided in *Kolev* et al. (2000). We provide here a brief summary of the 1D result. In a 3D vessel, Fig. 16.11.1, steam is injected as presented in Fig. 16.11.2. The steam may leave the vessel only through the horizontal pipe presented in Fig. 16.11.1 and in more detail in Fig. 16.11.2. The initial pressure and the pressure of the exit of the pipe are specified. The water and the steam temperatures are 141–142 °C, and 144 through 148 °C, respectively. The pressure level of this particular experiment was 0.39–0.43 MPa.

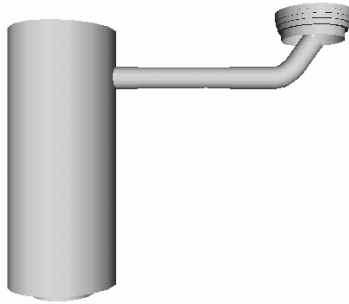


Fig. 16.11.1 IVA6 model for 1D network simulation including the steam generator inlet plenum



Fig. 16.11.2 IVA6 representation of the geometry – two-pipe system

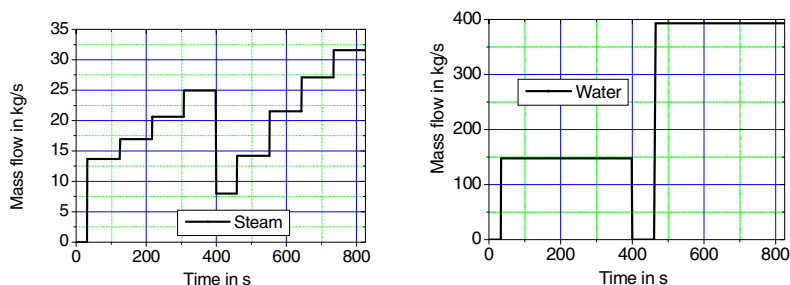


Fig. 16.11.3 a) Steam mass flow injected below the core simulator as a function of time. b) Water mass flow injected through the emergency core cooling pipe coaxial into the main coolant line as a function of time

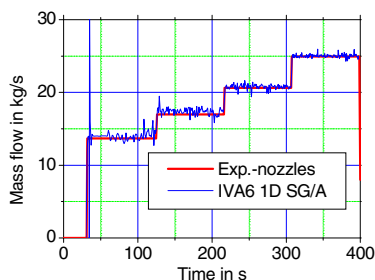


Fig. 16.11.4 Injected steam mass flow (exp.) below the core simulator as a function of time (red). Computed steam mass flow leaving the vessel as a function of time. 1D IVA6 simulation with modeling the steam generator simulators

Through the small pipe visible in Fig. 16.11.2 water is injected as shown in Fig. 16.11.3b. The target of the experiment was to study how much of the injected water is entrained from the countercurrent steam flow. From Fig. 16.11.3 we realize that there are two phases of this experiment – phase A and phase B corresponding to the stepwise water-injection function. The investigation in *Kolev et al. (2000)* indicated that in these two stages the entrainment phenomena happen at different places: in phase A in the pipe, and in phase B essentially inside the 3D vessel. In this section we consider only phase A. In this case we use a 5-pipe network model as presented in Fig. 16.11.1. Pipes 1 and 2 are shown in Fig. 16.11.2. Pipe 1 simulating the hot leg is discretized using 42 cells. Pipe 2 simulating the water injection is discretized using 5 equidistant cells. The main coolant pipe cross-section is correspondingly reduced with the injection pipe cross-section over the common distance. Pipe 3 is simulating the vessel, Fig. 16.11.2, and is discretized into 3 cells. The steam is injected through Pipe 4 in the uppermost cell of Pipe 3. The

main coolant Pipe 1 is connected to the middle cell of the Pipe 3. The lower vessel cell (Pipe 3) is large and serves to collect the gravitationally separated water.

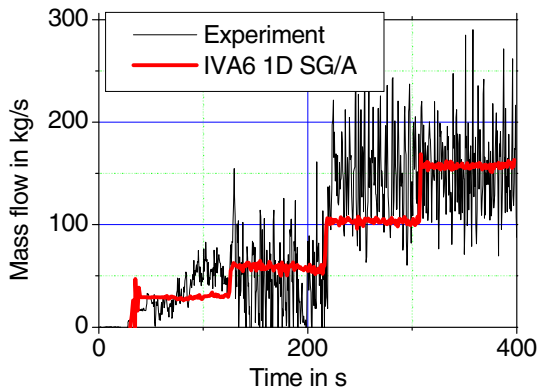


Fig. 16.11.5 Comparison between the measured and the computed total mass flow as a function of time at the gamma-densitometer position. The SG simulator considered in the 1D geometrical model

The results of the computation are presented in Figs. 16.11.4 and 16.11.5 and compared with the measurements.

Conclusion: Figure 16.11.5 presents the essence of this analysis showing that three velocity fields are a proper skeleton for the mathematical description of entrainment processes in pipe flows. One should be careful with replacing 3D flows by 1D cross-section-averaged flows and with the applicability of entrainment correlations for a particular problem – see the discussion in *Kolev et al. (2000)*. As already stated in *Kolev et al. (2000)* the particular data bank for developing better entrainment correlations has to be extended for liquid inertia-dominated flows. Experimental activities on this topic are in progress in the Research Center Karlsruhe, Germany.

Phase B of this experiment is discussed in one of the following sections.

Reference

Kolev, N.I., Seitz, H., Roloff-Bock, I.: Hot-leg injection: 3D versus 1D three velocity fields modeling and comparison with UPTF experiment, Siemens report KWU NA-T/00/E027, R&D Project 903060, Verification IVA6 (2000)

16.12 Water flashing in nozzle flow

In order to verify the capability of IVA5 to model flashing phenomena we use the steady-state flashing experiment of *Abuaf* et al. (1981) and the becoming classical *Edwards* and *O'Brien* pipe experiment documented in *Edwards* and *O'Brien* (1970) for transient pipe blow-down. The second experiment will be discussed in the next section.

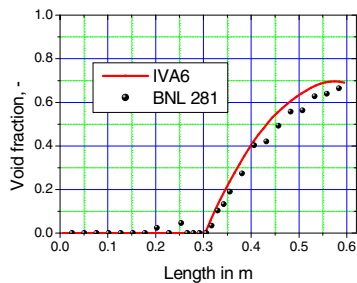
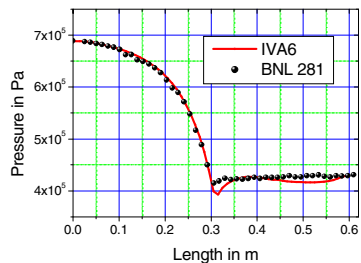
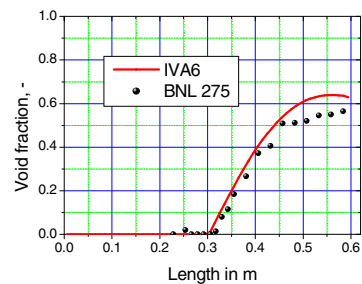
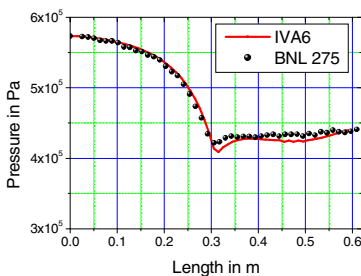
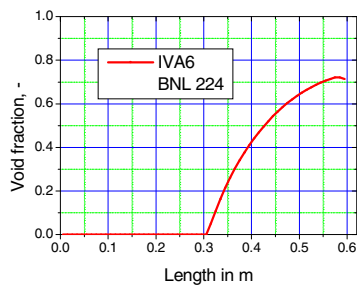
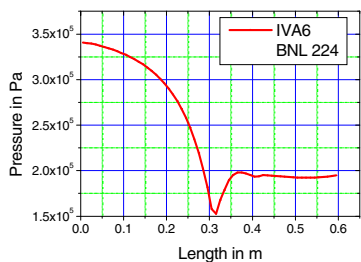
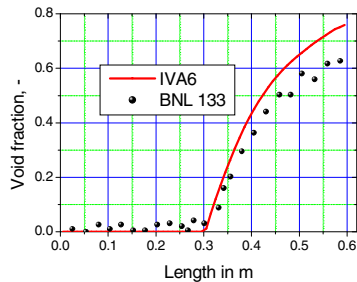
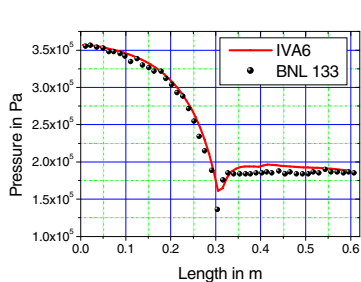
The geometry of the nozzle is given in Table 16.12.1. In Table 16.12.2 we summarize the initial and the boundary condition used in the test comparison here. Fig. 16.12.1 presents the result of the comparison.

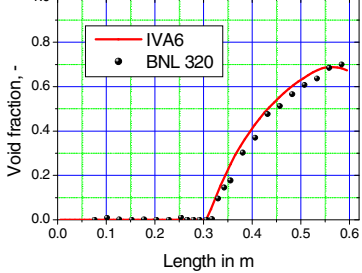
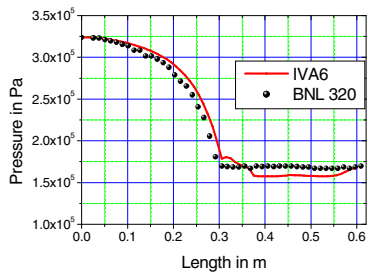
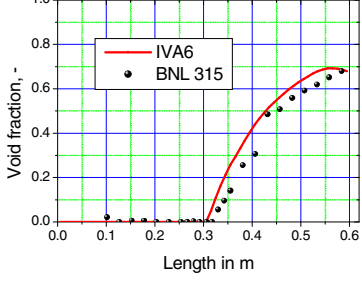
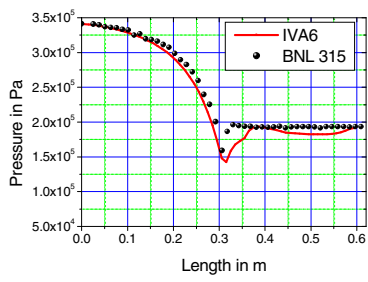
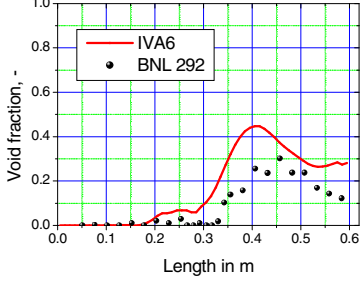
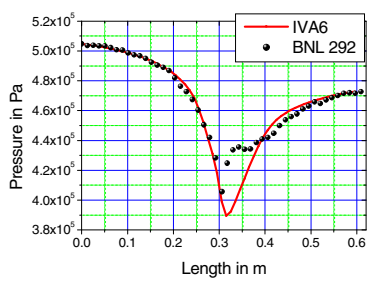
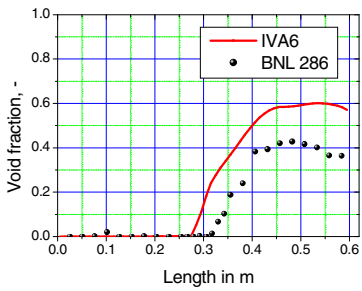
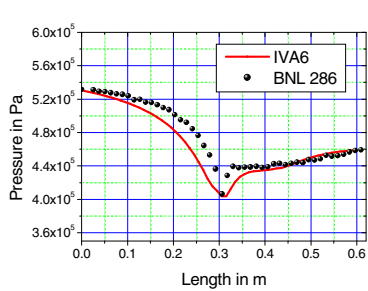
Table 16.12.1 Geometry of the test sections

Author	Geometry	Length	Hydraulic diameter	
			z / m	$D_{hyd,max} / m$
<i>BNL Abuaf</i> et al. (1981)	Circular nozzle	0.6	0	0.051
			0.02	0.051
			0.028	0.02546
			0.58	0.051
			0.6	0.051

Table 16.12.2 Initial conditions

Author	Test Nr.	Pressures		Mass flow rate (comp.)	Temperature
<i>Abuaf</i> et al. (1981)		p_{in}/bar	p_{out}/bar	$G / kg / (m^2 s)$	T_{in} / K
	133	357 485	185 030	$w_{2in} = 4.55 m/s$ (4190)	394.35
	224	341 200	196 000	4410 (4044)	394.05
	275	573 500	441 000	4290 (4193)	421.85
	281	688 700	431 000	5730 (5533)	421.95
	286	530 800	459 000	3580 (2706)	422.25
	292	504 700	473 000	2510 (2197)	422.05
	315	341 200	193 000	4410 (4202)	392.25
	320	323 700	169 000	4430 (4352)	387.55
	324	341 000	198 000	4410 (4004)	394.15
	340	321 000	249 000	4430 (3768)	394.45





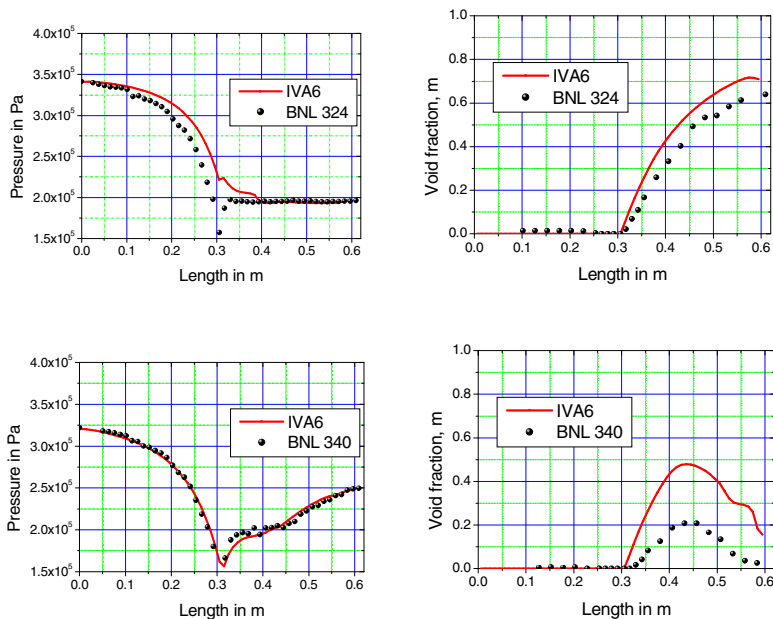


Fig. 16.12.1 An IVA5 prediction of the flashing flow in nozzle with variable cross-section. Comparison with the BNL measurements. In each pair of figures: left – pressure as a function of the spatial coordinate, right – local cross-section-averaged volume fraction as a function of the spatial coordinate

It is evident from Fig. 16.12.1 that the nucleation theory developed in *Kolev* (1995) and given in Chapters 15, 16 and 17 of this volume results in an appropriate pressure and void prediction.

Conclusion: The mean error of the predicted mass flow rate as a function of the pressure difference on the two ends is within 9%. In view of the complexity of this process the comparison of the pressure and the local cross-section-averaged vapor fraction with experimental data are classified as very good. Improvement can be achieved in the applications by using nonequidistant discretization.

References

- Abuaf, N., Wu, B.J.C., Zimmer, G.A., Saha, P.: A study of non equilibrium flashing of water in a converging diverging nozzle, vol 1 Experimental, vol 2 Modeling, NUREG/CR-1864, BNL-NUREG-51317 (June 1981)
- Edwards, A.R., O'Brien, T.P.: Studies of phenomena connected with the depressurization of water reactors. J. Brit. Nucl. Energy Soc. 9(1-4), 125–135 (1970)

Kolev, N.I.: The code IVA4: Nucleation and flashing model. *Kerntechnik* 60(6), 157–164 (1995); Also in: Proc. Second Int. Conf. On Multiphase Flow, Kyoto (April 3-7, 1995); ASME & JSME Fluid Engineering Conference International Symposium on Validation of System Transient Analysis Codes - Hilton Head (SC) USA (August 13-18, 1995); Int. Symposium on Two-Phase Flow Modeling and Experimentation, ERGIFE Place Hotel, Rome, Italy (October 9-11, 1995)

16.13 Pipe blow-down with flashing

16.13.1 Single pipe

As already mentioned, in order to verify the capability of IVA5 to model transient flashing phenomena we use the classical *Edwards and O'Brien* pipe experiment from 1970. In this experiment one of the ends of a horizontal pipe filled with subcooled water at high pressure is abruptly opened, Fig. 16.13.1.

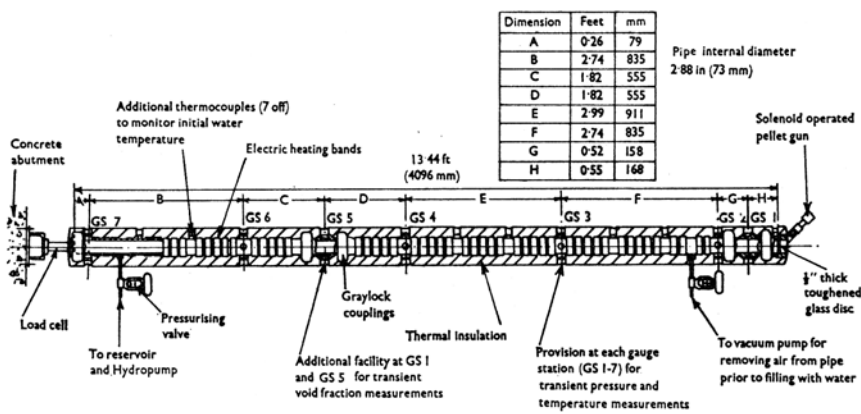


Fig. 16.13.1 General arrangement of the blow-down pipe of Edwards and O'Brien (1970)

The pressure reduction brings the water into a superheated state. The delayed nucleation and bubble growth cause the so-called pressure undershoot and then the relaxation to the saturation pressure corresponding to the initial water temperature. The results are given in Figs. 16.13.2, 16.13.3 and 16.13.4. It is evident from Figs. 16.13.2–16.13.4 that the nucleation theory developed in *Kolev* (1995) and presented in Chapters 15 to 17 of Vol. 2 results in an appropriate pressure prediction, Fig. 16.13.2. The somewhat faster emptying of the pipe in the computation for the later stage of the process, Figs. 16.13.3a and b is caused by several interactions in the computer code such as drag forces, flow pattern recognition, etc. which will not be discussed here. It can also be seen that the computed water temperature, Fig. 16.13.4a decreases faster than that determined

experimentally. This is evidence of the release of more energy from the liquid for evaporation in the model than indicated by experimental data. This is consistent with the predicted void fraction at a given position, Fig. 16.13.4c. The large void fraction increase in the first 0.1 s is not predicted by the model.

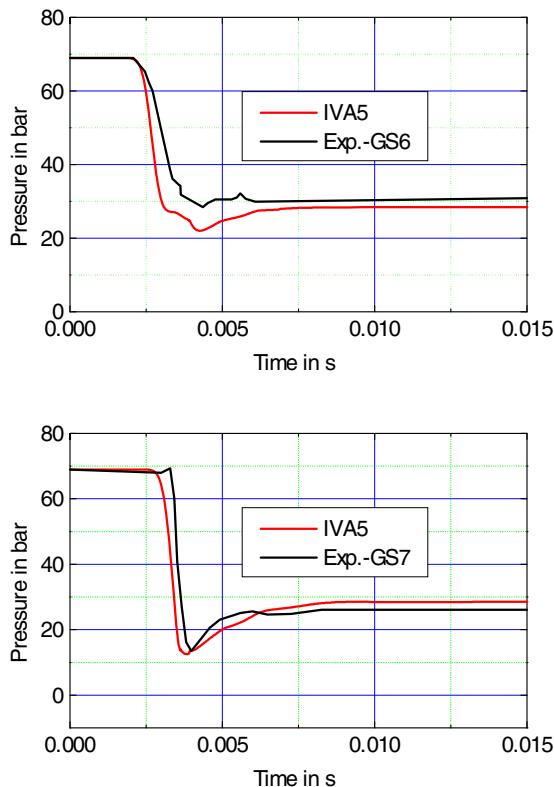


Fig. 16.13.2 Pressure at 0.072 and 0.914 m from the dead end of a pipe as a function of time. Comparison of IVA5 prediction with the experimental data of *Edwards* and *O'Brien*. Pipe diameter 0.0732 m, length 4.096 m

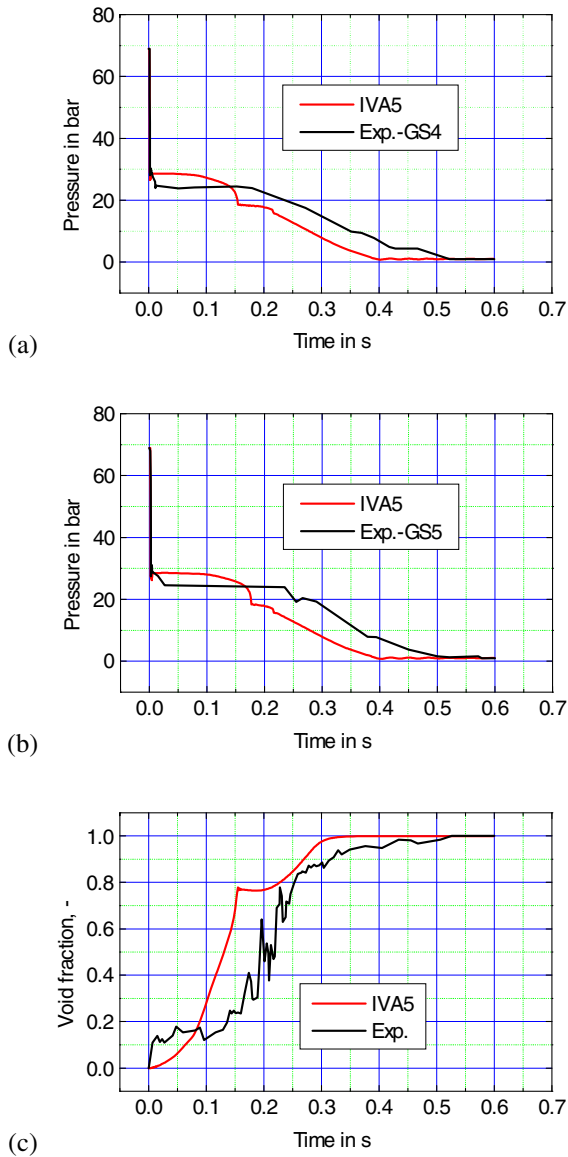


Fig. 16.13.3 a) b) Pressure at 2.024 and 2.469 m from the dead end of a pipe as a function of time. c) Steam volume fraction at 1.469 m from the dead end of the pipe as a function of time. Comparison of IVA5 prediction with the experimental data of *Edwards and O'Brien*. Pipe diameter 0.0732 m, length 4.096 m

The IVA5 force processor computes pipe forces related to hydrodynamics only in accordance with Chapter 8 of Volume 1. The results are presented in Fig. 16.13.4b

and correspond to the predicted pressure history. The oscillating character of the measurements, Fig. 16.13.4b, is a result of the fluid–structure interactions. These interactions are not simulated in the computation.

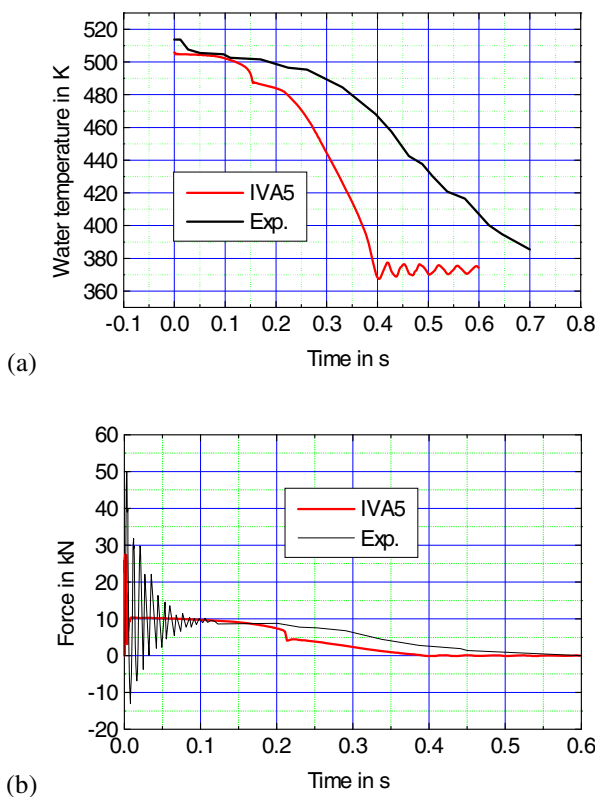


Fig. 16.13.4 a) Water temperature at 1.469 m from the dead end of the pipe as a function of time. Force as a function of time: b) IVA5 prediction without fluid-structure interactions compared with the *Edwards–O'Brien* measurements reflecting fluid structure interactions. Comparison of IVA5 prediction with the experimental data of *Edwards* and *O'Brien*. Pipe diameter 0.0732 m, length 4.096 m

Conclusion: From the comparison with experiments on pipe blow-down and water flashing we conclude that the nucleation theory presented in this monograph and used in the code results in an appropriate pressure prediction. The fast discharge pressure waves are well predicted. The evaporation model gives somewhat faster energy discharge from the liquid. In general, the blow-down process is properly predicted. The force processor works properly and provides the forces acting on a pipe network.

16.13.2 Complex pipe network

Figure 16.13.5 shows a complicated network consisting of a heat exchanger and pipes, valves etc. The heat exchanger has as primary medium water at 320 °C and about 172 bar pressure and as secondary medium water at 50 °C and about 9 bar. A break inside the heat exchanger is simulated. A flashing water–steam mixture enters the secondary side that is filled with subcooled water and creates a nonstable pressure increase and dramatic condensation shocks. As seen from Fig. 16.13.4 the first 0.2 s are characterized by strong condensation oscillation in the secondary side. Complicated interactions between the valves and the break are extremely challenging for the solution method. Analysis of processes in industrial network is becoming a routine activity in large companies.

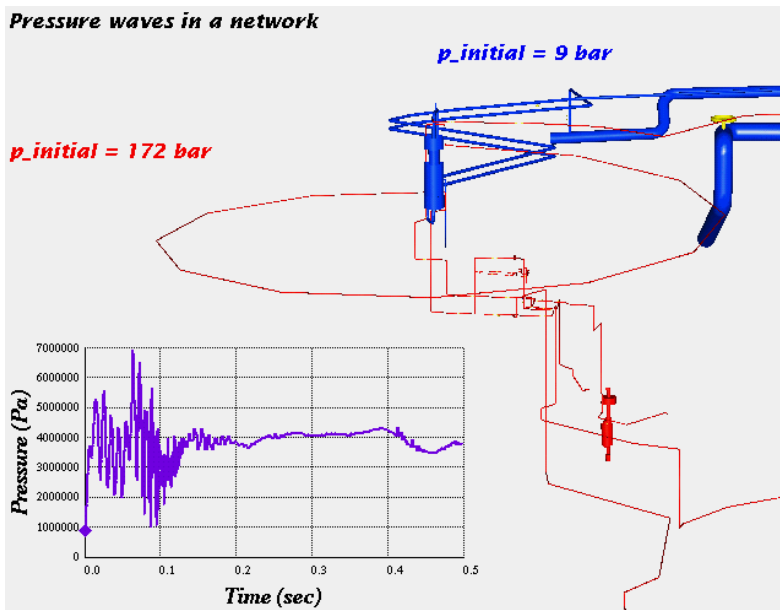


Fig. 16.13.5 Pipe break in a high-pressure heat exchanger. Pressure as a function of time. The visualization is performed using SONJA

References

Edwards, A.R., O'Brien, T.P.: Studies of phenomena connected with the depressurization of water reactors. J. Brit. Nucl. Energy Soc. 9(1-4), 125–135 (1970)

Kolev, N.I.: The code IVA4: Nucleation and flashing model. *Kerntechnik* 60(6), 157–164 (1995); Also in: Proc. Second Int. Conf. On Multiphase Flow, Kyoto (April 3–7, 1995); ASME & JSME Fluid Engineering Conference International Symposium on Validation of System Transient Analysis Codes - Hilton Head (SC) USA (August 13–18, 1995); Int. Symposium on Two-Phase Flow Modeling and Experimentation, ERGIFE Place Hotel, Rome, Italy (October 9–11, 1995)

16.14 1D boiling, critical heat flux, postcritical heat flux heat transfer

Boiling on a hot solid surface is an essential phenomenon in many technological processes. The purpose of this section is to compare the prediction of IVA6 with a variety of data from different authors for subcooled and saturated boiling in tubes and rod bundles.

Several authors measured the volume fraction of steam in heated channels. In this section we will use the set of data reported by *Sabotinov* (1974), *Pierre* (1965), *Egen et al.* (1957) and *Nylund et al.* (1968). The data vary over a relative wide range of parameters

$$38 \leq G \leq 2000 \text{ kg }/(m^2 s) \text{ ,}$$

$$1 \leq p \leq 140 \text{ bar} \text{ ,}$$

$$\Delta T_{sub} \leq 132 \text{ K} \text{ ,}$$

$$20.3 \leq \dot{q}_w'' \leq 1723 \text{ kW }/m^2 \text{ .}$$

The geometry of the test sections is summarized in the Table 16.14.1 and the boundary conditions in Table 16.14.2.

Table 16.14.1 Geometry of the test sections

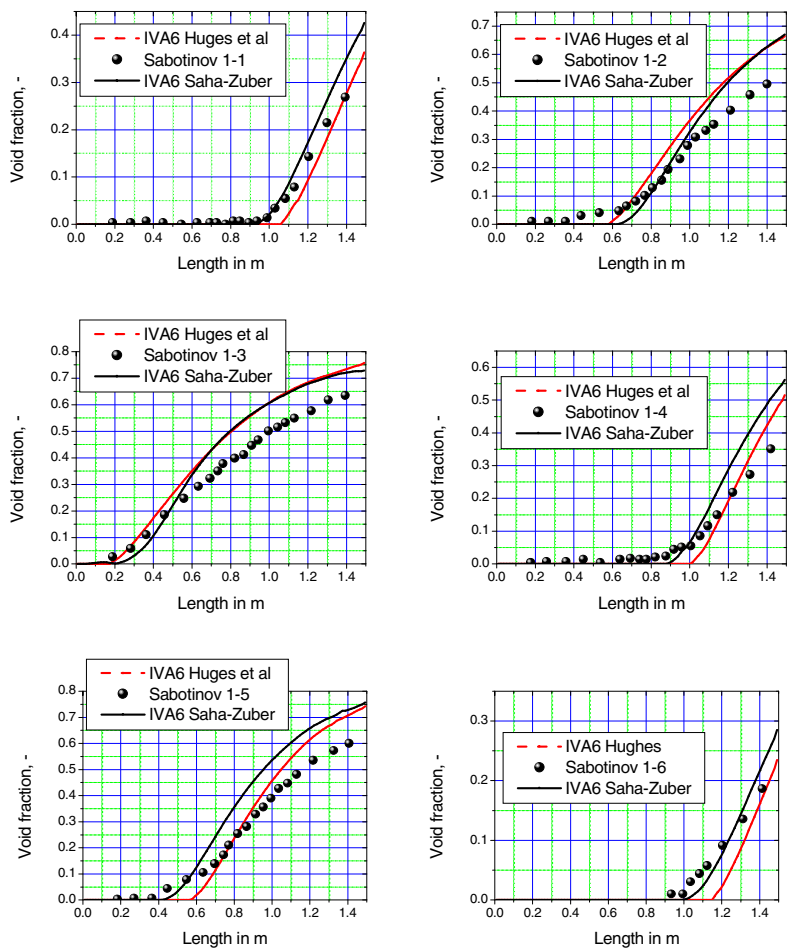
Author	Length	Hydraulic diameter	Heated diameter	Cross section
	m	D_{hyd} / m	D_{heat} / m	F / m^2
<i>Sabotinov</i> (1974), circular tube	1.5	0.0117	0.0117	0.0001075
<i>Pierre</i> (1965), rect. tube	1.2576	0.01777	0.01777	0.0004936
<i>Egen et al.</i> (1957), rect. tube	0.686	0.004756	0.004756	0.0000665
<i>Nylund et al.</i> (1968) 36 fuel rods, $d_{rod} = 0.0138 \text{ m}$	4.375	0.0269	0.0366	0.01428
<i>Bennett</i> (1967), circular tube	3.6576 5.5626	0.01262	0.01262	0.000125448

Table 16.14.2 Boundary conditions

Author	Test No.	Pressure	Mass flow rate	Heat flux	Temperature
		p / bar	$G / \text{kg} / (\text{m}^2 \text{s})$	$\dot{q}_w'' / (\text{kW} / \text{m}^2)$	T_{in} / K
<i>Sabotinov (1974)</i>					
	1	68.0585	2037	1137	504.15
	2	67.96043	1980	1130	523.15
	3	68.05849	1975	1138	539.15
	4	69.92177	1530	1360	476.15
	5	68.35269	1547	1367	504.15
	6	67.86236	2023	785	519.15
	7	68.05849	1979	786	536.15
	8	68.05849	2089	793	544.15
	9	67.86236	962	1688	461.15
	10	106.89303	1015	1723	456.15
	11	106.89303	2129	1723	514.15
	12	107.97176	2109	1718	539.15
					Subcooling
					$\Delta T_{sub} / K$
<i>Pierre (1965)</i>					
	1	13.79	1005	71.9	0.28
	9	41.38	921	287.7	2.3
	10	41.38	929	287.7	7
	13	55.17	890	287.7	2.6
<i>Egen et al. (1957)</i>					
	7	137.9	949	630.9	31
	8	137.9	895	946.4	34.3
	13	137.9	922	630.9	3.2
	16	137.9	1153	1577.3	74.3
<i>Nylund et al. (1968)</i>					
	313009	50	1107	436	4.4
	313018	49.7	1124	643	3.7
	313024	49.7	858	216	4.2
	313016	49.6	1208	426	19.3
	313014	49.7	1163	429	11
<i>Bennett (1967), $L = 3.6576 \text{ m}$</i>					
	5442	68.93	4 813.8	2 082	15.95
	5407	68.93	1 939.1	1 496	14.65
	5424	68.93	2 562.8	1 655	10.34
	5456	68.93	1 328.9	1 317	24.13

<i>Bennett (1967), L = 5.5626 m</i>					
	5253	68.93	1 356.0	902	18.96
	5293	68.93	1 979.8	1 074	18.96
	5332	68.93	664.4	648	25.43
	5280	68.93	3851.	1 691	11.64

Some of the specific models used for mass transfer are indicated in the text of the figures. The comparison for the pipes is given in Figs. 16.14.1–16.14.3. The comparison for the heated rod bundle is given in Fig. 16.14.4.



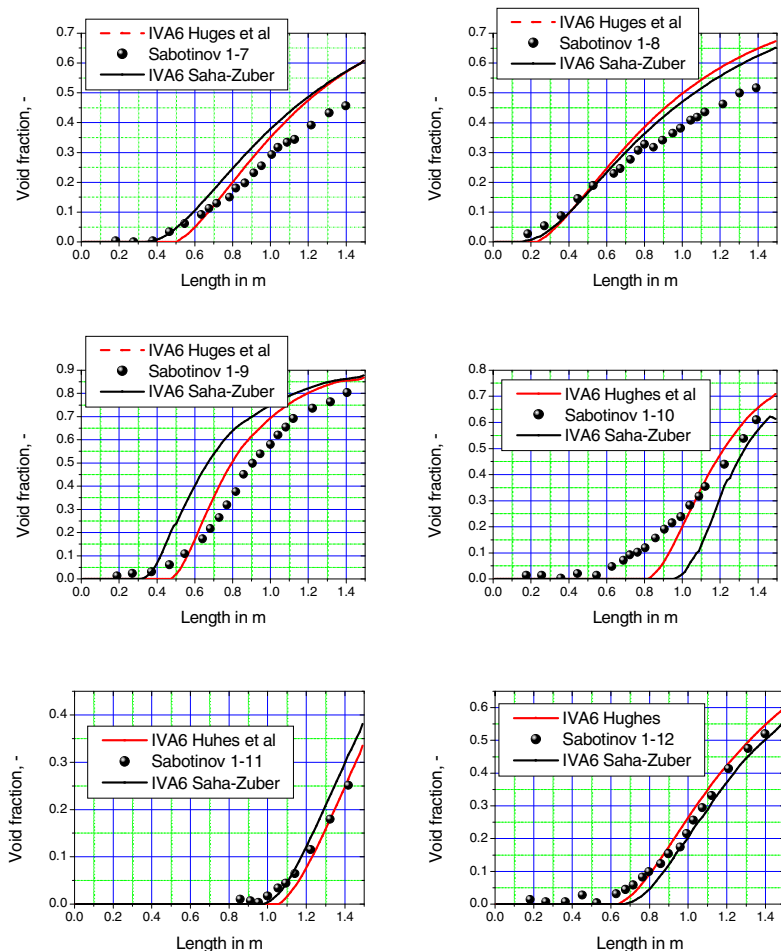


Fig. 16.14.1 a-f Steam volume fraction as a function of length measured from the bottom. Comparison between the IVA prediction and the data of *Sabotinov* (1974). The mass transfer is modeled using the proposal by *Hughes* et al. (1981) or using the approach by *Saha* and *Zuber* (1974) and *Levy* (1967). Saturated forced convection boiling is modeled using the *Chen* (1963) correlation

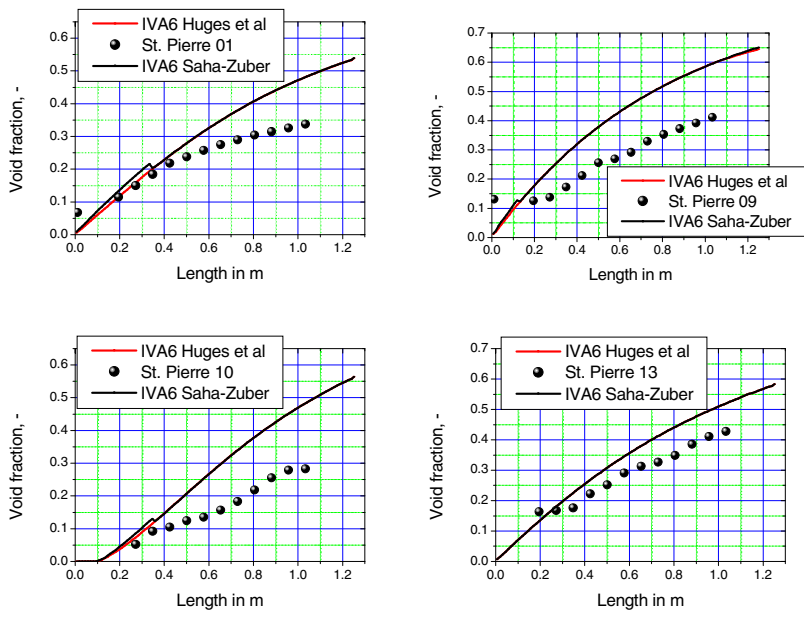
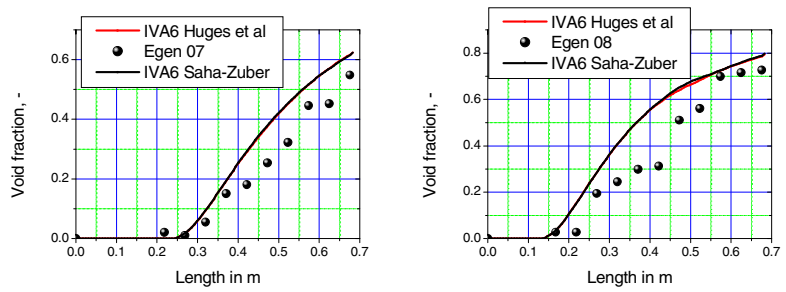


Fig. 16.14.2 Steam volume fraction as a function of length measured from the bottom. Comparison between the IVA6 prediction and the data of *Pierre* (1965). The mass transfer is modeled using the proposal by *Hughes* et al. (1981) or using the approach of *Saha* and *Zuber* (1974) and *Levy* (1967). Saturated forced convection boiling is modeled using the *Chen* (1963) correlation



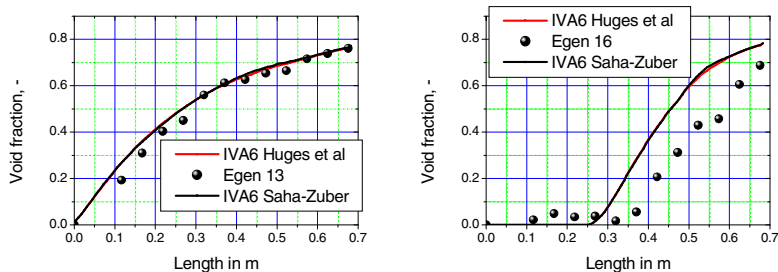
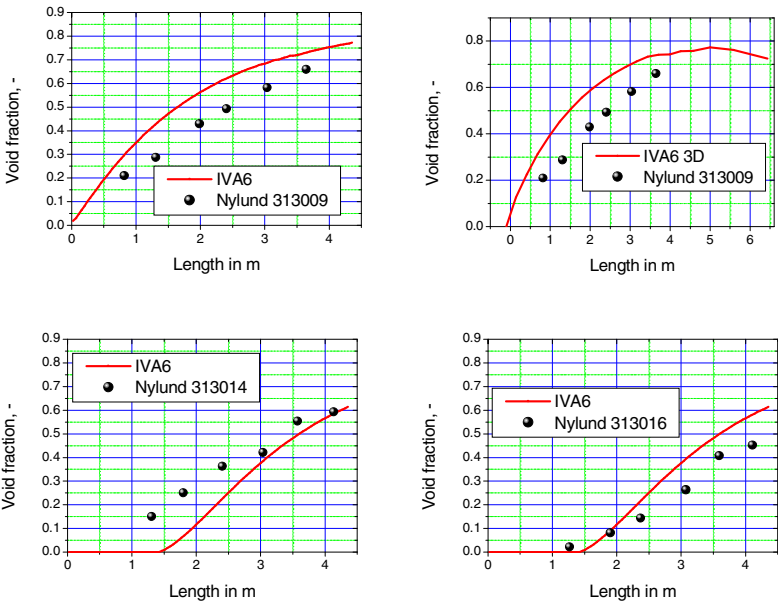


Fig. 16.14.3 Steam volume fraction as a function of length measured from the bottom. Comparison between the IVA6 prediction and the data of *Egen et al.* (1957). The mass transfer is modeled using the proposal by *Hughes et al.* (1981) or using the approach of *Saha and Zuber* (1974) and *Levy* (1967). Saturated forced convection boiling is modeled using the *Chen* (1963) correlation



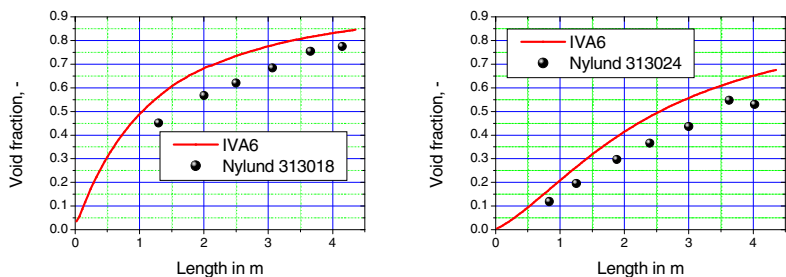


Fig. 16.14.4 Steam volume fraction as a function of length measured from the bottom. Comparison between the IVA prediction and the data of Nylund et al. (1968). The mass transfer is modeled using the proposal by Hughes et al. (1981). Saturated forced convection boiling is modeled using the Chen (1963) correlation

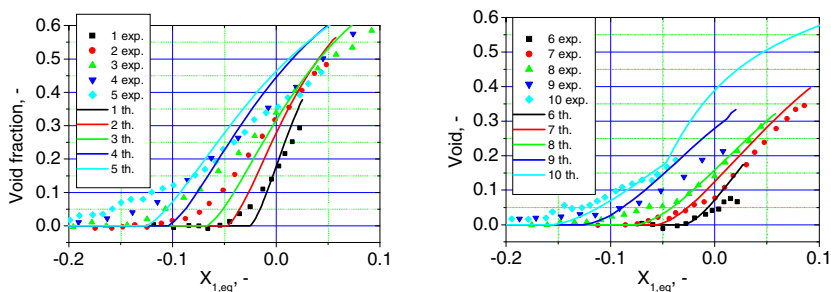
Valuable data set with systematic variation of one boundary condition by keeping the others constant for boiling in vertical pipes were reported by Bartolomei et al. (1982). 12-mm diameter uniformly heated pipe of 1.5 m length is used. Fixing the boundary conditions given in Table 16.14.3 the void fraction was measured by a gamma-ray densitometer within an error band of ± 0.04 . The accuracy of the measurements of the boundary conditions was as follows: pressure 1%, mass flow rate 2%, heat flux 3% and temperature ± 1 K. All data except the points 11 and 15 has *Peclet* number larger then 70 000. The experimental data are presented in Fig. 16.14.1 as real void fraction as a function of the equilibrium vapor mass flow ratio, $\alpha_1 = \alpha_1(X_{1,eq})$. At constant heat flux the equilibrium vapor mass flow ratio is proportional to the distance from the entrance of the pipe.

Table 16.14.3 Boundary conditions for the experiments performing by Bartolomei et al. (1982)

No.	p in Pa	ρw in kg/(m ² s)	\dot{q}''_{w2} in W/m ²	T_2 in K
$p \approx const, \rho w \approx const, T_2 \approx const, \dot{q}''_{w2} \rightarrow variable$				
1	6 810 000	998	440 000	521
2	6 890 000	965	780 000	493
3	6 840 000	961	1 130 000	466
4	6 740 000	988	1 700 000	416
5	7 010 000	996	1 980 000	434
6	14 790 000	1878	420 000	603
7	14 740 000	1847	770 000	598
8	14 750 000	2123	1 130 000	583
9	14 700 000	2014	1 720 000	545
10	14 890 000	2012	2 210 000	563

$p \approx \text{const}, \rho w \rightarrow \text{variable}, T_2 \approx \text{const}, \dot{q}_{w2}'' \approx \text{const}$				
11	6890 000	405	790 000	421
12	6890 000	986	780 000	493
13	6890 000	1467	770 000	519
14	6790 000	2024	780 000	520
15	11 020 000	503	990 000	494
15	10 810 000	966	1 130 000	502
17	10 810 000	1554	1 160 000	563
18	10 840 000	1959	1 130 000	563
$p \rightarrow \text{variable}, \rho w \approx \text{const}, T_2 \approx \text{const}, \dot{q}_{w2}'' \approx \text{const}$				
19	3010 000	990	980 000	445
20	4410 000	994	900 000	463
21	6840 000	961	1 130 000	466
22	10 810 000	966	1 130 000	502
23	14 580 000	1000	1 130 000	533
24	6810 000	2037	1 130 000	504
25	10 840 000	1959	1 130 000	563
26	14 750 000	2123	1 130 000	583

The prediction of the *Bartolomei*'s experiments is presented in Fig. 16.14.5.



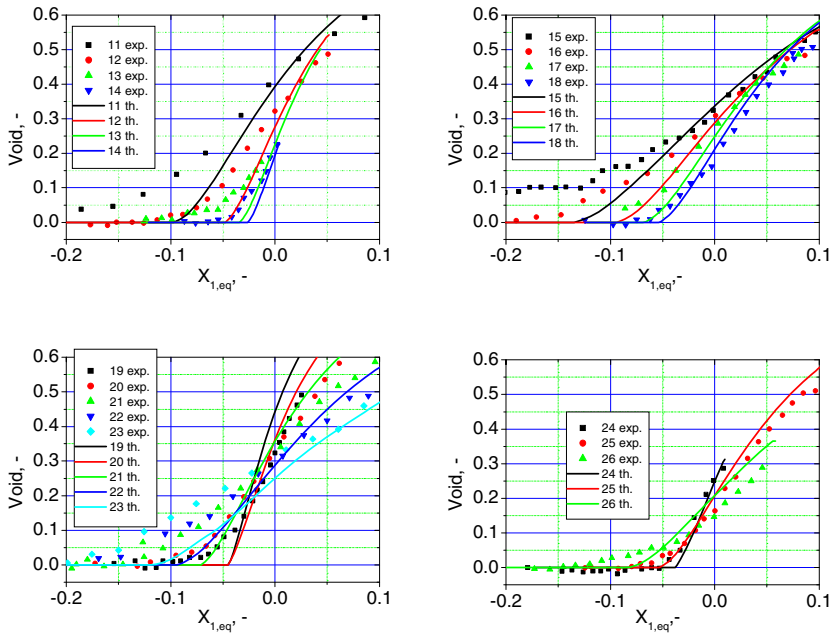
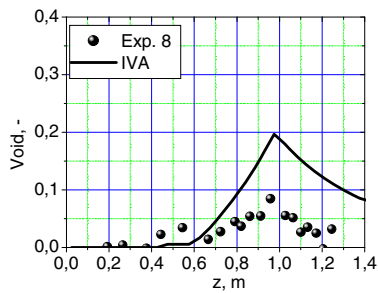
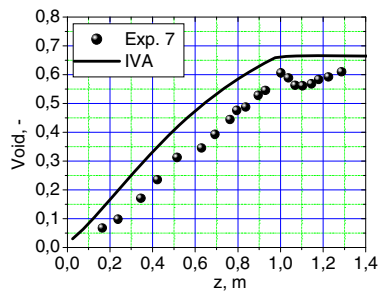
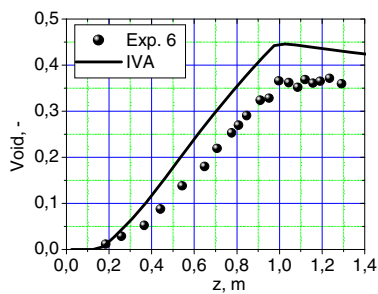
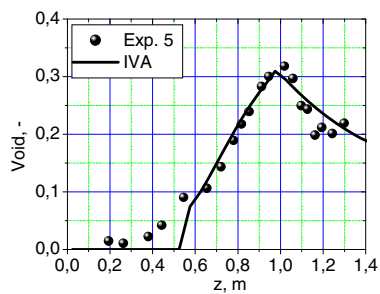
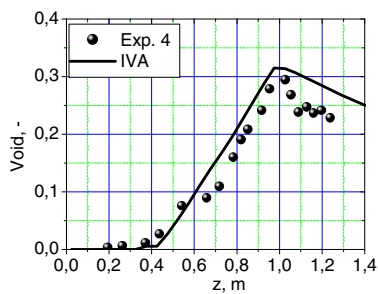
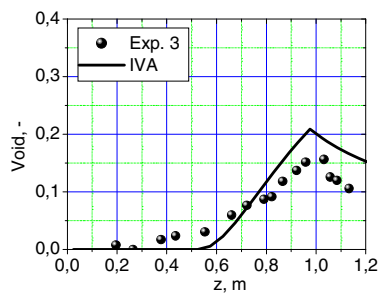
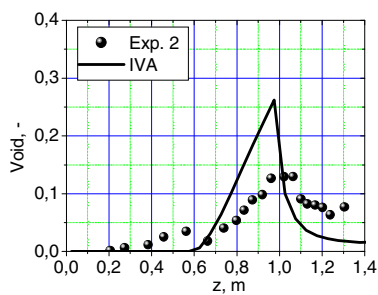
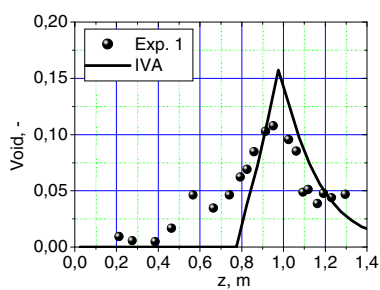


Fig. 16.14.5 Void fraction as a function of the homogeneous equilibrium mass fraction. Experimental data by Bartolomei et al. (1982). The mass transfer is modeled using the proposal by Hughes et al. (1981)

Conclusion. In general, we found slight overprediction of the volume fraction. This is attributed to the fact that the drag coefficient used in IVA6 particularly for channel flows is *not cross-section averaged*. It is well known that the void profile and the relative velocity profile have to be taken into account in the description of the mechanical interaction. This was the reason for the success of the drift flux model of Zuber and Findlay. Improvement of the model in this direction is possible if one uses the results of Section 4.2.

Bartolomei et al. (1980) performed experiments in a vertical 1.5 m pipe with 0.01203 m internal diameter and 2 mm wall thickness. The pipe was heated over the first 1 m. The flow was upwards directed. A gamma densitometer was used to measure the void fraction over the high of the pipe. The mean measurements errors reported are: p 1%, ρ_w 2%, \dot{q}_w'' 3%, $T_{2,in}$ 1 K, α_1 1%. The boundary conditions for the experiments considered here a given in Table 16.14.4.



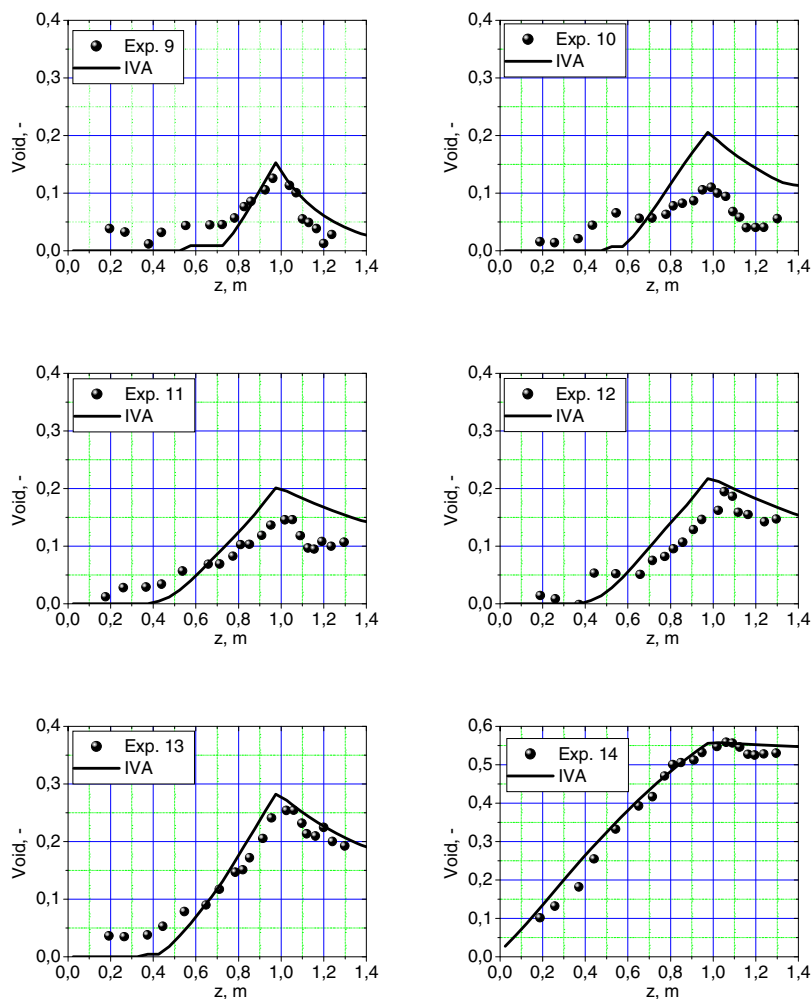


Fig. 16.14.6 Steam volume fraction as a function of length measured from the bottom. Comparison between the IVA prediction and the data of *Bartolomei et al. (1980)*. The mass transfer is modeled using the proposal by *Hughes et al. (1981)*. Modified *Hancox and Nicoll* multiplier: 0.2 instead 0.4. Saturated forced convection boiling is modeled using the *Chen (1963)* correlation

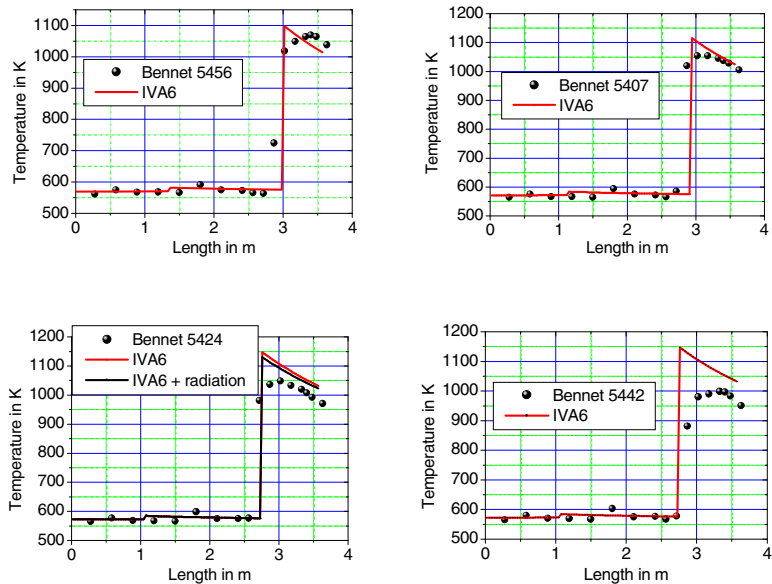
Table 16.14.4 Initial conditions for the *Bartolomei et al. (1980)* boiling pipe experiments

No	p	ρ^w	\dot{q}''_w	$T_{2,in}$
	MPa	kg/(m ² s)	MW/m ²	K
1	6.89	1000	1.2	452
2	6.89	1500	1.2	495

3	6.89	1500	0.8	519
4	6.89	2000	1.2	519
5	6.89	1000	0.8	503
6	6.89	1500	0.8	535
7	6.89	1000	0.8	534
8	10.8	1000	0.8	529
9	10.8	1000	1.2	493
10	10.8	1500	1.2	534
11	10.8	1500	0.8	558
12	10.8	2000	1.2	552
13	10.8	1000	0.8	544
14	10.8	1000	0.8	572

Here, the particular physical process that is tested in addition to the previous tests is the condensation in the nonheated part of the tube. The results are presented in Figures 16.14.6 a–j. We realize from this comparison the condensation coefficient in the *Hancox* and *Nicoll* model, see *Hughes et al. (1981)*, of 0.4 has to be reduced to 0.2. Note that this type of model excludes the tracing of the interfacial area density of the bubble/liquid interface.

Figure 16.14.7 gives the comparison with the *Bennet* data. In these experiments critical heat flux occurs and the characteristic jump of the wall temperature is very well expressed.



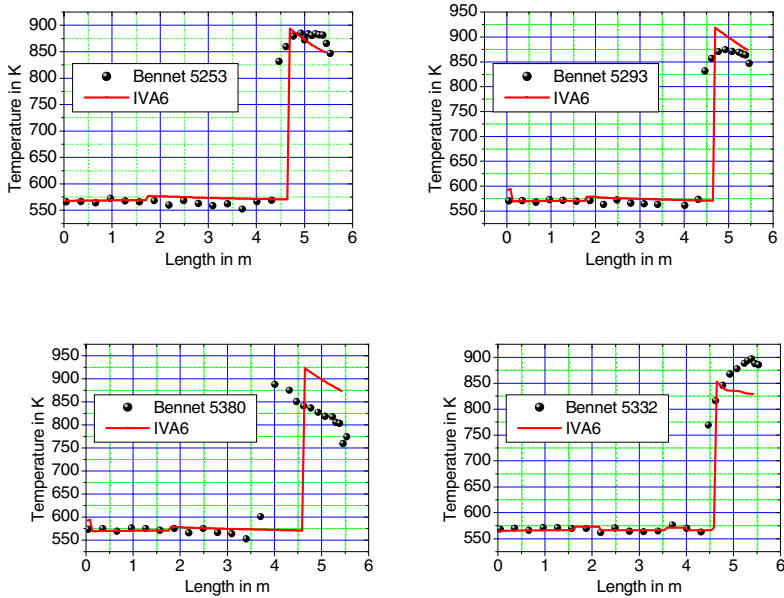


Fig. 16.14.7 a–h Wall temperature as a function of length measured from the bottom. Comparison between the IVA prediction and the data of *Bennet* (1967). The mass transfer in the sub-critical region is modeled using the proposal by *Hughes et al.* (1981). Saturated forced convection boiling is modeled using the *Chen* (1963) correlation. The critical heat flux is predicted by the 1995 look-up table (1996). The postcritical heat flux is computed using the correlation by *Miropolski* (1963) with a coefficient of 0.011

We see that the *Groeneveld et al.* (1996) look-up table predicts very well the onset of the critical heat flux. The forced convection nucleate boiling is also well predicted. The postcritical heat and mass-transfer modeling needs further sophistication especially for very long pipes. The effect of the radiative heat transfer is demonstrated for case 5424.

References

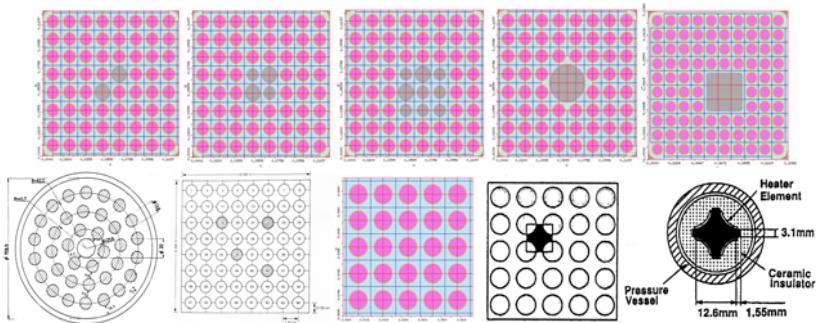
- Bennett, A.W., et al.: Heat transfer to steam-water mixtures flowing in uniformly heated tubes in which the critical heat flux has been exceeded, AERE-R5373 (1967)
- Bartolomei, G.G., Batashova, G.N., Brantov, V.G., et al.: Heat and Mass Transfer IV. Izd. ITMO AN BSSR, Minsk 5, 38 (1980) (in Russian)
- Bartolomei, G.G., Brantov, V.G., Molochnikov, Y.S., Kharitonov, Y.V., Solodkii, V.A., Batashova, G.N., Mikjailov, V.N.: An experimental investigation of true volumetric vapor content with subcooled boiling in tubes. *Thermal Eng.* 29(3), 132–135 (1982)
- Chen, J.C.: A correlation for film boiling heat transfer to saturated fluids in convective flow. *ASME Publication-63-HT* 34, 2–6 (1963)

- Egen, R.A., Dingee, D.A., Chastain, J.W.: Vapor formation and behavior in boiling heat transfer, AEC Report BMI – 1167 (1957)
- Groeneveld, D.C., et al.: The 1995 look-up table for critical heat flux in tubes. Nucl. Eng. Des. 163, 1–23 (1996)
- Hughes, E.D., Paulsen, M.P., Agee, L.J.: A drift-flux model of two phase flow for RETRAN. Nucl. Technol. 54, 410 (1981)
- Levy, S.: Int. J. Heat Transfer 10, 351–365 (1967)
- Miropolskij, Z.L.: Heat transfer in film boiling of steam-water mixture in steam generating tubes. Teploenergetika 10(5), 49–53 (1963)
- Nylund, D., et al.: Hydrodynamic and heat transfer measurements on a full-scale simulated 36-rod Marviken fuel element with uniform heat flux distribution, FRIG-2, Danish Atomic Energy Commission (1968)
- St. Pierre, C.C.: Frequency-response analysis of steam voids to sinusoidal power modulation in a thin-walled boiling water coolant channel, Argon National Lab. Report, ANL-7041 (1965)
- Sabotinov, L.S.: Experimental investigation of void fraction in subcooled boiling for different power distribution laws along the channel. Moskva PhD Thesis (1974) (in Russian)
- Saha, P., Zuber, N.: Proc. Int. Heat Transfer Conference, Tokyo, Paper B4.7 (1974)

16.15 Flow boiling in bundles: 333 experiments for variety of bundles, flow regimes including dry out, steady state and transients

The computational analysis presented in this section is performed with IVA computer code. It serves (a) as a verification base for IVA for simulation of steady-state and transient boiling processes in rod bundles and (b) as a source of inspiration for improving the accuracy of the mathematical description of such processes in the future.

Regarding (a): 333 3D tests in bundles with 1, 16, 25, 36 heated rods, 7 different bundles with 64 heated rods from different laboratories are simulated: : 273 3D experiments on 6 bundles for CHF, 54 3D experiments on 7 bundles for void fraction, 2 3D experiments in a bundles for transients and 4 1D experiments in a subchannel for transient.



The mass flow rates and the pressure varied from 3 to 2000 kg/(m² s) and from 1 bar to 200 bar, respectively. The subcooling have been less than 140 K and the thermal power varies from some tenths of a kW to 7 MW. The comparison revealed the capability of IVA to adequately simulate flow boiling processes in bundles in variety of flow regimes besides the already existing very large verification data base of IVA for many other processes.

Regarding (b): This comprehensive analysis shows that the scale of spatial resolution calls for a specific set of constitutive relations. Examples are given for the effective interfacial drag coefficients. Comparison with the results of other authors is made and discussion is provided. In addition, by using different spatial resolution it was demonstrated that the turbulent void and droplets transport have to be described much more accurately in distributed parameters to provide a universal way of prediction of void and droplet dispersion with such important consequences like accurate void and dry-out prediction.

16.15.1 Introduction

The subject of this work will be the application of IVA to the class of processes generally known as two-phase boiling flow in rod bundles in order to (a) establish a verification base for IVA for simulation of steady-state and transient boiling processes in rod bundles and (b) identify problems that have to be resolved in the future for improving the accuracy of the mathematical description of such processes. The results of this analysis are first reported in *Kolev* (2005a, b, c).

The problem with appropriate constitutive relations for a particular spatial scale resolution can be formulated as follows: Single-phase flow in bundles exhibits very heterogeneous spatial velocity profiles, *Rehme* (1978). In boiling two-phase flow the void fraction is also heterogeneous, *Hori et al.* (1994), *Hori et al.* (1995). Therefore, the cross-section-averaged properties differ significantly from the local flow properties. The constitutive relations for interfacial heat, mass, and momentum transfer are derived by procedures relying on averaging. So for instance, the bubble-drag coefficient derived in pool flow will not be appropriate for description of the mechanical interaction in gross spatial resolution analyses in rod bundles. Even bubble-drag coefficients derived for pipe flow and based on cross-section-averaged pipe flow will not be appropriate to describe the processes inside the pipe with *fine radial resolution*. A similar conclusion for the thermal profiles is also valid. So for instance, using a correlation for recognizing the point of net vapor generation, which is based on pipe cross-section-averaged water temperature, will not be appropriate to identify the same process in the boundary layer. Therefore one has to consciously apply the right set of constitutive equations to the desired type of discretization. We will demonstrate this with the example of void fraction prediction in rod bundles.

16.15.2 Steady-state boiling

16.15.2.1 The NUPEC experiment

Valuable experimental data for boiling in 8×8 rod unequally heated bundles have been collected by the Japanese Nuclear Power Engineering Corporation (NUPEC) and reported by *Morooka et al.* (1991), *Yagi et al.* (1992), *Inoue et al.* (1995a, b, c). We first concentrate our attention on the 8×8 bundle experiments having the geometry definition given in Table 16.15.1 and Fig. 16.15.1a. This experimental arrangement is referred to as a low-burn-up configuration. In addition the high-burn-up configuration as given in Fig. 16.15.1b is also used. The central rod in the last case has a diameter of 34 mm. $\ddot{\imath}$

Table 16.15.2 Boundary conditions, nonuniform power release, NUPEC *Yagi* et al. (1992) p. 163.

Exit. eq. quality	p in MPa	Power in MW	G in $\text{kg}/(\text{m}^2\text{s})$	Subc. in kJ/kg (K)
0.2415	7.2	1.143	284	50.2 (9.42)
0.2447	7.2	2.313	568	50.2 (9.42)
0.2479	7.2	3.509	852	50.2 (9.42)
0.2410	7.2	6.458	1562	50.2 (9.42)
0.2489	7.2	8.219	1988	50.2 (9.42)

The subcooling is taken from *Inoue* et al. (1995) p. 393. The exit equilibrium cross-section-averaged quality as well as the experimental cross-section void fractions are taken from *Yagi* et al. (1992) p. 163. The power is then computed by using the internal subcooling, the exit quality and the mass flow rate. The axial power distribution as presented in Fig. 16.15.1c is taken from Fig. 3 in *Inoue* et al. (1995) p. 391. The lateral power distribution is taken from Fig. 4a *Inoue* et al. (1995) p. 391. The later distribution required slight renormalization to achieve strict energy conservation of the total energy release as a boundary condition. The spacers receive an irreversible pressure drop coefficient equal to 1 based on the bundle velocity due to lack of better knowledge.

Table 16.15.3 Boundary conditions, nonuniform power release *Inoue* et al. (1995) p. 394, high-burn-up geometry

Exit. eq. quality	p in MPa	Power in MW	G in $\text{kg}/(\text{m}^2 \text{ s})$	Subc. in kJ/kg (K)
0.2479	7.2	3.509	852	50.2 (9.43)
0.2410	7.2	2.313	1562	50.2 (9.43)

The cross-section-averaged void fractions are presented in the original sources *Yagi* et al. (1992) p.163 and *Inoue* et al. (1995) p. 394 as a function of the equilibrium quality. The equilibrium quality is computed by using the inlet subcooling and integrating over the height of the bundle using the axial energy distribution. The type of the channels for the low burn-up bundle, their number, the hydraulic and the heated diameter and the corresponding cross-section are given in Table 16.15.4.

Table 16.15.4 Subchannel characteristics for the NUPEC 8×8 low-burn-up bundle

Type	nr.	γ_z	D_{hyd}	D_{heat}	F
1, internal	22	0.5472	1.4867E-02	1.4867E-02	1.4362E-04
2, corner	4	0.5930	9.9153E-03	1.7921E-02	1.7313E-04
3, periphery	36	0.5844	1.2188E-02	1.7298E-02	1.6711E-04
4, unheated	2	0.3266	7.2766E-03	0.	8.5725E-05
Total	64	0.5583	1.2994E-02	1.6291E-02	9.7575E-03

Note that *Aounalla* and *Coddington* (1999) used part of this data for verification of the two-fluid subchannel code VIPRE-02 in which the cross-flow is modeled by simplified momentum equations. *Naitoh* et al. (1999) and *Utsuno* et al. (2004)

used part of the NUPEC data for verification of drift flux subchannel code CAPE and TCAPE, respectively, in which the crossflow is modeled by mixing models defining crossflows, but not by momentum conservation.

Our computation in Cartesian coordinates uses $8 \times 8 \times 24$ cells that form 64 rod-centered subchannels, see Fig. 16.15.4. We start the simulation with an arbitrary but meaningful initial state and continue the simulation until the steady state was established, controlling this by plotting the relative difference between inlet and outlet flows in %. An example is given in Fig. 16.15.2 for the low-burn-up geometry with mass flow rate $1988 \text{ kg}/(\text{m}^2 \text{ s})$. For reaching a steady state solution through a transient analysis achieving a good accuracy of the time integration is crucial in order not to produce artificial density waves. In this case time steps of $1 \times 10^{-3} \text{ s}$ or less are appropriate.

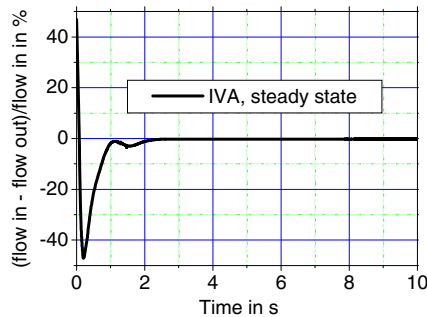


Fig. 16.15.2 Nonoscillating steady state for the NUPEC experiment with $1988 \text{ kg}/(\text{m}^2 \text{ s})$

Only the case with $284 \text{ kg}/(\text{m}^2 \text{ s})$ resulted in an oscillating but stable steady-state solution. This will be discussed in a separate section. All other cases manifest nonoscillating steady-state solutions, as those characterized by Fig. 16.15.2.

16.15.2.1.1 Comparison of the IVA predictions with the NUPEC data

16.15.2.1.1.1 Cross-section-averaged axial profiles

The results of the computational analyses for the low-burn-up cases are presented in Fig. 16.15.3. The upper curve present the unchanged IVA set of drag coefficients that are applicable to fine resolution analyses.

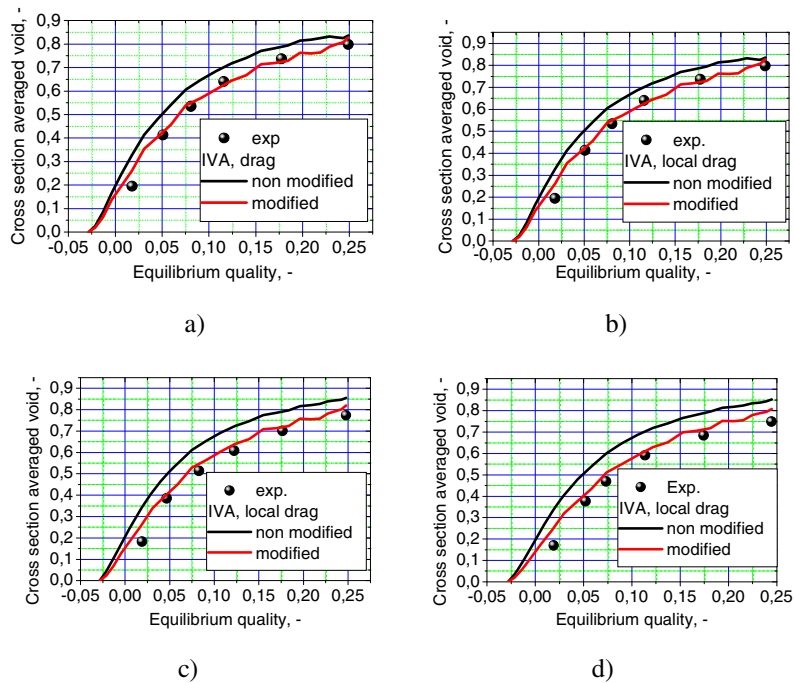
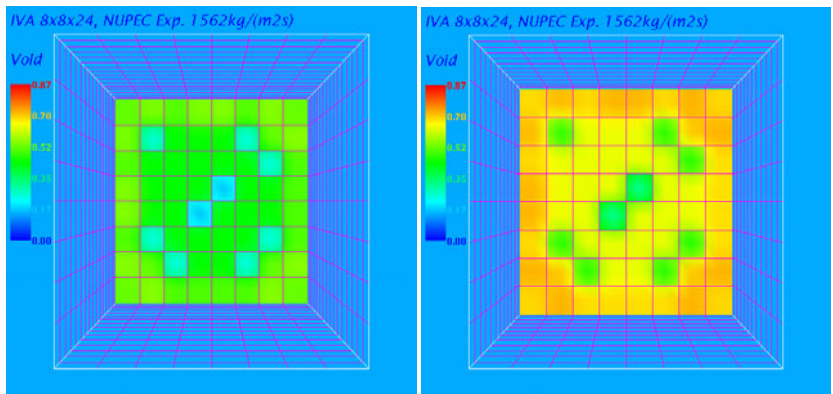


Fig. 16.15.3 NUPEC experiment with mass flow rate a) 1998 kg/(m² s); b) 1562 kg/(m² s); c) 852 kg/(m² s); d) 568 kg/(m² s). Void fraction as a function of the height. Parameter: local interfacial drag



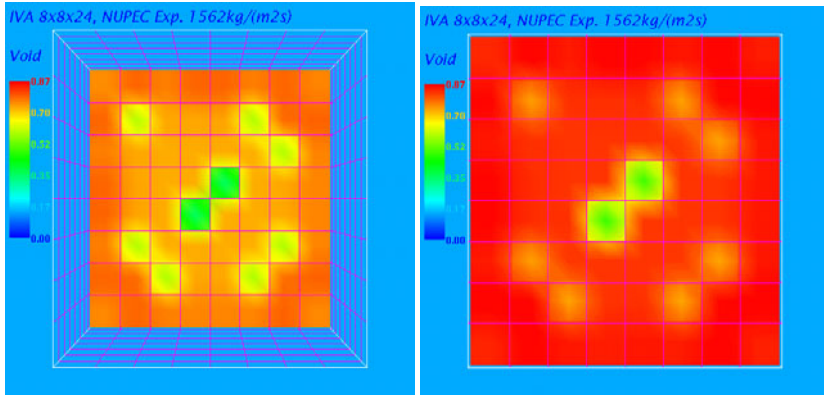


Fig. 16.15.4 NUPEC experiment with mass flow rate 1562 kg/(m²s): a) $z = 1.3133$ m, $X_1 = 0.0596$; b) $z = 1.9313$ m, $X_1 = 0.124$; c) $z = 2.5492$ m, $X_1 = 0.184$; d) $z_{\text{exit}} = 3.6307$ m, $X_{1,\text{exit}} = 0.2489$

The used rod-centered subchannel discretization is by far not a fine resolution. Unless otherwise noted we use the *Saha and Zuber* (1974) correlation for the initiation of the subcooled boiling and the *Levy* (1967) asymptotic model for the splitting of the heat into convection evaporation and condensation. As already mentioned in the introduction, there are velocity and void profiles that make the application of the local drag coefficient based on local parameters not appropriate. An ad hoc modification on the drag coefficients is made as presented in Appendix 16.15.1. The results with this modification are presented in each figure as a lower curve. The comparison with the data is then favorable. Figure 16.15.4 illustrates some details of the case with a mass flow rate 1562 kg/(m² s). The influence of the nonheated rods and of the low-power rods is clearly seen.

Now, let us compare the predictions with the measurements for the two high-burn-up cases using the modified drag coefficients. The solutions are presented in Figs. 16.15.5a and b.

In summary, the effect of the nonuniformity of the flow profiles inside the subchannels is manifested in effectively lower drag between the liquid and the vapor. The comparison with the data using the reduced effective drag is favorable. However, it can not be expected a priori to have a unique interfacial drag-reduction algorithm for all types of subchannels. To check this, we analyze in the following sections void fraction data collected in bundles of completely different types.

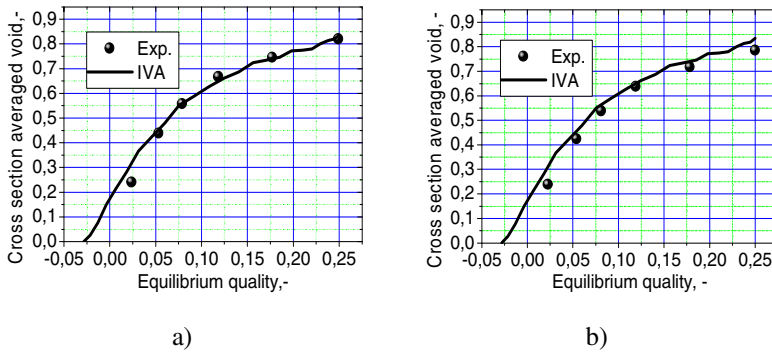


Fig. 16.15.5 NUPEC experiment with mass flow rate a) 1562 kg/(m² s); b) 852 kg/(m² s). Void fraction as a function of the height

16.15.2.1.2 Regions averaged exit void fractions at different power level

Inoue et al. (1995) reported region-averaged void fractions at the exit of the *low-burn-up bundle* for the case with 1562 kg/(m² s). The definitions of the five regions are given in Fig. 16.15.6a. The measured region-averaged void fractions at the exit of the bundle are presented in Fig. 16.15.6b for different bundle power defined by equilibrium exit quality 0.05, 0.12 and 0.18, respectively. The computed void fractions are also presented for comparison in Fig. 16.15.6b.

Inoue et al. (1995) also reported a region-averaged void fractions at the exit of the *high-burn-up bundle* for the case with 1562 kg/(m² s). The definitions of the four regions are given in Fig. 16.15.7a. The measured region-averaged void fractions at the exit of the bundle are presented in Fig. 16.15.7b for different bundle power defined by equilibrium exit quality 0.05, 0.12 and 0.18, respectively. The computed void fractions are also presented for comparison in Fig. 16.15.7b.

For both bundles the prediction accuracy is very similar. Low-burn-up bundle (Fig. 16.15.6b): We see “good” agreement for the three external regions. For the central region the prediction with such gross discretization underpredicts the void fraction. Comparing the cases with smaller and larger resolution, b) and c) in Fig. 16.15.6, we realize that the comparison with the data is “better” for the gross resolution. This is an indication that the void mixing computed based only on the transport equation without turbulence modeling is not enough to describe appropriately this process. High-burn-up bundle: For low power the computed results are higher than the measured. To our view, the reason for the discrepancy is partially in the low resolution of the subchannel analysis. As already mentioned increasing the resolution alone without turbulence modeling will not improve the result. As we will see later, the use of the Hughes et al. (1981) correlation for splitting of the heat fluxes instead of Saha-Zuber (1974), Levy (1967) improves the prediction accuracy in the low-void region.

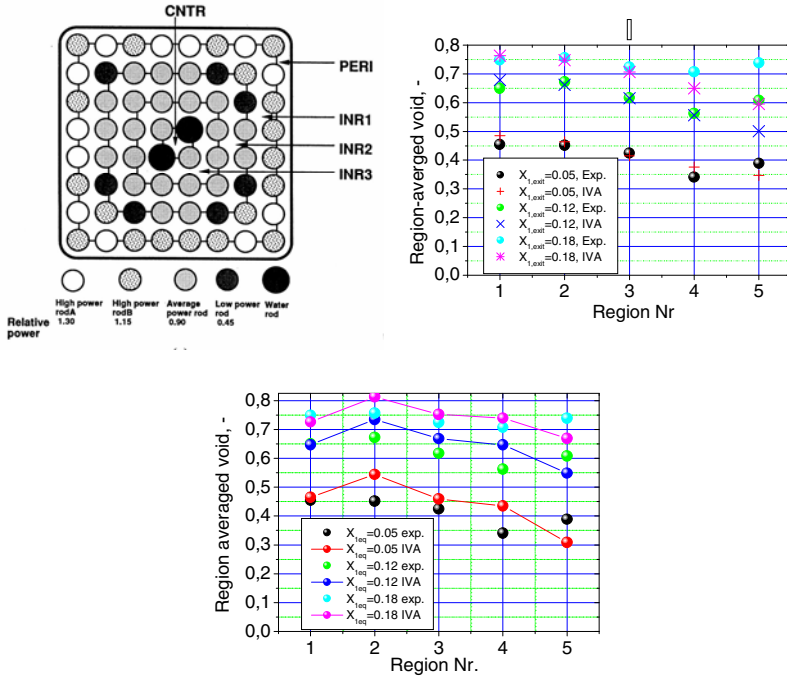


Fig. 16.15.6 a) Definition of the averaging regions, *Inoue et al. (1995)*: PERI = 1, INR1 = 2, INR2 = 3, INR3 = 4, CNTR = 5; Region-averaged void fractions at the exit of the bundle for different bundle power corresponding to constant conditions but specified exit equilibrium quality: Resolution: b) $8 \times 8 \times 24$; c) $20 \times 20 \times 24$

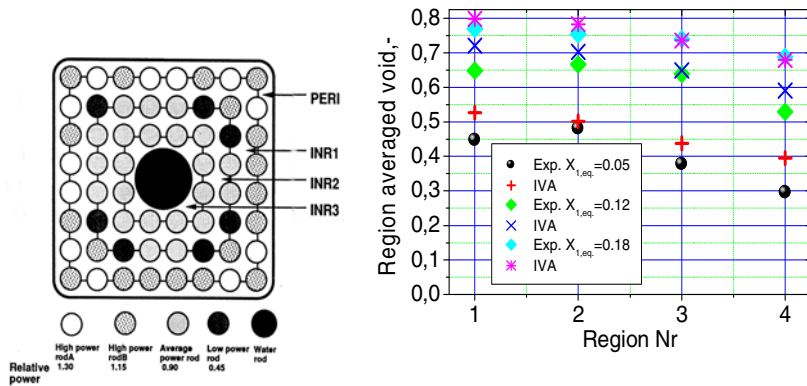


Fig. 16.15.7 a) Definition of the averaging regions, *Inoue et al. (1995)*: PERI = 1, INR1 = 2, INR2 = 3, INR3 = 4; b) Region-averaged void fractions at the exit of the bundle for different bundle power corresponding to constant conditions but specified exit equilibrium quality

16.15.2.1.3 Local exit void fractions at different power level

Prediction for 15 additional proprietary NUPEC experiments in a framework of an OECD/USNRC benchmark, *Kolev* (2005a), are compared with the outlet void fractions based on subchannels. The 1365 experimental data are available at the exit of the bundle as a cross-section-averaged void fraction and as a 9×9 local subchannel data, see Figs. 16.15.8 and 16.15.9.

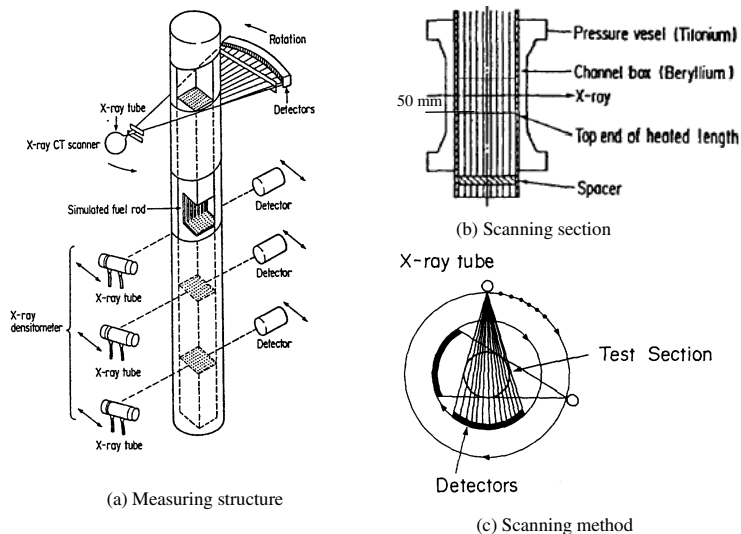


Fig. 16.15.8 Void-fraction measurement system

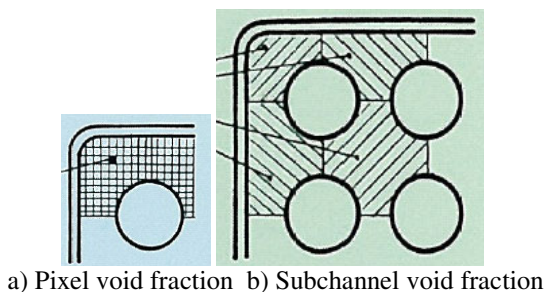


Fig. 16.15.9 Spatial resolution: a) of the experimentally measured void fractions; b) of the region averaged void fraction subject of comparison with the predicted void fractions

The geometry of the bundles is presented on Fig. 16.15.10. Comparison between the computed and measured exit void fractions are presented in Tables 16.15.5–16.15.12 for two different models especially for the subcooled boiling. Tables 16.15.5–16.15.8 contain the comparison for data predicted using the *Saha and Zuber* (1974) correlation for the initiation of the subcooled boiling and the *Levy* (1967) asymptotic

model for the splitting of the heat into convection evaporation and condensation. Tables 16.15.9–16.15.12 contain the comparison for data predicted using the *Hughes et al. (1981)* approach for the initiation of the subcooled boiling and for the splitting of the heat into convection evaporation and recondensation.

Table 16.15.5 Cross-section-averaged void fractions computed by IVA and measured by NUPEC. IVA heat partitioning models: *Saha-Zuber (1974)* and *Levy (1967)*

Test No.		0011, assembly 0-1			0021, assembly 0-2			0031, assembly 0-3		
z in m		55	58	61	16	18	21	16	18	21
	Exp.	0.409	0.630	0.794	0.394	0.626	0.783	0.393	0.623	0.783
3.758	IVA	0.461	0.667	0.797	0.450	0.655	0.791	0.447	0.638	0.778
	Dev.%	+12.7	+5.9	+0.38	+14.2	+4.6	+1.0	+13.7	+2.4	+0.6

Table 16.15.6 Cross-section-averaged void fractions computed by IVA and measured by NUPEC. IVA heat partitioning models: *Saha-Zuber (1974)* and *Levy (1967)*

Test No.		1071, assembly 1			4101, assembly 4		
z in m		55	58	61	55	58	61
	Exp.	0.430	0.637	0.791	0.438	0.645	0.807
3.758	IVA	0.453	0.654	0.799	0.467	0.670	0.803
	Dev.%	+5.3	+2.7	+1.0	+6.6	+3.9	-0.5

Table 16.15.7 Local void-fraction mean error at the exit of the bundle. IVA heat partitioning models: *Saha-Zuber (1974)* and *Levy (1967)*

Test No.	0011, assembly 0-1			0021, assembly 0-2			0031, assembly 0-3		
	55	58	61	16	18	21	16	18	21
Mean error%	6.43	5.48	4.61	7.22	6.31	5.00	7.20	7.22	6.66

Table 16.15.8 Local void-fraction mean error at the exit of the bundle. IVA heat partitioning models: *Saha-Zuber (1974)* and *Levy (1967)*

Test No.	1071, assembly 1			4101, assembly 4		
	55	58	61	55	58	61
Mean error%	5.38	4.57	4.22	4.77	4.71	4.49

Tables 16.15.7 and 16.15.8 contain the square root mean error for the 9×9 subchannel data. The total mean error is 5.62%. The data structure is presented on Fig. 16.15.11 where the measured void local subchannel fractions are presented versus the computed for all 1365 data points. The spread is within +20 and -25% with the main bulk of the data grouped around the diagonal.

Table 16.15.9 Cross-section-averaged void fractions computed by IVA and measured by NUPEC. IVA heat partitioning models: *Hughes et al.* (1981)

Test No.		0011, assembly 0-1			0021, assembly 0-2			0031, assembly 0-3		
z in m		55	58	61	16	18	21	16	18	21
	Exp.	0.409	0.630	0.794	0.394	0.626	0.783	0.393	0.623	0.783
3.758	IVA	0.426	0.637	0.782	0.415	0.627	0.777	0.414	0.610	0.765
	Dev.%	4.16	1.11	-1.51	5.33	0.16	-0.77	5.34	-2.09	-2.30

Table 16.15.10 Cross-section-averaged void fractions computed by IVA and measured by NUPEC. IVA heat partitioning models: *Hughes et al.* (1981)

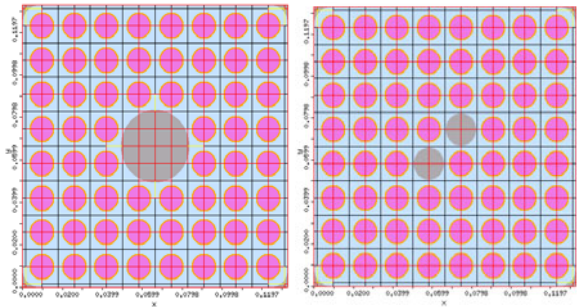
Test No.		1071, assembly 1			4101, assembly 4		
z in m		55	58	61	55	58	61
	Exp.	0.430	0.637	0.791	0.438	0.645	0.807
3.758	IVA	0.415	0.629	0.786	0.428	0.639	0.788
	Dev.%	-3.49	-1.26	-0.63	-2.28	-0.93	-2.35

Table 16.15.11 Local void-fractions mean error at the exit of the bundle. IVA heat partitioning models: *Hughes et al.* (1981)

Test No.	0011, assembly 0-1			0021, assembly 0-2			0031, assembly 0-3		
	55	58	61	16	18	21	16	18	21
Mean error%	4.97	4.70	4.53	5.33	5.82	4.81	5.66	6.87	6.47

Table 16.15.12 Local void-fractions mean error at the exit of the bundle. IVA heat partitioning models: *Hughes et al.* (1981)

Test No.	1071, assembly 1			4101, assembly 4		
	55	58	61	55	58	61
Mean error%	5.36	4.45	3.99	4.55	4.57	5.21



Assembly: 0-1, 1, 3

0-2

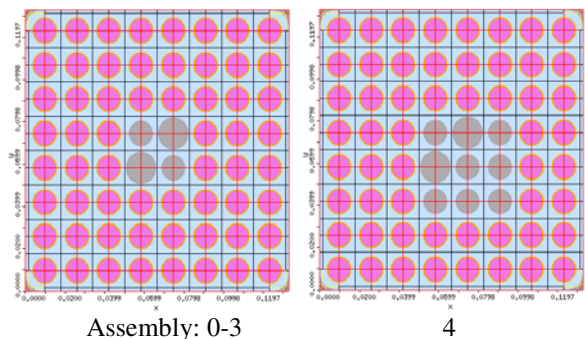


Fig. 16.15.10 IVA discretization models of the four bundles

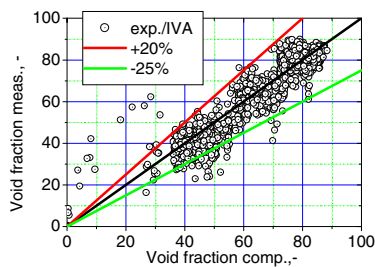


Fig. 16.15.11 Computed versus measured void fraction at the 91 subchannels at the exit of the bundle. Models for subcooled boiling: *Saha and Zuber* (1974) correlation for the initiation of the subcooled boiling and the *Levy* (1967) asymptotic model for the splitting of the heat into convection evaporation and recondensation. The total mean error is 5.62%

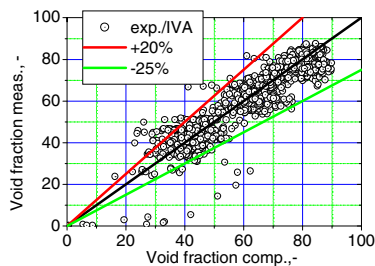


Fig. 16.15.12 Computed versus measured void fraction at the 91 subchannels at the exit of the bundle. Models for subcooled boiling: *Hughes et al.* (1981) approach for the initiation of the subcooled boiling and for the splitting of the heat into convection evaporation and recondensation. The total mean error is 5.15%

Tables 16.15.9 and 16.15.10 contain the square root mean error for the 9×9 subchannel data. The total mean error is 5.15%. The data structure is presented in Fig. 16.15.12 where the measured void local subchannel fractions are presented versus the computed for all 1365 data points. The spread is within +20 and -25% with the main bulk of the data grouped around the diagonal.

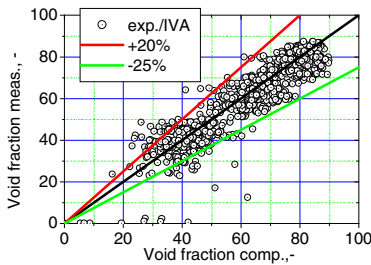


Fig. 16.15.13 As in Fig. 16.15.12: latest version of IVA. The total mean error is 5.07%

Table 16.15.13 Standard deviation for different computer codes reported in *Neykov et al. (2006)*

	1	2	3	4	5	6	7	8	9	10
01	0.18	1.7	1.2	1.44	1.55	2.13	0.94	0.63	2.36	1.86
02	0.09	1.67	0.89	1.44	1.98	4.98	4.21	0.12	2.15	1.14
03	0.39	2.01	1.25	1.24			4.49	0.3	2.13	1.4
1	1.08	0.76	0.28	0.0			3.18	1.76	1.1	1
4	2.11	1.02	1.09	0.88	4.45		2.01	1.58	0.37	0.84

- 1. MATRA (KAERI)
- 2. MARS (KAERI)
- 3. MONA (KTH)
- 4. CAPE Mod 1.0 (NUPEC)
- 5. TwoPorFlow (FZK)
- 6. COBRA-TF (PSU)
- 7. F-COBRA-TF (AREVA)
- 8. IVA (AREVA)
- 9. NEPTUNE -FLICA4 (CEA)
- 10. NASCA (TEPCO)

We recently recomputed again the discussed experiment with the last version of IVA. The total mean error is 5.07%, see Fig. 16.15.13. Having in mind that the reported experimental uncertainty is 3% the prediction without any turbulent mixing can be considered as very good. Recently, comparison of the prediction of this data set with several computer codes was presented by *Neykov et al. (2006)* with the result given in Table 16.15.13 for which the standard deviation computed as follows is used

$$\sigma = \sqrt{\frac{\sum_{k=1}^K (\alpha_{\text{exp},k} - \alpha_{\text{pred},k})^2}{(K-1)}}.$$

Conclusions:

- The cross-section-averaged void fractions predicted at the exit of the bundles with IVA depends on the used modeling approach for the subcooled boiling available in IVA: a) *Saha and Zuber* (1974) correlation for the initiation of the subcooled boiling and the *Levy* (1967) asymptotic model for the splitting of the heat into convection evaporation and recondensation; b) *Hughes et al.* (1981) approach for the initiation of the subcooled boiling and for the splitting of the heat into convection evaporation and recondensation.
- By using the model a) the predicted data agree excellent at high power (1%), agree well at averaged power (5.9%) and are up to 14.2% lower at 5% of the nominal power.
- By using the model b) the predicted data agree excellent at high power (2.3%) and well at averaged power (2.9%) and at 5% of the nominal power (5.34%). Obviously model b) is superior at low void fractions.
- The local void fractions at the exit of the bundle on a 9×9 subchannel basis are predicted with an error of 5.62% using model a) and of 5.15% using model b). The local accuracy increases with the increasing power. Again model b) contributes to better performance for all void fractions.
- As already reported in *Kolev* (2005b, 2005c) comparing the cases with smaller (10×10×24) and larger (18×18×24) resolution we obtain “better” agreement with the data for the gross resolution. This is an indication that the void mixing computed based only on the transport equation is not enough to describe appropriately this process. This is confirmed by this study too. In all cases the “void diffusion” from regions with higher void to regions with lower void is underestimated.
- Without appropriate turbulence modeling the accuracy of this method regarding predicting the local void fraction can not be increased.
- Fine resolution is required in the future and will be accomplished with appropriate constitutive relationships specially developed for fine resolution.

16.15.2.1.1.4 Comparison with *Utsuno et al.* (2004) analyses

Ursuno et al. (2004) reported analyses of the steady-state void data of NUPEC. The authors used the code TCAPE. The TCAPE code uses the drift-flux formulation of all axial equations. The crossflow is modeled by algebraic models that do not satisfy lateral momentum conservation. The simplified energy-conservation equation used is appropriate for slow transients only. In the case of

the film flow an additional one-dimensional mass balance is introduced using entrainment and deposition sources. Therefore, convective transport of film and droplets across the subchannel is not permitted in the model. The TCAPE code does not make use of dynamic fragmentation and coalescence. Even with this simplification the code predicts “reasonably” a gross scale void distribution by using flow-channel centered subchannels discretization. As already mentioned, the apparently demonstrated good void intermixing is due to numerical diffusion and not due to appropriate turbulence description.

16.15.2.1.1.5 3D versus 1D analysis

Consider the moisture analyses of a complete boiling water reactor as reported by *Kolev* (2002b) for the geometry given in Fig. 16.15.14. The question whether the core has to be simulated in a pin-by-pin or bundle-by-bundle approach is important because the pin-by-pin resolution is still expensive. To illustrate that bundle-by-bundles analysis is accurate enough for the moisture optimization analyses we simulate one of the NUPEC experiments as presented in Fig. 16.15.15 by using the characteristic thermohydraulic parameters for the overall rod bundle and compare the results with the 3D representation. As seen from Fig. 16.15.15 the cross-section-averaged void profiles are almost not distinguishable.

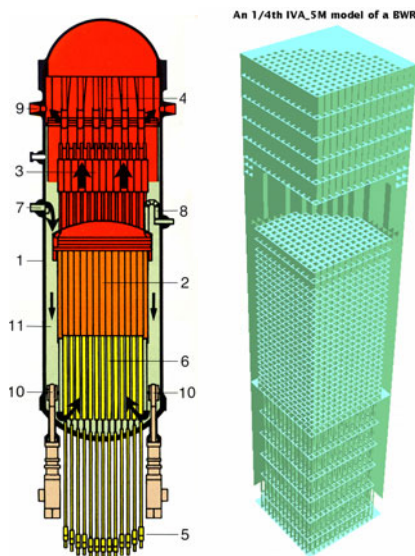


Fig. 16.15.14 a) Typical boiling water reactor: 1 reactor pressure vessel; 2 reactor core; 3 steam-water separators (cyclones); 4 steam dryer; 5 control rod drives; 6 control assemblies; 7 feed water inlet nozzles; 8 core spray line; 9 main steam outlet nozzle; 10 forced circulation pumps; 11 annular down comer. b) IVA_5M 1/4th geometry model of the control rod space, core, upper plenum and stand pipes.

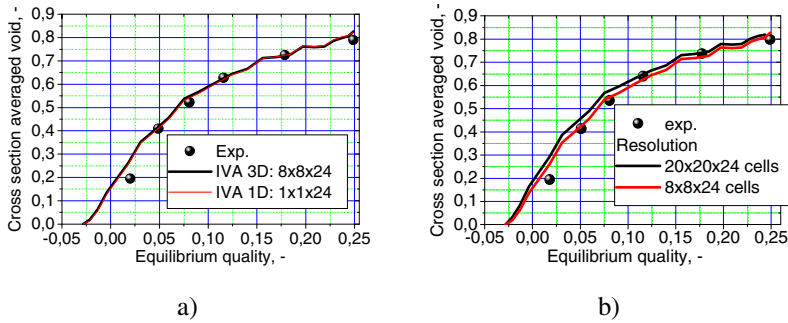


Fig. 16.15.15 NUPEC experiment with mass flow rate $1562 \text{ kg}/(\text{m}^2 \text{ s})$: Comparison between cross-section-averaged void fraction predictions using a) 3D (rod-centered channels) and 1D analysis; b) 3D rod centered channels $8 \times 8 \times 24$ cells and 3D separate periphery layers, one rod belongs to 4 cells, $20 \times 20 \times 24$ cells

Increasing the resolution to 20×20 horizontal cells gives slightly higher cross-section-averaged void fraction, as demonstrated in Fig. 16.15.15b. This allows the conclusion: For analyses of the moisture in BWRs the core representation in a bundle-by-bundle approach provide the appropriate large-scale three-dimensional void distributions at the exit of the core.

For approximating the bundle as a single channel for moisture analysis the averaged pressure drop coefficient for the bundle can be computed using the method proposed and verified on large data base by *Rehme* (1973, 1971, 1972). For the laminar regime the friction coefficient is $\lambda_{fr} \text{ Re} = Rm$, where the *Rehme's* number (*Rehme*, 1973) is $Rm = 63.172$. For the turbulent regime the friction factor in accordance with *Rehme* (1972) is $\sqrt{8/\lambda_{fr}} = 2.55 \ln(\text{Re} \sqrt{8/\lambda_{fr}}) - 0.255$. Here the bundle *Reynolds* number $\text{Re} = \dot{m} D_h / (F \eta)$ is based on the total mass flow, total flow cross-section and on the effective bundle hydraulic diameter.

16.15.2.1.1.6 The oscillating steady-state for low mass fluxes

For large mass flows through the boiling bundle channels the steady state is nonoscillating. For low mass flows, however, the steady state is oscillating. As reported by *Yagi et al.* (1992) and *Inoue et al.* (1995c), oscillating void measurements are smoothed so that the data points are not only cross-section averages but also time averages. An example for a stable but oscillating steady-state solution is given in Figs. 16.15.16a and 16.16.16b for the NUPEC experiment with mass flow rate $284 \text{ kg}/(\text{m}^2 \text{ s})$. Figure 16.15.17 presents the cross-section-averaged void fractions at different times within one cycle of oscillation. As we see they oscillate around the reported time-averaged values. This is an important advantage of looking for steady-state solutions as asymptotic solutions of transients. Important oscillating characteristics can be then recognized,

something that is impossible by solving only the steady-state part of the systems of PDEs.

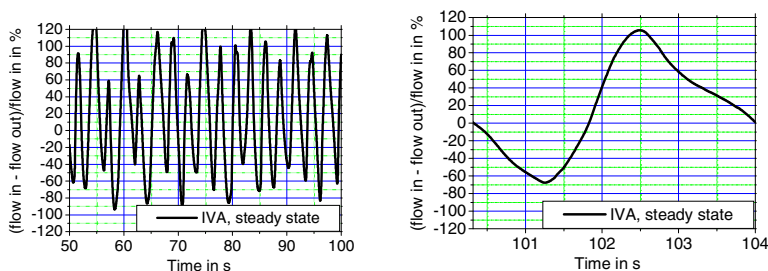


Fig. 16.15.16 Oscillating steady state for 284 kg/(m² s) case: a) long-term steady-state oscillations; b) one oscillation cycle

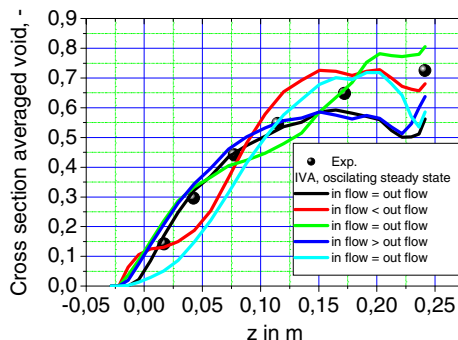


Fig. 16.15.17 NUPEC experiment with mass flow rate 284 kg/(m² s). Void fraction as a function of the height. Parameter – time within one oscillation period

16.15.2.2 The SIEMENS void data for the ATRIUM 10 fuel bundle

A set of proprietary data for void fraction in ATRIUM 10XP bundles at 4 peaking patterns was obtained by *Spierling* (2002) at the Karlstein Thermal Hydraulic Loop in AREVA NP, Germany. At about 70 bar 12 experiments with 2.2 m/s inlet velocity, 58 kJ/kg subcooling and axial choked cosine power profile chordal void profiles 3.24 m from the inlet are collected and then averaged over the cross-section *except* the water channel. 4 of the experiments are at low power and 8 at high power. All the 12 test sets are computed using IVA computer code. 10×10×37 3D-discretization (10×10 fuel centered subchannels with 37 axial cells) is applied. The structure of the errors is documented in Table 16.15.14. The

maximum deviation of the predicted from the measured void was less than 8.7 and 7.55% for set a) and b), respectively. The averaged deviation is about 6.12 and 4.19% for set a) and b), respectively. Obviously, again set b) gives better performance.

In summary, the void prediction for AREVA NP bundle test is with uncertainty of 4.19% is even better the prediction of the previously reported NUPEC data.

Table 16.15.14 Measured and predicted cross-section-averaged void fractions at 3.24m from the inlet

Exp no.	Lateral peaking pattern	Void exp.	Void IVA, a)*	Deviation in %	Void IVA, b)*	Deviation in %
257	STS-66.1	0.519	0.524	0.96	0.482	-7.13
258		0.813	0.842	3.57	0.827	1.72
259		0.819	0.843	2.93	0.828	1.10
270	STS-68.3	0.468	0.519	10.2	0.476	1.71
271		0.784	0.840	7.14	0.827	5.48
272		0.779	0.840	7.83	0.828	6.29
328	STS-52.1	0.543	0.499	-8.10	0.502	-7.55
332		0.804	0.816	1.49	0.798	-0.75
339		0.839	0.861	2.62	0.843	0.48
261	STS-68.5	0.479	0.529	10.6	0.500	4.38
262		0.774	0.839	8.4	0.826	6.72
263		0.771	0.838	8.7	0.825	7.00

* Models for subcooled boiling: a) *Saha and Zuber* (1974) correlation for the initiation of the subcooled boiling and the *Levy* (1967) asymptotic model for the splitting of the heat into convection evaporation and recondensation; b) *Hughes et al.* approach (1981) for the initiation of the subcooled boiling and for the splitting of the heat into convection evaporation and recondensation.

16.15.2.3 The FRIGG experiment

The FRIGG experiments are reported by *Nylund et al.* (1968, 1970). The geometry given in Fig. 16.15.18b is defined as follows: 36 rods with 13.8 mm diameter, heated, 1 central rod with 20 mm diameter, unheated. The heated length of the rods is 4.375 m. The rods are placed within a cylinder with internal diameter 159.5 mm and positioned in three circles with 21.6, 41.7, and 62.2 mm radius, respectively. The circles contain 6, 12 and 18 rods, respectively, at equal arc distance from axis to axis along the circle. The bundle is 1/6-symmetric so that 1/6 of the circular cross-section is simulated. 8 spacers keep the rods parallel to each other. The spacers receive an irreversible pressure drop coefficient equal to 0.6 based on the bundle velocity. Discretization used for the IVA computation: The flow in the bundle is considered as 3D axis symmetric flow in cylindrical coordinates. 1/6 segment is simulated with three radial annuli defined by the radii 0.01, 0.03165, 0.05195 and 0.07975 m, respectively. The height is discretized

using 36 cells. 8 spacers are modeled by a local irreversible pressure-loss coefficient.

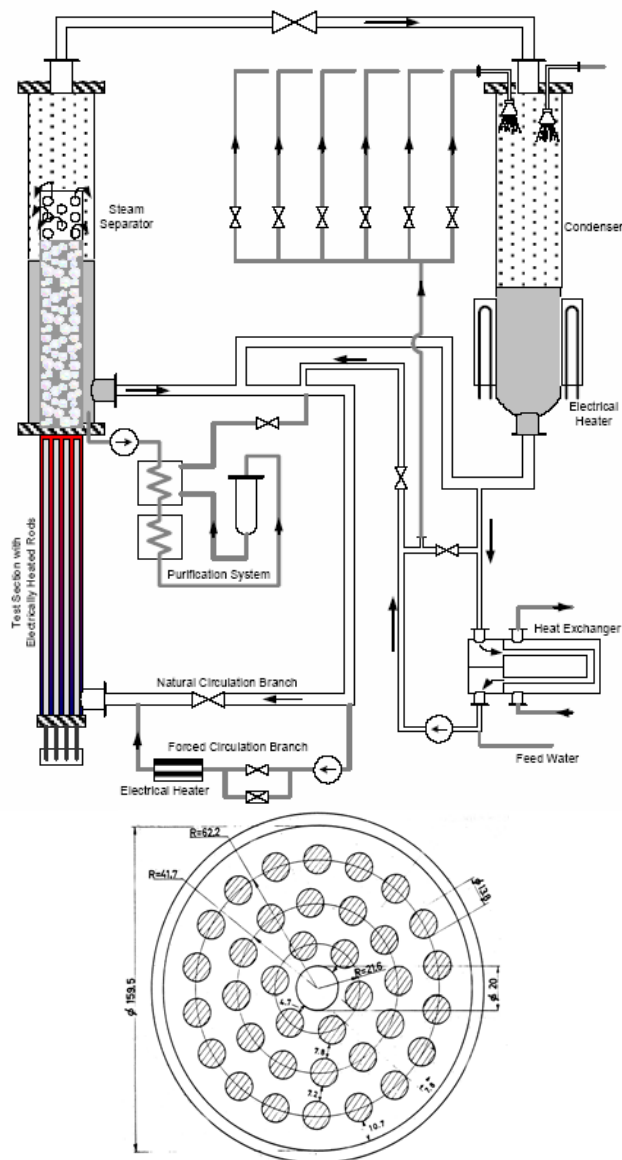


Fig. 16.15.18 a) Layout of the FRIGG loop; b) Cross-section of the FRIGG bundle

16.15.2.3.1 Uniform power distribution

We proceed with simulation of 5 experiments for which boundary conditions are defined in Table 16.15.15. The lateral and axial power distribution is uniform. The results are presented in Figs. 16.15.19 and 16.15.20.

Table 16.15.15 Boundary conditions, uniform power release FRIGG Nylund et al. (1968)

No.	p in MPa	Power in MW	G in kg/(m ² s)	Subc. in K
313009	5	2.98	1107	4.4
313016	4.96	2.91	1208	19.3
313018	4.97	4.39	1124	3.7
313024	4.97	1.475	858	4.2

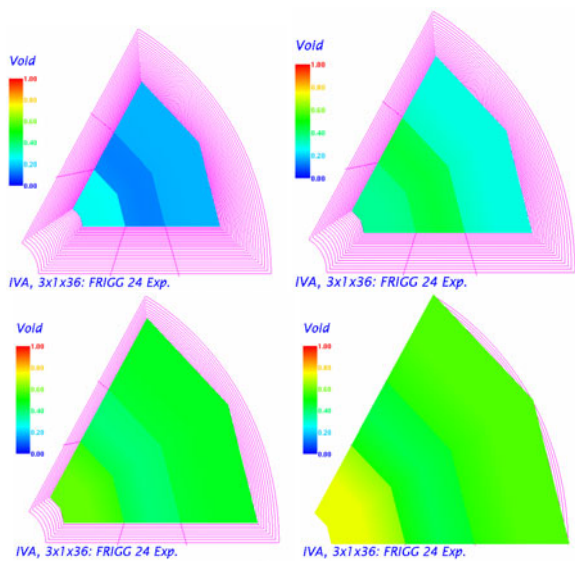


Fig. 16.15.19 1/6 of the FRIGG test section simulated by IVA (3×1×26cells). Void fraction at different levels (1, 2, 3, 4.3142 m) as a function of the radius

As for the NUPECC data the effect of the nonuniformity of the flow profiles inside the subchannels is manifested in effectively lower drag between the liquid and the vapor. The comparison at the predictions with the data using the reduced effective drag as in the previous section is favorable.

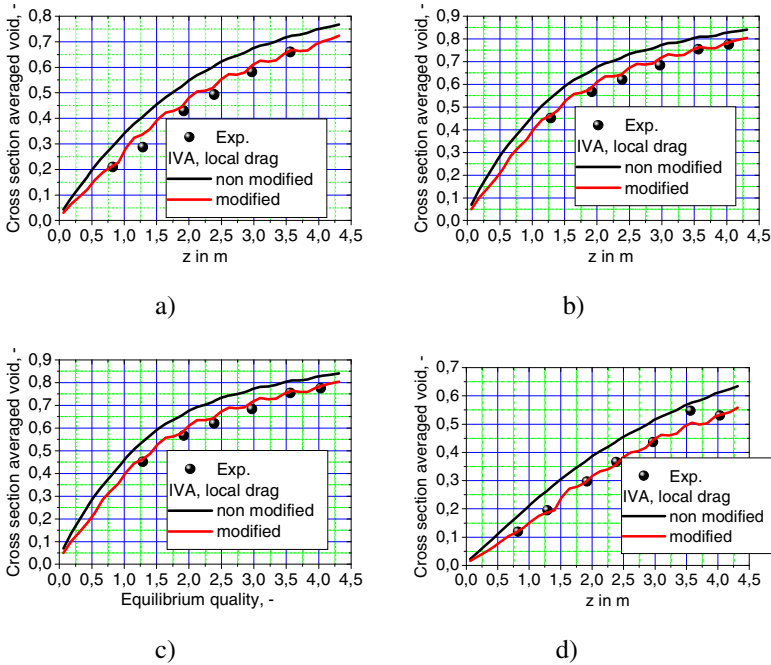


Fig. 16.15.20 FRIGG experiments: a) 3130009; b) 3130016; c) 3130018; d) 3130024: Void fraction as a function of the height. Parameter: local interfacial drag

16.15.2.3.2 Nonlinear axial power profile

We continue our analysis with simulation of other 4 experiments with boundary conditions defined in Table 16.15.16. The lateral power distribution is uniform. The smooth symmetric axial power distribution is defined by Table 16.15.17. We approximate the axial profile with 3% error with the Gauss function

$$f_z = 0.62914 + 1.74672 / \left\{ 2.47575 \sqrt{\pi/2} \exp \left[\frac{2(z - 2.182)^2}{2.47575^2} \right] \right\}.$$

After digitizing the profile a renormalization was necessary to guarantee the energy conservation.

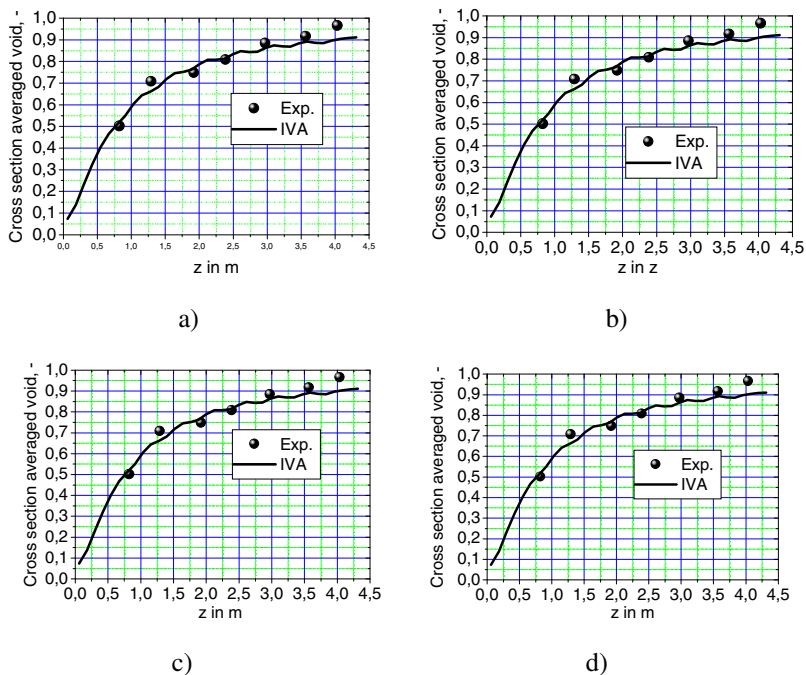


Fig. 16.15.21 FRIGG experiments: a) 1; b) 10; c) 13; d) 19: Void fraction as a function of the height. The modified drag coefficient for gas in flow is used

Table 16.15.16 Boundary conditions, nonuniform power release, FRIGG *Nylund et al. (1970)*

No.	p in MPa	Power in MW	G in $\text{kg}/(\text{m}^2 \text{ s})$	Subc. in K
1	4.88	1.66	703	1.5
10	4.87	5.55	645	2
13	4.99	5.55	688	22.89
19	5.03	4.52	681	26.11

Table 16.15.17 Axial power distribution

z in m	Ax. distr.
0.032	0.76
0.462	0.83
0.892	0.96
1.322	1.08
1.752	1.16
2.182	1.18
2.612	1.16
3.042	1.08
3.472	0.96
3.902	0.83
4.332	0.76

The results are presented in Figs. 16.15.21a–d. Again we see that the predictions coincide well with the measurements. Although the comparison with the data is favorable, a physically based model for the mechanical interaction for subchannel analyses is needed.

16.15.2.4 The THTF experiments: high pressure and low mass flow

The experiments performed in the Thermal Hydraulic Test Facility (THTF) by *Anklama and Miller (1982)* are characterized with such a low mass flows that in combination with appropriate low heat fluxes results in steady states in which the bundle is partially uncovered. The two-phase mixture level given in Table 16.15.18 is the essential parameter measured in these experiments. This is a very challenging problem for transient mathematical analysis because it possesses an oscillating steady state. The 8×8 rod bundle with quadratic arrangement is mounted in a 0.104×0.104 m shroud as shown in Fig. 16.15.23. The heated length was 3.66 m, the rod diameter 0.095 m and the axis to axis distance is 0.0127 m. 4 unheated rods with diameter 0.0102 m as indicated in Fig. 16.15.23 are used. The boundary conditions for the experiments analyzed are given in Table 16.15.18. The void fraction was intended to be measured by pressure difference along a given number of segments. This method works for real steady-state systems but is questionable for oscillating steady-state systems because the acceleration pressure drop components are not taken into account.

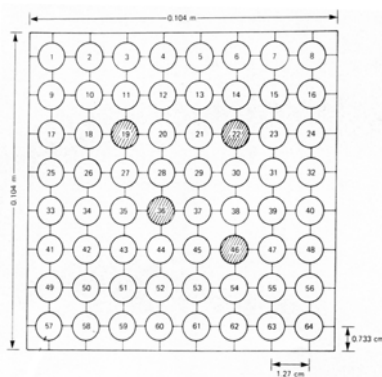
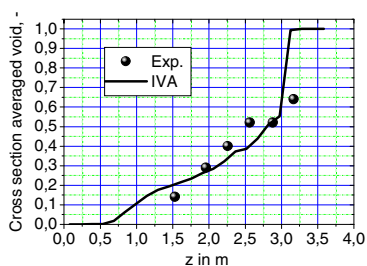
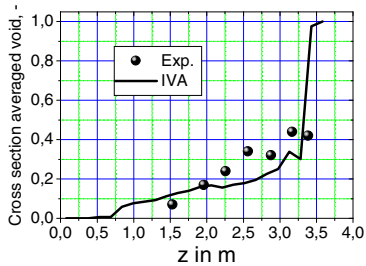


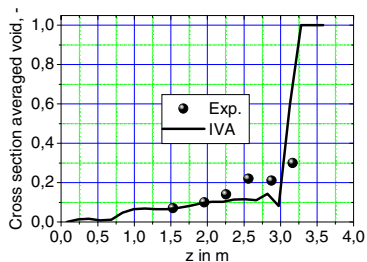
Fig. 16.15.22 Thermal Hydraulic Test Facility rod bundle cross-section, *Anklama and Miller (1982)*



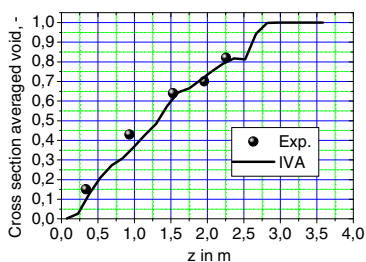
3.09.10DD



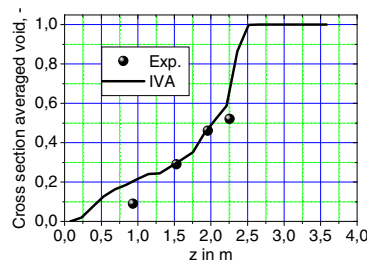
3.09.10EE



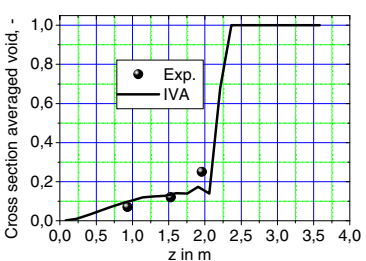
3.09.10FF



3.09.10I



3.09.10J



3.09.10K

Fig. 16.15.23 Snapshots of oscillating cross-section-averaged void fraction profiles in a bundle with partial uncovering of the bundle

Comparing the computed with the measured two-phase mixture level presented on Fig. 16.15.23 we see an acceptable agreement. This demonstrates also the IVA constitutive set to crossvariety of flow and heat-transfer regimes with their peculiarities.

Table 16.15.18 Boundary conditions, uniform power release, THTF *Anklama and Miller* (1982)

No.	p in MPa	Power in MW	G in kg/(m ² s)	Subc. in K	Mixture level in m
3.09.10DD	8.1	0.28329	19.7	129.7	3.23 ± 0.04
3.09.10EE	7.7	0.14055	10.9	102.4	3.47 ± 0.03
3.09.10FF	7.5	0.07027	4.8	116.13	3.23 ± 0.04
3.09.10I	4.5	0.48753	29.3	56	2.62 ± 0.04
3.09.10J	4.2	0.23498	12.9	45.9	2.47 ± 0.4
3.09.10K	4.0	0.7027	3.1	60.1	2.13 ± 0.3

16.15.2.5 Conclusions

Without special void-intermixing models the prediction of the void fraction of boiling flows in bundles with IVA computer code is possible with a square mean error of about 5%. The measurement error for such experiments is 3%. Future improvements are probably possible by introducing turbulence in the multiphase flow based on well-verified simulation techniques.

The production of turbulence due to increased skin friction is much smaller than the irreversible form-induced turbulence. However, the dissipation due to skin friction is substantial. The decay is well within the 30 hydraulic diameters as expected.

The recommended approach for large-scale analyses is to combine both effects: Changing of the hydraulic diameter and the cross-section over the grid length and setting the irreversible friction coefficient at the end of the grid reduced by the additional grid skin friction component. In this way the effect of the increased velocity on droplet fragmentation can be taken into account.

In general, using correlation for the interfacial drag coefficients derived from averaged pipe flows predicts strong cohesion between the phases. This was confirmed by all analysts using separated momentum equations worldwide. The ad hoc introduced reduction here has to be further investigated in the future.

The method proposed by *Hughes et al.* (1981) is recommended for description of the initiation of nucleate boiling in subcooled liquid and for the modeling of the splitting of the heat flux coming from the wall.

The so-called subchannel analysis or gross discretization analysis is discretization dependent. Therefore, fine-resolution analysis is required in the future to avoid this deficiency. For this purpose appropriate constitutive relationships have to be specially developed.

16.15.3 Transient boiling

16.15.3.1 The NUPEC transients in a channel simulating one subchannel of a PWR fuel assembly

Hori et al. (1994, 1995) reported a series of transient experiments on a specially designed 1.5-m long heated channel – Fig. 16.15.24a. The channel, Fig. 2 in *Hori et al.* (1995), simulates a single internal subchannel of a PWR fuel assembly. The initial conditions for the transients are defined in Table 16.15.19. Only one of the four parameters in Table 16.19.19 is varied in each experiment as shown in the left-hand side of Figs. 16.15.25–16.15.28. The others are kept constant.

Table 16.15.19 Initial conditions for the four transients, taken from Table 1 of *Hori et al.* (1994)

No.	Power in kW	Inlet tempe- rature in °C	Pressure in MPa	Mass flow rate in $\times 10^6$ kg/(m ² h)
Case 1	55	315	15.5	12
Case 2	55	315	15.5	12
Case 3	55	315	15.5	12
Case 4	75	305	15.5	12

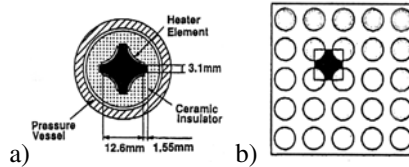


Fig. 16.15.24 a) Cross-section of the channel simulating one subchannel of a PWR fuel assembly; b) 5×5 experimental fuel assembly

On the right of the corresponding figures the computed and the measured mixture densities are compared as they evolve during the transients. The set of constitutive relations used is: high-fidelity EOS, models for subcooled boiling: *Hughes et al.* approach (1981) for the initiation of the subcooled boiling and for the splitting of the heat into convection evaporation and recondensation. Note that only the temporal part of the virtual mass force is used in this code version. Changing the virtual mass coefficient from $\frac{1}{2}$ for bubbly flow to the *Zuber's* solution does not change this picture. The figures indicate that probably the spatial part is also important for transients like these.

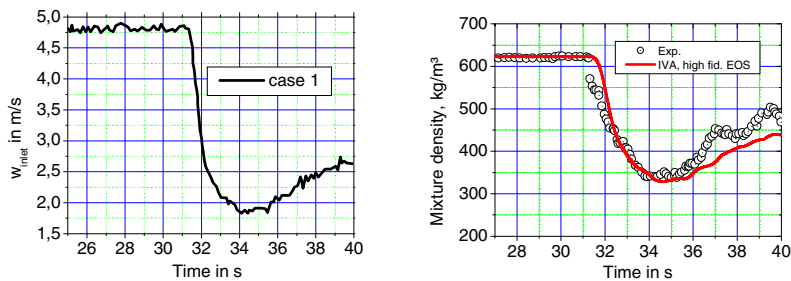


Fig. 16.5.25 Case 1: a) Velocity at the channel inlet as a function of time; Measured and computed mixture density at the exit of the channel as a function of time.

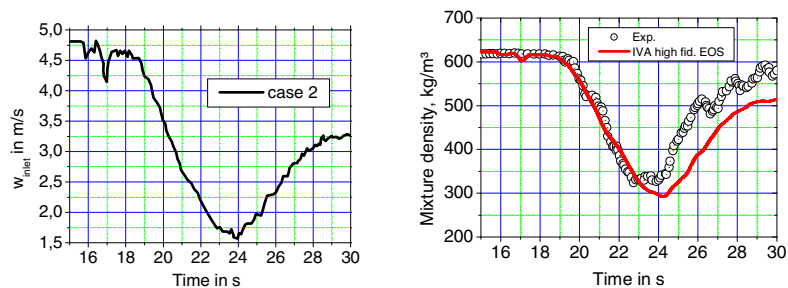


Fig. 16.15.26 Case 2: a) Velocity at the channel inlet as a function of time; Measured and computed mixture density at the exit of the channel as a function of time.

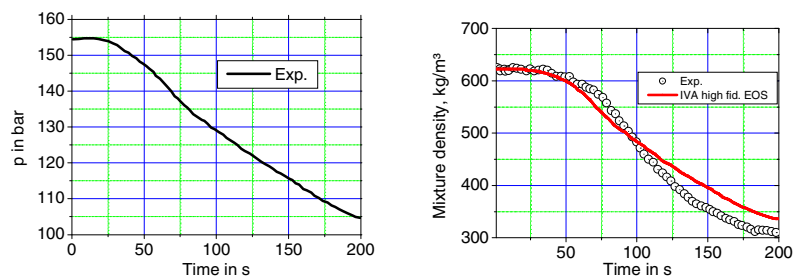


Fig. 16.15.27 Case 3: a) Averaged pressure as a function of time; Measured and computed mixture density at the exit of the channel as a function of time.

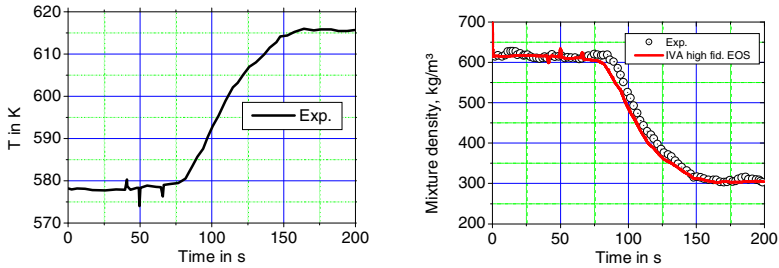


Fig. 16.15.28 Case 4: a) Inlet water temperature as a function of time; Measured and computed mixture density at the exit of the channel as a function of time.

The pressure reduction in Fig. 16.15.27 causes evaporation and decrease of the mixture density. In this case we have some uncertainties because we actually need the pressure histories at the both ends. Figure 16.15.27b gives the impression that the experimental pressure and density curves are not synchronized. The impression gained from the inlet-temperature-transient presented in Fig. 16.15.28b is similar. In any case, the agreement can be considered as good having in mind that we do not resolve the fine structure of the two-phase flow in the channel. The modification of the drag coefficients that has brought the improvement by the simulation of the steady-state experiments in rod bundles has brought also an improvement for prediction of the transient processes. In any case, we see again that the effective gas-liquid drag coefficients for rod-bundle-subchannel analyses are smaller than those correlated for averaged parameters on pipe geometry.

16.15.3.2 The NUPEC transients in PWR 5x5 fuel assembly

16.15.3.2.1 The IVA prediction

Hori et al. (1996, 1993) and Akiyama et al. (1995, 2005) reported series of transient experiments on a 3.66-m long heated 5×5 rod bundle, Fig. 16.15.24b, simulating a Japanese 17×17 PWR fuel assembly. The initial conditions for the transients are defined in Table 16.15.20. The axial power distribution is uniform. As reported by Hori et al. (1996) p. 802, the peripheral rods have 85% of the power of the internal rods. Averaged hydraulic characteristics of the bundle: for the laminar regime the friction coefficient is $\lambda_{fr} \text{ Re} = 61$ in accordance with Rehme's (1973, 1971), for the turbulent regime the friction factor in accordance with Rehme (1972) is $\sqrt{8/\lambda_{fr}} = 2.5 \ln(\text{Re} \sqrt{8/\lambda_{fr}}) - 0.17$. We selected from the 4 experiments only two because the variable boundary conditions are specified only for them, Akiyama et al. (1995) Fig. 8, and Fig. 9. One of the four parameters in

Table 16.15.20 is varied in every experiment, as shown in the left-hand side of the figures 16.15.29 and 16.15.30. The others are kept constant.

Table 16.15.20 Initial conditions for the NUPEC 5x5 bundle transients, taken from Appendix 1 of *Hori et al. (1996)*, p. 810.

Variable	Power in KW	Inlet temperature in °C	Pressure in MPa	Mass flow rate in $\times 10^6$ kg/(m ² h)
power	2250	300	15.5	12
flow rate	2250	300	15.5	12

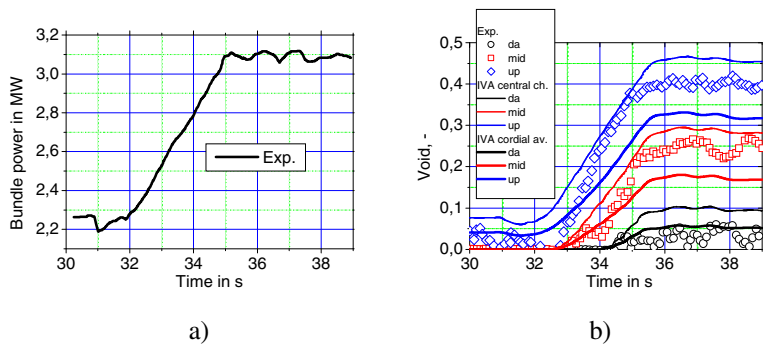


Fig. 16.15.29 a) Bundle power as a function of time; b) NUPEC measurements and IVA results (central subchannel and central chordial average) for the void fraction at three different elevations as a function of time. Initial conditions: $T_{in} = 300$ °C, $p = 155$ bar, $w_{in} = 4.588$ m/s, bundle power 2250 kW

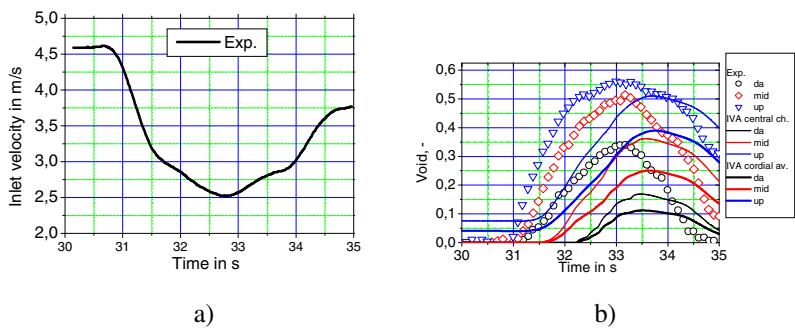


Fig. 16.15.30 a) Inlet velocity as a function of time; b) NUPEC measurements and IVA results (central subchannel and central chordial average) for the void fraction at three different elevations as a function of time. Initial conditions: $T_{in} = 300$ °C, $p = 155$ bar, $w_{in} = 4.588$ m/s, bundle power 2250 kW

Measured are the void fractions at three different geodetic levels. The distance between the levels is given by *Hori et al. (1996)* p. 811. The position of the first level is approximately taken from Fig. 1 of *Akiyama et al. (2005)*. The type of void averaging presented on the figures is confusing. In *Hori et al. (1993)* p. 74 the authors presented for the pressure transient in Fig. 12 a line-averaged void fraction, whereas in *Akiyama et al. (1995)* for the power- and mass-flow transients the authors compared their data with predictions of the void in the central channel of the bundle. This nonprecise information forced us to put on Figs. 16.15.27b and 16.15.28b both the central channel void and the line averaged void along the x -axis. As expected the central channel void is larger than the averaged void along the beam length.

Regarding the power transient: The experimental data for the upper two levels are between the predicted both void fractions. At the lowest measured position the void is overpredicted, indicating probably that the subcooled boiling model needs more attention. The gradient of the change reflects the experimental observations.

Regarding the flow transients: There is considerable discrepancy between prediction and measurements. The moment of the intensive void formation is predicted later, the inclination of the void increase is predicted to be smaller, saying that the heat partitioning between evaporation and condensation is different. The predicted maxima of the curves are lower than the measured.

16.15.3.2.2 Comparison with Aounallah et al. (1999), Macian et al. (2000) and Wang et al. (2005) analyses

Analyses with the two-fluid computer code VIPRE-02 (*Kelly et al. 1992*) of the openly published NUPEC data that are used also in this study are already reported by *Aounallah and Coddington (1999)* and by *Macian et al. (2000)*. VIPRE-02 is a two-fluid computer code using six equations for describing predominant axial flow. The momentum equations in the other two lateral directions are simplified for a normal velocity component from or to the neighboring channels using 1 instead of 9 nonhomogeneous convection terms in a transformed coordinate system. IVA possesses a three-fluid model with conservation equations that do not neglect any terms. Regarding selection of the drag coefficient correlations and boiling mechanisms for this particular class of processes as long as two of the fluids in IVA are addressed, the codes are similar except for the use of dynamic fragmentation and coalescence in IVA but not in VIPRE-02. The observation made by *Aounallah and Coddington (1999)* and by *Macian et al. (2000)* are confirmed by our study too.

In general, effectively less drag between void and liquid is observed in the experiments than in the separated-momentum equation predictions with correlation gained on flows with other geometry.

Macian et al. interpret the underprediction of the void as a possible deficiency of the subcooled boiling instead of the effectively lower drag. This difference in the interpretation can be clarified in the future only if fine-scale analyses are done.

The discrepancy with the data in Fig. 16.15.30 is also observed by *Macian et al.* The reasons remain to be clarified. *Wang et al.* (2005) performed a comparison between VIPRE two-fluid code and 6 FRIGG experiments comparing also void fraction in lateral bundle zones. The authors come to the conclusion that additional modeling of the radial redistribution is required to better predict void in neighboring subchannels with quite different power load. Over prediction of the axial voids in the low-power regions is also reported, which tells us that the subcooled boiling model in VIPRE needs further sophistication.

16.15.3.2.3 Comparison with Hori et al. (1994)

Hori et al. (1994) reported that the comparison with their transient measurements can be better reproduced in the acceleration phase by homogeneous models and in the deceleration phase by drift-flux models. This is in line with our observation here and with the observation made by *Aounallah and Coddington* (1999) and by *Macian et al.* (2000).

16.15.3.2.4 Conclusion

In general, averaged measurements over a beam line have to be compared with averages of rows of fine mesh cells extracted from computational results. The larger the size of the cells the less informative is the comparison.

16.15.4 Steady-state critical heat flux

Nucleate and flow boiling is a very good cooling mechanism. Increasing heat fluxes in the wall may lead to heat-transfer regimes that have considerably lower heat transfer. In such cases the frequency of the bubble production and their bubble departure size allow them to touch each other. Then, a film forms, reducing the heat-transfer coefficient. This regime is called departure from nucleate boiling and designated by DNB. Another important case is the boiling of a flowing film which is a good heat-transfer mechanism. If the film dries out, the heat transfer is controlled by the steam flow, which again makes the cooling much worse. This regime is called dry out and designated by DO. Both mechanisms may happen in technical facilities with the first one causing a strong temperature jump at the wall the second. If they last long enough both regimes can destroy the facility.

16.15.4.1 Initial OD guess

Problem: Check whether it is possible to use the 2005 look-up table primary designed for heated pipes also for heated rod bundles.

Solution: I exploit deliberately a set of simplifying assumptions usually used in the 1960s:

1. Fictive subchannels corresponding to the number of rods are so defined as to be equivalent in geometry.
2. Equal mass flow rate to each subchannel.
3. The critical heat flux occurs at the exit of the hot channel as a function of the exit parameters. The phenomenon is similar to pipe flow. Therefore, the *Groeneveld's* look-up table is expected to give the right dependence on mass flow rate, quality and subcooling.
4. Uniform boundary conditions for all channels.
5. Grid turbulization as well as the axial power distribution is not specifically treated.

The procedure I use is: Unless $\left| \frac{q''_{crit,i}(z_{max}) - q''_i(z_{max})}{q''_{crit,i}(z_{max})} \right| < \varepsilon$ increase q with a Δq

starting with q_0 . Here the power of the hot channel is $q_i = f_{lat,i} q / n_{rods}$, where, as per the definition, the bundles power is the sum of the subchannel powers

$q = \sum_{i=1}^{n_{rods}} q_i$ and the lateral distribution factor obeys $\frac{1}{n_{rods}} \sum_{i=1}^{n_{rods}} f_{lat,i} = 1$. The exit

equilibrium mass flow quality is $X_{1,i} = \frac{1}{\Delta h} \left(\frac{q_i}{\dot{m}_i} - \Delta h_{sub} \right) = \frac{1}{\Delta h} \left(f_{lat,i} \frac{q}{\dot{m}} - \Delta h_{sub} \right)$.

Here, by virtue of assumption 2 I use $\dot{m}/\dot{m}_i = n_{rods}$. The local heat flux at the exit

of the hot channel i , $q''_i(z_{max}) = f_{lat,i} \frac{q/n_{rods}}{\pi D_{rod} L_{rod}}$, is compared with the local

critical heat flux. The critical heat flux at the exit of channel i is defined by the 2005 look-up table $q''_{crit,i}(z_{max}) = f(p, G, X_{1,i}, D_{hyd})$. Dividing this value by the lateral hot channel factor and recomputing the averaged flux into bundle power we

obtain the final result $q = \frac{q''_{crit,i}(z_{max})}{f_{lat,i}} \pi D_{rod} L_{rod} n_{rods}$. Note that the last expression

is based on the intuitive assumption that this value may represent the averaged heat flux in the hot channel. It is only a *hypothesis*. It is very interesting to compare the prediction of this “primitive” approach with experimental data and to see how it works.

8x8 NUPEC BWR bundle tests: First I simulate three data sets for experiments with the 8x8 NUPEC BWR bundle tests (Fig. 16.15.31) as proposed in the international benchmark by *Neykov et al. (2005)*. The *first* and the *second* tests are performed with the same axial power distribution but with different lateral power-peaking pattern. They serve for analysis of the influence of the lateral power distribution. The *first* and the *third* tests are performed with the same lateral

power-peaking pattern but with different axial power distribution. They serve for analysis of the influence of the axial power distribution.

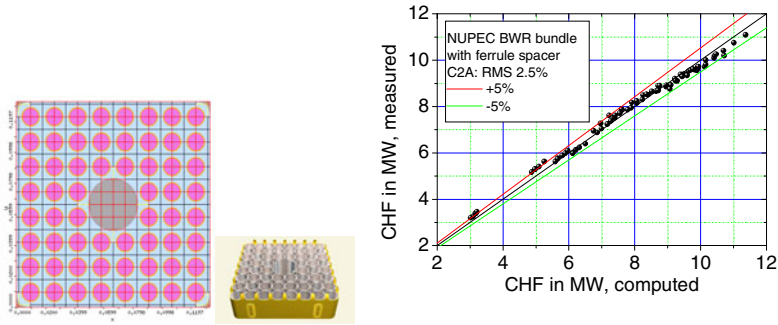


Fig. 16.15.31 Geometry of the 8x8 NUPEC CHF bundle tests: a) cross-section; b) ferrule spacer; c) Measured versus computed critical bundle power for *cosine* profile with $f_{z,\max} = 1.4$ and lateral peaking pattern characterized by $f_{xy} = 0.89$ to 1.3. Data by NUPEC: $p = 5.48$ to 8.67 MPa, $\Delta h_{2,\text{sub}} = 22.61$ to 137.26 kJ/kg, $\dot{m} = 9.98$ to 65.52 t/h. C2A tests, 79 points

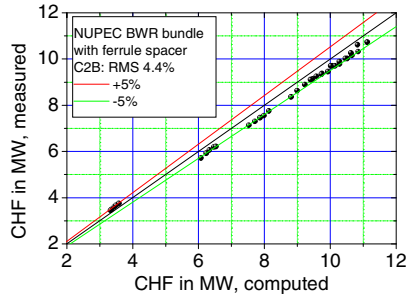


Fig. 16.15.32 Measured versus computed critical bundle power for *cosine* profile with $f_{z,\max} = 1.4$ and lateral peaking pattern characterized by $f_{xy} = 0.99$ to 1.18. Data by NUPEC: $p = 7.14$ to 7.20 MPa, $\Delta h_{2,\text{sub}} = 21.06$ to 128.57 kJ/kg, $\dot{m} = 9.93$ to 64.85 t/h. C2B test, 36 points

The measured versus the predicted bundle power is presented in Figs. 16.15.31c, 16.15.32 and 16.15.33.

Comparing Figs. 16.15.31c and 16.15.2 we see that for flatter lateral profiles this method slightly systematically underpredicts the measurements.

Comparing Figs. 16.15.32 and 16.15.33 we see that for the two different axial power profiles this method predicts similar measurements.

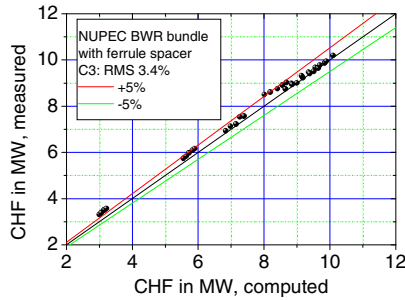


Fig. 16.15.33 Measured versus computed critical bundle power for *inlet peak* profile with $f_{z,\max} = 1.4$ and lateral peaking pattern characterized by $f_{xy} = 0.89$ to 1.3. Data by NUPEC: $p = 7.10$ to 7.19 MPa, $\Delta h_{2,\text{sub}} = 21.7$ to 125.74 kJ/kg, $\dot{m} = 9.93$ to 65.02 t/h. C3 test, 36 points

Having in mind the 2005 look-up table possesses mean error of 7.1% the above predictions with mean error of 2.5, 4.4 and 3.4% can hardly be made better.

AREVA ATRIUM10 BWR tests: Figures 16.15.34 and 16.15.35 present the measured versus the predicted bundle power for a specific tests for AREVA BWR bundles ATRIUM 10.

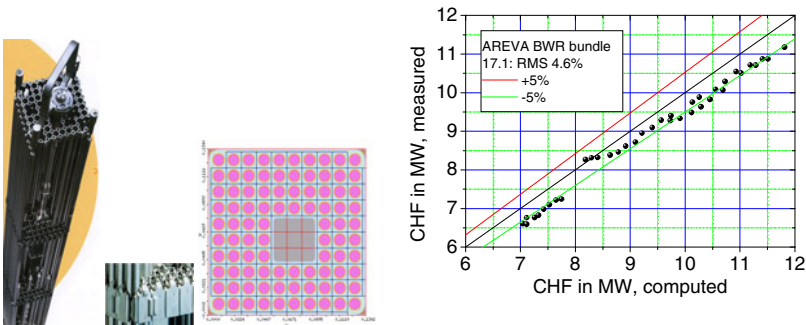


Fig. 16.15.34 a) BWR ATRIUMTM 10 bundle with ULTRAFLOWTM spacer; b) Measured versus computed critical bundle power for *cosine* profile with $f_{z,\max} = 1.4$ and lateral peaking pattern characterized by $f_{xy} = 0.751$ to 1.255: mean error 4.6%, slight systematic under prediction. Data by Fleiss et al. (1992): $p = 69$ bar, $\Delta h_{2,\text{sub}} = 23$ to 184 kJ/kg, $\dot{m} = 6.3$ to 18.90 kg/s. 40 points

There are slight differences in the geometry. For both cases we see mean errors of 4.6 and 3.95%, respectively, which again lie inside the accuracy of the 2005 look-up table. Again, prediction with better accuracy can hardly be achieved.

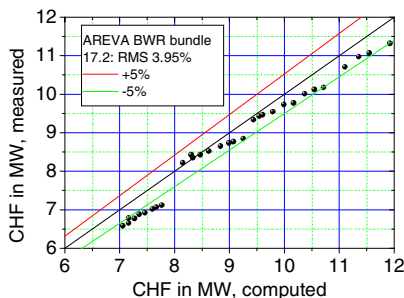


Fig. 16.15.35 Measured versus computed critical bundle power for *cosine* profile with $f_{z,\max} = 1.4$ and lateral peaking pattern characterized by $f_{xy} = 0.731$ to 1.251: mean error 3.95%, slight systematic under prediction. Data by *Fleiss* et al. (1992): $p = 68.8$ to 69.5 bar, $\Delta h_{2,\text{sub}} = 23$ to 188 kJ/kg, $\dot{m} = 6.33$ to 15.7 kg/s. 37points

AREVA tests for PWR bundles with FOCUS grids: Unlike the previous four data sets this one is for pressures up to 165 bar. The bundle contains 5x5 rods and 5 grids. Again, the simple method predicts the CHF with mean error of 7.24 that is within the accuracy of the 2005 look-up table, see Fig. 16.15.36.

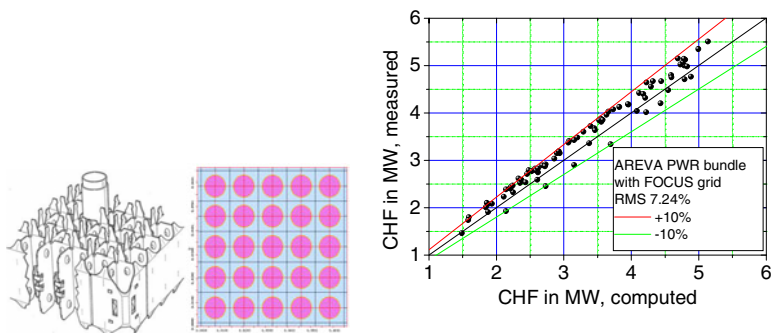


Fig. 16.15.36 AREVA PWR bundle with FOCUS grid: Computed versus measured bundle power: mean error 7.5%, slight systematic under prediction. Data by *Vogel* et al. [34] (1991): $p = 69.3$ to 166.6 bar, $T_{2,\text{in}} = 179.4$ to 329.5 °C, $G = 1186.6$ to 3629 kg/(m² s), $q = 1.4643$ to 5.5015 MW. 82 points

Conclusion

The check whether it is possible to use the 2005 look-up table primary designed for heated pipes also for heated rod bundles gives the surprising result that the bundle critical power for 5 data sets of three different bundles and different power distributions all together 273 experiments are predicted by a simple method described above using the 2005 look-up table within the accuracy reported by the authors of this table. Therefore, unless a better prediction method is developed it is a good idea to use the above method as the best predictive instrument. The influence of the grid design can in addition be taken into account by an empirical coefficient derived from experiment.

16.15.4.2 Pressure drop for boiling flow in bundles

Finally the check of the pressure drop in boiling bundles will be briefly discussed. First, I use the data sets for experiments with the 8×8 NUPEC BWR bundle tests (Fig. 16.15.31) as proposed in the international benchmark by *Neykov et al.* (2005). The single-phase friction coefficient for the specific ferule grid spacer is fitted to the data with a mean error of 1%. The predicted versus the computed friction pressure drop only is given in Fig. 16.15.37.

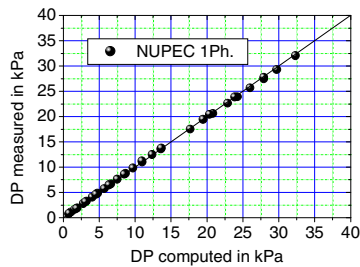


Fig. 16.15.37 Measured versus computed friction pressure drop (wall friction+7 grids). mean error 1%.

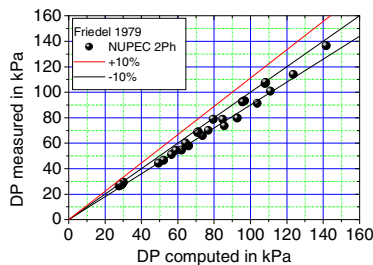


Fig. 16.15.38 Measured versus computed pressure drop for boiling channels. Two-phase friction multiplier by *Friedel* (1979), mean error 7.38%.

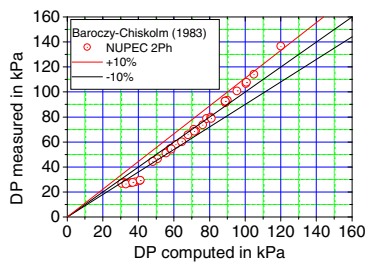


Fig. 16.15.39 Measured versus computed pressure drop for boiling channels, 33 experiments. Two-phase friction multiplier by *Baroczy-Chisholm* modified by *Chisholm* (1983), mean error 11.8%

In the next step, I analyze the two-phase flow data. I use the already-obtained correlation for the irreversible pressure loss coefficient at the grid and two phase flow multiplier proposed by *Friedel* (1979). We see from Fig. 16.15.38 that *Friedel's* correlation predicts the data with mean error 7.38% and from Fig. 16.15.39 that the *Baroczy* correlation from 1965 modified by *Chisholm* (1983) predicts the data with mean error 11.8%.

Next, we analyze 96 data points for the AREVA bundles with the FOCUS grid spacers. Again the single-phase irreversible pressure loss coefficients of the spacers are fitted with an accuracy of 1%. Then, the total pressure loss for boiling flow is computed. The *Friedel* 1979 correlation for the two-phase multiplier is used. A mean error of 9% is found.

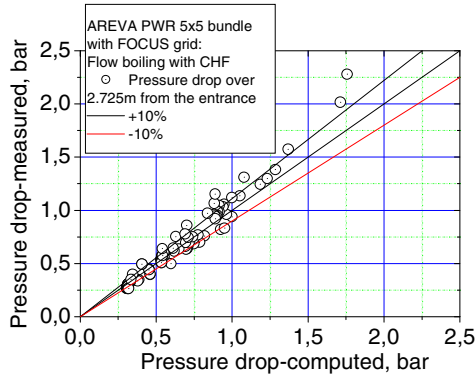


Fig. 16.15.40 Measured versus computed total pressure drop in a 5×5 bundle with FOCUS grid. 96 experiments

Conclusion: Note that *Friedel's* correlation approximates 25 000 experimental points for vertical upwards cocurrent flow and for horizontal flow with 30 to 40% standard deviation for one- and two-component flow. Therefore, better accuracy can not be expected for this particular comparison. The two-phase total pressure drop in bundles with boiling flows is best predicted by *Friedel's* correlation with a mean error between 7.38 and 9%. So we recommend the use of *Friedel's* correlation for such cases.

16.15.4.3 3D analysis

First, I design a preprocessor and function for IVA that for given mass flow, pressure, subcooling and geometry of the bundles that predicts the critical bundle power and parameter by the simplified procedure presented in the previous section. Then I perform 3 computations: (a) with the so estimated power; in (b) and (c) we vary this power by $\pm 5\%$, respectively, and for each of them compute the portion of the surface that is dry. Dry is defined as either film thickness less the 10 μm in the cell or the 2005 look-up table predicts conditions fro CHF (DO or DNB). In most of the BWR cases I have analyzed, dry out is observed. However there are cases in which the film thicknesses are large and the look-up table identifies DNB. How important the grid modeling is, is demonstrated in the following example: For the case 505500 of the NUPEC experiments I consider the grid in Fig. 16.15.31b without and with small vanes at the periphery. Figure 16.15.41 shows the differences.

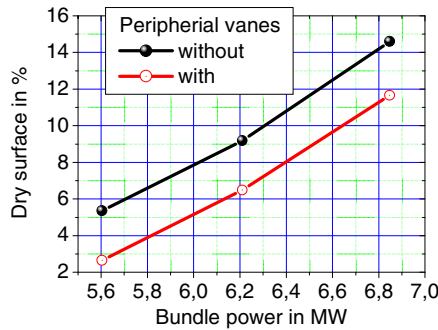


Fig. 16.15.41 Portion of the dry surface as a function of the power without and with blades

It is obvious that the vanes redirect unused liquid from the periphery to the fuels and improve the wetting process. It is remarkable that such an effect is possible to be taken into account in large-scale discretization as those shown in Fig. 16.15.31a. Therefore, in all future computation I do consider the peripheral blades. One example of the results obtained with this procedure is given in Table 16.15.21. The computations in this subject are still going on and the final analysis will be provided later.

Table 16.15.21 Computed dry out heat flux and the corresponding dry portion of the surface of the fuels in the bundle.

Exp. ID	\dot{m} kg/s	P bar	ΔT_{sub} K	\dot{Q}_{comp} MW	\dot{Q}_{exp} MW	F_{dry} / F_{heated} % for		
						\dot{Q}_{comp} -5%	\dot{Q}_{comp}	\dot{Q}_{comp} +5%
SA505500	5.60	54.9	-10.07	6.216	6.13	2.65	6.49	11.66
SA505501	5.58	54.9	-10.15	6.203	6.13	2.37	4.87	8.56
SA505600	5.59	55.1	-16.92	6.323	6.23	0.63	1.86	3.15
SA505800	5.61	55.0	-26.14	6.504	6.39	0.57	1.83	3.14
SA505900	5.59	54.9	-5.11	6.121	5.98	0.63	1.72	3.48
SA510500	15.29	54.8	-11.17	10.129	9.72	0.61	1.64	3.41
SA510501	15.31	55.1	-12.39	10.159	9.81	0.66	1.69	3.54
SA510600	15.19	55.1	-19.25	10.413	10.09	0.54	1.38	2.84
SA510601	15.37	55.2	-19.37	10.431	10.19	0.61	1.46	2.89
SA510800	15.23	55.1	-27.30	10.720	10.20	0.56	1.39	3.03
SA510900	15.19	55.2	-6.94	9.895	9.560	0.54	1.38	2.84
SA510901	15.29	55.1	-6.88	9.920	9.660	0.61	1.46	2.89
SA512500	18.19	55.4	-12.75	10.702	10.410	0.56	1.39	3.03
SA605500	5.58	71.6	-9.46	5.667	5.770	0.21	2.39	5.40
SA605502	5.58	71.7	-9.63	5.661	5.730	0.19	2.46	6.76
SA610503	15.33	71.7	-11.15	8.956	8.850	0.00	0.38	1.01
SA610504	15.41	71.7	-10.90	8.966	8.910	0.00	0.38	0.99
SA610600	15.29	71.8	-16.97	9.217	9.200	0.02	0.35	1.08
SA610700	15.33	71.3	-20.56	9.445	9.370	0.00	0.49	1.34
SA610701	15.24	72.1	-21.63	9.397	9.380	0.00	0.37	1.15
SA610800	15.36	72.4	-26.39	9.634	9.520	0.00	0.54	1.15
SA610900	15.31	72.7	-7.00	8.654	8.660	0.00	0.10	0.73

The portion of the fuel surface that is dry is an inherent property of the process. It is detected by measuring with a finite number of thermocouples. It is simulated with a finite number of volumes containing again a finite number of portions of the fuel bundle-surface.

Therefore, there is a specific definition of CHF associated with the density of the thermocouples and their distribution in each experiment. This important source of uncertainty was never considered in the literature as far I know but it has to be considered in the future by transferring experimental observation to real plant behavior.

As will be demonstrated in the next section the mean error of the 1D prediction of the location of the dry out is about 40 cm due to the uncertainties in the involved constitutive models that are going to be next discussed. They remain also in 3D. Therefore, more effort is necessary to increase the accuracy of the involved correlation, to derive a complete set of source terms for generation of turbulence in all flow patterns, to accomplish the right coupling between deposition and local degree of turbulence, and finally to derive an appropriate mechanistic criterion for identification of dry out. I strongly recommend continuation of this line of research theoretically and experimentally.

16.15.4.4 Uncertainties

Trying to compute dry-out heat flux by using three fluid models with constitutive relations gained from adiabatic flow I found in *Kolev* 1985a, b that the uncertainty of the entrainment and deposition models does not allow very accurate prediction of the location of the dry out. Let us analyze some reasons for this situation, which still has not changed very much since those days.

16.15.4.4.1 Interfacial drag

The interfacial drag between gas and film in annular two-phase flow controls the relative velocity between bulk flow and film. This relative velocity controls the entrainment of droplets. For the computation of the drag coefficients different approximations exist, all of them reported by their authors to be based on experiments. For comparison between the predictions of different correlations, see the review in *Kolev* 2004b, as a function of the gas *Reynolds* number is given in Fig. 16.15.42.

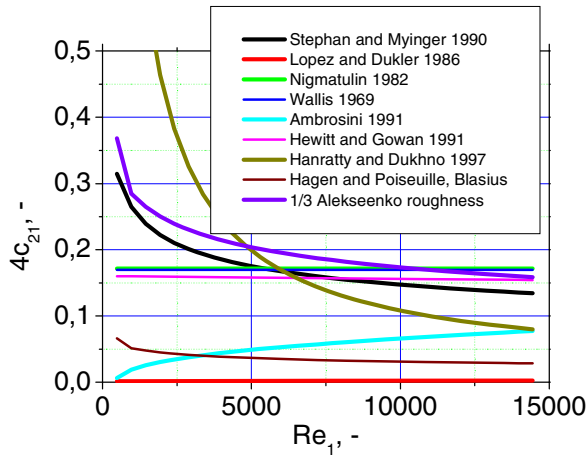


Fig. 16.15.42 Gas–film friction coefficient as a function of the gas *Reynolds* number

The correlations by *Wallis*, et al. and *Nigmatulin* do not differ from each other much. The prediction of the correlation by *Stephan* and *Myinger* converges to the prediction of the above-mentioned correlations for higher *Reynolds* number, but differs greatly for low *Reynolds* numbers. If one uses the formula of *Alekseenko* and takes 1/3th of the film amplitude as the effective roughness the *Nikuradze* formula predict results close to those predicted by *Stephan* and *Myinger*. For comparison the prediction by the *Blasius* correlation for *Reynolds* number larger than 1187 and by the *Hagen* and *Poiseuille* correlation for lower *Reynolds* numbers is also given in Fig. 16.15.42. It is obvious that the final state of the knowledge in this field is not achieved.

16.15.4.4.2 Entrainment

The droplet entrainment in annular two-phase flow influences the film thickness. For the computation of the entrainment different approximations exists, all of them reported by their authors to be based on adiabatic experiments.

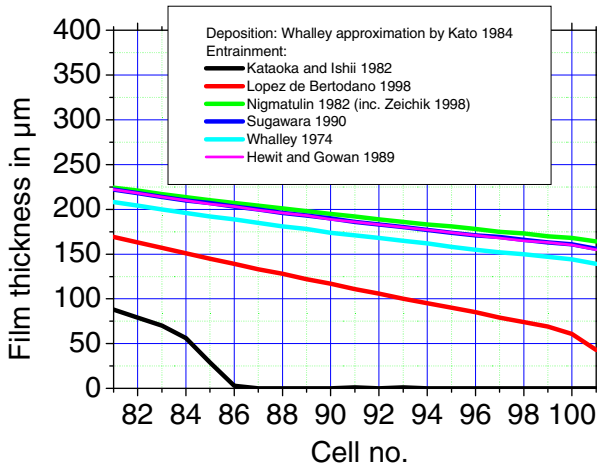


Fig. 16.15.43 Film thickness as a function of the distance from the entrance. Boiling water in vertical circular pipe, *Bennett et al. 1967*: Test nr. 5253, vertical pipe, 0.01262 m inner diameter, 5.5626 m length, uniformly heated with 199 kW, inlet water flow from the bottom: 68.93 bar and 538.90 K

Kawara et al. (1998) compared 9 correlations for entrainment obtained by different authors or teams. They found differences of six orders of magnitude at low entrainment ratios and three orders of magnitude at high entrainment ratios. We give here another example. We consider here one of the many vertical boiling pipe experiment by *Bennett et al. 1967* experiment. Simulating the flow with a three-fluid model (IVA) using different entrainment correlations, see the review in *Kolev 2004b*, we obtain the film thickness as a function of the axial coordinate as presented in Fig. 16.15.43. We know from the measurements that the film disappear in position 8/10 of the total pipe length.

The largest entrainment, and therefore the closest to the observed result, is predicted by *Kataoka and Ishii's* correlation. None of the models takes the change of the entrainment due to the wall boiling into account. Therefore, a final state of this research field is still not reached.

16.15.4.4.3 Deposition

Kawara et al. 1998 compared 11 deposition coefficients obtained by different authors or teams. They found differences up to two orders of magnitude, depending on the local droplet concentration.

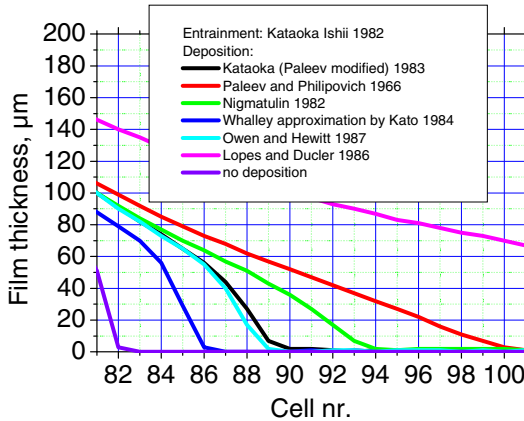


Fig. 16.15.44 As in Fig. 16.15.39.

I make 7 computations changing only the deposition models keeping the entrainment model unchanged. The results regarding the film thickness are presented in Fig. 16.15.44. The smallest deposition, and therefore the closest to the observed result, is predicted by the *Kato's* correlation. Note that we do not take into account the deposition suppression due to boiling of the film, which is obviously important. Repeating the computation with virtually no deposition gives the best results. Note that *Hoyer* and *Stepniewski* reported already in 1999 that deposition suppression due to boiling is important for dry-out prediction at high void fractions in boiling flows.

Therefore, a final state of this research field is still not reached.

The influence of the boiling on the deposition will be discussed next.

16.15.4.4.4 Deposition and entrainment changes due to nucleate boiling

Boiling films manifest a few additional phenomena controlling the film dynamics that are not present in adiabatic films.

Modified deposition: Vapor produced through the film blows into the gas core and dumps the penetration of the gas pulsation into the boundary layer. Therefore, there is an impact on the gas boundary layer close to the interface resembling blowing of gas from the film/gas interface. This phenomenon hinders deposition. Assuming that all generated vapor enters the bulk flow perpendicular to the wall we have for the effective gas velocity

$$u_{1_blow} = \frac{D_{heat}}{4} \frac{\mu_{21}}{\rho_1}. \quad (16.15.6)$$

If $u_{1_blow} > V_1'$ the deposition is effectively nonexistent. If $u_{1_blow} > V_1'$ the effective gas fluctuation velocity is reduced to $V_1' - u_{1_blow}$. *Doroschuk* and *Levitani* (1971), *Guguchkin* et al. (1985) reported data that prove that the vapor blow from the film into the gas bulk reduces deposition. *Milashenko* et al. 1989 recommended ignoring the deposition in boiling flows.

Modified entrainment: The steam mass flow generated at the wall surface contributes substantially to the fragmentation of the liquid by two mechanisms: At low film velocity if the bubble departure diameter is larger than the film thickness the bubble burst causes additional entrainment. At high film velocities the bubble departure diameter is small but there is a vapor net flow perpendicular to the wall crossing the film. The vapor creates two-phase unstable structure that eventually break up and release the vapor into the gas core flow by entraining additional droplets.

Milashenko et al. collected in 1989 data for boiling flow in a 0.0131-m inside-diameter pipe of 0.15 and 1 m heated lengths. Setting the deposition rate μ_{32} equal to zero the authors correlated their data for an effective entrainment by the following correlation

$$\mu_{23_boiling_film} + \mu_{23_adiabat} - \mu_{32} = \frac{1.75}{\pi D_h} \alpha_2 \rho_2 w_2 \left(\dot{q}_{w2} 10^{-6} \frac{\rho''}{\rho'} \right)^{1.3}, \quad (16.15.7)$$

indicating a strong dependence on the wall heat flux. Note that the asymptotic value for zero heat flux will produce zero effective entrainment, which can not be true. Nevertheless, this is the ultimate prove that boiling process influence the effective entrainment.

Probably a better scaling velocity of the additional to the adiabatic entrainment is given by Eq. (16.15.6), which will be linearly dependent on the heat flux, $w_{1_blow} = \dot{q}_{w2} / (\rho_1 \Delta h)$, for saturated film. This explains why *Milashenko* et al. are forced to introduce the constant 10^{-6} being of order of $1/\Delta h$. Therefore

$$\mu_{23_boiling_film} = f \rho_2 \frac{\mu_{21}}{\rho_1} \frac{D_{heat}}{4} \quad (16.15.8)$$

with function $f < 1$ that remains to be found is probably the better physical basis for data correlation. *Kodama* and *Kataoka* reported in 2002 a dimensional correlation for the net entrainment rate due to the bubble break up with accuracy up to a constant that has to be derived from experiments

$$\begin{aligned} & (\rho w)_{23_boiling_film} + (\rho w)_{23_adiabat} - (\rho w)_{32} \\ & = const \frac{\dot{q}_{w2}}{\Delta h \rho''} \exp \left[- \frac{\delta_2 \sqrt{\tau_{2w} / \rho_2}}{158.7 (\eta'' / \eta')^{2.66} 30 w_2} \right]. \end{aligned} \quad (16.15.9)$$

We see here that the group $w_{1_blow} = \dot{q}''_{w2}/(\rho_1 \Delta h)$ is used correctly but again for adiabatic flow the asymptotic is not correct.

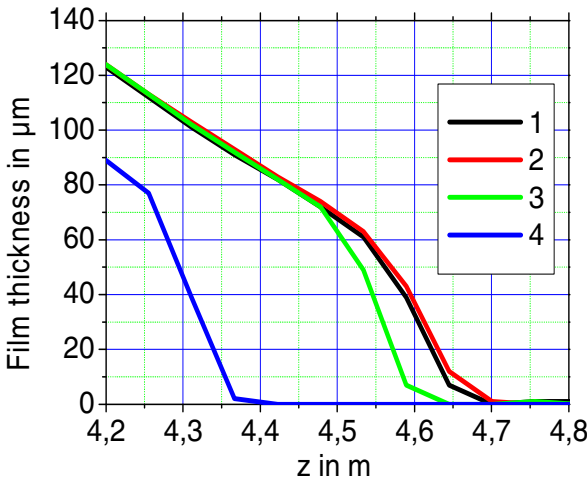


Fig. 16.15.45 Film thickness as a function of the axial coordinate for conditions of Bennett 5253 experiment. (1) Entrainment, deposition like in adiabatic flow; (2) Like (1) with deposition multiplied by ratio of the gas turbulent kinetic energy to the equilibrium turbulent kinetic energy; (3) Like (1) + (2) with suppression of the deposition due to the vapor blow from the film; Like (1) + (2) + (3) with entrainment enhancement due to the vapor blow through the film; Experimental position of the dry out about 4.4 m.

Now, we demonstrate the effect of the above-discussed phenomena again on the *Bennett* experiment as given in Fig. 16.15.45. Using f of the order of 0.02 and repeating the computations for other experiments as given in Table 16.15.22 we see that the position of the dry out of the film can be predicted with mean error of 0.41 m.

Table 16.15.22 Position of predicted and computed film dry out for some *Bennett* heated-pipe experiments (Mean error 0.41 m)

Bennett exp. ID	z_{DO} exp. ± 0.076	z_{DO} IVA	Δ
5253	3.89	4.31	0.42
5293	3.89	4.42	0.53
5332	4.39	3.37	-1.02
5380	3.81	3.7	-0.11
5407	2.79	3.02	0.23
5424	2.64	2.94	0.30
5442	2.79	3.27	0.48
5456	2.79	2.94	0.15

Conclusion: Important elements of the three-fluid models are developed based on adiabatic flows and are associated with considerable uncertainty. One can not expect to reach a better description of the dry-out performance only improving the grid models without substantial reduction of those uncertainties for boiling flows.

The mean error of the 1D prediction of the location of the dry out is about 40 cm due to the uncertainties in the involved constitutive models. These uncertainties remain also in 3D predictions. Therefore, more effort is necessary to increase the accuracy of the involved correlation, to derive a complete set of source terms for generation of turbulence in all flow pattern, to accomplish the right coupling between deposition and local degree of turbulence, and finally to derive appropriate mechanistic criterion for identification of dry out.

16.15.4.4.5 Residual film thickness at DO?

Using correlation for entrainment and deposition gained from adiabatic experiments results obviously to overprediction of the deposition and underprediction of the entrainment. The results of such computations are always predicting some film thickness at places where the wall has to be dry. This led some authors to introduce some critical film thickness depending on the local parameter as already mentioned in the introduction. Regarding the experimental evidence: At the dry out *Milashenko et al.* 1989 experimentally observed a residual film mass flow rate of 0.02 kg/s. *Shiralkar and Lahey* (1973) reported finite film flow rates at the location of the CHF appearance. Regarding the dry-out film thickness *Groeneveld* 2001 reported that in all of his dry-out experiments (more than 30 years experimental research) a complete drying of the film was observed that contradicts *Milashenko et al.* 1989.

Conclusion: The influence of the boiling film on enhancing of the entrainment and suppression of the deposition has to be taken in any case into account. Then, the film nucleate boiling has to be examined for departure from nucleate boiling. If there are no local conditions for DNB then the DO requires dry film. This logic allows finite film thickness and boiling crisis simultaneously in cases of DNB.

16.15.4.4.6 Amount of the liquid in the core at the onset of film flow

Some authors reported that at the onset of the film flow there is an immediate amount of entrained liquid inside the gas core; see *Barbosa et al.* (2002). This is still source of uncertainty because the dry out point depends on such information too.

16.15.5 Outlook – towards the fine-resolution analysis

Associating large flow cross-sections in one subchannel as still practiced worldwide naturally limits the prediction accuracy. Therefore, future analyses

have to concentrate on much finer resolution of the processes as demonstrated in Fig. 16.15.46.

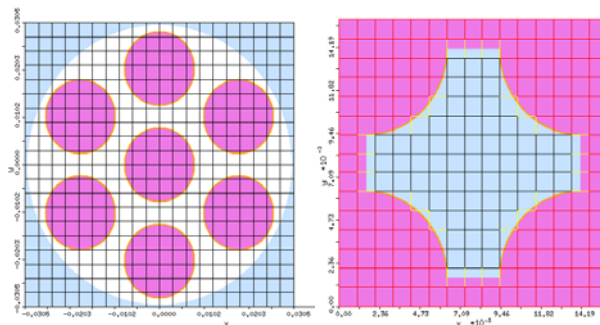


Fig. 16.15.46 Abandoning of the subchannel analyses – a challenge for the near future

The challenges in this area are associated with the constitutive relationships. Empirical correlations that are gained by averaging values across pipe cross-section are not valid for the subscale and have to be systematically replaced by new ones.

16.15.6 Conclusions

This work is a demonstration of the achievable accuracy that can be obtained by simulating steady-state and transient boiling in rod bundles by IVA computer code crossing all known three-fluid flow pattern and heat-transfer mechanisms and using large-scale discretization. 333 three-dimensional tests in bundles with 1, 16, 25, 36 heated rods, 7 different bundles with 64 heated rods from different laboratories are simulated: 273 3D experiments on 6 bundles for CHF, 54 3D experiments on 7 bundles for void fraction, 2 3D experiments in a bundles for transients and 4 1D experiments in a subchannel for transient. The mass flow rates and the pressure varied from 3 to 2000 kg/(m² s) and from 1 bar to 200 bar, respectively. The subcoolings were less than 140 K and the thermal power varies from some tenths of a kW to 7 MW. The comparison revealed the capability of IVA to adequately simulate flow boiling processes in bundles in variety of flow regimes besides the already existing very large verification data base of IVA for many other processes.

Simultaneously, this work was also a source of inspiration for improving the accuracy of the mathematical description of such processes in the future. This comprehensive analysis shows that the scale of spatial resolution calls for a specific set of constitutive relations. Examples are given for the effective interfacial drag coefficients. Comparison with the results of other authors was made and discussion was provided. In addition, by using different spatial resolution was demonstrated that the turbulent void and droplets transport have to

be described much more accurately in distributed parameters to provide a universal way of prediction of void and droplet dispersion with such important consequences like accurate void and dry-out prediction.

Appendix 16.15.1 Some relevant constitutive relationship addressed in this analysis

IVA computer code has absorbed in the last 25 years hundreds of constitutive relationships for variety of processes as described by *Kolev* (2004). We address here only those that are subject of modification influencing the void fraction prediction in bundles. Note that for the computation of the drag coefficients the procedure described in *Kolev* (vol. 1, 2004). Chapter 2 was initially used.

1. Transition between bubbly and slug flow: If $D_1 > 6\lambda_{RT}$ $\alpha_{1,B-Ch} = 0.25$, else if $D_1 < \lambda_{RT}$ $\alpha_{1,B-Ch} = 0.3$, else $\alpha_{1,B-Ch} = 0.3 - 0.01(D_1 / \lambda_{RT} - 1)$, where λ_{RT} is the *Raleigh–Taylor* wavelength defined as follows $\lambda_{RT} = \sqrt{\sigma_2 / (g\Delta\rho_{21})}$. For the cases considered here the *Mishima* and *Ishii* (1984) correlation for transition from slug into churn turbulent flow $\alpha_{1,slug \text{ to } churn} = 1 - 0.813 \left\{ \frac{(C_0 - 1) |j| + 0.35 V_{TB}}{|j| + 0.75 V_{TB} b_1} \right\}^{0.75}$ does predict transition to from bubble to slug but not to churn turbulent flow. Here the drift flux distribution coefficient for slug flow is $C_0 = 1.2$, the slug (*Taylor* bubble) raising velocity is $V_{TB} = \sqrt{\frac{\rho_2 - \rho_1}{\rho_2} g D_h}$, the mixture volumetric flux is $j = \alpha_1 V_1 + (1 - \alpha_1) V_2$, and $b_1 = \left(\frac{\rho_2 - \rho_1}{\eta_2^2 / \rho_2} g D_h^3 \right)^{1/18}$.

2. Drag force for distorted bubbles: Nonmodified *Ishii* and *Chawla* (1979)

$$c_{21}^d = \frac{2}{3} (D_1 / \lambda_{RT}) \left(\frac{1 + 17.67 f^{6/7}}{18.67 f} \right)^2; f = (1 - \alpha_d)^{1.5}.$$

3. Drag force for slug flow: None modified *Ishii* and *Chawla* (1979)

$$c_{21}^d = 9.8(1 - \alpha_1)^3.$$

4. Drag force for distorted bubbles: Modified

$$c_{21}^d = 0.01 \frac{2}{3} (D_1 / \lambda_{RT}) \left(\frac{1 + 17.67 f^{6/7}}{18.67 f} \right)^2.$$

5. Drag force for slug flow modified: Here we use the expression derived for cup bubbles instead for slugs multiplied by 0.1,

$$c_{21}^d = 0.1 \frac{8}{3} (1 - \alpha_1)^2.$$

6. Instead of the primarily used model by *Kataoka et al.* (1983), *Bertodano et al.* (1998) model for entrainment was used here. It was verified for low pressure $p = 1.2$ bar and $10 < \rho_2 w_2 4 \delta_{2f} / \eta_2 < 9700$, $2.5 < \alpha_1 \rho_1 V_1 D_h / \eta_1 < 17.e4$, $3 < \rho_1 (\alpha_1 V_1)^2 D_{3E} / \sigma < 20$. The *Bertodano et al.* correlation gives the same results as the *Kataoka et al.* correlation for low pressure and relative low mass flow rates but better agreement with the data for high pressure and large gas mass flow rates.

7. The diffusion droplet deposition rate was computed using the correlation by *Paleev's and Filipovich* (1966) slightly modified by *Kataoka and Ishii* (1983). *Kataoka and Ishii* provided verification based on data in the following region

$$\begin{aligned}
 &< \rho_2 (1 - \alpha_1) |w_{23}| D_h / \eta_2 < 5041, 1414 < \frac{\rho_1 (\alpha_1 w_1)^2 D_h}{\sigma_2} \left(\frac{\rho_2 - \rho_1}{\rho_1} \right)^{1/3} < 9602, 0.0095 \\
 &< D_h < 0.032.
 \end{aligned}$$

Nomenclature

c_{21}^d	bubble drag coefficient due to liquid action, dimensionless
D_1	bubble diameter, m
g	gravitational acceleration, m/s ²
V_l	velocity of field l , m/s
α_l	local volume fractions of the fields l , dimensionless
λ_{RT}	<i>Rayleigh-Taylor</i> wavelength, m
ρ_1	gas density, kg/m ³
ρ_2	liquid density, kg/m ³
ρw	mixture mass flow rate, kg/(m ² s)
σ_2	viscous tension, N/m
η_1	dynamic gas viscosity, kg/(m s)
η_2	dynamic liquid viscosity, kg/(m s)

References

- Akiyama, Y., Hori, K., Miyazaki, K., Nishioka, H., Sugiyama, S.: Evaluation of the bundle void fraction measurement data of PWR fuel assembly. In: The 3rd JSME/ASME Joint International Conference on Nuclear Engineering, Kyoto International Conference Hall, Kyoto, Japan, April 23-27, vol. 1, pp. 211-216 (1995)
- Akiyama, Y., Hori, K., Miyazaki, K., Nishioka, H., Sugiyama, S.: Pressurized water reactor fuel assembly subchannel void measurement. *Nucl. Technol.* 112, 412-421 (2005)
- Anglart, H., Nylund, O.: CFD application to prediction of void distribution in two pahas bubbly flow in rod bundles. *Nucl. Eng. Des.* 163, 81-98 (1996)
- Anklama, T.M., Miller, R.F.: Void fraction under high pressure, low flow conditions in rod bundle geometry. *Nucl. Eng. Des.* 75, 99-108 (1982)
- Aounalla, Y., Coddington, P.: Assessment of VIPRE-02 void fraction prediction against NUPEC experimental BWR data. In: 9th International Topical Meeting on Nuclear Thermal Hydraulics (NUTETH-9) San Francisco, California (October 3-8 , 1999)
- Barbosa, J.R., Hewitt, G.F., König, G., Richardson, S.M.: Liquid entrainment, droplet concentration and pressure gradient at the onset of annular flow in vertical pipe. *Int. J. Multiphase Flow* 28, 943-961 (2002)
- Bennett, A.W., et al.: Heat transfer to steam-water mixtures flowing in uniformly heated tubes in which the critical heat flux has been exceeded, AERE-R5373 (1967b)
- Chisholm, D.: Two-phase flow in pipelines and heat exchanger, p. 110. George Godwin, London and New York (1983)
- Doroshchuk, V.E., Levitan, L.L.: Investigation of droplet deposition from annular dispersed steam-water flow core and wall liquid film. *Therm. Phys. High Temp.* 9, 591-596 (1971)
- Fuel Economic and Reliable, AREVA, France (2004), see also in *Adv. Nucl. Power* No 3, The Magazine of Framatome ANP (January 2002)
- Fleiss, Knapp, Which: STS-17.2, STS-17.1: Messung der Siedeübergangsleistungen und Druckverluste am ATRIUM-10-9Q-Testbündel, e321/92/43, e321/92/44, Karlstein, proprietary (1992)
- Friedel, L.: New friction pressure drop correlations for upward, horizontal, and downward two-phase pipe flow. Presented at the HTFS Symposium, Oxford, September 1979 (Hoechst AG Reference No. 372217/24 698) (1979)
- Groeneveld, D.C.: Private communication (2001)
- Guguchkin, V.V., Nigmatulin, B.I., Markovich, E.E., Vasilev, N.I., Arestenko, Y.P., Ivanovskaya, V.I.: Peculiarities in droplet movement and bubbles in wall region. The- ses of a report Presented at VII All-Union Conf. an Two Phase Flow in Power Ma- chines and Apparatus, Leningrad, vol. 3, pp. 316-317 (1995)
- Hori, K., Miyazaki, K., Kurosu, T., Sugiyama, S., Matsumoto, J., Akiyama, Y.: In bundle void fraction measurement of PWR fuel assembly. In: Proceedings of ICONE 2, vol. 1, pp. 69-76 (1993)
- Hori, K., Akiyama, Y., Miyazaki, K., Kurosu, T., Sugiyama, S.: Transient void fraction measurement in a single Channel simulating one channel for a PWR Fuel Assembly. In: 10th Proceeding of Nuclear Thermal-Hydraulics, ANS Winter Meeting, pp. 56-68 (1994)
- Hori, K., Akiyama, Y., Miyazaki, K., Kurosu, T., Sugiyama, S.: Void fraction in a single channel simulating one subchannel of a PWR fuel assembly. In: Proceedings of the First International Symposium an Two-Phase Flow Modelling and Experimentation (1995)

- Hori, K., Akiyama, Y., Miyazaki, K., Nishioka, H., Takeda, N.: Total evaluation of in bundle void fraction measurement test of PWR fuel assembly. In: Proceedings of ICONE-4, vol 1, Part B, pp. 801–811 (1996)
- Hoyer, N., Stepniewski, M.: Dry out prediction in bundle geometry. In: 9th Int. Top. Meeting on Nuclear Reactor Thermal Hydraulics (NURETH-9), San Francisco, California, October 3–8 (1999)
- Hughes, E.D., Paulsen, M.P., Agee, L.: A drift-flux model of two-phase flow for RETRAN. Nucl. Technol. 54, 410–420 (1981)
- Inoue, A., Futakuchi, M., Yagi, M., Kurosu, T., Mitsutake, T., Morooka, S.: Void fraction distribution in a boiling water reactor fuel assembly and the evaluation of subchannel analysis codes. Nucl. Technol. 112(3), 388–400 (1995)
- Inoue, A., Kurosu, T., Oaki, T., Futaguchi, M., Yagi, M., Morooka, S., Hoshide, A., Ishizuka, T., Yoshimura, K., Yoshida, H., Mitsutake, T., Abe, N., Kozima, A., Nakajima, T., Nakamura, S., Sawa, T.: Void measurement of BWR fuel assembly. J. At. Energy Soc. Japan 37(8), 710–720 (1995) (in Japanese)
- Inoue, A., Kurosu, T., Oaki, T., Yagi, M., Mitsutake, T., Morooka, S.: Void fraction distribution in boiling water reactor fuel assembly and evaluation of subchannel code. J. Nucl. Sci. Technol. 32(7), 629–640 (1995)
- Ishii, M., Chawla, T.C.: Local drag laws in dispersed two-phase flow, NUREG/CR-1230, ANL-79-105 (December 1979)
- Kataoka, I., Ishii, M., Mishima, K.: Trans. ASME 5, 230–238 (1983)
- Kataoka, I., Ishii, M.: Entrainment and deposition rates of droplets in annular two-phase flow. In: Mori, Y., Yang, W.-J. (eds.) ASME-JSME Thermal Engineering Joint Conference Proceedings, Honolulu, Hawaii, vol. 1, pp. 69–80 (1983)
- Kawara, Z., Kataoka, I., Serizawa, A., Ko, Y.J., Takahashi, O.: Analysis of forced convective CHF based on two-fluid and three-fluid model. In: Heat Transfer 1998, Proc. of the 11th IHTC, Kyongju, Korea, August 23–28, vol. 2, pp. 103–108 (1998)
- Kelly, J.M., Stewart, C.W., Cuta, J.M.: VIPRE-02 – A two-fluid thermal-hydraulics code for reactor core and vessel analysis: Mathematical modelling and solution methods. Nucl. Technol. 100, 246–259 (1992)
- Kodama, S., Kataoka, I.: Study on analytical prediction of forced convective CHF in the wide range of quality. In: Proceedings of ICONE10, 10TH International Conference on Nuclear Engineering Arlington, VA, USA, Paper nr ICONE10-22128 (April 14–18, 2002)
- Kolev, N.I.: Transient three-phase three-component non-equilibrium non-homogeneous flow described by 1D-three-velocity fields slip model. In: Proc. Specialists Meeting on Small Break LOCA Analysis in LWRs, Pisa, vol 3, June 23–27, pp 363–378 (1985a)
- Kolev, N.I.: Transiente Dreiphasen Dreikomponenten Strömung, Teil 2: Eindimensionales Schlupfmodell Vergleich Theorie experiment. KfK 3926 (August 1985b)
- Kolev, N.I.: Simple analytical U-tube benchmarks appropriate for testing of pipe-network computer codes. In: Proceedings of ICONE10: Tenth International Conference on Nuclear Engineering – Arlington, Virginia, Washington, D.C., USA ICONE10-22711 (April 14–18, 2002a)
- Kolev, N.I.: 3D-Multiphase-Fluid-Dynamik: Reduzierung der Dampffechte am RDB-Austritt der Siedewasserreaktoren, Betriebsleitertagung, Geneve (November 27–29, 2002b); in English: Controlling the moisture content in the steam by using nozzles in BWR's. In: Eleventh International Conference on Nuclear Engineering, ICONE 11, Keio Plaza Inter-Continental, Shinjuku, Tokyo, Japan, ICONE11-36306 (April 20–23, 2003)

- Kolev, N.I.: Multiphase Flow Dynamics, 2nd edn., with 114 Figures and CD-ROM. Fundamentals, vol. 1. Springer, Berlin (2002, 2004), <http://www.springeronline.com/east/3-540-22106-9>, ISBN 3-540-2206-0
- Kolev, N.I.: Multiphase Flow Dynamics, 2nd edn., with 81 Figures. Thermal and mechanical interactions, vol. 2. Springer, Berlin, <http://www.springeronline.com/east/3-540-22107-7>, ISBN 3-540-22107-7
- Kolev, N.I.: 25-Years three-fluid modeling-experience: successes and limits. In: Proceedings of ICONE-12 2004, Arlington VA, USA, Paper ICONE12-49054 (April 25-29, 2004); Also in 4th ECCOMAS (European Congress on Computational Methods in Applied Sciences and Engineering, Finland (July 24-28, 2004); Also in 6th WCCM (World Congress of Computational Mechanics), Beijing (September 5-10, 2004); In extended form in 6th International Topical Meeting on Nuclear Reactor Thermal Hydraulics, Operations and Safety, Nara-Ken New Public Hall, Nara, Japan, NUTHOS6-N6P380 (October 4-8, 2004)
- Kolev, N.I.: IVA Simulations of exercises 1 of phase 1 and 2 of the OECD/NRC benchmark based on NUPEC BWR full-size fine-mesh bundle tests (preliminary). In: Second Workshop on OECD/NRC Benchmark based on NUPEC BWR Full-size Fine-mesh Bundle Tests (BFBT), State College, PA, USA (June 27-29, 2005a)
- Kolev, N.I.: Do we have appropriate constitutive sets for sub-channel and fine-resolution 3D-analyses of two-phase flows in rod bundles? In: Mathematics and Computation, Supercomputing, Reactor Physics and Nuclear and Biological Applications Palais des Papes, Avignon, France, September 12-15, on CD-ROM. American Nuclear Society, LaGrange Park (2005b)
- Kolev, N.I.: Flow boiling in bundles: Comparison of IVA predictions for 153 experiments for variety of bundles, flow regimes including DO, steady state and transients. In: The 11th International Topical Meeting on Nuclear Reactor Thermal-Hydraulics (NURETH-11) Log Number: 547, Popes Palace Conference Center, Avignon, France, October 2-6 (2005c)
- Levy, S.: Int. J. Heat Mass. Transfer 10, 351-365 (1967)
- Lopez de Bertodano, M.A., Assad, A., Beus, S.: Entrainment rate of droplets in the ripple-annular regime for small vertical ducts. In: CD Proceedings of the Third International Conference on Multiphase Flow, ICMF 1998, Lyon, France (June 8-12, 1988)
- Lucchini, F., Marinelli, V.: Experimental data on burn-out in simulated BWR fuel bundle. Nucl. Eng. Des. 31, 371-378 (1974)
- Macian, R., Aounallah, Y., Coddington, P., Stangroom, P.: Assessment of RETRAN-3D and VIPRE-02 void prediction against experimental transient data. In: Proc. of ICONE 8, 8th Int. Conf. on Nuclear Engineering, Baltimore, MD, USA, April 2-6 (2000)
- Milashenko, V.I., Nigmatulin, B.I., Petukhov, V.V., Trubkin, N.I.: Burnout and distribution of liquid in evaporative channels of various lengths. Int. J. Multiphase Flow 15(3), 393-402 (1989)
- Mishima, K., Ishii, M.: Flow regime transition criteria for upward two-phase flow in vertical tubes. Int. J. Heat Mass Transfer 27(5), 723-737 (1984)
- Morooka, S., Inoue, A., Oishi, M., Aoki, T., Nagaoka, K., Yoshida, H.: In-bundle void measurement of BWR fuel assembly by X-ray CT Scanner. In: The 1st JSME/ASME Joint International Conference on Nuclear Engineering, pp. 237-243 (1991)
- Naitoh, M., Iwashita, T., Ando, Y.: Boiling transition analysis code for LWR fuel bundles in the IMPACT project. In: 9th International Topical Meeting on Nuclear Thermal Hydraulics (NUTETH-9) San Francisco, California (October 3-8, 1999)

- Neykov, B., Aydogan, F., Hochreiter, L., Ivanov, K., Utsuno, H., Fumio, K., Sartori, E., Martin, M.: NUPEC BWR full-size fine-mesh bundle test (BFBT) nenchmark, vol 1: Specifications, US NRC, OECD Nuclear Energy Agency, NEA/NSC/DOC, p. 5 (November 2005)
- Neykov, B., Ivanov, K., Hochreiter, L.E., Avramova, M.: Summary of comparison and analysis of submitted resiltis for exercise I-1. In: 3rd Workshop on OECD/NRC BFBT Benchmark, Pisa, Italy, April 27-29 (2006)
- Nylund, O., et al.: Hydrodynamic and heat transfer measurements on a full scale simulated 36-rod Marviken fuel element with uniform heat flux distribution. In: FRIGG-2, AB Atomenergi, Stockholm, Sweden, ASEA, VÄSTERAS, R-4-447/RTL-1007 (1968)
- Nylund, O., et al.: Hydrodynamic and heat transfer measurements on a full scale simulated 36-rod BHWL fuel element with non-uniform axial and radial heat flux distribution. In: FRIGG-4, AB Atomenergi, Stockholm, Sweden, ASEA, VÄSTERAS, R-4-502/RL-1253 (1970)
- Paleev II, Filipovich, B.S.: Phenomena of liquid transfer in two-phase dispersed annular flow. *Int. J. Heat Mass Transfer* 9, 1089 (1966)
- Rehme, K.: Laminar Strömung in Stabbündeln. *Chemie-Ing-Tech* 43, 962–966 (1971)
- Rehme, K.: Pressure drop performance of rod bundles in hexagonal arrangements. *Int. J. Heat Mass Transfer* 15, 2499–2517 (1972)
- Rehme, K.: Simple method of predicting friction factors of turbulent flow in non-circular channels. *Int. J. Heat Mass Transfer* 16, 933–950 (1973)
- Rehme, K.: The structure of turbulent flow trough a wall subchannel of rods bundle. *Nucl. Eng. Des.* 45, 311–323 (1978)
- Roloff-Bock, I.: 2D-grid generator for heterogeneous porous structures in structured Cartesian coordinates, Framatome ANP, proprietary (2005)
- Saha, P., Zuber, N.: *Proc. Int. Heat Transfer Conf.*, Tokyo, Paper 134.7 (1974)
- Schäfer, H., Beisiegel, A.: Feasibility of stability tests under natural circulation conditions in the Karlstein test loop, Siemens technical report E32/92/e14a, proprietary (March 17, 1992)
- Shiralkar, B.S., Lahey, R.T.: The effect of obstacles on a liquid film. *J. Heat Tansfer, Trans. ASME* 95, 528–533 (1973)
- Spierling, H.: Regional void fraction in ATRIUM 10XP at various peaking patterns, Framatome-ANP report, FGT, A1C-1311669-1, proprietary (September 24, 2002)
- Utsuno, H., Ishida, N., Masuhara, Y., Kasahara, F.: Assessment of boiling transition analysis code against data from NUPEC BWR full-size fine-mesh bundle tests. In: The 6th International Conference on Nuclear Thermal Hydraulics, Operations and Safety (NUTHOS-6) Nara, Japan, Paper ID. N6P041 (October 4-8, 2004)
- Wang, G., Hochreiter, L.E., Sung, Y., Karoutas, Z.E.: VIPRE code void fraction prediction assessment using FRIGG loop data. In: 13th Int. Conf. On Nuclear Engineering, Beijing, China, May 16-20 (2005)
- Windecker, G., Anglart, H.: Phase distribution in BWR assembly and evaluation of multi-dimensional multi-field model. In: 9th Int. Top. Meeting on Nuclear Reactor Thermo-hydraulics, NURETH-9, San Francisco, California (October 3-8, 1999)
- Vogel, Bruch, Wang: SIEMENS Test Section 52 (DTS52) Description of experiments, KWZ BT23 1991 e 244, Erlangen, proprietary (August 19, 1991)
- Yagi, M., Mitsutake, T., Morooka, S., Inoue, A.: Void fraction distribution in BWR fuel assembly and the evaluation of subchannel code. In: Ninokata, H., Aritomi, M. (eds.) *Subchannel Analysis in Nuclear Reactors*, Tokyo, Japan, pp. 141–167 (1992)

16.16 Film boiling

Film boiling on spheres, Fig. 16.16.1, is a basic heat-transfer mechanism in melt–water interaction processes. For this reason, we will address this topic in depth.

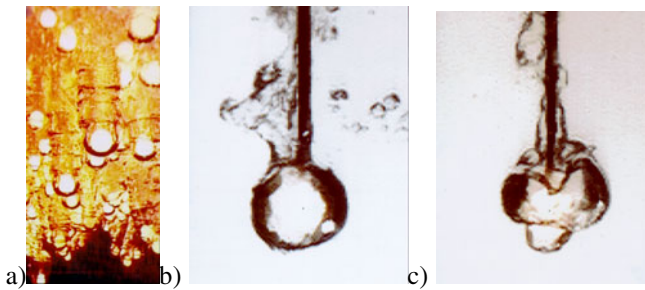


Fig. 16.16.1 a) Film boiling in a family of 2500 K spheres dropped into water. b-c) Film boiling on a single sphere in natural convection. With the courtesy of *L. Meyer*, FzK Karlsruhe, Germany

First we derived in Chapter 21 of Vol. 2 an analytical solution for film boiling heat transfer at a heated vertical surface, *Kolev* (1997a, c, 1998) and verified it with experimental data obtained at the Royal Institute of Technology in Sweden by *Okkonen* et al. (1996). The data are for vertical heated walls with $\Delta z = 1.5$ m. Water at atmospheric pressure and subcooling of $\Delta T_{sc} = 3$ to 42 K was used as a coolant. The wall superheating was considerable: $\Delta T_{sp} = 487$ to 1236 K. The heat-transfer coefficient was defined by *Okkonen* with respect to the wall–liquid temperature difference. This is recomputed here with respect to the wall–saturation temperature difference for comparison. Predicted values were obtained the theoretical result from Section 22.1 of this volume 2, see also in *Kolev* (1997b). A comparison of the predicted heat-transfer coefficients with 43 experimental points is given in Fig. 16.16.2. It is evident that all data predicted are inside the error band of $\pm 10\%$, with a mean-averaged error of less than $\pm 4\%$ when the modified theory expressed by Eq. (22.86) in Vol. 2 is used.

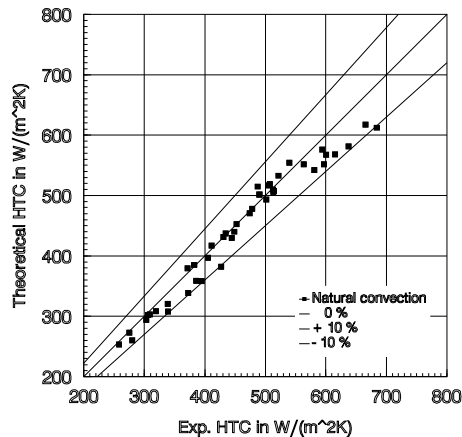


Fig. 16.16.2 Comparison between the film-boiling model and the data base of the Royal Institute of Technology (KTH Sweden), *Okkonen et al. (1996)*. The *Lanzenberger* radiation model (1998) is incorporated. $\Delta z = 1.5m$ vertical wall. Water at atmospheric pressure and subcooling $\Delta T_{sc} = 3$ to 42 K. Wall superheating $\Delta T_{sp} = 487$ to 1236 K

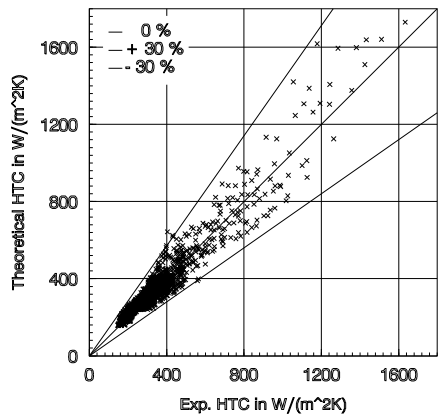


Fig. 16.16.3 Comparison between predicted and calculated heat-transfer coefficients for all data for spheres. Error band: $\pm 30\%$

We then modify the plane solution to one appropriate for spherical geometry in Chapter 22 Vol. 2 and verify it with a large number of experimental data provided by *Liu and Theofanous* in 1995. The data consist of single- and two-phase flow cases. The single-phase data cover subcooling from 0 to 40 K, liquid velocity from 0 to 2.3 m/s, sphere superheating from 200 to 900 K and sphere diameter from 6 to 19 mm. The two-phase data are obtained for

- (a) upward flow with a void fraction from 0.2 to 0.65, water velocity from 0.6 to 3.2 m/s, and steam velocity from 3 to 9 m/s, and
- (b) downward flow with a void fraction from 0.7 to 0.95, water velocity from 1.9 to 6.5 m/s, and steam velocity from 1.1 to 9 m/s.

Figure 16.16.3 presents the comparison between the predicted and calculated heat-transfer coefficients for all data. The error band is found to be $\pm 30\%$.

References

- Kolev, N.I.: Verification of the IVA4 film boiling model with the data base of Liu and Theofanous. In: Proceedings of OECD/CSNI Specialists Meeting on Fuel-Coolant Interactions (FCI), JAERI-Tokai Research Establishment, Japan (May 19-21 1997a)
- Kolev, N.I.: IVA4 analysis of the FARO L14 experiment (ISP 39). In: International Seminar on Vapor Explosions and Explosive Eruptions (AMIGO-IMI), Aoba Kinen Kaikan of Tohoku University, Sendai-City, Japan (May 22-24, 1997b)
- Kolev, N.I.: Film boiling: vertical plates. In: Proceedings of 4th World Conference on Experimental Heat Transfer, Fluid Mechanics and Thermodynamics EXHFT 4, Brussels, Belgium (June 2-6, 1997c)
- Lanzenberger, K.: Thermal radiation in multiphase flow, KWU NA-T/98/E011. 1998 Karl Wirtz Award for Young Scientists: K. Lanzenberger, Thermal radiation in multiphase flow - Application to the severe accident scenario of molten fuel coolant interaction (MFCI), Siemens AG, Power Generation (KWU) (1998)
- Liu, C., Theofanous, T.G.: Film boiling on spheres in single- and two-phase flows part 1: Experimental studies ANS Proceedings, Part 2: A Theoretical Study, National Heat Transfer Conference, Portland (August 1995)
- Okkonen, T., et al.: Film boiling on a long vertical surface under high heat flux and water subcooling conditions. In: Proc. of the 31st Nat. Heat Transfer Conference, Houston, Texas (August 3-6, 1996)

16.17 Behavior of clouds of cold and very hot spheres in water

We now verify the capability of IVA5 to describe multiphase flows consisting of cold or hot spheres dropped into water. In this way, the mechanical and thermal interaction is checked without having the effect of the melt fragmentation. We use for this purpose QUEOS experiments performed at Forschungszentrum Karlsruhe, Germany. In the QUEOS facility, see Fig. 16.17.1 (left), 62 experiments have been performed. The first 12 are documented by *Meyer and Schumacher (1996)*. Experiments with numbers 13 to 39 are presented by *Meyer (1997)*. A comparison between experiments with cold and hot spheres, employing three different sphere types in each case in a wide (180 mm) and short jet was presented by *Meyer (1996)*. The data of an experimental series with a smaller jet diameter (100 mm) and longer pours were published by *Meyer (1998)*. Important measurements of void fraction in hot sphere three-phase flow are reported by *Meyer and Kuhn (1999)*.

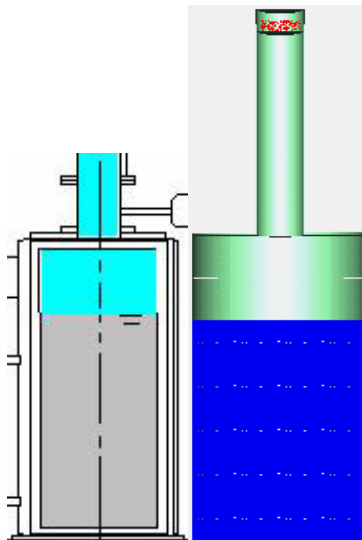


Fig. 16.17.1 Modeling of the QUEOS facility (left) by the IVA5 computer code (right)

We select from the 62 experiments three characteristic ones as listed in Table 16.17.1, and compare the predictions of IVA5 with the reported observations. The geometrical model for IVA5 is presented in Fig. 16.17.1 (right).

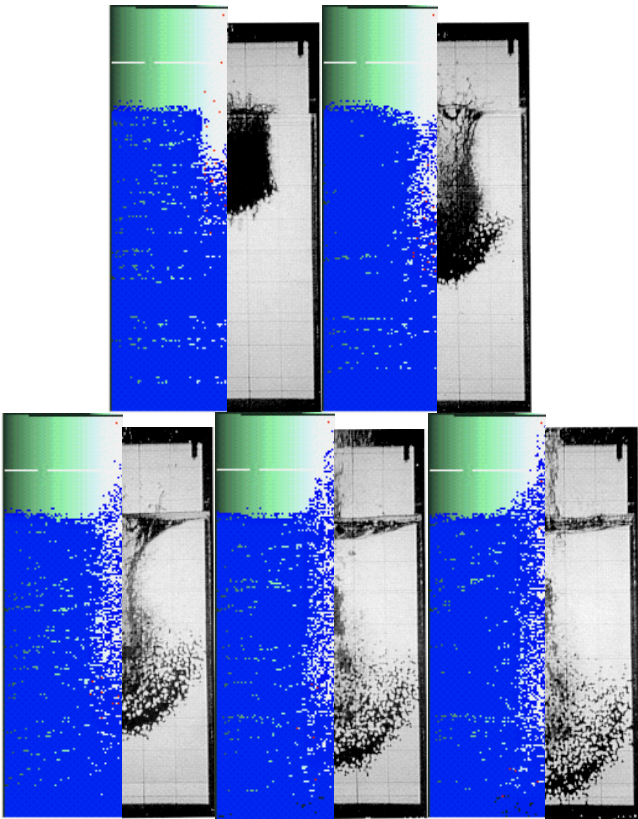


Fig. 16.17.2 Comparison between IVA5 predictions and the Q06 experiment for a cloud of cold solid zirconia spheres dropped into water: 0.62, 0.70, 0.78, 0.86, 0.94 s

Table 16.17.1. Summary of the QUEOS experimental conditions

No.	Material of spheres	D_3	Mass	Volume	Number	T_3	Pipe ID	T_2
		mm	kg	cm ³	-	K	mm	
06	ZrO ₂	10	7	1900	2340	300	207 open	Sat
12	Mo	4.2	6.9	1183	16600	2300	207 open	Sat
47	ZrO ₂	4.95	10	2600	25900	1833	100 open	Sat

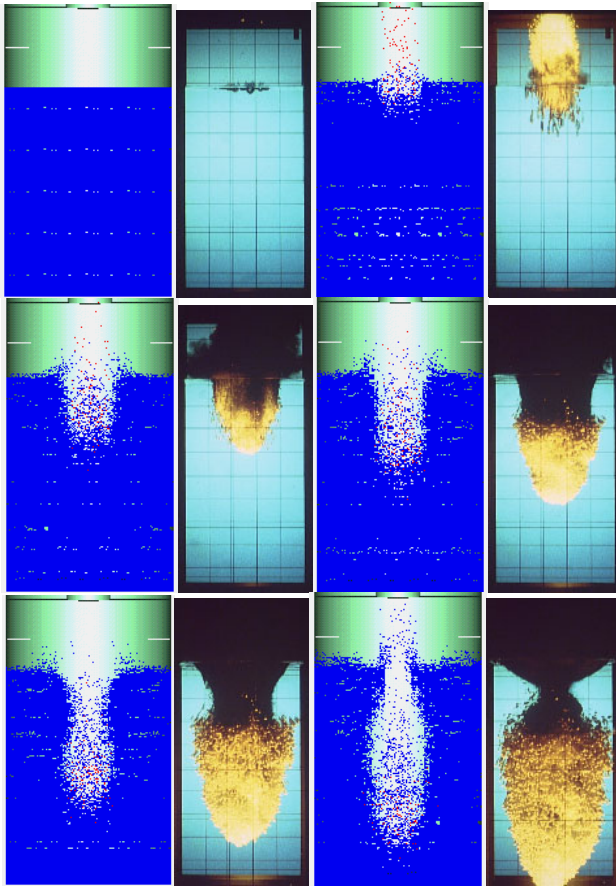


Fig. 16.17.3 An IVA5 prediction of the *Meyer* and *Schumacher* hot spheres-in-water experiment. Water volume fraction as a function of time: 0, 0.0238, 0.0734, 0.13, 0.1924, 0.2452 s. Experiment Q12: cloud of hot solid molybdenum spheres dropped into water

The particle penetration into the water and the corresponding water relocation are best illustrated using the experiment with No. 06 characterized by cold particles. Only the mechanical interaction is therefore modeled. The results are presented in Fig. 16.17.2. The time elapsing between the first particles touching the water surface and their touching the bottom is measured to be 0.4 s. The computed time was 0.397 s.

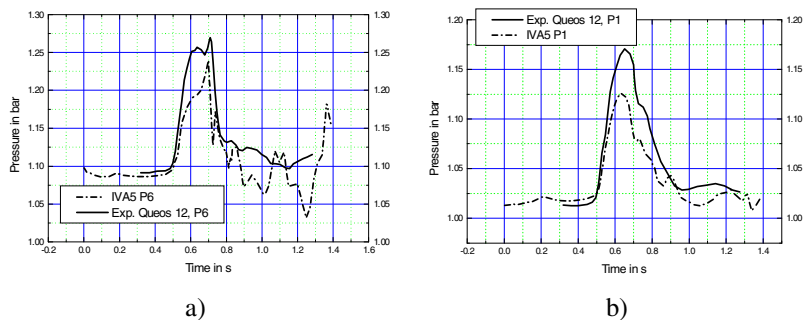


Fig. 16.17.4 Pressure as a function of time at a) P6 position – underwater space; b) P1 position – gas space

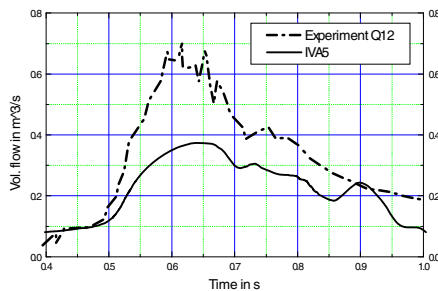


Fig. 16.17.5 Outlet volumetric flow as a function of time

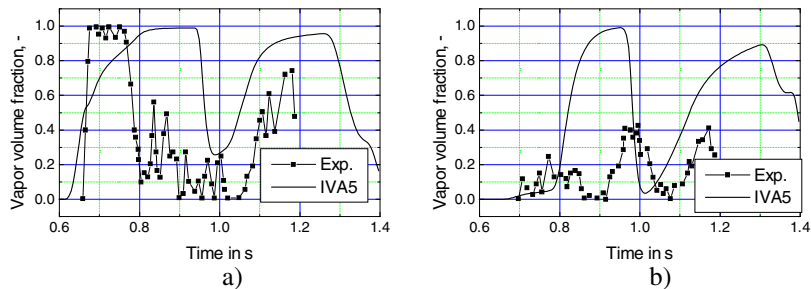


Fig. 16.17.6 Void fraction as a function of time at a) the centerline 40 cm from the bottom; b) 15 cm from the centerline, 40 cm from the bottom as a function of time

Experiment No. 12 was performed with the same geometry but the spheres consisted of a very good heat conductor heated up to 2300 K, the highest temperature ever reached in this kind of experiment. The predicted water volume

fractions are presented in Fig. 16.17.3. The photographs associated with this experiment are also shown in Fig. 16.17.3. A good agreement between the predicted and the experimental propagation velocity and level swell is obtained. Probably the lack of turbulence description makes the predicted radial expansion of the particles less than that measured.

The generated pressure as a function of time at two different positions is presented in Figs. 16.17.4a and b. The corresponding outlet steam flow is given in Fig. 16.17.5. IVA5 underpredicts the vapor generation in this case, which is consistent with the pressure under prediction in Figs. 16.17.4a and b. For this simulation the steady-state friction loss coefficient of 4.54 is used *Meyer and Schumacher* (1996). The appropriate modeling of this coefficient is very important and can be considerably improved for this case.

Void fraction measurements are extremely difficult in multiphase systems. In the QUEOS No. 47 experiment void fraction measurements are provided for points located 40 cm from the bottom at the symmetry axis and 15 cm from the symmetry axis without specifying the uncertainty band. The predicted and the measured results are presented in Figs. 16.17.6a and b. The secondary bubble release as observed by the experiment is predicted by IVA5. The gas front in the measurements on the centerline is very sharp. IVA5 predicts smooth origination of the gas front. The deviation between prediction and measurements for the secondary cycle increases.

Conclusions. The comparison presented in this chapter demonstrates that the main features of the mixing of cold and hot solid spheres with water are well predicted by IVA5.

One should keep in mind that *Lagrangian* presentation of the motion of each single particle would considerably improve the position prediction of the clouds of particles. For small-scale experiments this has already been implemented by several authors. However, with the computational technology currently available it is not yet possible to apply this technique to large industrial systems having hundreds of m^3 with 10^{10} particles per m^3 . Instead, master particles are used to represent a number of real particles, and this procedure has been used since the original PIC codes *Crowe et al.* Replacing large number of particles with a single master particle also results in numerical diffusion.

References

- Crowe, C.T., Stock, D.E., Sharma, M.P.: The particle-in-cell (PSI-cell) model for gas droplets flows. ASME, Trans., Series I-J. Fluids Eng. 99, 325–332 (1977)
- Meyer, L., Schumacher, G.: QUEOS a simulation-experiment of the premixing phase of steam explosion with hot spheres in water base case experiments, Wissenschaftliche Berichte FZKA 5612, Forschungszentrum Karlsruhe Technik und Umwelt, Karlsruhe (April 1996)

- Meyer, L.: The interaction of falling mass of hot spheres with water. In: ANS Proceedings 1996 National Heat Transfer Conference, Houston, Tx, August 3-6, vol. 9, pp. 105–114. American Nuclear Society, La Grange Park (1996)
- Meyer, L.: QUEOS a simulation-experiment of the premixing phase of steam explosion with hot spheres in water, Results of the Second Test Series, Internal Report 32.21.02/INR1962/PSF3267, Forschungszentrum Karlsruhe Technik und Umwelt, Karlsruhe (July 1997)
- Meyer, L.: QUEOS, an experimental investigation of premixing phase with hot spheres. Nucl. Eng. Des. 18 (1998)
- Meyer, L., Kuhn, D.: The interaction of very hot particles falling into water. In: 2nd Int. Symp. on Two-Phase Flow Modeling and Experimentation, Pisa, Italy, May 23-25 (1999)

16.18 Experiments with dynamic fragmentation and coalescence

Experiments with real molten material that are prototypic nuclear reactor materials are very important in the course of the code validation for melt–water interactions. Now, we step forward to model four of the FARO tests performed by JRC Ispra in Italy. The purpose of this section is to verify the code for a class of processes called nonexplosive melt–water interaction. All elements of the code are addressed in such a demanding simulation, e.g., code architecture, numerical methods, constitutive models, etc. The simulation of the FARO test will reveal the capability of the code to handle such flows with simultaneous evaporation condensation, and fragmentation of all participating velocity fields, etc. Among these, there are some important constitutive models, which are addressed during the computation, and their performance within the overall system will be also tested.

16.18.1 L14 experiment

Geometrical model, initial and boundary conditions. Detailed information about this test is available in *Magallon and Leva* (1996), *Hohmann et al.* (1994), *Annunziato et al.* (1996), *Benuzzi and Magalon* (1994). The geometry of the TERMOS vessel used is reproduced from *Benuzzi and Magalon* (1994) in Fig. 16.18.1a. The initial and boundary conditions, and an analysis of the observed phenomena are presented in *Hohmann et al.* (1994), *Annunziato et al.* (1996). The water volume was 0.798 m³ and the gas volume 0.761 (Fig. 16.18.1) + 0.5 (separator, connection lines) m³ including the expansion volume. This means that the initial gas volume fraction was of the order of 0.612. 125 kg melt (80/20 w% UO₂/ w% ZrO₂) with initial temperature ~3073 K are dropped in 623 kg saturated water having 2.05 m depth. The gas (77 w% steam + 23 w% argon) was under 5.1 MPa initial pressure and 536 K initial temperature. The simulation was performed assuming an axisymmetric process in 2D geometry with (12×64=768, 648 in the vessel) cells.

Results. Figure 16.18.2a shows the predicted melt release as a function of time and space. The computed melt outlet velocity multiplied by the local melt volume fraction in the axis of the outlet nozzle is presented in Fig. 16.18.2b. In *Hohmann et al.* (1994) the outlet velocity was estimated approximately without feedback

from pressure buildup and assuming a one-dimensional process and no flow separation in the nozzle. On the basis of such assumptions, the maximum of the predicted velocity in *Hohmann et al. (1994)* was 3 m/s. IVA5 predicts a maximum of about 3m/s. Figure 16.18.2b demonstrates the feedback effects of the pressure in the vessel on the outflow and the flow separation at the end of the discharge process.

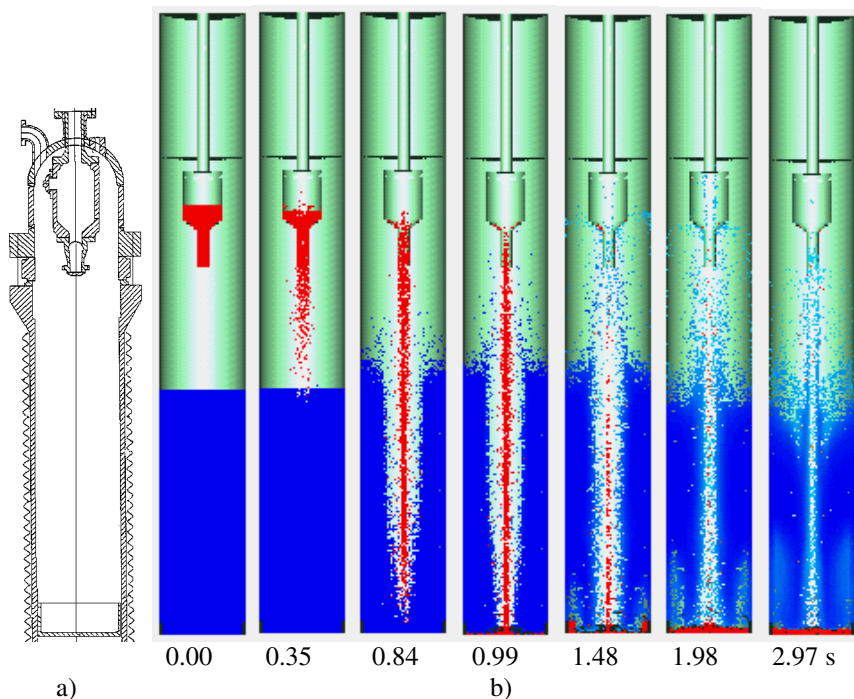


Fig. 16.18.1. a) IVA5 geometry model of the FARO L14 experiment. Number of cells: 768. Number of cells in the FARO vessel 648. b) Gas volume fraction as a function of space. Parameter: time

Melt falls down, interacts with water, and reaches the bottom. The processes of melt sloshing at the vessel bottom are presented in Fig. 16.18.3.

The experimentally observed leading edge position as a function of time is given in Fig. 16.18.4a. It is indicated by thermocouples placed at discrete positions in the vessel. The computed leading edge position is diffuse due to (a) fragmentation and (b) numerical diffusion. We take as a measure the easily recognizable interface between water and gas as seen in Fig. 16.18.1b. From Fig. 16.18.4a we see a good agreement between the IVA5 prediction and the measurements. Nevertheless, numerical diffusion associated with the first-order donor-cell method has to be reduced in future refinement of the IVA5 method.

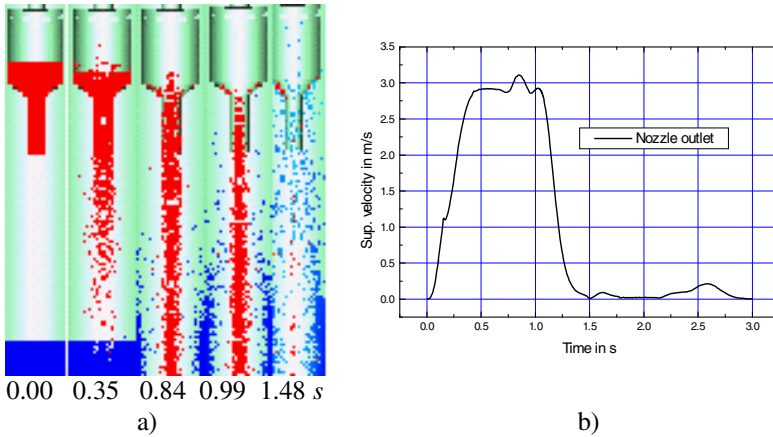


Fig. 16.18.2 a) Melt discharge as a function of time and space. b) Superficial velocity in the outlet nozzle as a function of time

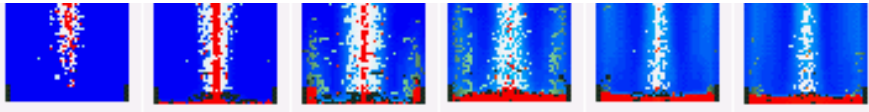


Fig. 16.18.3 Temperature of the melt presented only at places occupied by melt at the bottom as a function of space. Parameter – time: 0.84, 0.99, 1.48, 1.98, 2.51, 2.97 s

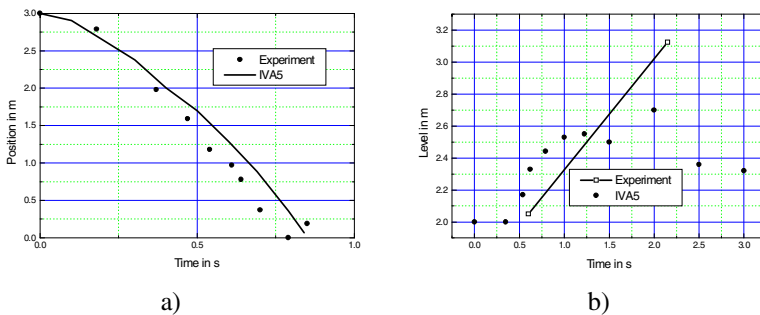


Fig. 16.18.4 a) Jet leading edge position in m versus time in s . b) Mixture level (IVA5: $r = 0.18$ m, volume fraction of water between 5 and 10 %) as a function of time

Figure 16.18.4b gives the water displacement in the course of the melt–water interaction. Discrete signals indicating the approximate position of the water level are available. The level in the computation was defined as the boundary with cells with less than or more than 5% water volume concentration. As seen from Fig. 16.18.4b the level is a very strong function of the radius and one signal curve is not representative. The estimated computed position for the level in accordance

with the above criterion is given in Fig. 16.18.4b. In view of the many uncertainties associated with this comparison this prediction seems reasonable.

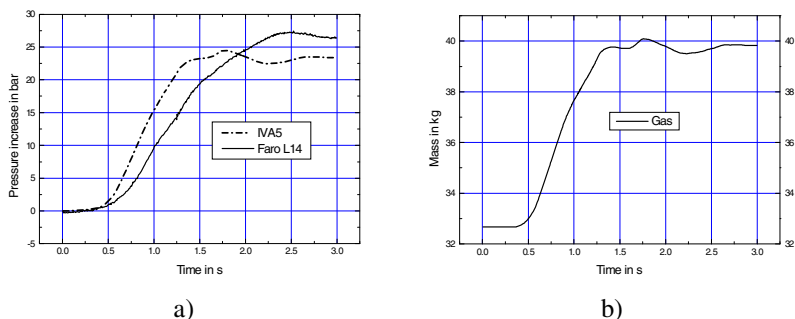


Fig. 16.18.5 a) Pressure increase as a function of time; b) Gas mass as a function of time

Figure 16.18.5a gives the most important information – the comparison between the predicted and the measured pressure as a function of time. The agreement is good. Comparing Figs. 16.18.5a and b we realize the proportionality between the evaporated mass and the pressure increase of the system. Presenting the pressure change with respect to the initial pressure as a function of the vapor mass change with respect to the initial vapor mass results in Fig. 16.4.1 in Section 16.4. It is a very interesting effect, as discussed in the introduction. The final turn off is due to the condensation at the end of the process.

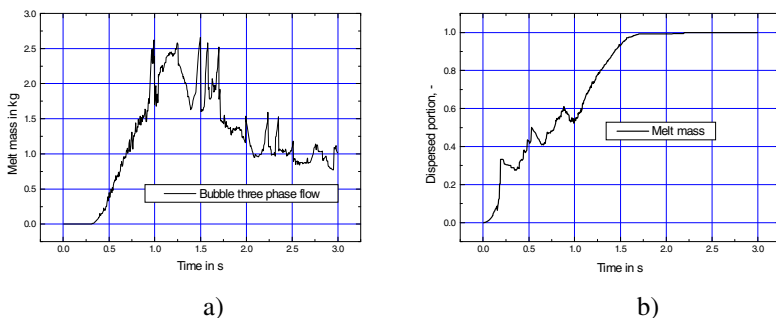


Fig. 16.18.6 a) Premixing melt mass in kg-melt mass being in dispersed melt-continuous water-gas bubble flow as a function of time in s; b) Part of the total melt being fragmented (dimensionless) as a function of time in s

Figure 16.18.6a shows the predicted mass of melt in the film boiling bubble flows. This is the most effective vapor production mechanism. From the comparison between Figs. 16.18.5a, 16.18.5b and 16.18.6a we see that the pressure increase in the first second is caused mainly by film boiling in three-phase flow. IVA5 predicts complete melt fragmentation after 1.7 s in this case, as indicated on Fig. 16.18.6b. The debris bed analysis after the experiment shows 16% nonfragmented

melt. The reason for this disagreement is simple. IVA5 does not predict the freezing interaction with the cold bottom and allows the melt to slosh further in the lower head as presented in Fig. 16.18.3. In the computation this causes freezing of the fragments before building a cake at the bottom. The computed arrival time for the melt at the water surface is about 0.38 s, which is some 17% faster than the measured 0.46 s. The computed arrival of the melt at the bottom is about 0.862 s, which is some 4.2% faster than the measured 0.9 s. The maximum of the cumulative energy conservation error in this computation was below 0.4%. For more discussion on this issue see *Kolev (1997a)*.

16.18.2 L20 and L24 experiments

The effect of the pressure on the nonexplosive melt–water interaction was studied in experiments L20 and L24 *Annunziato, et al. (1996, 1997)*. They were performed in the same geometry with some minor changes of the initial conditions except the initial pressure. The initial pressure was 20 and 5 bar, respectively. Figure 16.18.7 shows the material relocation as a function of space 1 s after the beginning of the experiments. We see that the lower the pressure the larger the produced volume due to evaporation.

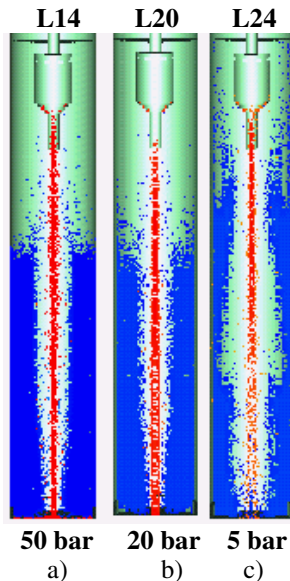


Fig. 16.18.7 The influence of the initial pressure on FCI. Material relocation after 1 s in the FARO experiments within the same geometry under virtually the same initial and boundary conditions except the initial pressure. Initial pressure: a) 50 bar; b) 20 bar; c) 5 bar

This causes much stronger material relocation if a gas volume is available for water depletion. This is an extremely important observation for the low-pressure melt–water interaction in real nuclear systems. Figures 16.18.5a, 16.18.8a and 16.18.8b present the comparison between the predicted and measured pressures as a function of time. We see an interesting tendency of IVA5 to slightly over predict the initial pressure change with time at 50bar, to predict a very good pressure change at 20 bar and to underpredict the pressure change at low pressure.

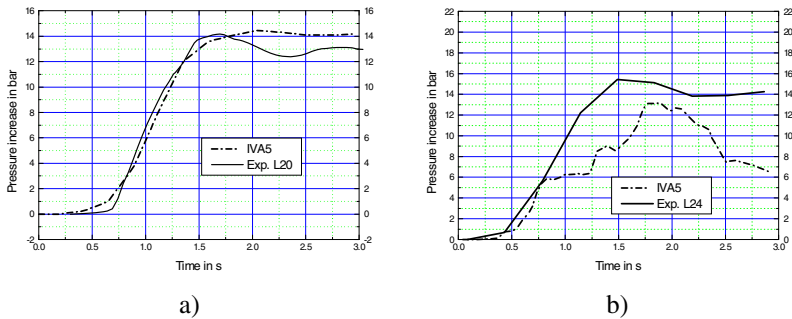


Fig. 16.18.8. a) Pressure as a function of time for the FARO L20 experiment. Initial pressure: 20 bar. b) Pressure as a function of time for the FARO L24 experiment. Initial pressure: 5 bar

Bearing in mind the complexity of the problem and the fact that many of the experimentally obtained empirical models are subject to known uncertainty, this agreement can be classified as good.

Note that *Yamano et al.* (1992) performed experiments with 20 kg of molten thermite penetrating 0.78 m³ of water at atmospheric conditions and initial relocation velocity 8 m/s. Increasing the pressure from 1 to 16 bar suppresses the explosion. *Mitchel et al.* (1981) reported a similar experiment with 54 kg of melt. Increasing the pressure to 10.9 bar suppresses the steam explosion. *Nelson and Duda* (1981, 1985) performed a small-scale droplet test in which increasing the external trigger pressure (impulse and energy) was required in order to induce an explosion by increasing the ambient pressure.

Thus, the increase in pressure has two effects on melt–water interaction: a) it decreases the intensity of the macroscopic material relocation and b) it increases the vapor film stability.

16.18.3 Uncertainty in the prediction of nonexplosive melt–water interactions

Results from applications of computer models are subject to uncertainty. This is basically due to model and parameter uncertainties. Model uncertainty arises in areas such as phenomenology, model formulation and numerical algorithms and is often partly due to intentional simplifications.

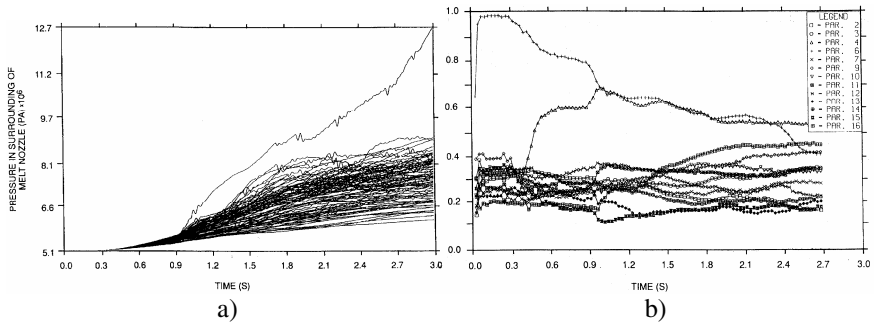


Fig. 16.18.9 a) Pressure in the vessel as a function of time. The pressure time history is the most important information if the code is used for practical design purposes. 96 alternative time histories were obtained with 96 randomly selected vectors of parameter values. b) Sensitivity measures of the pressure with respect to each of the 13 considered uncertainties. The main contributions to the uncertainty of the pressure as a function of time come from the emissivity coefficient (No.6) and from the stable particle size (No. 4). The initial temperature (No. 16) exhibits growing influence over time. The influence of the latter two is in the opposite direction to the emissivity coefficient

An uncertainty analysis is to provide a quantitative statement about the combined influence of potentially important uncertainties on the results. Additionally, and often most important, it provides quantitative sensitivity statements that rank the uncertainties with respect to their contribution to model output uncertainty. In this way it helps to guide research, model development and measurement efforts in order to reduce model output uncertainty most effectively *Kolev and Hofer (1996)*.

Uncertainty analyses for nonexplosive interactions using IVA4 computer code are reported by *Kolev and Hofer (1996)*. The FARO L14 experiment was simulated at that time and the two main results are given in Figs. 16.18.9a and b. The lessons from this analysis are also applicable for IVA5 computer code. They are summarized in the conclusion section.

16.18.4 Conclusions

1. The local volume- and time-averaged multifield conservation equations in porous media presented in Volume 1, Chapters 1 and 5, as well as in *Kolev (1995b, 1998, 1994a, 1994b, 1997b)* and the concept of dynamic fragmentation and coalescence for all of the velocity fields described in Vol. 2 *Kolev (1993)* and implemented in IVA5 computer code *Kolev (1995a)* are powerful tools for simulation of such complicated multiphase flows with strongly nonlinear interfield interactions.
2. Due to the combined influence of the uncertainty of the initial melt temperature and of the model uncertainties for the analyzed FARO L14 nonexplosive melt–water interactions, prediction is only possible for the following:

- (a) pressure increases within a (90%, 95%) tolerance interval of 24 bar width;
- (b) gas temperatures within a (90%, 95%) tolerance interval of 50 K width;
- (c) water temperatures within a (90%, 95%) tolerance interval of 30 K width;
- (d) melt temperatures within a (90%, 95%) tolerance interval of 110 K width.

The uncertainties of the

- (a) radiation emissivity coefficient of the melt surface;
- (b) final particle size after fragmentation in the separate effect fragmentation models (attention: not included in the FARO experiment); and
- (c) initial melt temperature;

are responsible for most of the uncertainty of the final results over most of the time.

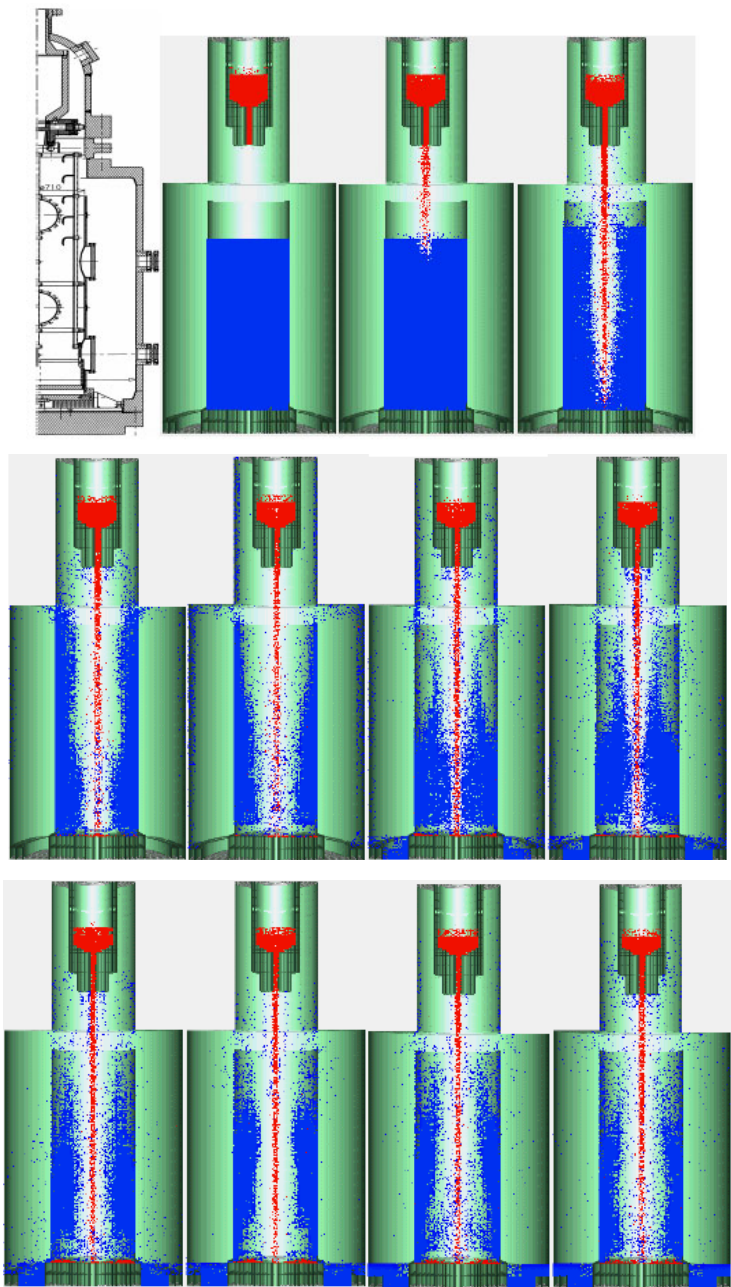
- 3. The IVA5 computational model essentially gives a good prediction of the main characteristics of the FARO L14, L20 and L24 experiments.
- 4. The fragmentation and film boiling models, as described in this volume form a sound basis for nonexplosive melt–water interaction modeling.
- 5. Numerical diffusion associated with the first-order donor-cell method has to be reduced in future refinement of the IVA5 method – see Chapter 12 in Volume 1 for ideas for high-order numerical methods.
- 6. The modeling of the stagnation of packed solid particles at horizontal surfaces requires further attention.
- 7. The influence of the errors inevitably associated with the numerical integration of the 21 nonlinear conservation equations with strongly nonlinear source terms has to be monitored in practical applications.

16.18.5 L28, L31 experiment

The last experiment of the FARO research team, L28, was performed in the modified geometry given in Fig. 16.18.10a *Silverii* and *Annunziato* (1999). The initial conditions and the geometry for the simulations performed with IVA5 are given in Fig. 16.18.10b, first picture. The melt mass is 174.9 kg. The initial pressure 5 bar, the water temperature 151.4 °C, the steam temperature 181 °C and the melt temperature 2973 °C. Figure 16.18.10 b) shows the volume fractions of melt and water as a function of time and space.

Figure 16.18.11a shows the pressure as a function of time. Compared with the material relocation we see that the pressure in the computation is controlled by the depletion dynamics. IVA5 predicts an increase in pressure about 4bar larger at the end of the process compared to the measurements. Figure 16.18.11b shows the accumulative melt mass transported into the external region. We see that IVA5 also predicts this phenomenon, 6.8 kg are measured and about 12 kg are computed. The maximum depleted water in the external region is computed to be

about 290 kg. The measured value for this is about 180 kg. The computed water expulsion after 3.5 s does not take place in the experiment.



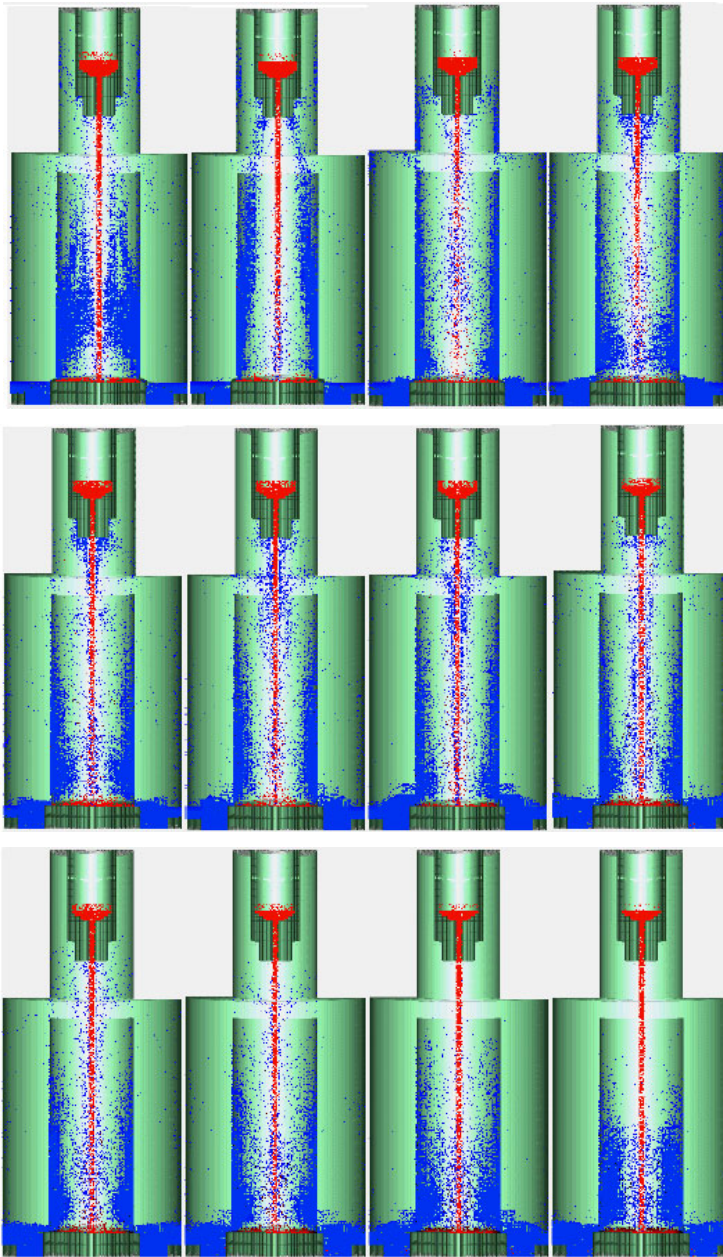


Fig. 16.18.10 a) Geometry of the FARO FAT vessel. b) Geometry representation of the IVA5 computation. Initial conditions. An IVA5 pretest simulation of FARO-FAT L28 experiment. 179.4 kg corium dropped into water. Volumetric fractions of melt and water as a function of time: 0, 0.34, 0.74, 1, 1.26, 1.76, 2.00, 2.26, 2.5, 2.76, 3, 3.26, 3.5, 3.76, 4, 4.26, 4.5, 4.76, 5, 5.26, 5.5, 5.75, 6 s.

Conclusions. a) The important two-dimensional depletion phenomena are predicted by the code. b) Keeping in mind the uncertainty inherent in the mathematical modeling of melt-coolant interactions the general pressure level is predicted well by the code. c) The pressure signature as a function of time indicated that there is still room for improvements to the model.

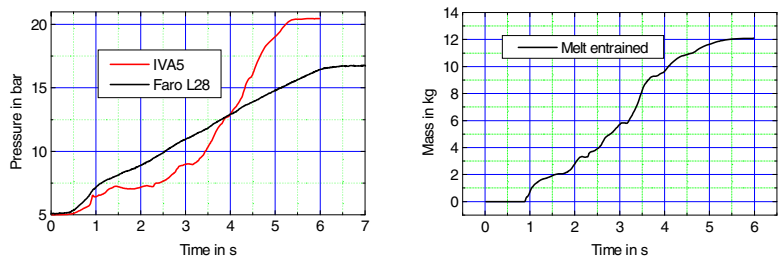


Fig. 16.18.11 a) An IVA5 pretest simulation of FARO-FAT L28 experiment. 174.9 kg corium dropped into water. Pressure as a function of time. b) Melt carried by the water-steam mixture into the external region. Measured carryover 6.8 kg, computed 12 kg

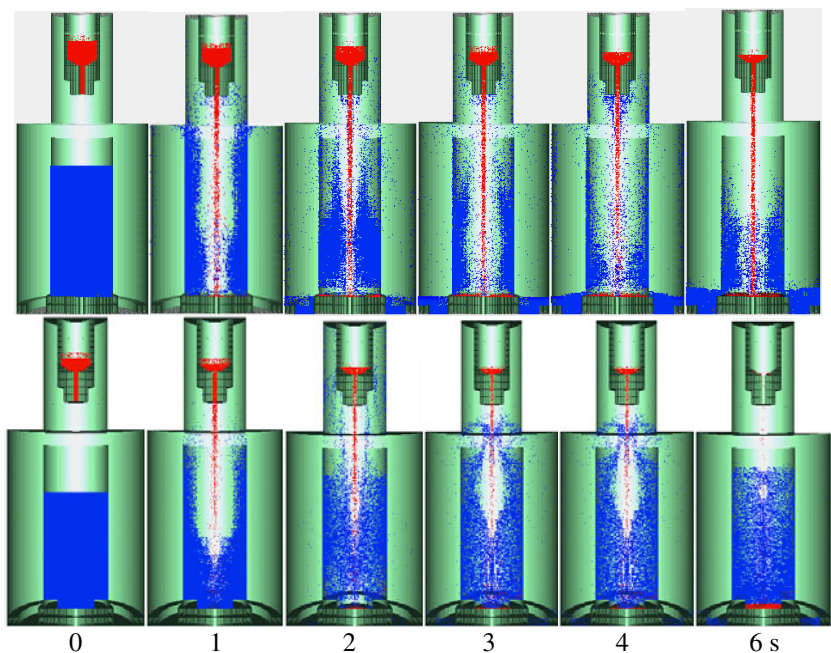


Fig. 16.18.12 Comparison between the material relocation predicted by IVA5 for the L28 (top) and L31 (bottom) tests

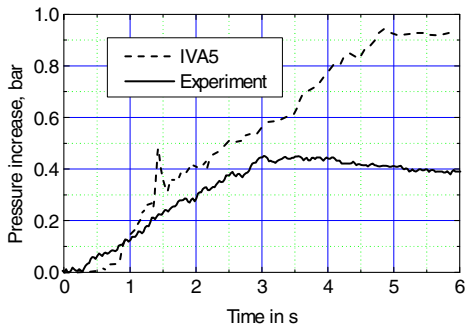


Fig. 16.18.13 L31 pressure increase as a function of time

The counterpart experiment to L28 having subcooled water at the beginning of the experiment was L31 *Silverii* and *Magallon* (1999). The simulation with IVA5 as shown in Fig. 16.18.12 predicts properly the strongly reduced vapor production due to the water subcooling, the resulting reduced material relocation and reduced increase in pressure, Fig. 16.18.13, compared to L28.

16.18.6 PREMIX-13 experiment

Introduction. Over the last 30 years experiments with melt dropped into water in different modes have shown that there are considerable differences in the behavior of different materials. One prominent example is the different behavior of UO_2 and alumina. The explanation we have for these differences and the arguments are presented in Chapter 9 of Volume 1. In order to investigate the physical nature of this difference experiment activities are performed. The PREMIX experiments, *Keiser*, et al. (1998a, b, 1999, 2001), *Huber* et al. (1996) performed at the Research Center Karlsruhe, Germany form part of these activities – see Table 16.18.1 and Figs. 16.18.20 and 16.18.21. The subject of this section is the simulation of the PREMIX 13 experiment and drawing of conclusions about the quality of the modeling technique.

Table 16.18.1 Conditions for the PREMIX tests PM12 through PM18

No	Melt						Water			Syste m
	Mass released kg	Nozz le diam mm	Init. Driv. Press. MPa	Speed ¹ m/s	Falling height mm	Release time s	Depth m	Temp. K	ΔT_{sub} K	Press. MPa
12	29.0	60	0.046	3.8– 4.2	193	0.95	1.36	372	1	0.1
13	23.8	60	0.052	4.0– 4.2	213	1.05	1.34	372	1	0.1

14	23.2	60	0.066	4.5–4.7	213	0.95	1.34	372	1	0.1
15	23.1	60	0.03	3.2–3.3	323	1.25	1.23	416	8	0.5
16	60.4	48	0.01 ²	1.9–2.5	223	5.00	1.33	419	5	0.5
17	16.0	48	0.01 ²	1.7–2.6	223	1.70	1.33	290	104	0.22
18	14.6	48	0.015 ²	1.9–2.9	223	1.50	1.33	370–263 ³	26–34	0.22

¹ on first melt–water contact–maximum; both values are calculated by the experimentalists.

² averaged value; pressure was controlled during the melt release.

³ the scatter was due to internal convection prior to the start of the melt release.

The PREMIX-13 experiment. Briefly, the PREMIX 13 experiment consisted of the injection of about 23.8 kg of alumina at 2600 K through a nozzle of inner diameter 6 cm and length 21 cm into a water pool 1.34 m deep with initial temperature 372 K at atmospheric pressure. The geometry of the test section is given in Figs. 16.18.22 and 16.18.23. The dynamic viscosity of the melt was measured at 2217 K and reported to be less than 4 cp. The equivalent diameter of the cylinder containing the water was 0.684 m. The melt was injected by inert gas with a volume of 0.0761 m³ and an initial pressure of 0.152 MPa. The distance between the nozzle outlet and the water surface was 21.3 cm. The circumferential space around the melt supplier with an external diameter of 40 cm forms a release path for the expansion. Release pipes of diameter 10 cm were installed at four azimuthal positions on the top of the vessel. The variables measured were pressure at various positions, temperatures and collapsed water level. The form of the interaction was filmed with a high-speed camera through appropriate glass windows.

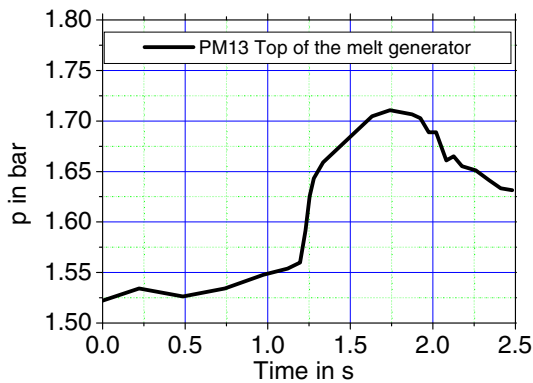


Fig. 16.18.14 Boundary condition: pressure at the crucible gas supply-and-venting pipe for PM13

IVA5 model. The initial conditions and the geometrical model used in IVA5 simulation are shown in Fig. 16.18.16. All parameters are kept as in the experiment. The exceptions are that a) the model cuts the space below the core catcher filled with water and b) the pressure at the gas venting pipe atop of the melt generator was not set as a boundary condition as given in Fig. 16.18.14. Instead, the venting pipe is considered to be isolated from the test section. As we will show in a moment, we will remove this assumption for the analysis of PREMIX 17 and 18. Use is made of the geometrical symmetry and the process is simulated as two dimensional inside the $\frac{1}{4}$ sector. 32×67 discretization cells are used for the r and z directions, respectively.

Results of the simulation. Figure 16.18.16 shows the material displacement and interaction. The participating phases are represented by different colors only at those positions occupied by them during the transient. This kind of presentation makes the figures self-explanatory. The experimentally observed jet dispersion is given in Fig. 16.18.17. The pressures at various different positions are shown in Fig. 16.18.18. The measured pressures are also shown in this figure.

PREMIX 15 differs from PREMIX 13 mainly in the initial pressure, which was 0.5 MPa.

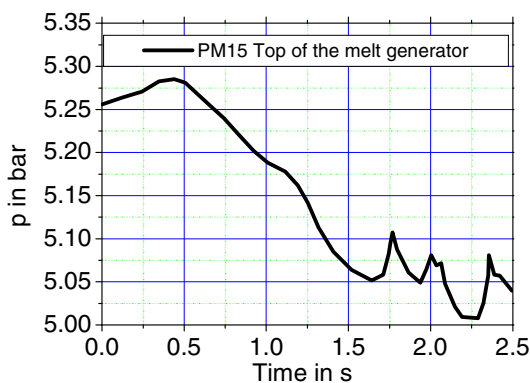


Fig. 16.18.15 Boundary condition: pressure at the crucible gas supply-and-venting pipe for PM15

Similarly to the previous case the venting pipe pressure history recorded in Fig. 16.18.15 was isolated. The IVA5 predictions of the PREMIX 15 are given in Figs. 16.18.19 and 16.18.21. The observed material relocation is presented in Fig. 16.18.20.

Conclusions

1. The overall level of predicted pressure is similar to those observed. At elevated pressure IVA5 over predicts the pressure. The trend of higher initial pressure

and a lower pressure increase is properly predicted by IVA5. Surprisingly, the fluctuations predicted in the computations were not observed experimentally. This is even more surprising, as such processes are well known to be very noisy.

2. The computed volumetric flow rate starts with a similar gradient to that observed, but reaches a plateau that is two orders lower than that measured, a result of not modeling the turbulent jet disintegration as will be discussed later. The drop in the gas volumetric flow rate for a period of 0.5 s is due to water accumulation in the region ahead of the discharge pipe. The representation of the discharge pipe 10 cm diameter by porosity in a 2D manner is not appropriate. Real 3D analysis is recommended.
3. One of the greatest discrepancies between the experiment and the computation is the form of the melt downstream of the nozzle. The observed form resembles very much the process after a spray nozzle. The observed diameter of the dispersed jet increases from 6 to 10 cm from the nozzle outlet to the initial water level. As a result, the melt reaches the water surface prefragmented. This influences greatly the later behavior of the process. The experiment gives the impression of cooling of a predispersed family of droplets that reaches the surface and descends slowly by “eroding” water with a large horizontal cross-section providing appropriate venting of the generated steam without substantial water entrainment. The code simulates jet behavior characterized by no fragmentation in the gas and intensive fragmentation during the interaction with the water. A kind of channeling produces large-scale instabilities in the water environment with a cyclic character, degraded in a later phase to complete intermixing behavior. To explain the differences a new simple jet fragmentation model was derived in Chapter 10, Eq. (10.43),

$$\Delta L_j / D_j = \frac{1}{2} V_j / \left\{ \left(c_{ej} / 2 \right)^{1/2} \left(\rho_c / \rho_j \right)^{1/2} \Delta V_{ej} + c V_j \right\},$$

where ΔL_j is the fragmentation length, D_j is the jet diameter, V_j is the jet velocity, c_{ej} is drag coefficient exerted by the jet submerged in continuum, ρ_c and ρ_j are the densities of the surrounding continuum and of the jet, ΔV_{ej} is the velocity difference between the continuum and the jet, and $c V_j$ is the lateral fluctuation velocity with a constant c being around 0.1. The simple model reproduces well the existing limiting cases known from the literature. Simple jet-fragmentation analysis assuming a radial velocity fluctuation of 10% from the axial velocity magnitude results in complete fragmentation of 30 cm, which is exactly what was observed in the experiment. Thus, the following conclusion is made:

Turbulence modeling in multiphase flow is important for predicting fragmentation processes. In cases where the fragmentation is the main driving force of the process the turbulence modeling starts to be the crucial element of the model.

4. The pressure boundary conditions as specified in Figs. 16.18.14 and 16.18.15 have to be taken into account. This will be done in the next section by simulating PREMIX 17 and 18 where substantial improvement of the pressure prediction is obtained.

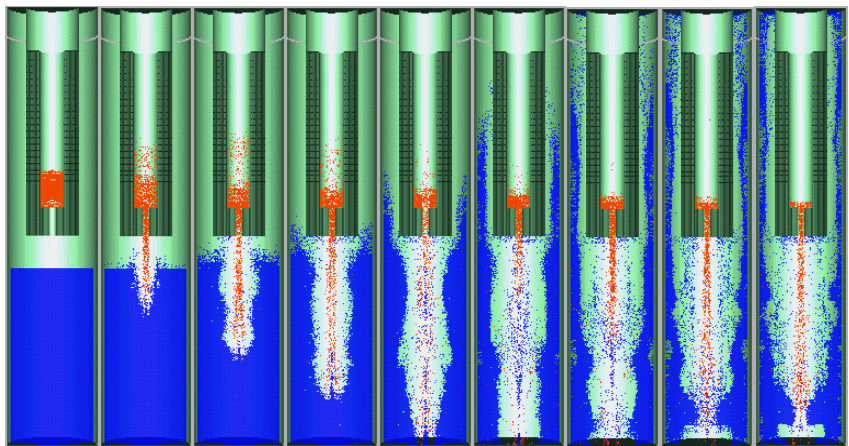


Fig. 16.18.16 An IVA5 simulation of PREMIX 13. Volumetric fractions of alumina and water as a function of space. Parameter: time; the time step between the pictures is 0.1 s

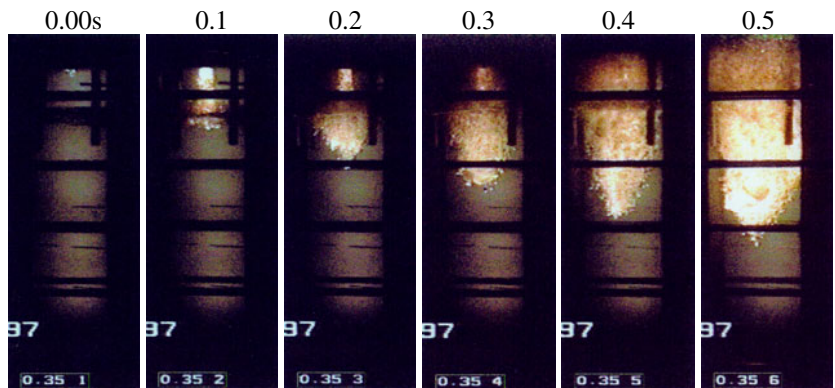


Fig. 16.18.17 Photographs of hot alumina in water. PREMIX 13 experiment, *Kaiser, et al.* (1998a)

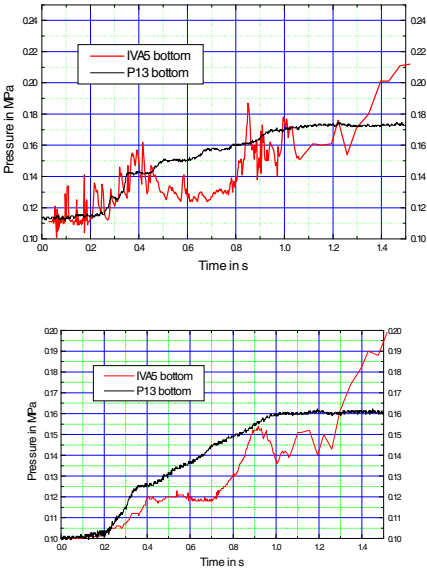
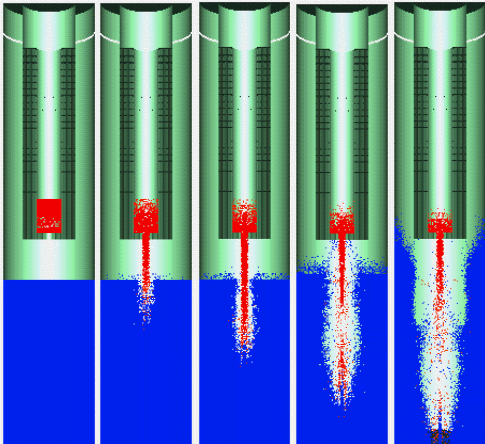


Fig. 16.18.18 Pressure as a function of time at different vertical positions



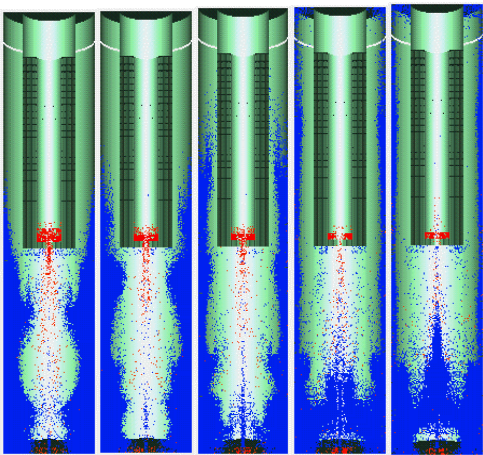


Fig. 16.18.19 PREMIX 15: Pressure as a function of time at different vertical positions. Parameter: time, the time step between the pictures is 0.1 s

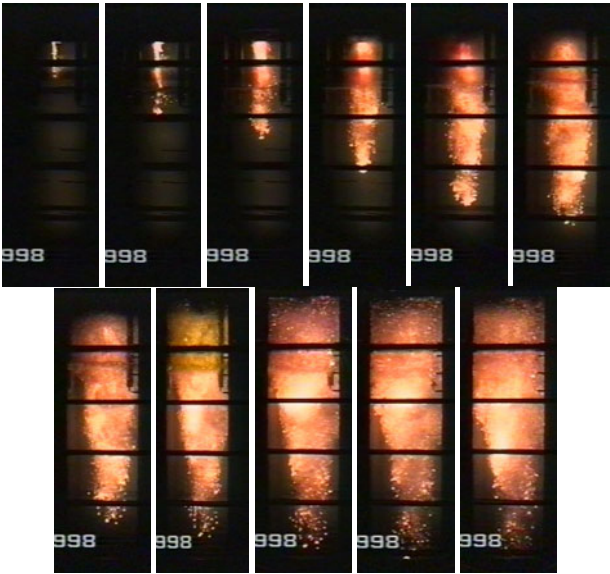


Fig. 16.18.20 Photographs of hot alumina in water. PREMIX 15 experiment *Kaiser, et al. (1998b)*. First picture: water level reached by the melt jet. The time between two pictures is 0.1 s

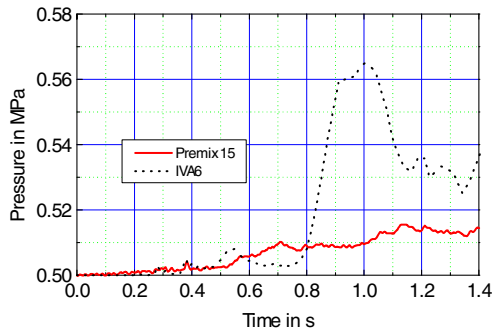


Fig. 16.18.21 IVA5 prediction of the PREMIX 15 experiment

16.18.7 PREMIX 17 and 18 experiments

Geometry: As mentioned before, the PREMIX experimental program was carried out over the years 1996 to 2001, *Kaiser*, et al. (1998a, b, 1999, 2001), *Huber* et al. (1996) at Research Center Karlsruhe (FzK) in Germany. The geometrical arrangement used serves (a) to produce alumina in a melt container by igniting thermite, (b) to separate the iron from the thermite by the melting of the first steel membrane that has a ring form, and (c) to release predominantly alumina, if possible, through the melting of the second steel membrane (0.2 mm thick). The melt container geometry is reproduced from *Kaiser*, et al. (2001) in Fig. 16.18.22. The container is connected to the gas supply and venting systems at the top. The melt is then released into a water container as shown in Fig. 16.18.23. Above the bottom there is a fragment catcher. The products of the melt–water interactions are convected in the internal space of the facility. In some of the experiments, but not in the particular PM17 and 18 that are of interest here, a venting system as shown in Fig. 16.18.22b was used.

Initial conditions: The initial conditions relevant for the computational analysis are given in Table 16.18.2. Note that not all the melted mass was found in the interaction volume probably due to crust formation. The melt-release temperature was given in *Kaiser*, et al. (2001) as 2600 K. The content of iron in the released alumina was estimated in *Kaiser*, et al. (2001) to be less than 10%. The distance between the nozzle outlet and the water surface was 223 mm.

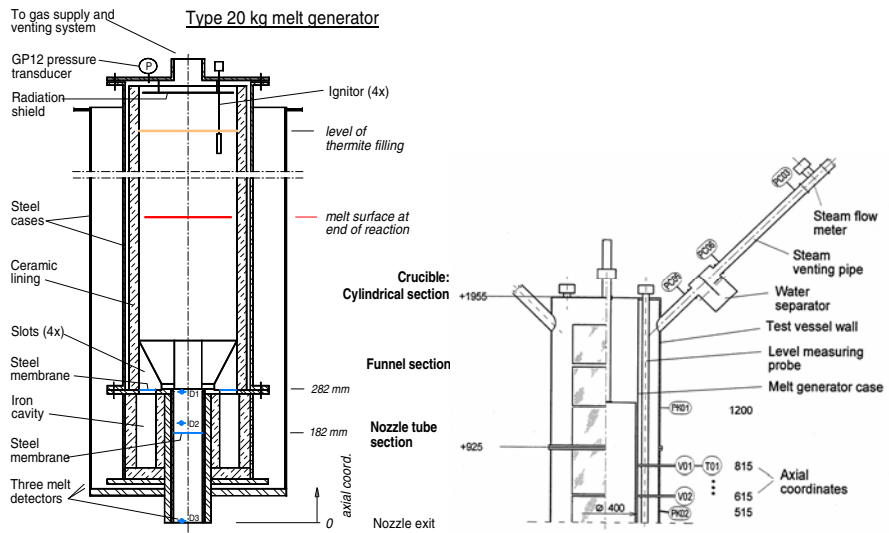


Fig. 16.18.22 a) Schematic diagram of the melt generator. b) Venting lines. Locations of the pressure transducers mounted in the annular gas space and in the venting line no. 3

Boundary conditions: The experimental space of interest is a closed space except for the so-called “gas supply-and-venting pipe”. The only variable boundary condition was applied by the specially designed automatic procedure at the crucible gas supply-and-venting pipe.

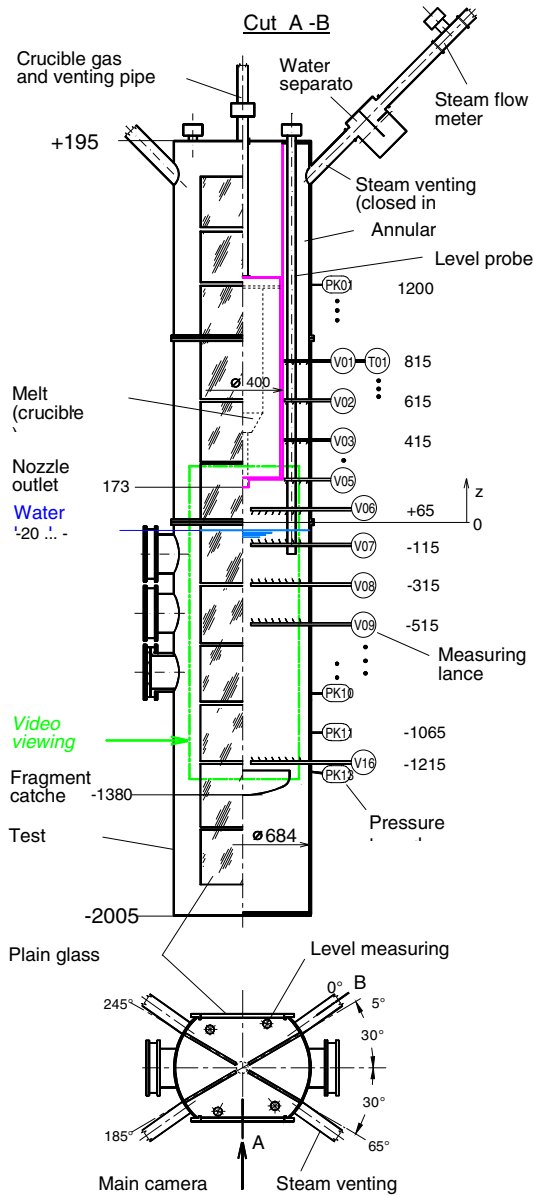


Fig. 16.18.23 The PREMIX test facility

We will not simulate this pipe but replace its action by a boundary condition prescribing pressure as a time function at the pipe cross-section just at the top of the interaction vessel. We reproduce for convenience the measured curves given in

Fig. 16.18.24 for PM17 and 18 with a much smaller number of characteristic points than that experimentally obtained.

Table 16.18.2 Initial conditions

No	Date	Melt mass/kg produced/released	Melt mass/kg interacting*	T-water sub. /K	p/MPa	Duration of melt release/s
PM17	20.4.99	15/14.36	7.1+5.9+0.66+0.76	104	0.2	2
PM18	07.7.99	15/14.56	5.48+5.68+3.44+0.	26	0.2	2

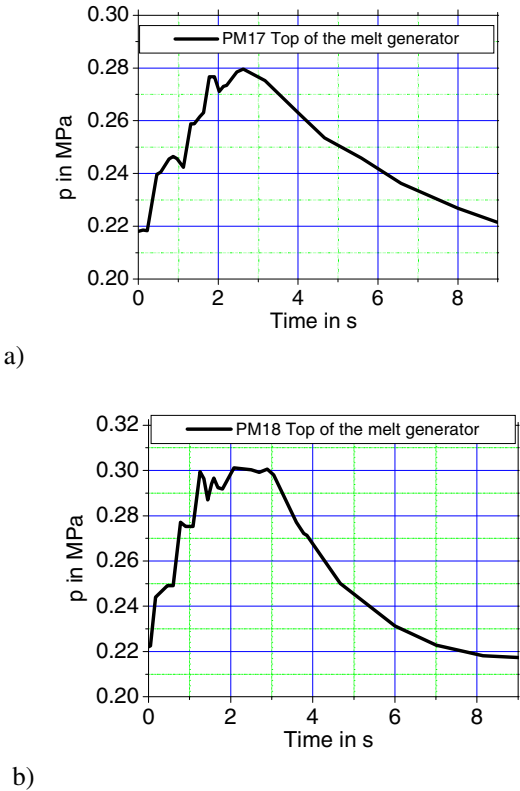


Fig. 16.18.24 IVA_5M boundary condition: pressure at the crucible gas supply-and-venting pipe: a) for PM17; b) PM18

Important. Note that in the experiment all curves are related to a zero time point defined as the moment at which the jet touches the water surface.

What was measured? The experimentally measured pressures at different positions were acquired with a frequency of 10 kHz (some pressures have been redundantly measured with 50 kHz). The data made available from the experimentalists are then compressed to 1 kHz without smoothing. Another important part of the data acquisition system was the film production taken through specially designed glass windows as shown in Fig. 16.18.23. The installed mass flow measurement at the venting pipes was not active during PM17 and 18 because the pipes are isolated from the interaction vessel.

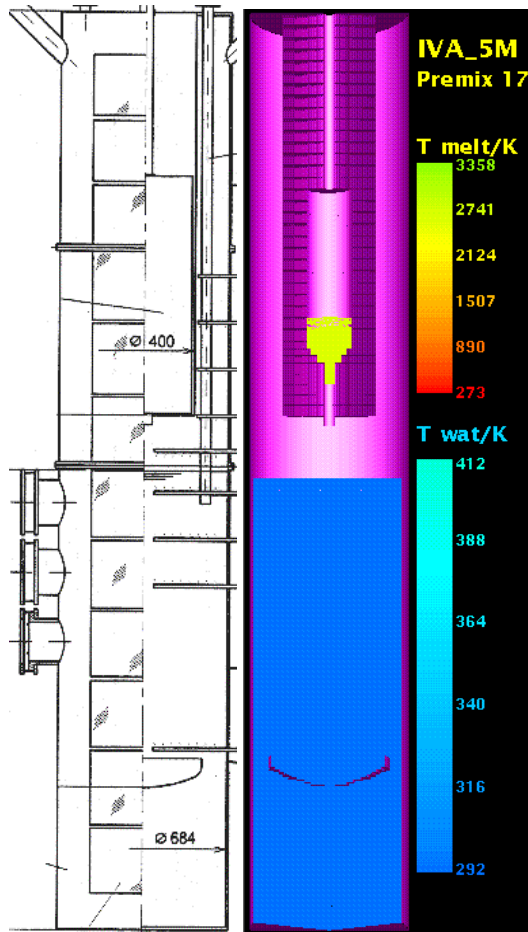


Fig. 16.18.25 Comparison between the real PREMIX vessel geometry and the IVA_5M geometry model

The IVA_5M model: Geometry: as will be demonstrated in a moment, many details of the geometrical representation have an important impact on the adequate

description of the processes. We assume that the process is axisymmetric, and represent the process as a two-dimensional using 2268 finite-volume cells – 27 radial and 84 axial nonequidistant steps in cylindrical geometry as presented in Fig. 16.18.25. Realizing the impact of appropriate modeling of the form of the debris catcher we increase the resolution in this region.

Variable-geometry boundary conditions. We start with a closed lower steel membrane. Experiments in IKET-FzK demonstrated that steel membranes sustain oxide jets for longer before melting completely compared for instance with brass membranes. We do not know exactly the time delay of melting of the lower membrane with respect to the upper one and judge the opening characteristics from the diameter of the jet filmed during the experiment.

Initial conditions. The initial conditions for the water are posed exactly as reported from the experiment. We use air as an inert gas with the environmental temperature outside the melt generator and with a melt temperature above the melt.

Some natural uncertainties in the initial conditions still remain due to the nature of such experiments. During the processes in the melt crucible we do not take into account that the thermite reaction is usually inhomogeneous, and that the resulting mixture consists of the nonmiscible alumina and iron with 53.1 mass% iron – see the discussion in Huber et al. (1996) p. 3. In Huber et al. (1996) p. 4 only 81% alumina was found in the released debris and in Kaiser, et al. (2001) the figure of 90% is given. We use thermal and transport properties for pure alumina but not for the alumina–iron suspension.

Comparison between theory and experiment, Kolev (2003)

PM17. Figure 16.18.26 shows the predicted and measured pressures in the gas. The agreement is good.

Figure 16.18.27 shows the predicted and measured pressures in the water. We realize that the magnitude of the averaged pressure excursion is properly predicted by the code. The strong water subcooling is the reason for the high-frequency oscillation. The oscillations by IVA_5M are predicted with a numerical resolution of 500 kHz. The pressure oscillation frequency found in the computation was about 70% higher than those found in the experimental measurements. A parametric study using PM18 reveals that the stepwise modeling of the smooth core catcher introduces its own numerical frequencies, which overlay those generated by the condensation oscillations.

Figure 16.18.28 shows the observed melt–water interaction. The time zero is set to be about the time of the first melt–water contact. The simulated results are presented in Fig. 16.18.29. From the velocity vectors that are not given here, we realize that the process consists of two well-separated phases: (a) the release phase, and (b) the natural three-phase circulation phase of cooling the sloshing melt in the catcher. In the first phase the descending melt jet fragments without strong net vapor production because of the water subcooling. In the second, the

melt sloshing from the center to the external boundary and back interacts with water, producing much more steam and building the pressure in this strong nonequilibrium system.

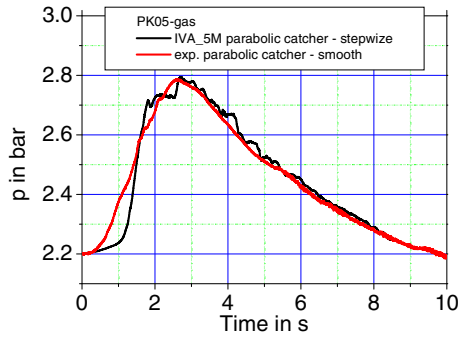


Fig. 16.18.26 Wall pressure in the gas PK05 ($z = 2.12$ m) as a function of time

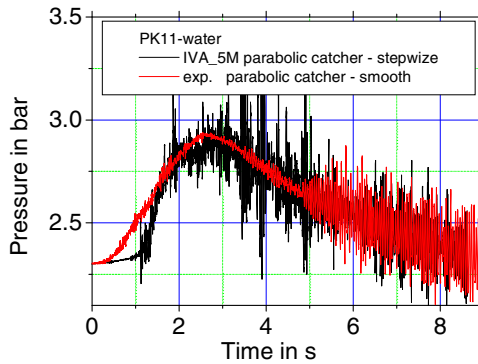
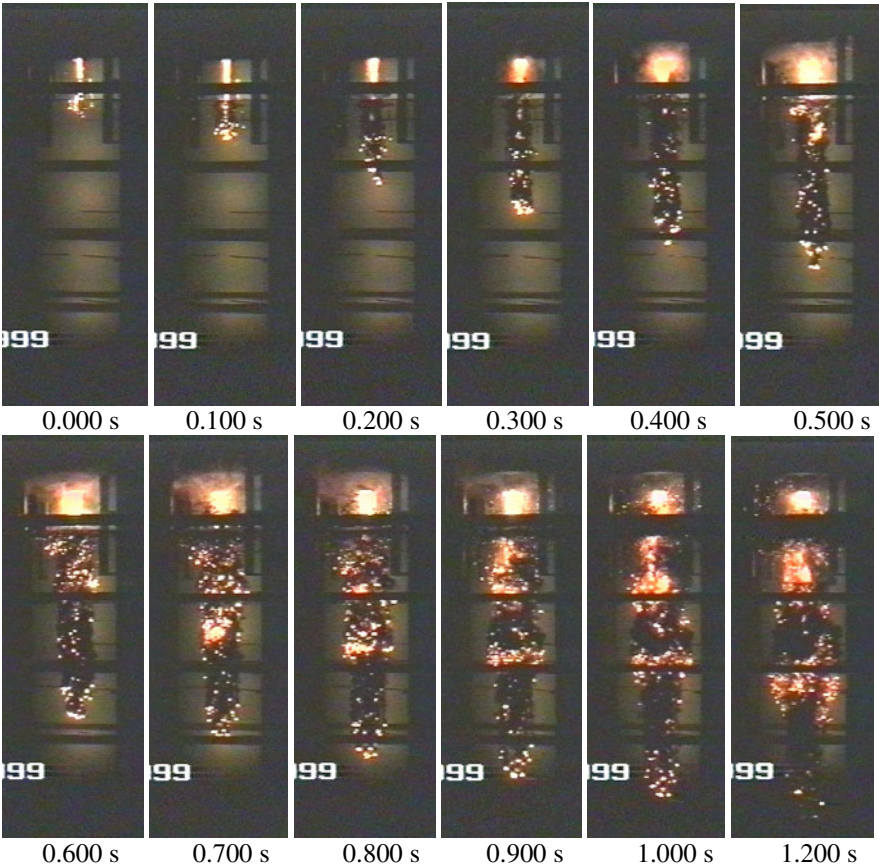


Fig. 16.18.27 Wall pressure in the water PK11 ($z = 0.94$ m) as a function of time



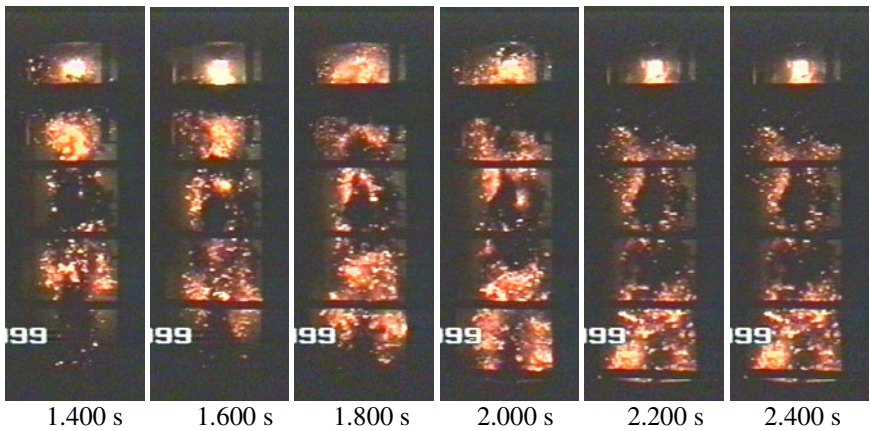
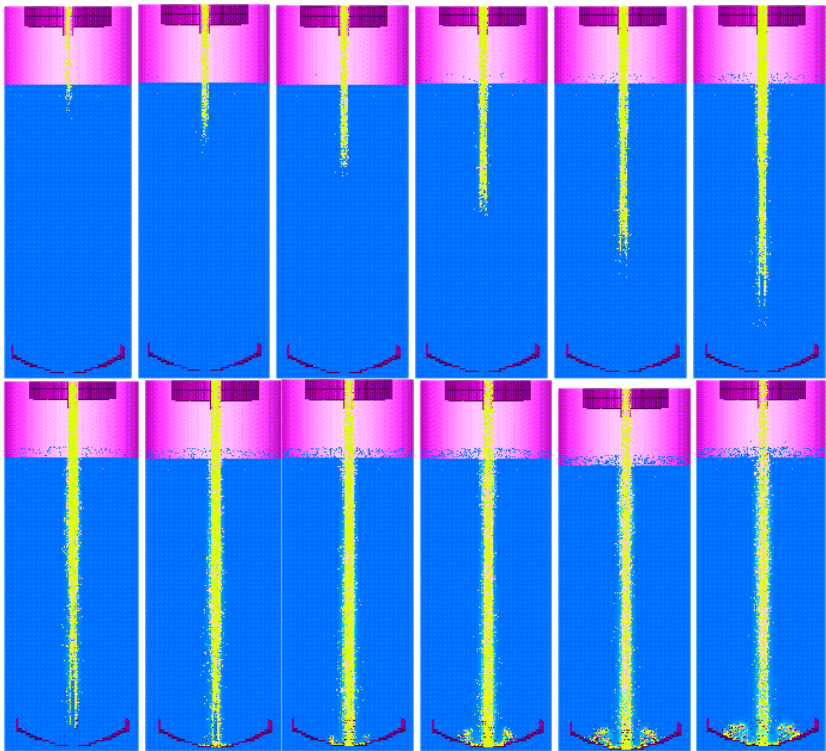


Fig. 16.18.28 PM17: Video pictures showing the three-phase flow in the interaction zone (larger time steps)



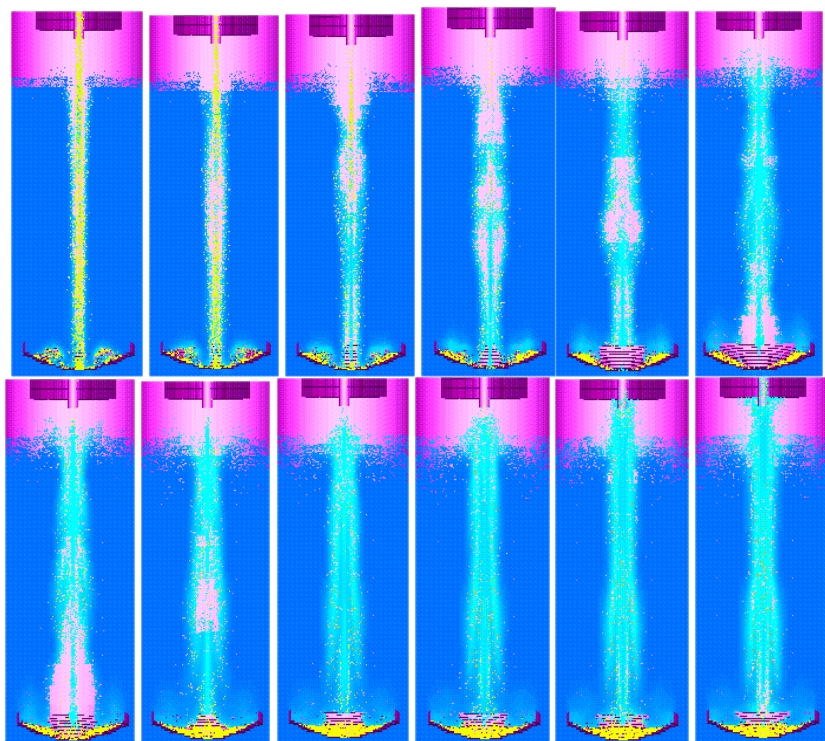


Fig. 16.18.29 IVA_5M simulation of PM17: video pictures showing the three-phase flow in the interaction zone (time step 0.1 s)

The resultant three-phase mixture moves upwards along the axis, and downwards in the external region. The suspension of the melt fragments is an observed fact in the experiment and is well predicted by the code. Strong radial temperature differences are predicted inside the water, as shown in Fig. 16.18.30, which explain the increasing net vapor production with the time. Then, the three-phase convection enforces mixing and the steam produced is predominantly condensed. The sloshing process in the catcher disappears with the time, thus reducing surface fragmentation and slowing down the interaction.

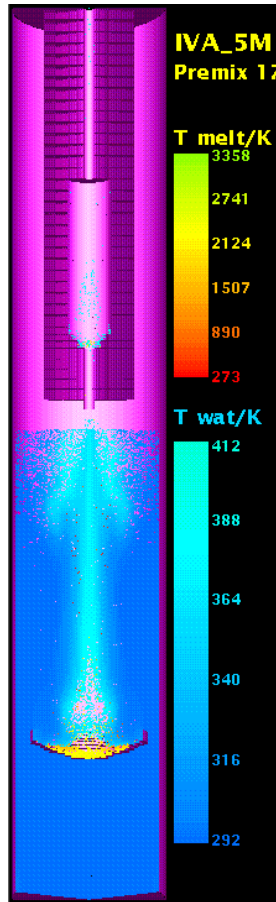


Fig. 16.18.30 Water temperature 5.55 s after the first melt–water contact

Not modeled in the simulation is the heat transfer from the melt through the catcher into the water, which is associated with additional melt freezing at the bottom.

PM18. In the next simulation we use the same initial conditions as in the case of PM17, except for the initial water temperature. The resulting pressures are presented in Figs. 16.18.31 and 16.18.32. As already mentioned in the case of PM17 the processes inside the catcher strongly influence the pressure build. The catcher used has a smooth surface. In the simulation the parabolic form of the catcher is represented by steps. In the next simulation we represent the catcher with a cylindrical container having a plane bottom. The results are presented in Figs. 16.18.33 and 16.18.34. We see that the flat bottom catcher does not generate high-frequency oscillations in the initial phase but does generate such oscillations

in the second phase. The magnitude of the pressure is higher. In the case of the stepwise catcher the magnitude of the pressure increase is the right one, but the condensation oscillations are suppressed in the second phase. This analysis clearly indicates (a) that the essential physics of melt–water interaction is contained in the code and (b) that a further increase of the quality of the simulation of this process can be obtained only by using a boundary fitted representation of the form of the core catcher. Interpreting the simulation of PM17 in this light we see that the stepwise representation of the parabolic catcher really introduces numerical oscillation in the first part of the experiment and this is superimposed on the actual existing condensation oscillations that are also predicted by the code.

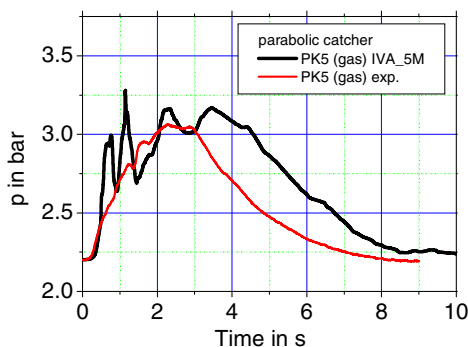


Fig. 16.18.31 Wall pressure in the gas PK05 as a function of time. Parabolic core catcher as presented in Figs. 16.18.25 and 16.18.30

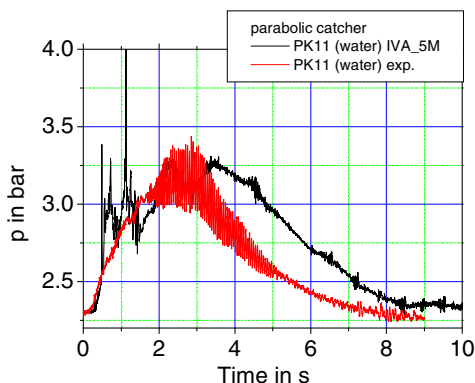


Fig. 16.18.32 Wall pressure in the water PK11 as a function of time. Parabolic core catcher as presented in Figs. 16.18.25 and 16.18.30

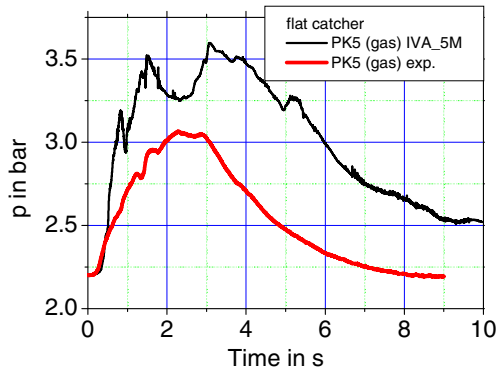


Fig. 16.18.33 Wall pressure in the gas PK05 as a function of time. Cylindrical catcher with flat bottom

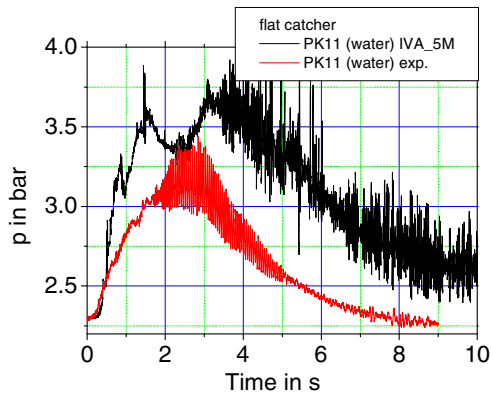


Fig. 16.18.34 Wall pressure in the water PK11 as a function of time. Cylindrical catcher with flat bottom

Conclusions. Using the PREMIX 17 and 18 experiments the capability of the IVA_5M computer code is tested to predict interaction of molten alumina with strongly subcooled water for release of melt close to the water surface. The following conclusions are drawn from this study:

- (a) The experiment shows two very different characteristic features: the first is jet–water interaction without strong net vapor production, and the second is three-phase natural circulation that cools the sloshing melt inside the core catcher, the so-called three-phase chimney effect. The second phase is characterized by entrainment of melt into the buoyancy-driven upward three-phase mixture along

the axis and cyclic removal of steam clouds. Both processes are well recognizable in the computer code simulation.

- (b) The magnitude of the pressure increase is properly predicted.
- (c) The importance of the appropriate representation of the geometry of the melt catcher is clearly demonstrated. Replacing the smooth parabolic surface of the catcher with a stepwise wall generates fluctuations that are not observed in the initial phase.
- (d) The approximate representation of the catcher as a cylinder with a flat bottom demonstrates the lack of such oscillations in the initial phase, and the generation of such oscillations in the second phase in the computations, a phenomenon that was in fact observed;
- (e) A boundary-fitted representation of the flow catcher is recommended for such types of analysis.
- (f) The constitutive models addressed to control the processes in such interactions are functioning properly in the code.

As far as this author knows this is the first successful simulation of PREMIX 17 and 18 with a system computer code.

16.18.8 RIT and IKE experiments

The findings obtained by RIT experiments are systematically compared with the formalism used in IVA5, *Kolev* (1999). The most important conclusions are as follows. a) The void fraction in the region of continuous water does not influence the fragmentation characteristics. This simply says that it is permissible to use models for liquid–liquid fragmentation also in bubbly three-phase flows without boiling *Haraldsson et al.* (1999). b) The liquid-liquid jet fragmentation obeys the *Taylor* solution, *Batchelor* (1958). The L over D relation of *Taylor* is useful with a constant of about 10. It confirms *Bracco's* result that this constant is about 7 *Bracco* (1985).

Finally, it became clear that the spectral distribution of particles, as observed in FARO, PREMIX and RIT, could not be obtained by computer models with a single group model for the dispersed field.

Bürger and coworkers, *Bürger*, et al. (1996), *Bürger* (1998), *Bürger*, et al. (1998), *Coste*, et al. (1999) found out that the hydrodynamic fragmentation is the most important fragmentation mechanism in high *Weber* number droplet fragmentation and that the thermal enhancement may be of the order of 15% at maximum. Comparing different fragmentation models in this region *Coste*, et al. (1999) find that the *Pilch* based hydrodynamic models represent best the findings of the RIT experiments, *Kolev* (1999). It confirms the decision to use in the IVA code series *Pilch*-based models for melt-droplet fragmentation description – see *Silverii and Magallon* (1999), *Kolev* (1999).

References

- Annunziato, A., Addabbo, C., Leva, G.: OECD-CSNI International standard problem 39 on FARO test L-14, Reference specification, JRC Technical Note I.96.xx, Draft (1996)
- Annunziato, A., Addabbo, C., Magallon, D.: FARO test L-20 quick look report, Technical Note No. I.96.163, JRC Ispra, Italy (October 1996)
- Annunziato, A., Addabbo, C., Magallon, D.: FARO Test L-24 Quick Look Report, Technical Note No. I.97.185, JRC Ispra, Italy (1997)
- Batchelor, G.K. (ed.): Collected works of G. I. Taylor. Cambridge Univ. Press, Cambridge (1958)
- Bracco, F.V.: Modeling of engine sprays. In: Proc. International Congress & Exposition Detroit, Michigan, February 25-March 1, pp. 113–136 (1985)
- Benuzzi, A., Magallon, D.: FARO-LWR programme L-14 test quick look report, JRC Technical Note I.94.171 (December 1994)
- Bürger, M., Buck, M., Saied-Ahmad, A., Schatz, A.: Experimental and theoretical investigation on the fragmentation of melt drops in relative flow, Report INV-MFC (98)-D016, Institut für Kernenergie und Energiesysteme, Universität Stuttgart, IKE 2–135 (December 1996)
- Bürger, M.: Comparison and theoretical interpretation of the experiments on hydrodynamic drop fragmentation, Report INV-MFC (98)-D014, Institut für Kernenergie und Energiesysteme, Universität Stuttgart, IKE 2-FB-16 (Juli 1998)
- Bürger, M., Cho, S.H., von Berg, E., Schatz, A.: Modeling of drop fragmentation in thermal detonation waves and experimental verification, Report INV-MFC (98)-D016, Institut für Kernenergie und Energiesysteme, Universität Stuttgart, IKE 2-FB-15 (November 1998)
- Coste, P., Valette, M., Berthoud, G.: Pb-Bi droplets fragmentation in liquid water (Li et al. experiment, ICMF 98): comparison of the existing code correlations and calculations with MC3D. In: 6th MFCI Project Meeting, CEA Grenoble, France, June 23–24 (1999)
- Haraldsson, H.O., Li, H.X., Dinh, T.N., Green, J.A., Sehgal, B.R.: Effect of solidification and coolant voiding on breakup of molten metal jet in water, Royal Institut of Technology (KTH), NPS, EU report INV-MFCI(00)-D048, Report EU-KTH/NPS/MFCI-9907-SE, Stockholm (July 6, 1999)
- Hohmann, H., Magallon, D., Huhtiniemi, I., Annunziato, A., Yerkess, A.: Advance in the FARO/KROTOS Melt Quenching Test Series. In: 22nd Water Reactor Safety Meeting, Bethesda (Maryland) (October 24–26, 1994)
- Huber, F., Keiser, A., Steinbrück, M., Will, H.: PREMIX, Documentation of the results of experiments PM01 to PM06, FZKA 5756, Forschungszentrum Karlsruhe, Germany (März 1996)
- Kaiser, A., Schütz, W., Will, H.: PREMIX experiment, EC 4th Framework Program on Reactor Safety Shared Cost Actions, Contract no FI4s-CT96-0037, MFCI PROJECT, Yearly Progress Report no 1 (1998a)
- Kaiser, A., Schütz, W., Will, H.: PREMIX: Investigation of premixing behavior of a hot melt being poured into water. Test PM15 (December 17, 1998b); 5th MFCI Project Meeting, Forschungszentrum Karlsruhe, Germany (September 16, 1998)
- Keiser, A., Schütz, W., Will, H.: PREMIX Tests PM12, PM13 and PM14, Documentation and evaluation of experimental data, FZKA 6370, Forschungszentrum Karlsruhe, Germany (November 1999)
- Keiser, A., Schütz, W., Will, H.: PREMIX Experiments PM12-PM18 to investigate the mixing of hot melt with water, FZKA 6380, Forschungszentrum Karlsruhe, Germany (Juli (2001)

- Kolev, N.I.: Fragmentation and coalescence dynamics in multi-phase flows. *Exp. Thermal Fluid Sci.* 6, 211–251 (1993)
- Kolev, N.I.: The code IVA4: Modeling of mass conservation in multi-phase multi-component flows in heterogeneous porous media. *Kerntechnik* 59(4-5), 226–237 (1994a)
- Kolev, N.I.: The code IVA4: Modeling of momentum conservation in multi-phase multi component flows in heterogeneous porous media. *Kerntechnik* 59(6), 249–258 (1994b)
- Kolev, N.I.: IVA4 Computer code: Dynamic fragmentation model for liquid and its application to melt water interaction. In: *Proc. ICON-3, The Third International Conf. on Nucl. Engineering, Nuclear Power and Energy Future*, Kyoto, Japan, April 23–27 (1995a); Presented at the Workshop zur Kühlmittel/ Schmelze - Wechselwirkung, Köln, Germany (November 14–15, 1994)
- Kolev, N.I.: The code IVA4: Second law of thermodynamics for multi phase flows in heterogeneous porous media. *Kerntechnik* 60(1), 1–39 (1995b)
- Kolev, N.I., Hofer, E.: Uncertainty and sensitivity analysis of post experimental IVA4 simulations of melt water interaction. *Exp. Thermal Fluid Sci.* 13, 98–116 (1996)
- Kolev, N.I.: IVA4 analysis of the FARO L14 experiment (ISP 39). In: *International Seminar on Vapor Explosions and Explosive Eruptions (AMIGO-IMI)*, Aoba Kinen Kaikan of Tohoku University, Sendai-City, Japan (May 22–24, 1997a)
- Kolev, N.I.: Comments on the entropy concept. *Kerntechnik* 62(1), 67–70 (1997b)
- Kolev, N.I.: On the variety of notation of the energy conservation principle for single phase flow. *Kerntechnik* 63(3), 145–156 (1998)
- Kolev, N.I.: The IVA5 dynamic droplet fragmentation and coalescence models and their verification data base: Part 1 (INV-MFCI(99)-D027) and Part 2 (INV-MFCI(99)-D028) (1999)
- Kolev, N.I., Seitz, H., Roloff-Bock, I.: Hot-leg injection: 3D versus 1D three velocity fields modeling and comparison with UPTF experiment, Siemens report KWU NA-T/00/E027, R&D Project 903060, Verification IVA6 (2000)
- Kolev, N.I.: Analysis of the PREMIX 17 and 18 experiments with IVA_5M computer code. In: *The 10th International Topical Meeting on Nuclear Reactor Thermal Hydraulics*, Seoul, Korea, E00106 (October 5–9, 2003)
- Magallon, D., Leva, G.: FARO LWR programme test L-14 data report, JRC Technical Note I.96.25 (February 1996)
- Mitchel, D.E., et al.: Intermediate scales steam explosion phenomena: Experimental analysis SAND8-0124 (1981)
- Nelson, L.S., Duda, P.M.: Steam explosion experiments with single droplet of CO₂ laser melted with iron oxide. Report NUREG/CR-2295 (SAND 81-1346) (September 1981)
- Nelson, L.S., Duda, P.M.: Steam explosion experiments with single droplet of CO₂ laser melted with iron oxide. Part 2. Parametric Studies. Report NUREG/CR-2718 (SAND 81-1105) (September 1985)
- Silverii, R., Annunziato, A.: FARO LWR program, Test L-28 data report, Technical Note No.I.99.76, INV-MFCI(99)-D033, JRC Ispra, Italy (1999)
- Silverii, R., Magallon, D.: FARO LWR Programme Test L-31 Data Report, Technical Note No. I.99.100, INV-MFCI(99)-D035, JRC, ISIS, Ispra (VA), Italy (June 1999)
- Yamano, N., Sugimoto, J., Moryama, Y., Soda, K.: Studies of fuel coolant interactions during core melt accident of nuclear power plants. In: *NURETH-6th Int. Meeting On Thermal-Hydraulics*, pp. 271–281 (1992)

16.19 Assessment for detonation analysis

In order to assess the IVA5 capabilities for detonation analysis is underway. We first check the capability of the thermal properties to operate properly in such conditions. The thermal properties for the materials: uranium dioxide, nuclear reactor corium (mixture consisting of 76% UO_2 , 24% ZrO_2), zirconium, zirconium dioxide, stainless steel, alumina, silicon dioxide, iron oxide, molybdenum, aluminum and boron oxide are obtained by using the recommendations of Chapter 3 of Volume 1.

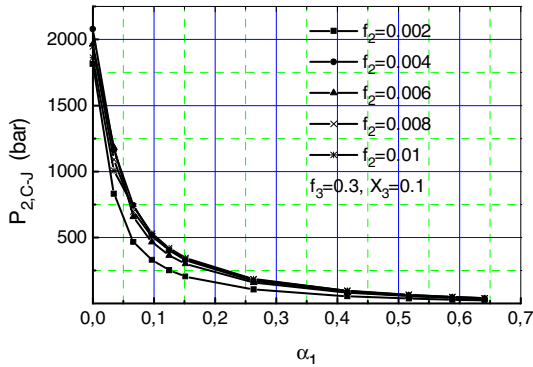


Fig. 16.19.1 Pressure behind the detonation discontinuity as a function of the void fraction before the discontinuity for UO_2 . α_3 and X_3 are the void fraction and the melt mass concentration in front of the detonation wave, and f_2 and f_3 are the entrainment fractions of the coolant and of the melt after the detonation front

Then we perform detonation analysis with the solution proposed in Chapter 9 of Vol. 1. Figures 16.19.1, 16.19.2 and 16.19.3 show the pressure behind the detonation discontinuity as a function of the void fraction before the discontinuity for UO_2 , Al_2O_3 and Fe for the same initial conditions. The entrainment of the melt into fine particles was set to 30%. The entrained water in thermal equilibrium behind the discontinuity is varied between 2 and 8%. We learn from this analysis that Al_2O_3 and Fe are able to produce a stronger detonation wave than UO_2 . This phenomenon really happens in the experiments and seemed to be unexplained up to now in spite of the large number of theories in the literature.

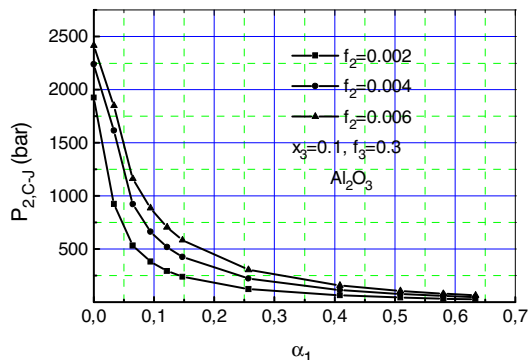


Fig. 16.19.2 Pressure behind the detonation discontinuity as a function of the void fraction before the discontinuity for Al_2O_3

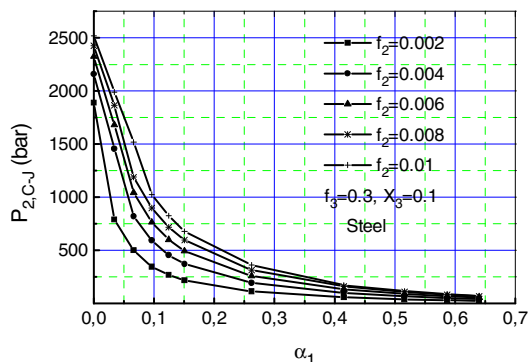


Fig. 16.19.3 Pressure behind the detonation discontinuity as a function of the void fraction before the discontinuity for Fe

Conclusion. The melt, water and gas properties work well in the detonation case. The substantial differences of the explosivity of the mixtures of different molten materials with water is explained with the differences of the caloric properties of the melt.

The reader will find additional information on this topic in *Kolev and Hulin (1999)*, *Kolev (2000)*.

References

- Kolev, N.I., Hulin, H.: Detonation waves in melt-coolant interaction, Part.2: Applied analysis, MFCI Project. In: 6th Progress Meeting, CEA, Grenoble. EU Nr. (June 23-24, 1999)
- Kolev, N.I.: Detonation waves in melt-coolant interaction. Part 1: Kernenergie 65, 254–260 (2000)

16.20 Other examples of 3D capabilities

16.20.1 Case 1. Rigid-body steady-rotation problem

This test problem reported in *Harison and Johnson (1992)* presents a hollow cylinder with symmetric flow in the azimuthal direction – Fig. 16.20.1. No axial and radial flow exists. The mass-conservation equation gives $\frac{\partial v}{\partial \theta} = 0$. The r direction

momentum equation simplifies to $\rho \frac{v^2}{r} = \frac{\partial p}{\partial r}$, and the θ direction momentum equation gives $\frac{\partial p}{\partial \theta} = 0$. For constant rotational frequency ω , ($v(r) = r\omega$), the ana-

lytical solution of the radial momentum equation is $p - p_0 = \frac{1}{2} \rho \omega^2 (r^2 - r_0^2)$ or

$$p - p_0 = \frac{1}{2} \rho [v(r)]^2 \left[1 - \left(\frac{r_0}{r} \right)^2 \right].$$

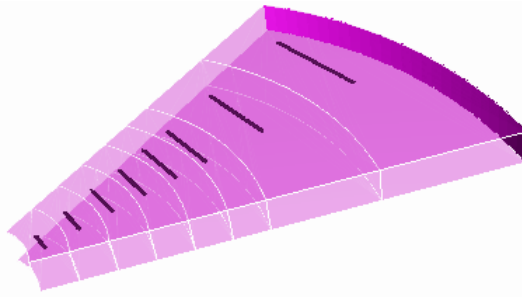


Fig. 16.20.1 Geometry of the test problem for rigid-body steady rotation

The discretization is presented in Fig. 16.20.1. The prescribed azimuthal velocity, the analytical pressure and the IVA5 prediction are presented in Table 16.20.1 and in Fig. 16.20.2. We see a very good agreement.

Table 16.20.1 Angular velocity and pressure as function of the radius

r [m]	v_{θ} [m/s]	$p_{analyt.}$ [10^5 Pa]	p_{IVA5} [10^5 Pa]
0.75	-	5.0	5.0
1.25	0.1923	5.00012	5.00009
1.75	0.2692	5.00030	5.00027
2.25	0.3462	5.00053	5.00051
2.75	0.4231	5.00083	5.00080
3.25	0.5	5.00118	5.00116
3.75	0.5769	5.00159	5.00157
4.75	0.7308	5.00260	5.00270
6.5	1.0	5.00492	5.00513

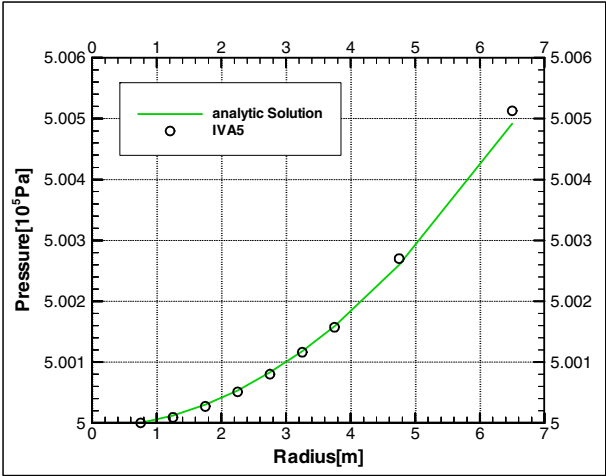


Fig. 16.20.2 Pressure as function of the radius

16.20.2 Case 2. Pure radial symmetric flow

This test problem reported in *Harison and Johnson* (1992) presents a hollow cylinder with symmetric flow in the radial direction. No axial and azimuthal flow exists. The

mass conservation equation gives $\frac{\partial}{\partial r}(ru) = 0$. The r direction momentum equation

simplifies to $\rho \frac{1}{2} \frac{\partial u^2}{\partial r} = -\frac{\partial p}{\partial r}$, and the θ direction momentum equation gives

$\frac{\partial p}{\partial \theta} = 0$. From the mass conservation we have $u = u_0 \frac{r_0}{r}$. The analytical solution of

the radial momentum equation is the well-known *Bernoulli* equation

$$p - p_0 = -\frac{1}{2} \rho (u^2 - u_0^2) \text{ or } p - p_0 = \frac{1}{2} \rho u_0^2 \left[1 - \left(\frac{r_0}{r} \right)^2 \right].$$

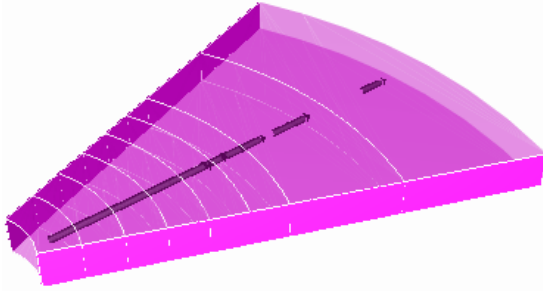


Fig. 16.20.3 Geometry of the test problem for pure radial symmetric flow

The discretization is presented in Fig. 16.20.3. The analytical pressure and the IVA5 prediction are presented in Table 16.20.2 and in Fig. 16.20.4 for radial velocities given in Table 16.20.3. Only the inlet radial velocity is prescribed. All others are computed by the code. We see a very good agreement.

Table 16.20.2 Pressure as function of the radius

r [m]	$p_{analyt.} [10^5 Pa]$	$p_{IVA5} [10^5 Pa]$
1.25	5.0	5.0
1.75	5.0661	5.06615
2.25	5.0934	5.09337
2.75	5.1071	5.10715
3.25	5.1151	5.11508
3.75	5.1200	5.12005
4.75	5.1257	5.1257
6.5	5.1301	5.13006

Table 16.20.3 Radial velocity as a function of the radius

r [m]	v_r [m/s]
1.0	6.5
1.5	4.3333
2.0	3.25
2.5	2.6
3.0	2.1667
3.5	1.8571
4.0	1.625
5.5	1.1818
7.5	0.8667

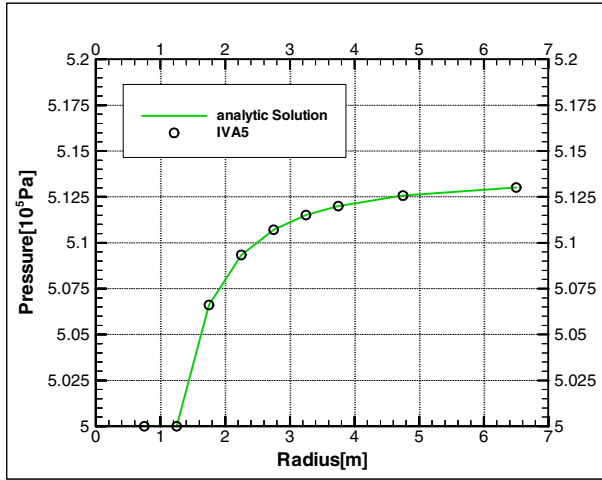


Fig. 16.20.4 Pressure as a function of the radius

16.20.3 Case 3. Radial-azimuthal symmetric flow

This test problem reported in *Harison and Johnson* (1992) presents a hollow cylinder with symmetric flow in the radial and azimuthal directions, Fig. 16.20.5, in fact a superposition of the previous two cases, rigid-body steady rotation and pure radial symmetric flow. No axial flow exists.

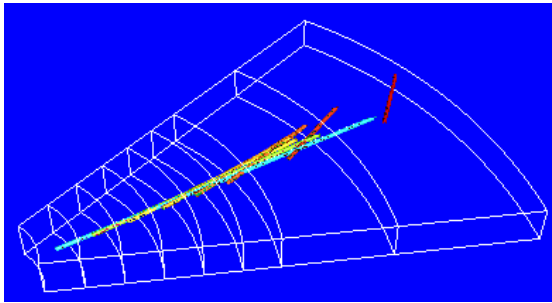


Fig. 16.20.5 Geometry of the test of the problem for radial-azimuthal symmetric flow

The mass conservation equation gives $\frac{\partial}{\partial r}(ru) = 0$. The r direction momentum equation simplifies to $\rho \left(\frac{1}{2} \frac{\partial u^2}{\partial r} - \frac{v^2}{r} \right) = -\frac{\partial p}{\partial r}$, and the θ direction momentum

equation gives $\rho u \left(\frac{\partial v}{\partial r} + \frac{v}{r} \right) = -\frac{1}{r} \frac{\partial p}{\partial \theta}$. From the mass conservation we have

$u = u_0 \frac{r_0}{r}$. From the azimuthal symmetry, $\frac{\partial p}{\partial \theta} = 0$, the θ direction momentum

equation gives $\frac{\partial v}{\partial r} + \frac{v}{r} = 0$ or $v = v_0 \frac{r_0}{r}$. Taking into account the two solutions of

the mass and of the θ momentum equation the radial momentum equations gives

$$\rho \frac{1}{r} (u^2 + v^2) = \frac{\partial p}{\partial r} \text{ or } \rho (u_0^2 + v_0^2) r_0^2 \frac{1}{r^3} = \frac{\partial p}{\partial r} \text{ or}$$

$$p - p_0 = \rho (u_0^2 + v_0^2) r_0^2 \frac{1}{2} \left(\frac{1}{r_0^2} - \frac{1}{r^2} \right).$$

The analytical pressure and the IVA5 prediction are presented in Table 16.20.4 and in Fig. 16.20.6. We see a very good agreement.

Table 16.20.4 Pressure as function of the radius

r [m]	$p_{analyt.}$ [10^5 Pa]	p_{IVA5} [10^5 Pa]
0.75	5.0	5.0
1.25	5.0	5.00009
1.75	5.06624	5.06642
2.25	5.09350	5.09388
2.75	5.10729	5.10795
3.25	5.11523	5.11623
3.75	5.12021	5.12162
4.75	5.12587	5.12840
6.5	5.13023	5.13519

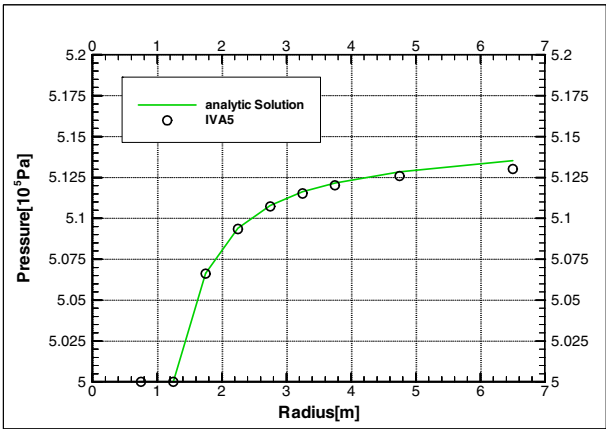


Fig. 16.20.6 Pressure as a function of the radius

16.20.4 Case 4. Small-break loss of coolant

The *Kevchishvili* and *Dementev* small-break loss-of-coolant experiment was performed at the Moscow Energetic Institute to study strong separation effects *Kevchishvili* and *Dementev* (1985). The 36 uniformly heated rods 16 mm in diameter and 1700 mm long are mounted within a shroud 159 mm in diameter in a pressure vessel 309 mm in diameter and 2100 mm high as shown in Fig. 16.20.7a. We simulate an experiment with a thermal power input of 67 kW and a cold leak from a break nozzle 22 mm in diameter. The initial state of the water inside the vessel was $p = 123$ bar, $T = 558$ K, and void fraction equal to zero. The void fractions in the rod bundle in the three different locations shown in Figs. 16.20.8a, b and c were recorded as a function of time.

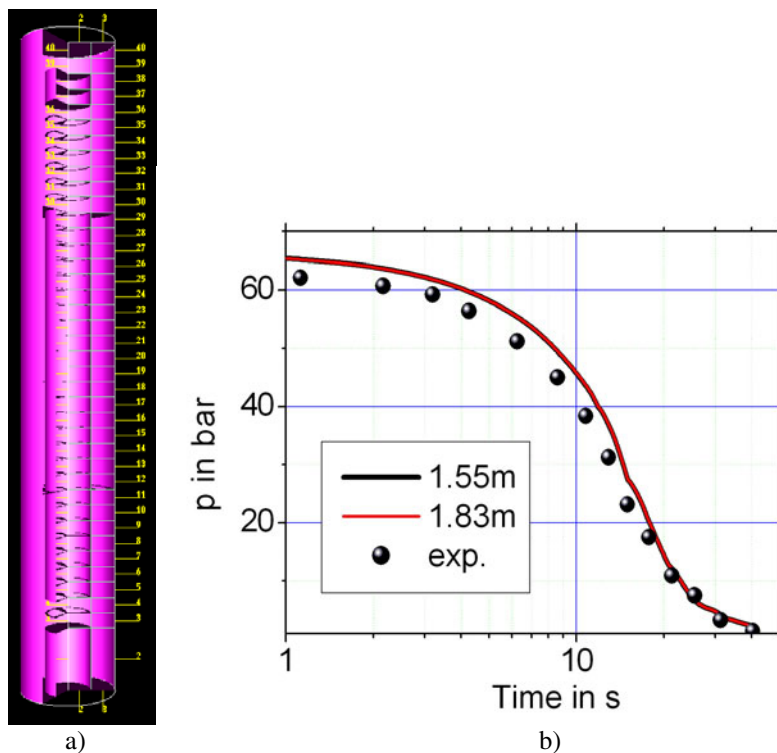


Fig. 16.20.7 a) IVA6 geometry model for the *Kevchishvili* and *Dementev* small-break loss-of-coolant experiment. b) Pressure at level $z = 1.83$ m as a function of time. Comparison of the IVA6 prediction with the experiment of *Kevchishvili* and *Dementev* (1985). Heated bundle, 67 kW

I simulate the geometry with 2 radial, 3 angular, and 39 axial zones – 117 cells – as shown in Fig. 16.20.7a. I assume that the “vena contracta” coefficient at the nozzle is 0.8. The comparison with the experimental data is shown in Figs. 16.20.7b and 16.20.8. From this comparison the following conclusions can be

drawn. The steam discharge between 7 and 11 s is stronger due to friction in the discharge pipe, which was not considered. The pressure compares well with the measurement. The end of the stratification at the three different positions of the test section is well predicted. In the upper part the stratification is well predicted. In the mid and lower parts the stratification is well predicted except for the region between 7 and 10 s where it happens faster in the simulation.

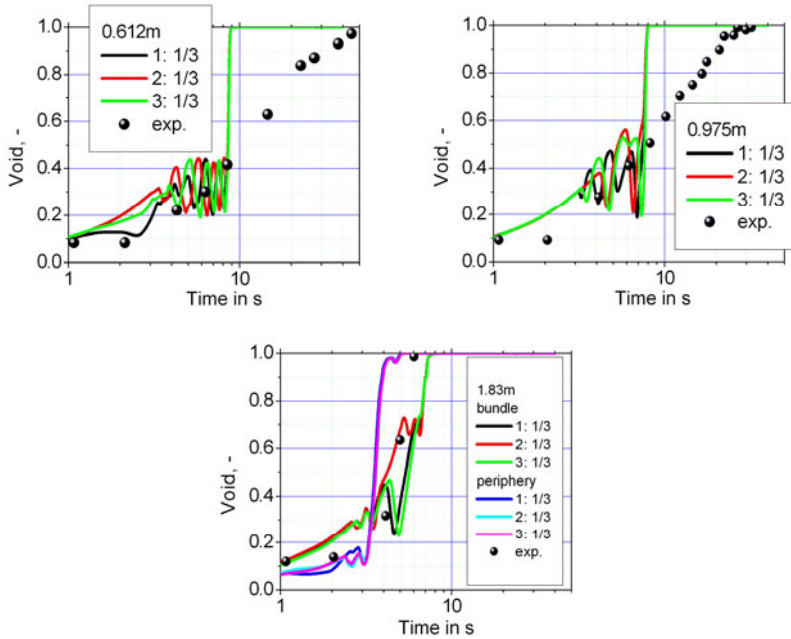


Fig. 16.20.8 The void fraction in a rod bundle on level $z = 1.83, 0.975, 0.612$ m as a function of time. Comparison of the IVA6 prediction with the experiment of *Kevchishvili* and *Dementev* (1985). Heated bundle, 67 kW

16.20.5 Case 5. Asymmetric steam–water interaction in a vessel

Now we turn back to the UPTF test No. 26 already introduced in Section 16.7. The phase B is of particular interest in this section. As already found in *Kolev* (1999) through a 3D simulation, in phase B the main steam–water interaction processes leading to entrainment happen in the vessel, whereas in phase A the 3D analysis results in no carryover from the vessel, supporting the correctness of the 1D analysis in Section 16.7. We present here details of the 3D analysis. The geometry of the vessel is presented in Fig. 16.20.1. We take advantage of the symmetry and simulate half of the vessel using 1200 ($12 \times 5 \times 20$) computational cells as shown in Fig. 16.20.2. The resolution of the discretization is higher in the

upper plenum of the vessel. We simulate the asymmetric injection inside the integration volume by defining distributed mass sources at the corresponding level. The water injection is simulated as if directly injected into the vessel at the vessel wall and not as in the real experiment 1.5 m apart from the vessel inside the main coolant line. The steam mass conservation on average is clearly demonstrated in Fig. 16.20.3 where the steam injection nozzle mass flow is also presented.

As we realize from Fig. 16.20.3, there is a strong feedback of the water mass flow rate on the steam mass flow causing strong oscillations. Figure 16.20.3 presents the main result of this analysis. It shows no in-vessel water carryover during phase A and almost complete carryover after 600 s. There was water suction from the bottom of the test vessel as presented in Fig. 16.20.4a. This suction was not considered in our computation, which explains the overprediction of the entrainment in phase B.

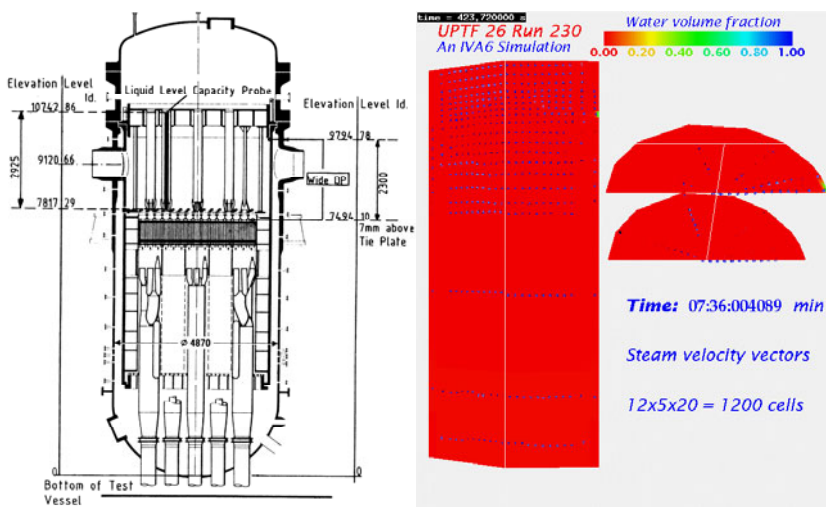


Fig. 16.20.9 3D test section simulating a full scale PWR for hot-leg water injection in a steaming core. Initial conditions for Phase A and intermediate state between Phase A and Phase B

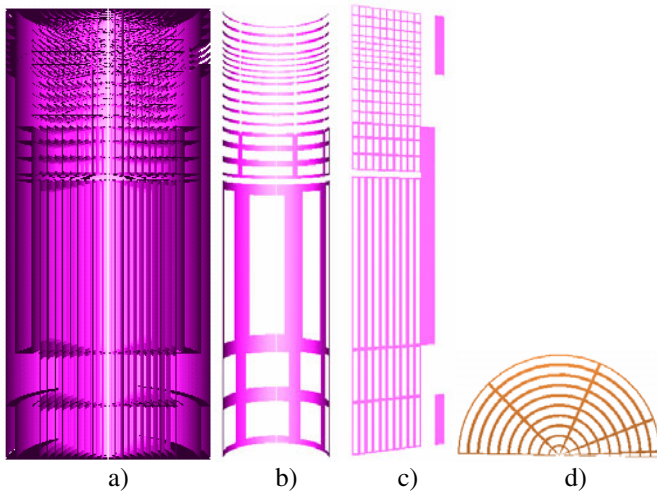


Fig. 16.20.10 a) IVA6 reactor pressure vessel geometry model for UPTF-Test 26 Run 230 simulation. b, c, d) Illustration of how the complicated technical structures are modeled by means of radial, angular, and axial surface permeabilities, respectively. The colored surface in the last three pictures is nonpermeable for flow in the corresponding plane

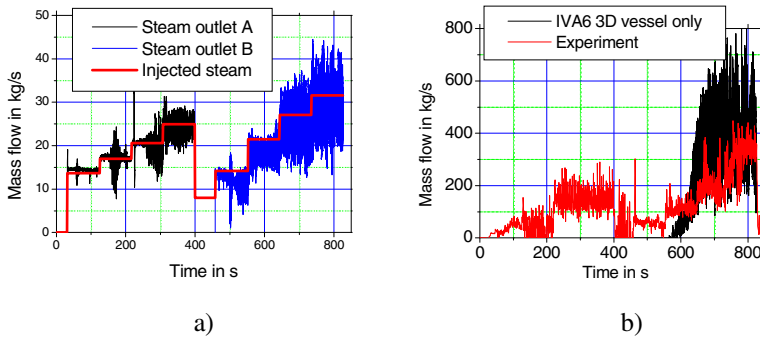


Fig. 16.20.11 3D case. a) Mass flow of injected steam and of the steam leaving the vessel as a function of time. b) Total mass flow of steam + water at the densitometer position as a function of time

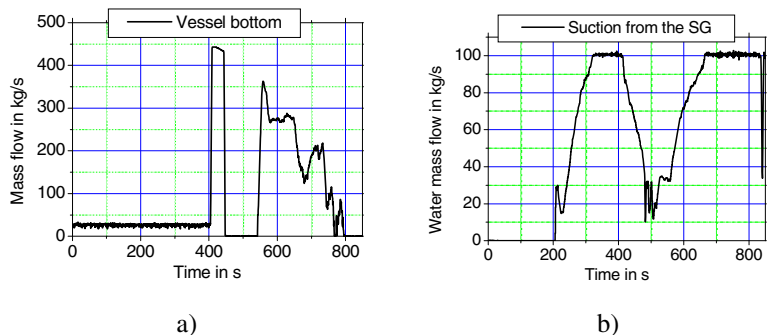
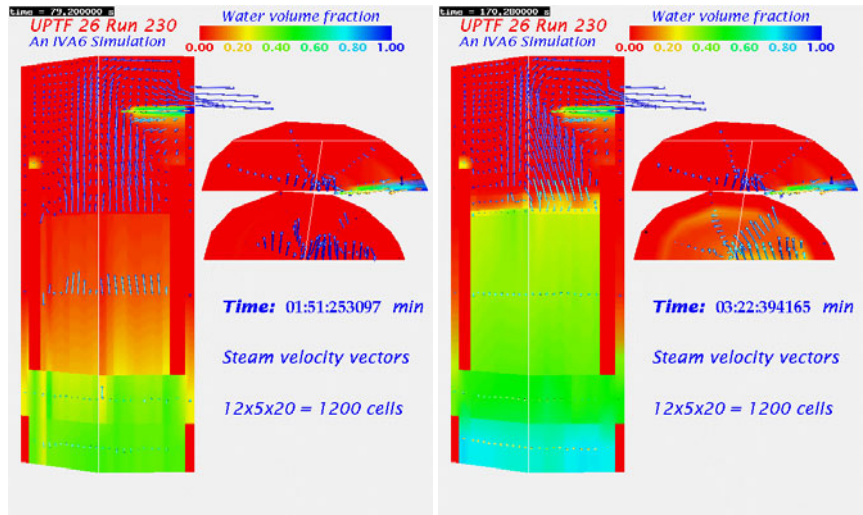


Fig. 16.20.12 a) Water mass flow suction through the bottom of the vessel as a function of time. b) Water mass flow suction from the steam generator separator as a function of time

A time-averaged Fig. 16.20.11 indicates the stepwise character of the total mass flow rate reflecting in a way the stepwise character of the steam injection. This is a clear indication that in both cases entrainment is happening inside the pipe. While, as already mentioned, in phase A this entrainment is dominant, in phase B we have superposition of entrainment inside the vessel and inside the pipe. The next 3D representation of the water content and the steam velocity vectors additionally clarifies this point – Figs. 16.20.5 and 16.20.6.



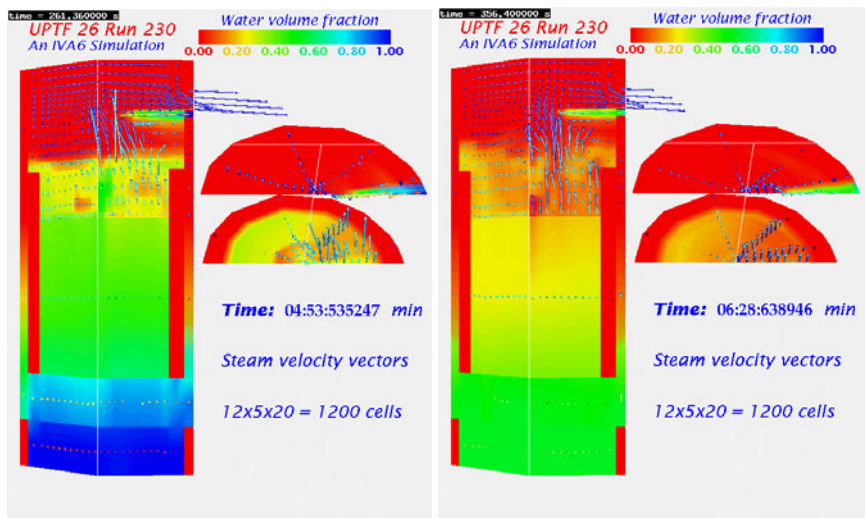
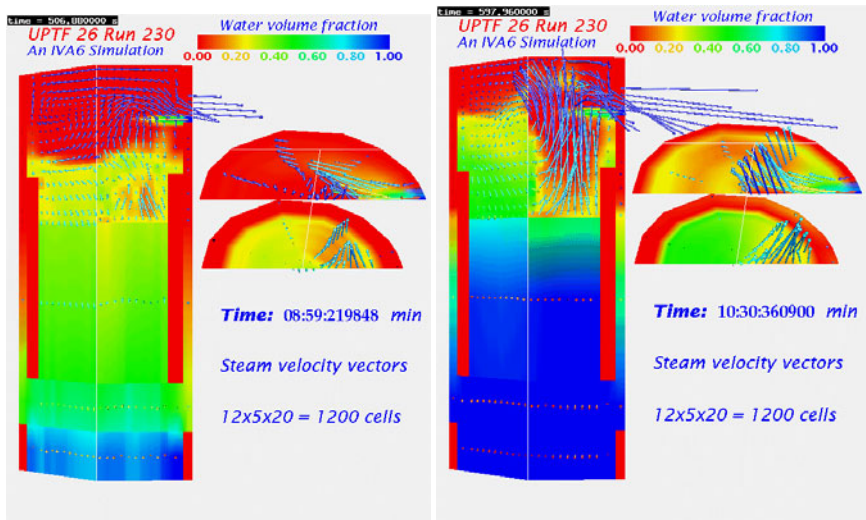


Fig. 16.20.13 Phase A-1, 2, 3, 4 Water volume fraction and steam velocity vectors as a function of space. The two horizontal cuts (left) are at the level above the steam injection and at the water injection

Conclusions. We observe a reasonable response of IVA6 during the simulation of UPTF experiment No. 26 run 230. We learn from this analysis that the combination of 3D representation of the vessel with 1D representation of the pipe will improve the result. Furthermore, complete multiblock simulation of the vessel and the large (0.75 m diameter) pipe is the desired approach for the future sophistication of the modeling technology.



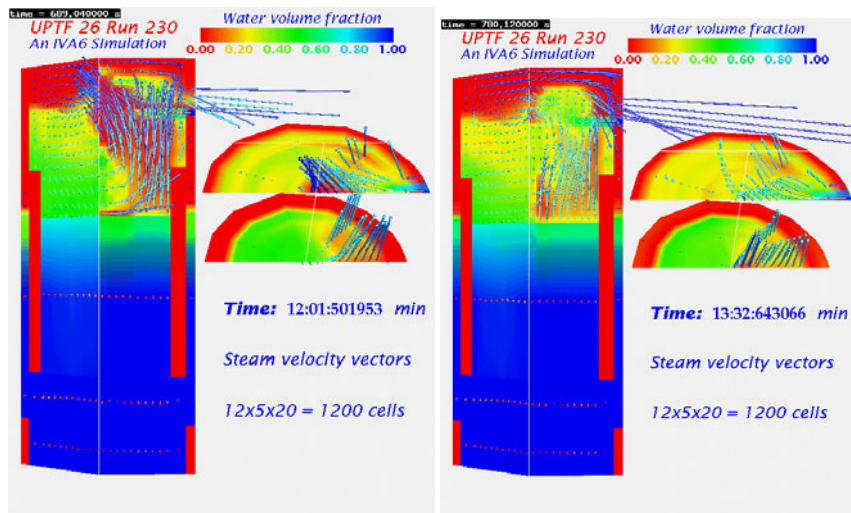


Fig. 16.20.14 Phase B-1, 2, 3, 4 Water volume fraction and steam velocity vectors as a function of space. The two horizontal cuts (left) are at the level above the steam injection and at the water injection

16.20.6 Case 6. Melt relocation in a pressure vessel

Between 1995 and 1998 we performed hundreds of 2D and 3D simulations mainly applied to the typical pressurized-water reactors (PWRs). Some of them are presented in Chapter 13 of Volume 1. The PWRs Steam Explosion Study is not a subject of this publication. We only give one example demonstrating the 3D capabilities of the code. Figure 16.20.7 presents the results of the IVA5-simulation using $16 \times 8 \times 69 = 8832$ computational cells. Side failure of the heavy reflector is postulated.

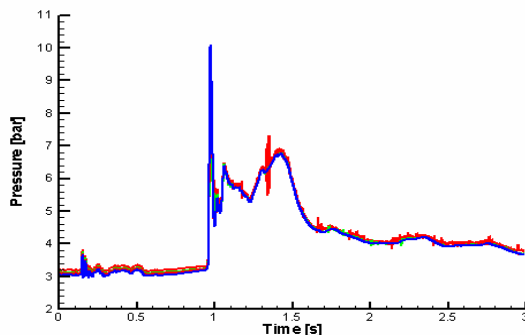


Fig. 16.20.15 Pressure on the rotational axis as a function of time at four different positions in the lower head

The material relocation is presented in Figs. 16.20.7a–c. The pressure on the axis as a function of time is given in Fig. 16.20.7. We see the full capability of IVA5 to model transient multiphase 3D flows in complicated geometry.

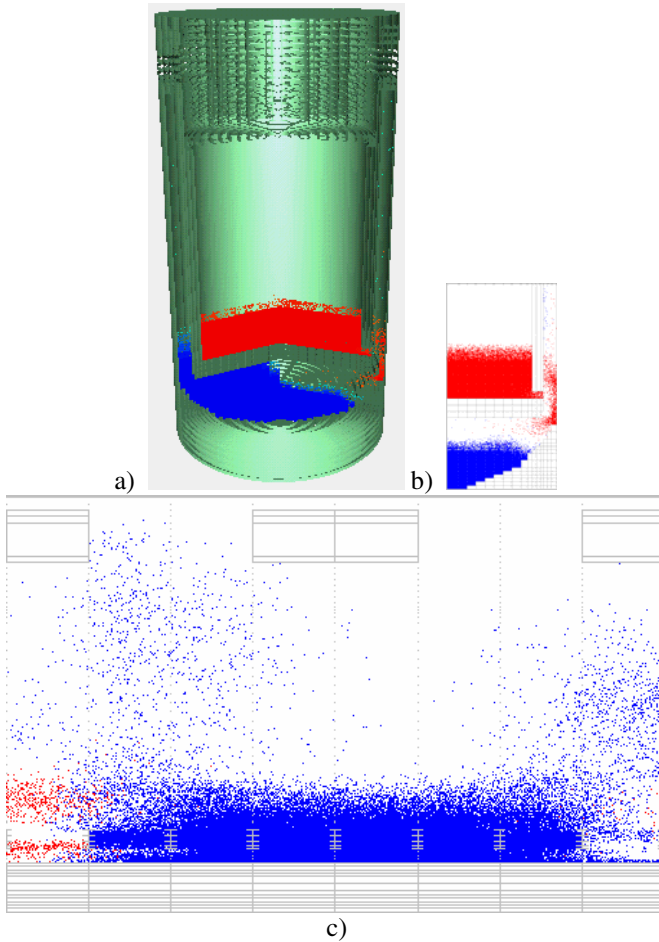


Fig. 16.20.16 a) Melt and water relocation in two different vertical planes 1 s after the begging of the failure of the heavy reflector. b) Melt and water inverter in the vertical plane crossing the failure of the heavy reflector. c) Melt and water in the downcomer, cylindrical surface close to the RPV wall

References

- Harison, R.G., Johnson, E.C. (eds.): Developmental assessment of the multidimensional component in RELAP5 for Savannah River Site thermal hydraulic analysis, EGG-EAST-9803, DE93 001942. EG&G Idaho, Inc., Idaho Falls (1992)
- Kevchishvili, N.A., Dementev, B.S.: Investigation of the influence of the decay heat on the blow down characteristics of steam-water mixtures. *Teploenergetika* 7, 67 (1985)
- Kolev, N.I.: Verification of IVA5 computer code for melt-water interaction analysis, Part 1: Single-phase flow, Part 2: Two-phase flow, three-phase flow with cold and hot solid spheres, Part 3: Three-phase flow with dynamic fragmentation and coalescence, Part 4: Three-phase flow with dynamic fragmentation and coalescence – alumina experiments. In: Proc of the Ninth International Topical Meeting on Nuclear Reactor Thermal Hydraulics (NURETH-9), San Francisco, California, October 3-8 (1999)
- Kolev, N.I., Seitz, H., Roloff-Bock, I.: Hot-leg injection: 3D versus 1D three velocity fields modeling and comparison with UPTF experiment, Siemens report KWU NA-T/00/E027, R&D Project 903060, Verification IVA6 (2000)

16.21 General conclusions: Is it possible to design a universal multiphase flow analyzer?

Comparison with a variety of experiments demonstrated the power and the weaknesses of the methods described in this monograph and qualified IVA computer code as a code representing the state-of-the-art in the field of multiphase flows. The code is capable of predicting multiphase flow behavior in complicated 3D geometries and industrial networks. The code is able to predict melt–water interaction with a well-quantified uncertainty band. Reducing this uncertainty band will demand future sophistication in the directions indicated in many places in this work.

IVA has already been successfully applied for the melt–water interaction study of the Framatome European Pressurized Water Reactor (EPR), for the Boiling Water Reactor SWR1000—for more details see *Kolev* (2002, 2003, 2004), for the research reactor FRM II in Munich and many other studies of multiphase processes in the nuclear industry.

After years of research in this field I ask myself the following question: Is it possible to design a universal multiphase flow analyzer? In what follows I will try to give the answer.

Engineers and scientists created hundreds of computer codes for description of more or less specific realizations of multiphase flows. If one compares the structure of these codes one is astonished by the waste of human resources for programming repeating model elements like equations of state, friction laws in a variety of geometry, heat-transfer coefficients, algebraic equation solvers, data-handling procedures, graphical environment, etc. It is hard to believe that the best solution for the specific subphenomenon is available in all codes. Looking in other branches of technology like computer-chips production we realize that the revolutionary idea of having common “chips” within complex applications is very far from its practical realization in computational multiphase flow dynamics. Following this line of arguments I expressed several times in my publications explicitly or implicitly (see *Kolev* 1990, 2000) the idea that it is possible to create a universal multiphase flow analyzer in the sense of computer architecture, that is capable of absorbing adequate multiphase knowledge data base specified in Appendix 1. The subject of this chapter is to summarize some of the main ideas, some of them already realized by this author, on the way of creating such a computer-code architecture, to illustrate how they work, and to propose an outlook regarding what are the challenges in the future developments.

We confine our attention deliberately to the solution of the so-called local volume and time-averaged system of PDEs for a simple reason: Direct numerical

resolution of interacting fluids is possible as demonstrated for small scales by many researchers, but for real large-scale engineering problems it is still very expensive. I believe that this will remain so for decades.

16.21.1 The idea of multiple velocity fields

A field is defined as a part of the flow having its own well-defined spatially and temporally evolving boundary to its environment: another field or a wall. *Zimansky* (1968) uses the same definition for phase but we understand phase as a synonym for state of aggregate. A field possesses many attributes. One flow attribute is for instance the velocity. Thermodynamic attributes are the density specific enthalpy, entropy, etc. Transport attributes are, e.g., viscosities, conductivities, etc. Constituent attributes are for instance the number of chemical components inside the field, their mass concentration etc. The field is in itself a heterogeneous structure, e.g., internal circulation of a drop, boundary layers for thermal and mechanical interactions, etc. The field can be represented with its internal averaged properties and boundary-layer properties. A complex flow model may then be constructing as consisting of many fields inside the mixture.

The mixture is characterized by the number of the fields and their volumetric concentrations inside the field. The scale at which the mixture is modeled may be large enough to contain several processes that happen in subscales. This is valid for the time scale as well for the spatial resolution scale. Therefore, local volume and time averaging is necessary to obtain the conservation laws valid on the macroscale. During the averaging a record is kept for the subscale especially how formally the processes are incorporated in the large-scale method. Mathematical consistency is crucial for creating functioning general architecture.

16.21.2 Do we have adequate mathematical reflection of the conservation laws based on averaging?

The answer is yes. The system of partial differential equations reflecting the instantaneous and local conservation of mass, momentum und energy has existed since the 19th century. The 20th century generated many ideas about averaging this equation over large-scale volume, e.g., assembly averaging, statistical averaging etc. Among the mathematical tools for averaging the spatial averaging theorem by *Slattery* (1967), *Whitaker* (1967, 1969, 1977, 1985), *Anderson* and *Jackson* (1967), together with the *Leibnitz* rule allows application of averaging of the instant conservation equations over a volume. Considering as one special field the structure defining the channel, results in the so-called porous body concept *Sha*, et al. (1984). In *Kolev* (1990) and in this book the fields are considered as consisting of many chemical components allowing molecular diffusion inside them if they are continuous. The next step is time averaging also called Reynolds

averaging of the resulting systems. The resulting system is then what we need to integrate in space and time to describe in averaged terms the behavior of the field. During the averaging processes a large number of terms originate having particular meaning. The elaboration of these terms is a long-lived task in the science. A useful representation of the state-of-the-art in this field is given in Vol. 2 of this monograph.

16.21.3 Coexisting fields

Now, we can define the number of the abstract fields to which we would like to associate physical properties. The maximum number of the fields have to be specified and then the place holders for the interaction terms. The general approach requires clear physical and mathematical understanding of the structure of these terms. Usually they are strongly nonlinear.

16.21.4 Geometry definition

We adopt the following strategy: We consider the technical systems as a combination of pipe-networks with valves, pumps and other components that may be connected with 3D volumes. That is why our geometry definition contains three elements: (1) pipe network; (2) multiple blocks in boundary fitted coordinates interconnected to each other. In many daily applications (3) a single 3D-block in Cartesian or cylindrical geometry is sufficient and very useful. It is useful also for development purposes. The set of conservation equations is then defined in this region. The separation of the computational region from the real wall requires boundary conditions defining the action of the environment on the specified volume.

16.21.5 Solvers

The system of partial differential equations is usually transferred in a discrete form with a priori specified accuracy of discretization. Designing working solvers for the resulting nonhomogeneous algebraic system with variable coefficients is an art. The challenge is to design as strong as possible coupling within the different processes within a single step. A powerful tool for this is the entropy concept presented in this book. Some examples are given in this work. This method will surely be improved in the future.

16.21.6 Summary of the ideas

I deliberately do not go into details in this presentation in order to make the main structure of the universal flow analyzer clear:

- (1) The flow is represented by coexisting fields inside a control volume.
- (2) The control volume having simple or complex geometry is separated from the environment by surfaces at which the action of the environment is replaced by boundary conditions.
- (3) Each field possesses a variety of attributes originating from the interaction with the environment and from the mathematical procedure of the averaging.
- (4) The coexisting fields are described by a system of well-founded partial differential equations that are local volume and time averaged.
- (5) The geometry is a combination of pipe networks, multiple interconnected volumes that are boundary fitted.
- (6) The solution of discretized form is based on strong coupling of the interactions between the fields. The entropy concept is a powerful tool for simplifying the mathematical description without losing generality.

16.21.7 Is there any chance to overcome the overwhelming complexity and design algorithms that are of practical use?

Yes. We will give here one example based on three multicomponent velocity fields in porous structure that may change its geometry in time. The foundations of the computer code IVA described in this book allows applications of this multiphase flow analyzer for mathematical simulation of variety of processes. From two-phase gas-plasma multicomponent hydrogen detonation in pipe-network with dissociation of the gases, Fig. 16.1.3, through condensation water-steam shock waves in complex pipe networks, Fig. 16.1.4, gas solution and dissolution in liquids, dissolved gas release from water in pipe network and gas-slug formation and transport, Fig. 16.1.5, diesel injection problems, Fig. 16.1.6, particles sedimentation in water, Fig. 16.1.7, turbulent mixing and transport in a NPP sump, Fig. 16.1.8, thermite injection by a high-pressure steam-hydrogen mixture into an air environment, melt-water interaction in postulated SWR 1000 severe accidents, alumina melt jet dropped into a subcooled water, urania melt jet dropped into water, Fig. 16.1.9, void formation in existing, Fig. 16.1.10, or future boiling water reactors, Fig. 16.1.11, all this demonstrates the capability of the single model architecture to handle different material systems, different intensities of interactions, large variety of the spatial and temporal scales of the simulated processes.

However, if moving to new application, validation with a set of particular experimental data is mandatory, for elaboration of the achievable prediction

accuracy, experience for the integration of the conservation equations under the particular initial and boundary conditions, etc.

Conclusions

- 1) Computational analysis of multiphase flows in practice requires special computer code architecture that is not trivially derivable from the single-phase fluid mechanics and thermodynamics.
- 2) Universal code architecture follows rigorously the analytical procedure of gaining the local volume- and time-averaged conservation equations reflecting elements like fields, their attributes, their interfacial exchange terms, etc.
- 3) The coupling between the nonlinear equations with variable coefficients in the system is designed as close as possible within a single analytical step. The entropy concept facilitates the coupling most efficiently.
- 4) Such an approach allows the best single model of a particular process or mathematical manipulation procedure to be multiply used by all different applications.
- 5) Such an approach unifies the efforts of teams in using components with prescribed interfaces derived from the basic derivation of the conservation equations. So, with time the number of the model elements will grow and become exchangeable. The data base behind the analyzer will also grow.
- 6) Graphical visualization of the processes is crucial not only for the development but later also for understanding better the simulated processes.

Appendix 1 Knowledge data base required to design a universal multiphase flow analyzer

1. technical thermodynamics; simple and multicomponent systems, equations of state;
2. behavior of metastable liquids;
3. heat and mass transfer in single- and complex multiphase systems;
4. fluid mechanics;
5. review of the world literature in particular fields of multiphase flows and processes associated with them;
6. multiphase flows; transient; one-, two- and three-dimensional; in simple geometry; in complicated geometry;
7. interaction of multiphase flows with technical structures; evaporation; condensation; spontaneous evaporation; spontaneous condensation; cavitation; flow instabilities; flow-induced vibrations; starting of steam generators; computation of forces caused by fluid transients;

8. design of components, apparatus and facilities based on mathematical modeling of complex thermal processes including complicated multiphase flows;
9. pressure and concentration waves in pipes, complex pipe systems, complex three-dimensional equipment;
10. analysis of explosive fluid–fluid interactions, melt–water interactions; steam explosion in nuclear facilities, in metallurgical facilities, in manufacturing, in space technology, in combustion motors; hydrogen deflagration and detonation, powder combustion and powder detonation; detonation of metastable fluids;
11. numerical methods for analysis of complex flow processes;
12. design of complex computer codes for simulation of the system behavior of coupled components in single-, two-, and multiphase flow region;
13. computing: numerical methods for integration of systems of ordinary and partial differential equations;
14. uncertainty analysis of computational methods;
15. nuclear technology: developing and applying mathematical methods for description and simulation of the physics of thermohydraulic processes in the reactor, primary-, secondary, and tertiary circuit, in the containment in normal operation, in transients and by severe accidents with catastrophic consequences;
16. quality assurance of complicated thermohydraulic computations;
17. quality assurance of developments of code systems for modeling of complex thermodynamic processes;
18. education of specialists in all of the above fields, courses, consultations

References

- Anderson, T.B., Jackson, R.: A fluid mechanical description of fluidized beds. *Ind. Eng. Fundam.* 6, 527 (1967)
- Kolev, N.I.: Derivatives for the state equations of multi-component mixtures for universal multi-component flow models. *Nuclear Science and Engineering* 108, 74–87 (1990)
- Kolev, N.I.: Needs of industrial fluid dynamics applications. Invited lecture, 2000 ASME Fluids Engineering Division Summer Meeting (FEDSM), Industry Exchange Program, Sheraton Boston Hotel, Boston, Massachusetts, June 11–15 (2000)
- Kolev, N.I.: 3D-Multiphase-Fluid-Dynamik: Reduzierung der Dampffuchte am RDB-Austritt der Siedewasserreaktoren, Betriebsleitertagung, Geneve (November 27–29, 2002); in English: Controlling the moisture content in the steam by using nozzles in BWR's, Eleventh International Conference on Nuclear Engineering, ICONE 11, Keio Plaza Inter-Continental, Shinjuku, Tokyo, Japan (April 20–23, 2003); ICONE11-36306, The 10th International Topical Meeting on Nuclear Reactor Thermal Hydraulics, Seoul, Korea, p. E00301 (October 5–9, 2003)

- Kolev, N.I.: Controlling the moisture content in the steam by using nozzles in BWR'S. In: Eleventh International Conference on Nuclear Engineering, ICONE 11, Keio Plaza Inter-Continental, Shinjuku, Tokyo, Japan, ICONE11-36306; ETPFG, European Two-Phase Flow Group Meeting 2003 Norway (April 20-23, 2003); The 10th International Topical Meeting on Nuclear Reactor Thermal Hydraulics (NURETH-10) Seoul, Korea (October 5-9, 2003)
- Kolev, N.I.: External cooling - the SWR 1000 severe accident management strategy Part 1: Motivation, strategy, analysis: melt phase, vessel integrity during melt-water interaction. In: Proceedings of 6th International Topical Meeting on Nuclear Reactor Thermal Hydraulics, Operations and Safety, Nara-Ken New Public Hall, Nara, Japan, NUTHOS6-N6P381 (October 4-8, 2004)
- Sha, T., Chao, B.T., Soo, S.L.: Porous-media formulation for multi-phase flow with heat transfer. *Nucl. Eng. Des.* 82, 93-106 (1984)
- Slattery, J.C.: Flow of viscoelastic fluids through porous media. *AI. Ch. E. J.* 13, 1066 (1967)
- Whitaker, S.: Diffusion and dispersion in porous media. *AI. Ch. E. J.* 13, 420 (1967)
- Whitaker, S.: Advances in theory of fluid motion in porous media. *Ind. Eng. Chem.* 61(12), 14-28 (1969)
- Whitaker, S.: Experimental principles of heat transfer. Pergamon Press Inc., New York (1977)
- Whitaker, S.: A simple geometrical derivation of the spatial averaging theorem. *Chem. Eng. Educ.*, 18-21, 50-52 (1985)
- Zemansky, M.W.: Heat and thermodynamics, 5th edn. McGraw-Hill Book Company, New York (1968)